

# **Quantitative 3D Characterization of Graphite Morphologies in Cast Iron using FIB Microstructure Tomography**

## **DISSERTATION**

zur Erlangung des Grades des  
DOKTORS DER INGENIEURWISSENSCHAFTEN  
der Naturwissenschaftlich-Technischen Fakultät III  
Chemie, Pharmazie, Bio- und Werkstoffwissenschaften  
der Universität des Saarlandes

von

**ALEXANDRA VELICHKO**

Saarbrücken

2008

Tag des Kolloquiums: 22.08.08

Dekan: Prof. Dr. Uli Müller

Berichterstatter: Prof. Dr. Frank Mücklich  
Prof. Dr. Stefan Diebels

*Посвящается родителям и деду*

*In den Wissenschaften ist viel Gewisses,  
sobald man sich von den Ausnahmen nicht irre machen lässt  
und die Probleme zu ehren weiß.*

Johann Wolfgang von Goethe



---

## PREFACE

---

The present work reports about the study of the microstructure of the graphite morphologies in cast iron and its influence on the effective properties of this material. It was performed between 01.03.2003 and 30.11.2007 at the Institute of Functional Materials at the University of Saarland.

Parts of the work have been already published by:

- A. Velichko, C. Holzapfel, A. Siefers, K. Schladitz, F. Mücklich, „*Unambiguous classification of complex microstructures by its 3D parameters applied to graphite in cast iron*“, *Acta Materialia*, 56(2008), 1981-1990
- Th. Magenreuter, A. Velichko, F. Mücklich, „*The Dependence of the Shape Parameters Roundness and Compactness of Various Graphite Morphologies on Magnification*“, *Pract. Metallography*, 45(2008), 53-71
- A. Velichko, F. Mücklich, „*Neue Möglichkeiten der objektiven Graphitklassifizierung in Gusseisen durch Nano-Tomographie und internetbasierte Online-Verfahren*“, *VDI-Berichte Giesstechnik im Motorenbau*, 1949(2007), 21-36
- A. Velichko, C. Holzapfel, F. Mücklich, „*3D Characterization of Graphite Morphologies in Cast Iron*“, *Advanced Engineering Materials*, 9(2007), 1-2, 39-45
- A. Velichko, F. Mücklich, „*Shape Analysis and Classification of Irregular Graphite Morphology in Cast Iron*“, *Pract. Metallography*, 43(2006), 4, 192-208

This work could not have come into being without support of number of persons, whom I would like to express at this point my generous gratitude.

First of all, I would like to express my gratitude to my supervisor Prof. Dr.-Ing. Frank Mücklich, for his trust in me, personal and scientific support. I am very thankful for his discussions which have been a constant source of scientific inspiration.

I am thankful to Prof. Dr.-Ing. Stefan Diebels for co-refereeing this thesis.

I acknowledge the efficient collaboration with the following partners who have contributed their interesting problems within the project Nr. 03N3119 sponsored by German Federal Ministry of Education and Research: Herbert Junk, Andreas Spick, Dirk Radebach, Halberg Guss GmbH, Saarbrücken; Rolf Heinemann, Volkswagen AG, Wolfsburg; Dr. Iris Altpeter, Prof. Walter Arnold, Dr. Udo Netzelman, Dr. Michael Maisl and Ute Maisl, Fraunhofer IZfP, Saarbrücken.

I am thankful to Prof. Dr.-Ing. Weikum for successful cooperation by the development of the on-line classification of graphite.

I would like to thank:

Dr. Christian Holzapfel, Dr. Flavio Soldera, Christoph Pauly for the help with microstructure analysis using Dual Beam workstation;

Peter Leibenguth for TEM study and valuable discussions;

Dr. Jorge Fiscina for the help with the electrical measurements;

Dr. Katja Schladitz, Dr. Claudia Lautensack Fraunhofer ITWM, Kaiserslautern for the help with 3D analysis and interesting discussions;

Hans Jakoby, Sasha Schneider, Wolfgang Ott for the sectioning of the numerous cast iron samples and constructing the four point measuring setup;

Claudia Maas for metallographical tips and enjoyable working atmosphere through all this years;

Dr. Andrés Lasagni for some suggestions with data analysis;

Nicolas Jeanvoine for the help with FlexPDE simulations;

Dr. Andreas Wiegmann for providing 3D simulation software;

Students Thomas Magenreuter, Corina Richter, Isabelle Galmiche, Andrea Siefers, and Bérenger Florence who contributed with their work to the different aspects of the current thesis.

I gratefully acknowledge all the colleges of the chair of Functional Materials, of University of Saarland for the wonderful atmosphere and support. I owe special thanks to Michael Engstler, Carsten Gachot and Jules Dake for the accurate reviewing of this manuscript.

Thanks to many others, who have contributed in one way or another to a good working atmosphere, with advice or just by sharing good time: Alexandra, Amadou, Antoine, Awa, Christian, Hakima, Irina, Karsten, Laure, Mathias, Mikael, Muriel, Olga, Sebastien, Xavier and all those I forgot to mention.

Finally, I would like to thank my family for their constant support, unconditional love and their faith in me.

Saarbrücken, May 2008

Alexandra Velichko

---

# TABLE OF CONTENTS

---

PREFACE.....	V
TABLE OF CONTENTS .....	VII
ABSTRACT.....	XI
ZUSAMMENFASSUNG.....	XII
TABLE OF SYMBOLS AND ABBREVIATIONS.....	XIII
1 INTRODUCTION.....	1
<b>I. THEORY .....</b>	<b>3</b>
2 CAST IRON MICROSTRUCTURE AND PROPERTIES .....	5
2.1 Different Graphite Morphologies in Cast Iron .....	7
2.1.1 Cast Iron with Flake Graphite (FG) .....	7
2.1.2 Cast Iron with Spheroidal Graphite (SG).....	9
2.1.3 Cast Iron with Vermicular Graphite (CG).....	11
2.1.4 Malleable Cast Iron (TG).....	13
2.2 Influence of the Graphite Morphology on the Properties of Cast Iron.....	14
2.2.1 Mechanical Properties and Density of Cast Iron.....	14
2.2.2 Thermal and Electrical Conductivity .....	17
2.2.3 Electromagnetic Properties for Non-Destructive Microstructure Characterization .....	18
2.3 Analytical Models and Prediction of Material Properties .....	19
2.3.1 Calculation of the Effective Properties of the Composites .....	20
2.3.2 Existing Correlations for Cast Iron .....	24
3 QUANTITATIVE MICROSTRUCTURE CHARACTERIZATION .....	29
3.1 Basic Characteristics of Quantitative Image Analysis .....	29
3.1.1 Particle Based Parameters .....	29
3.1.2 Field Based Parameters .....	30
3.1.3 Stereological Equations for Calculation of the Basic Characteristics.....	31
3.2 Characterization and Classification of Graphite Morphology in 2D.....	32
3.2.1 Classification According to Norm DIN EN ISO 945.....	32
3.2.2 Shape Characterization.....	33
3.2.3 Other Approaches to Graphite Classifications .....	35
3.3 Characterization in 3D.....	37
3.3.1 X-ray and Synchrotron Microtomography .....	39
3.3.2 FIB-Tomography – New Tool.....	40
3.3.3 Analysis of Spatial Tomography Images .....	42

<b>II.</b>	<b>EXPERIMENTAL .....</b>	<b>43</b>
4	EXPERIMENTAL PROCEDURE .....	45
4.1	Sample Preparation.....	45
4.1.1	Chemical Composition.....	45
4.1.2	Metallographic Preparation .....	45
4.1.3	Surface Quality.....	46
4.1.4	Chemical Etching .....	48
4.2	Microscopic Characterization of the Microstructure.....	49
4.2.1	Optical and Scanning Electron Microscopy.....	49
4.2.2	Transmission Electron Microscope (TEM) Study .....	50
4.2.3	FIB Nanotomography.....	52
4.3	Quantitative Image Analysis in 2D and 3D.....	56
4.3.1	Image Processing and Binarization .....	56
4.3.2	Determination of Basic Parameters from 2D Images.....	56
4.3.3	Quantitative Analysis of 3D Images .....	60
4.4	Measurement of the Electrical Resistivity .....	60
4.4.1	Four-Point Method for Measuring Electrical Resistivity .....	60
4.4.2	Determination of Electrical Resistivity ( $\rho$ ) .....	61
4.5	FEM Simulations in 2D and 3D .....	62
4.5.1	Using FlexPDE.....	62
4.5.2	Using GeoDict.....	64
<b>III.</b>	<b>RESULTS AND DISCUSSIONS .....</b>	<b>67</b>
5	ELECTRICAL PROPERTIES .....	69
5.1	Electrical Resistivity of Cast Iron with Different Graphite Morphologies .....	69
5.2	Influence of Particle Volume Fraction, 2D Particle Density, 2D Size .....	70
5.3	Comparison with the Analytical Bounds.....	72
6	GRAPHITE CLASSIFICATION.....	77
6.1	2D Shape Analysis of Graphite Morphologies.....	77
6.1.1	Analysis of DIN Series Images Using Particle Based Method .....	77
6.1.2	Analysis of the Real Graphite Morphologies .....	79
6.1.3	Shape Size Dependency .....	81
6.2	Classification Using Image Analysis Techniques .....	83
6.2.1	Classification Algorithm .....	83
6.2.2	Results of the Automatic Classification of Graphite.....	84
6.2.3	Extension of Graphite Classification on Different Magnifications.....	86
6.3	Summary and Application of 2D Graphite Classification.....	92
6.3.1	Outline for 2D Graphite Classification .....	92
6.3.2	Influence of the Fraction of Graphite of Different Morphologies on the Physical Properties .....	93

7	3D GRAPHITE CHARACTERIZATION.....	95
7.1	Graphite Morphology and Crystal Structure .....	95
7.1.1	Description of the 3D Graphite Morphology .....	95
7.1.2	Graphite Nucleation, Crystal Structure and Growth Mechanisms .....	105
7.2	3D Analysis of Reconstructed 3D Models .....	112
7.2.1	Comparison of the Parameters for the Individual Graphite Particles of Different Morphology.....	112
7.2.2	Analysis of the Connected Flake Graphite Structure with the Help of 2D and 3D Field Based Parameters.....	118
7.3	Analysis of 2D Sections Through Reconstructed 3D Models.....	125
7.3.1	Size-Shape Dependency and Comparison with 2D Analysis.....	126
7.3.2	Identification of the Limits of 2D Classification .....	127
7.4	Summary and Applications of the 3D Results.....	129
7.4.1	Development of On-line POCA Application .....	130
7.4.2	Simulations of Physical Properties and Comparison with Experimental Results.. ..	134
8	CONCLUSIONS .....	141
<b>IV.</b>	<b>APPENDIX .....</b>	<b>145</b>
9	APPENDIX.....	147
9.1	Calculation of Effective Properties of Microstructural Constituents .....	147
9.2	Classification Limits.....	149
9.3	Roundness: Dependency on the Maximum Feret Diameter .....	150
9.4	Parameters of the Regression Analysis [144].....	151
9.5	Estimation of the Effective Conductivity of Graphite.....	154
10	REFERENCES .....	157
	CURRICULUM VITAE .....	165



---

## ABSTRACT

---

Cast iron with different graphite morphologies were thoroughly analyzed and their influence on the thermal and electrical properties was studied with the goal of determining clear correlations between manufacturing parameters, microstructure and properties for advanced material development and non-destructive quality control.

It was shown, that there is no simple relationship to describe these properties based only on the microstructural parameters volume fraction and specific surface area. Cast iron properties depend mainly on the graphite type. To provide objective graphite classification an automatic algorithm was developed. Particle parameters: roundness, compactness and MaxFerret provide a straight forward classification.

Graphite morphology was analyzed with FIB tomography. Graphite crystal structure, nucleation and growth mechanisms were studied using chemical analysis and analysis on TEM-foils. 3D quantitative characterization of the size, shape and spatial connectivity, as well as the growth mechanisms and thus the structure of different graphite morphologies was done. Analysis of 2D sections of the 3D particles suggested improving the 2D classification by using “support vector machine”.

Effective properties of cast iron were simulated using tomographic data. It was shown, that for the correct estimation not only volume fraction, size and shape of the graphite particle, but also their crystallographic structure and spatial connectivity has to be taken into consideration.

---

## ZUSAMMENFASSUNG

---

Mit dem Ziel der Feststellung eines Zusammenhangs zwischen Herstellungsparameter, Mikrostruktur und Eigenschaften für die fortgeschrittene Werkstoffentwicklung und zerstörungsfreie Qualitätskontrolle wurde das Gusseisen mit unterschiedlichen Graphitmorphologien sorgfältig analysiert und sein Einfluss auf thermische und elektrische Eigenschaften studiert.

Die Beschreibung der Eigenschaften basierend ausschließlich auf den Gefügeparametern Volumenanteil und spezifische Grenzfläche ist nicht möglich, da keine direkte Beziehung erkennbar ist. Die Eigenschaften des Gusseisens hängen überwiegend von dem Graphittyp ab. Ein automatischer Algorithmus wurde entwickelt, der mit Hilfe von den Parametern Rundheit, Kompaktheit und MaxFeret eine eindeutige objektive Graphitklassifizierung liefert.

Unterschiedliche Graphitmorphologien wurden mit FIB-Tomographie analysiert. Ihre Kristallstruktur, Keimbildung und Wachstumsmechanismen wurden mittels chemischer Analyse und Analyse an TEM-Folien untersucht und quantitativ in 3D charakterisiert. Die Analyse der 2D Schnitte durch 3D Graphitteilchen lässt erkennen, dass die 2D Klassifizierung durch die Anwendung von „Stutzvektor Verfahren“ verbessert werden kann.

Effektive Eigenschaften von Gusseisen wurden basierend auf tomographischen Daten simuliert. Für ihre korrekte Abschätzung muss nicht nur Volumenanteil, Größe und Form von Graphitpartikeln, sondern auch deren kristallographische Struktur und räumliche Konnektivität beachtet werden.

---

## TABLE OF SYMBOLS AND ABBREVIATIONS

---

### SYMBOLS

<i>I, III, IV-V, VI</i>	flake/ vermicular/ temper/ nodular graphite types		parameters $x$ and $y$
<i>A, B, C, D, E</i>	flake graphite arrangements	$h, w$	height/ width of the sample
$a$	size of the analyzed region	$I$	current
$a, b$	parameters of the regression analysis	$J$	heat flux
$a, b, c$	lattice parameters	$\vec{j}$	electrical current density
$A$	object area	$K$	integral of the total curvature
$A_{cir}$	area of the circle	$K_V$	density of the integral of total curvature
$A_i$	area of projection in $i$ -direction	$ka, kc$	conductivity of graphite in $a$ and $c$ crystallographic direction
$A_A$	area fraction	$kx, ky$	conductivity in $x$ - and $y$ -direction
$A_{Ak}$	area fraction of all particles of the size class $k$	$L_A$	length of the line per unit of surface
$A'_i$	calculated constants describing the effect of the alloying elements on the $\lambda_{ph}$	$L_i$	length of projection in $i$ -direction
$A_i$	atomic weights of the alloying elements	$L_0$	Lorenz number
$C$	compactness	$L_e$	measured Lorenz number at 300 K for the term involving $\rho(\text{Fe})$
$C$	connectivity	$L_L$	linear fraction
$C_V$	connectivity per unit volume	$M$	integral of the mean curvature
$c_i$	concentration (at. %) of the alloying elements	$M_V$	density of the integral of mean curvature
$C_{eutectic}$	eutectic C-content	$m_i$	concentration (weight %)
$C_{total}$	total C-content	$MaxFeret$	object's maximum Feret diameter
$CI$	confidence interval	$MinFeret$	object's minimum Feret diameter
$ConvexP$	convex perimeter	$N_A$	Avogadro constant
$D$	distance between Cu-wires	$N$	particle number/ number
$D_{cir}$	diameter of the circle	$N_A$	particle number per unit area
$ds$	surface element	$N_{Holes}$	number of holes
$d_S, d_M$	fractal dimension for the measured values $S$ and $M$	$N_L$	number of points per line length
$E$	elastic modulus	$N_{Tunnels}$	number of tunnels
$\vec{E}$	electrical field strength	$N_V$	particle number per unit volume
$f_1, f_2, f_3$	3D shape parameters	$P$	perimeter
$f_4, f_5, f_6$	3D shape parameters for compactness/ roundness/ convexity	$P_P$	point fraction
$Feret$	Feret diameter	$Pro$	projection
$g_{ix}, G_{ix}$	minimum and maximum limits of the classification regions for the	$PV$	distance in $\mu\text{m}$ between the highest and the deepest point of the surface
$g_{iy}, G_{iy}$		$q$	aspect ratio of the spheroid
		$R$	electrical resistance
		$r$	curvature radius

$r_1, r_2$	the minimum and the maximum curvature radii		to the thermal conductivity
$R_a$	linear deviation of all measuring points of the surface from the mean value	$\lambda_a, \lambda_c$	thermal conductivity of graphite in $a$ - and $c$ -crystallographic direction
$R_m$	tensile strength	$\lambda_{\parallel}, \lambda_{\perp}$	thermal conductivity in the direction parallel and perpendicular to lamellae
$rms$	square deviation of all measuring points $N$ of the surface from the mean value	$\lambda_{Sphere}$	estimated thermal conductivity of the ideal graphite nodule
$S^{eq}$	effective polarization factor	$\mu$	maximum permeability
$S_{\perp}$	polarization factor perpendicular to the shortest main axis of an oblate spheroid	$\bar{\mu}$	mean value
		$\bar{\mu}_k$	mean value for the size class $k$
		$\bar{\bar{\mu}}$	area weighted mean value
$S_c$	saturation degree	$\rho$	electrical resistivity
$S$	surface area	$\rho'_i$	resistivity per at. % of the alloying elements
$S_{close}, S_{open}$	particle surface after morphological operations "close"/ "open"	$\rho_{\parallel}, \rho_{\perp}$	electrical resistivity in the direction parallel and perpendicular to lamellae
$S_{FillHoles}, S_{FH}$	particle exterior surface		
$S_V$	density of the surface area		
$T$	temperature	$\rho_{el-ph}$	contribution to the electrical resistivity due to scattering of conduction electrons by phonons, magnetic excitations and static lattice defects
$T_m$	mean temperature	$\rho_{el-magn}$	
$U$	voltage	$\rho_{el-def}$	
$V$	volume		
$V_{nucl.}, V_{Fe}$	volume of the nucleus/ impurities		
$V_V$	volume fraction	$\sigma$	electrical conductivity
$V_{Gr}, V_{Pearl}$	volume fraction of graphite/ pearlite	$\sigma_{Gr}, \sigma_{Pearl}$	electrical conductivity of graphite/ pearlite
$V_{Sphere}, V_a, V_c$	portion of conductivities	$\sigma_{eff}$	effective electrical conductivity
$V_h$	volume fraction of the high-conductive phase	$\sigma_h, \sigma_{lo}$	electrical conductivity of the high- / low-conductive phase
$V_i$	volume fraction of inclusion phase		
$x, y, z$	variables, coordinates	$\sigma_{upper}, \sigma_{lower}$	upper and lower bounds on the effective electrical conductivity
$x_i, y_i$	individual measured value		$\sigma_{eff}$
$Z$	atomic number	$\sigma_m, \sigma_i$	electrical conductivity of the matrix/ inclusions
$\nabla T$	temperature gradient		
$\nabla V$	voltage gradient	$\sigma_{\parallel}, \sigma_{\perp}$	electric conductivity in the direction parallel and perpendicular to lamellae
$\varepsilon_f$	fracture strain		
$\zeta_i$	microstructural parameter		
$\kappa(P)$	curvature at the point $P$	$\bar{\sigma}$	standard deviation
$\kappa_1(P), \kappa_2(P)$	the minimum and the maximum curvature at the point $P$	$\bar{\bar{\sigma}}$	standard deviation of value $\bar{\mu}$
$\Lambda$	thermal conductivity	$\chi$	Euler number
$\lambda_{eff}$	effective thermal conductivity	$\chi_A$	Euler number per unit area
$\lambda_{Gr}$	thermal conductivity of graphite	$\chi_V$	Euler number per unit volume
$\lambda_{ph}, \lambda_{el}$	phonon and electron contribution		

## ABBREVIATIONS

2D	Two dimensional	GD	Crystallographic growth direction
3D	Three dimensional	HS	Hashin-Shtrikman bounds
3MA	Micromagnetic Multiparameter Microstructure and Stress Analysis	IEEE	Institute of Electrical and Electronics Engineers
ASM	American Society for Metals	ISO	International Organization for Standardization
ASTM	American Society for Testing and Materials	MAVI	Modular Algorithms for Volume Images
bcc	Body-centered cubic	MD	Magnetic disc
BSE	Backscattered electrons	OM	Optical microscope
CBXRT	Cone-beam x-ray tomography	PMMA	Polymethylmethacrylate
CCD	Charge-coupled device	POCA	Particle-Oriented Classification and Analysis
CG	Cast iron with vermicular graphite/vermicular (compacted) graphite	ROM	Rule of mixtures
CT	Computed Tomography	SCM	Selective carbon milling precursor
DEM	Differential effective medium approach	SE	Secondary electrons
DIN	Deutsches Institut für Normung eV German Institute for Standardization	SE-I	Ion induced secondary electrons
EBSD	Electron backscatter diffraction	SEM	Scanning electron microscope
EDX	Energy dispersive x-ray	SG	Cast iron with spheroidal graphite/spheroidal graphite
EN	European Norm	STEM	Scanning transmission electron microscope
FE	Finite element	SVM	Support vector machine
FEM	Finite element methods	TEM	Transmission electron microscope
FG	Cast iron with flake graphite/ flake graphite	TG	Malleable cast iron/ temper graphite
FIB	Focused ion beam	TXM	Transmission x-ray microscope



---

# 1 INTRODUCTION

---

The development of new, more powerful technologies in the automobile industry offers enormous performance advantages, while at the same time providing high safety standards and obeying the emission regulations. The growing requirements on the material properties for such advanced applications have resulted in the pursuit of new alloys, but also in the attempt to improve the existing wide-spread materials. Cast iron, known in Europe for more than six centuries, recently experienced a renaissance. The reasons for its high potential are the low production costs and new well-controlled casting technologies, which allow the exact tailoring of the wide range of microstructural configurations and thus a wide range of properties. Further variation of casting procedure and additives can even be used to produce a gradually changing microstructure. Such adaptive microstructural design makes this traditional material highly competitive even in comparison with aluminum alloys.

The significant drawback is that still only empirical correlations between manufacturing parameters and microstructure, and microstructure and properties are known. This is predominantly due to the insufficient description of the graphite morphology which is, in most cases, still based on the subjective comparison of two dimensional micrographs with the series images of the DIN EN ISO 945 [1] standard. Whereas the essential link between the materials processing and its properties is the 3D nature of materials microstructure.

Thus, it is important to provide a quantitative characterization of the graphite morphology, size, and arrangement in order to unambiguously clarify its influence on the mechanical and physical properties of cast iron. Theoretical assumptions of graphite's effect on different properties have been broadly presented in the literature. Although considering its complex shape, the research was often limited to only one graphite morphology and no fundamental models were proposed. Such models can build the basis for clear correlations with different material properties, e.g. electro-magnetic, which can be used for non-destructive quality control.

Hence, the goal of the work is to identify the main quantitative characteristics of the different graphite morphologies which play the decisive role in determining the properties for cast iron. Chapter 2 presents cast iron in view of different graphite morphologies. It summarizes the known empirical correlations for different mechanical and physical properties and reviews the existing models for the estimation of the effective properties of the material from its microstructural characteristics.

Chapter 3 is dedicated to the fundamentals of the quantitative image analysis. It sums up the known approaches to the problem of the graphite classification and presents the possibilities of 3D image analysis.

In chapter 4 methods of the microstructural characterization and quantification are described in detail. The experimental setup for the measurement of the electrical conductivity and the principle of estimation of the effective properties of composite materials with the help of 2D and 3D simulations are presented.

Chapter 5 presents the results of the electrical measurements. First correlations with the microstructural characteristics as well as the comparisons with the existing models are shown. It becomes clear that only volume fraction of graphite inclusions is not sufficient for the correct estimation of the effective properties of cast iron. It was confirmed that the properties are principally determined by the graphite morphology.

As a first step the automatic, reliable and reproducible classification technique based on the conventional 2D images of the microstructure is developed in the chapter 6. Such a procedure can be used in any research or quality control laboratory as it does not require any sophisticated equipment.

Chapter 7 describes the second step – 3D analysis of morphology variations of different typical graphite precipitations by serial sectioning in the FIB/SEM dual beam facility. These examinations were used to improve the technically relevant 2D classification through the evaluation of the most significant microstructural parameters for the correct classification and sequential development of the on-line available classification system. The application of a support vector machine to analyze the sensitivity and the precision of this study enabled the definition of a new image analyzing strategy to classify the graphite categories with highest possible and even calculable precision.

Additionally, the nucleation and growth mechanisms of different graphite morphologies were studied and quantified using advanced image analysis techniques. This provided essential information concerning graphite crystallographic structure and thus graphite properties, which made it possible to estimate the effective properties of the cast iron with the help of 2D and 3D simulations and to draw the important conclusions about the significance of the different microstructural characteristics on the material properties.

Chapter 8 summarizes the important results with regard to the objective of the work.

## I. THEORY



---

## 2 CAST IRON MICROSTRUCTURE AND PROPERTIES

---

The term cast iron identifies a large family of ferrous alloys. The ASM Specialty Handbook [2] defines cast irons as irons that are “multicomponent ferrous alloys, which solidify with a eutectic”. They contain major amounts of iron, carbon (2-4 %), and silicon (> 1.5 %) and minor amounts of alloying elements. Cast iron is experiencing a renaissance in modern technology. It has many advantages over some even modern materials. The fluidity of cast iron, due to the eutectic or near eutectic composition, is far better than that of steel because the casting temperature is considerably higher than the melting point. The fluidity of any metal, including cast iron, is a direct function of the difference between the pouring temperature and the solidification temperature. Cast iron can also be melted in conventional furnaces, including the electric, crucible and the air furnace, which is similar to an open hearth except that the air is not preheated. This process makes creating cast iron by far the cheapest method of melting and is also a reason for the low cost of installation [3]. In addition to these process advantages, cast iron also has some product advantages deriving directly from the fact that it contains free graphite. During the solidification of gray cast iron the graphite phase builds a lattice with low atomic packing density, which leads to very low volume oscillations [4]. Thus, the danger of shrinkage cavity formation is reduced.

Cast iron can be classified according to solidification in gray and white iron. Gray cast iron is formed through the solidification of the thermodynamic stable graphite phase, i.e. elementary carbon, namely graphite forms from the liquid. Brittle carbide phase  $\text{Fe}_3\text{C}$  (cementite) forms next to the  $\gamma\text{-Fe}$ , when the Fe-C-alloy solidifies according to the metastable diagram. The terms white and gray are historically based on the color of the fracture surface. White iron fractures along the iron carbide plates, and gray iron fractures along the graphite plates (flakes). The mixture of both variants is known as mottled cast iron.

Alloying elements and cooling rates during the phase transformation control the choice of stable or metastable solidification. Silicon plays a decisive role. It moves the eutectic point in the Fe-C-diagram towards lower C-contents. The so known “saturation degree”  $S_c$  shows to what extent cast iron varies from the eutectic composition. It describes the quotient from the total and eutectic C-content:

$$S_c = \frac{C_{total}}{C_{eutectic}} \quad 2.1$$

The shift of the eutectic C-content is conducted by Si as well as by the accompanying elements such as e. g. P and Mn.  $C_{eutectic}$  can be calculated according to the following formula [5]:

$$C_{eutectic} = 4.23 - 0.312 \cdot Si - 0.33 \cdot P + 0.006 \cdot Mn \quad 2.2$$

$S_c$  value  $< 1$  means hypoeutectic,  $S_c = 1$  eutectic and  $S_c > 1$  hypereutectic solidification. The diagram of Maurer in Figure 2.1 shows the dependency of solidification from the C and Si content. Stable (gray) solidification is promoted by high C- and Si-content.

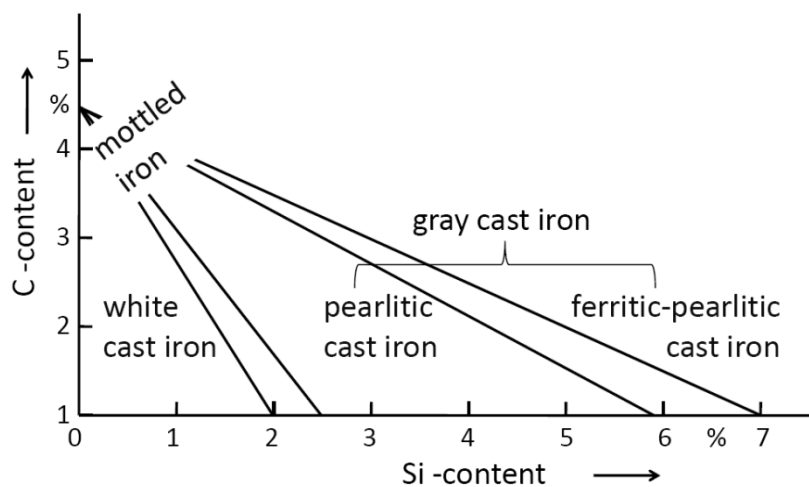


Figure 2.1 Phase formation in cast iron according to Maurer diagram (after [4]).

Silicon supports the dissolution of cementite, which results in formation of elemental C. High contents of Al, Ti, Ni or Cu promote this type of solidification. Whereas, Mn, Cr, Mo or V favor the white (metastable) solidification.

In addition to that, it must be noticed, that the various properties of these irons can be enhanced by altering their internal structure, by elemental manipulation through processing. Alloying elements, including silicon when it exceeds about 3 %, are usually added to increase the strength, hardness, hardenability, or corrosion resistance of the basic iron and they are often added in quantities sufficient to affect the occurrence, properties, or distribution of constituents in the microstructure [6]. Alloying elements are used almost exclusively to enhance resistance to abrasive wear or chemical corrosion or to extend service at elevated temperatures. Adding small amounts of alloying elements such as chromium, molybdenum or nickel can give gray and ductile irons a higher strength to ensure the attainment of a specified minimum strength in heavy sections. Next to alloying the inoculation, i.e. the addition of a small amount of substances, like ferrosilicon, cerium, or magnesium, is used to control size, shape,

and/or distribution of graphite particles. The quantities of material used for inoculation neither change the basic composition of the solidified iron nor alter the properties of individual constituents [6].

Modern cast iron materials (as well as the samples used in this work) base almost exclusively on the gray solidification. During the cast iron solidification the non metallic graphite phase can appear in very different morphologies. They will be described in the following section.

## 2.1 DIFFERENT GRAPHITE MORPHOLOGIES IN CAST IRON

Graphite morphology and size can be more or less efficiently controlled in the modern foundry industry using certain alloying elements and inoculation, as well as varying processing technology. Certain norms have been developed which precise the chemical composition and mechanical properties of some groups of cast irons e.g. FG DIN-EN 1561, SG DIN-EN 1563, and TG DIN-EN 1562. Deviations from the standard values can unfortunately occur due to unique casting procedure in each individual foundry. The graphite microstructure stays the most important factor influencing the required properties [7], [8], [9]. Thus its exact characterization (see section 3.2) is the only reliable indicator for mechanical properties proposed by foundries and required by customers. DIN EN ISO 945 [1] defines six types of graphite morphologies (see Figure 2.2). The following sections present different graphite shapes and their formation.

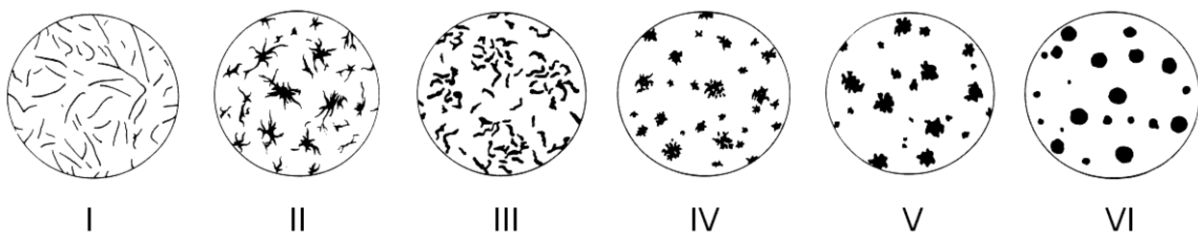


Figure 2.2 Standard series images of the six graphite types according to DIN EN ISO 945 [1].

### 2.1.1 CAST IRON WITH FLAKE GRAPHITE (FG)

Flake graphite in cast iron appears on the metallographic two-dimensional section (Figure 2.3) as separate platelets: thin, coarse, in knots or nest like. In three-dimensional space these plates are interconnected with each other and build a complex network. Graphite skeleton interrupts the continuity of the metallic matrix, which is, depending on the chemical composition and cooling rates, ferritic ( $\alpha$ -Fe), pearlitic ( $\alpha$ -Fe + Fe<sub>3</sub>C) or the mixture of ferritic and pearlitic

structure. Pearlitic microstructure of matrix is often strived for due to its good tensile strength [10].

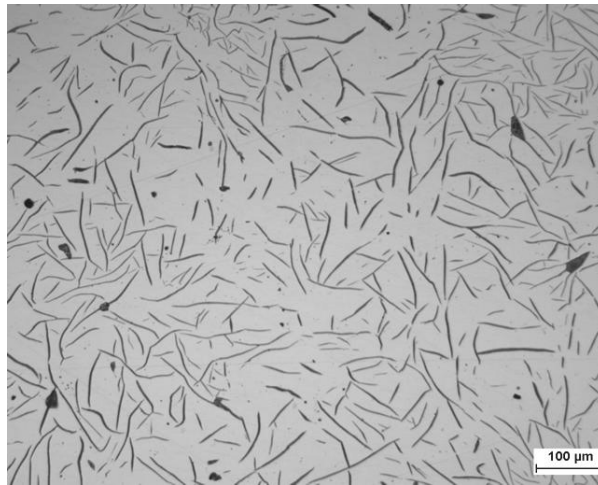


Figure 2.3 Cast iron with flake graphite (optical micrograph, magnification 200x).

Brittle graphite has a very low bonding to surrounding matrix. Thus, flake graphite tends to build micro cracks on the lamella's tips under even small tension stresses. The tensile stresses here are higher than the applied external tensile stress, which leads to inhomogeneous stress distribution [4]. On the other hand, the compression stresses can be much better tolerated; the elastic modulus is comparable with the one for steel. The upper limit of the tensile strength reaches approximately 400 MPa (EN-JL1050 according to DIN EN 1561). Next to its good fluidity and machinability cast iron with flake graphite is characterized by a very good damping capacity which is able to reduce noise and minimize the level of applied stresses.

Graphite in gray iron solidifies mostly in form of platelets, when no particular alloying elements were added. The eutectic microstructure by the stable solidification consists of metallic ( $\gamma$ -Fe) and non metallic (C) phases. No common growing front line is observed, due to the different growing mechanisms of these two phases. The growing frontier is somewhat ball-shaped, caused by the graphite flakes to rush in front in all different direction. So known eutectic cells are formed, where the lamellae splits into numerous branches during the further growing [4]. This leads to plate-like branched out graphite skeleton and appears in a two-dimensional section in form of separate lamellae (Figure 2.3).

Graphite, the layered structure of honeycomb-like hexagonal plates, has two growing axes (Figure 2.4).

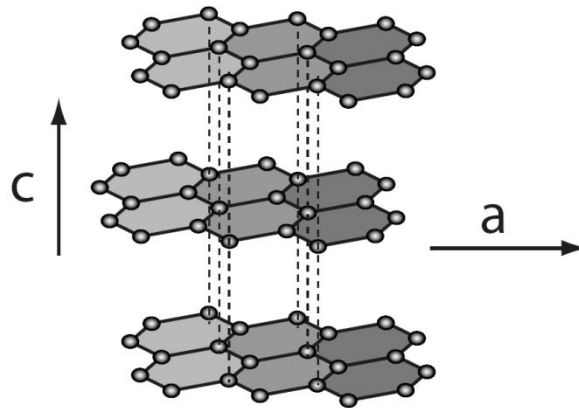


Figure 2.4 Schema of graphite structure. Each basal plane consists of honeycomb-like hexagonal lattice. The growing axes are a-axis, parallel to basal plane, and c-axis, perpendicular to basal plane.

Theory says, that the flake growth occurs parallel to base plane of the hexagonal layered structure of graphite, so along the a-axis. This deposition is most rapid and has highest probability. Adsorption of S- or O-atoms on this plane supports this type of graphite formation [4], [11]. Graphite size, shape and distribution can vary depending on cooling rates, cast additives or impurities and overheating of the melt [1], [10] (see also Figure 2.5).

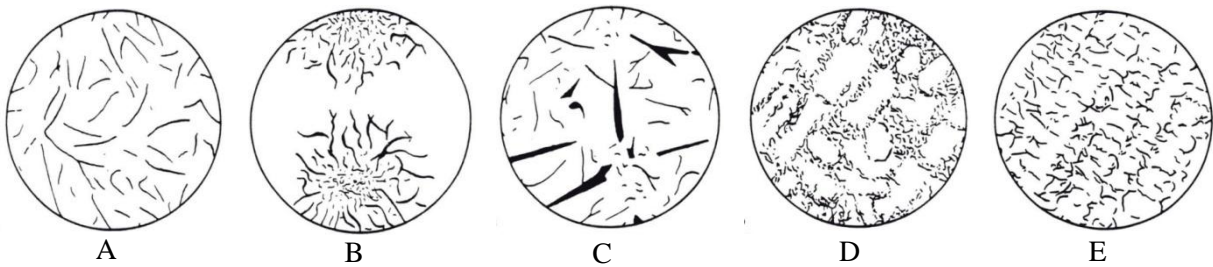


Figure 2.5 Five classes A through E of lamellar graphite type I [1].

### 2.1.2 CAST IRON WITH SPHEROIDAL GRAPHITE (SG)

For ductile iron (spheroidal graphite iron), minor elements can significantly alter the structure in terms of graphite morphology, chilling tendency, and matrix structure. Minor elements can either promote the spheroidization of graphite or can have an adverse effect on graphite shape. Ideally graphite in ductile iron is almost entirely of nodular shape. These ball-like objects appear on the two-dimensional section as small and large, more or less circular particles (Figure 2.6). Graphite with such shape is hardly strength reducing, causing only fair notch effect. Due to this reason properties of ductile iron are mainly defined by matrix structure. The matrix can be ferritic, ferritic-pearlitic or pearlitic. The mechanical properties of ductile iron approach the properties of steel, i.e. different strain and strength values can be tailored depending on the

chemical composition (according to DIN-EN 1563, EN-JS-1020 till EN-JS-1080 are currently available materials). Tensile strength of SG is considerably higher than for FG. On the other hand the damping capacity is lower. Ductile iron in the annealed condition has now been accepted as a construction-material for a variety of applications including electric motor frames, compressor cylinders, valves and other parts.

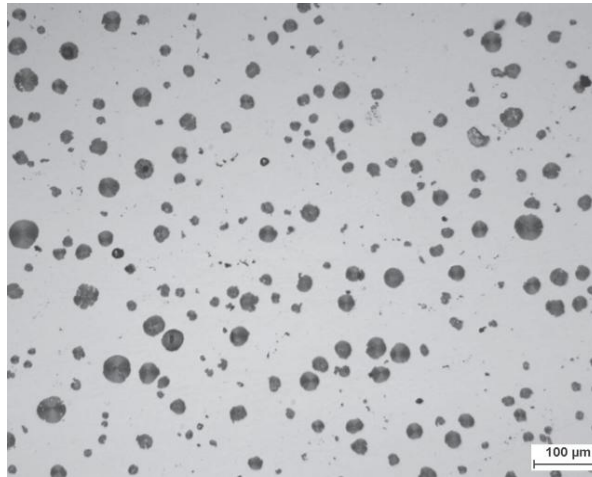


Figure 2.6 Cast iron with spheroidal graphite (optical micrograph, magnification 200x).

Certain requirements are set on pig iron for the fabrication of cast iron with spheroidal graphite. Next to the certain contents of silicon and carbon the strong desulfurization and desoxidation of the melt is very important. This is reached by the melt treatment with magnesium (or cerium). Magnesium is added to the 1200 - 1400 °C hot Fe-C melt in form of wires from MgNi- or MgSi-alloys. The evaporation temperature of Mg is somewhat over 1100 °C, and Mg is a very reactive metal. Hence fierce mixing reaction occurs by introducing Mg in the melt, which leads to homogeneous distribution of the magnesium in the melt. The trace elements oxygen and sulfur are thus bound [4].

The growth of nodular graphite is different than that of flake graphite (FG). Essentially two different theories of nodular graphite formation exist [12], the heterogenic nucleation theory and the so known bubble theory.

According to the heterogenic nucleation theory, nuclei form first out of melt. These consist mostly of sulfides and oxides of magnesium. Inoculation (e.g. with fine grained ferrosilicon) shortly before casting also provides the nuclei for crystallization, which eventually influence the amount and size of the spheroids. The growth of the graphite nodules begins on the nuclei. So formed graphite spheroids are enclosed in austenite, so that the nodule is completely isolated from the melt. The further growth of small nodule occurs through the diffusion of car-

bon through the austenite cover. The spheroidal graphite grows in the direction of c-axis, so perpendicular to the basis plane of graphite structure. The actually preferred growing direction, the a-direction, is apparently blocked by the nodularizing additives, which forces the graphite to grow layer by layer. The suitable growth scheme, which respects the favorable growth in the a-direction and at the same time supports the observation of the crystallographic structure of the nodular graphite, was presented by Double and Hellawell [11] and refined by Miao et al. [13].

The theory of heterogenic nucleation becomes doubtful if no nucleus is found in the center of some graphite nodules. Gorshkov et al. [14] has published the bubble theory for the first time. It assumes that carbon starts to grow on the gaseous magnesium, which exists in the melt in form of gas bubbles. Graphite grows striving for the center of the gas bubble. When this process is completed, the graphite nodule grows to the outside following the heterogenic nucleation theory. The amount of the Mg gas bubbles and thus the amount of the graphite nodules depend on the temperature of the cast. Higher temperature denotes a lot of small bubbles. Yamamoto et al. [15] has further developed the bubble theory.

### 2.1.3 CAST IRON WITH VERMICULAR GRAPHITE (CG)

The worm-like<sup>1</sup> shape of graphite is characteristic for the cast iron with vermicular graphite (Figure 2.7).

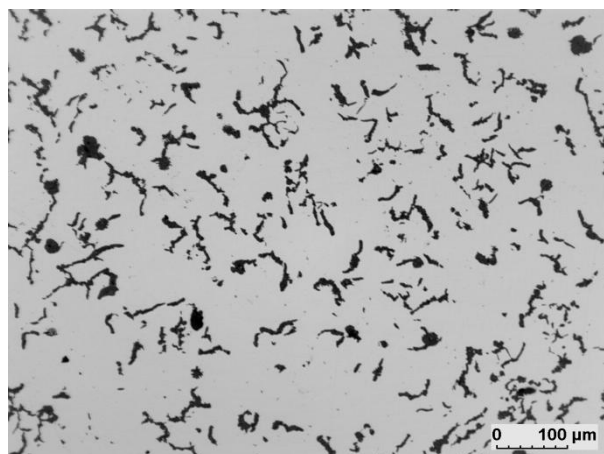


Figure 2.7 Cast iron with vermicular graphite (optical micrograph, magnification 200x).

Compacted graphite (CG) irons have a graphite shape between spheroidal and flake, and most of the properties of CG irons lie between those of gray and ductile iron. Less intensely pro-

---

<sup>1</sup> lat. vermiculus = the worm

nounced interruption of the iron matrix is caused by the rounded shape of graphite branches in contrast to flake graphite. Hence depending on the matrix microstructure, tensile strength of CG reaches from 300 to 500 N/mm<sup>2</sup>. Moreover the ductility is much higher than for the cast iron with flake graphite with the same tensile strength, whereas the thermal conductivity is only slightly lower [10], [16]. This fact makes CG attractive for foundry products which have to provide high performance under thermal stresses, in particular thermal cycled stresses. Such components are steelwork molds, engine blocks for diesel motors and components of the automobile breaks [10]. The drawback of the CG is its poor machinability.

Investigations with the help of thermal analysis shows, that vermicular graphite particles, alike the nodular graphite, are formed according to the inoculation process. The supercooling at the beginning of the eutectic reaction is almost identical with the one for nodular graphite. Although lies the growing temperature in the stationary case near the growing temperature for the flake graphite [17]. Another theory of the formation of vermicular graphite is the site theory of Itofuji [12], which is based on the bubble theory. The growth of the graphite structure depends here on a so known liquid channel. If the graphite nodule still has a contact with the melt, the further growth in this direction will occur. The growth is thus similar to SG, although for SG the graphite nodule is completely isolated from the melt. Further details to the formation of vermicular graphite can be found in [18] and [19]. Liu et al. [20] and Stefanescu et al. [21] have shown that the undisturbed growth of vermicular graphite occurs mainly in direction of the c-axis.

Vermicular graphite can be produced by the intended partial treatment with magnesium or other treatment methods [22]. The Mg-content is not as high as in the case of producing cast iron with nodular graphite. Figure 2.8 shows, that vermicular graphite is formed only in the narrow percentage region of magnesium. Sinter Cast procedure established itself as the currently most widely used procedure [23]. It is based on the measurement of the heat conductivity of the melt. Upon this measurement, it is possible to predict the nucleation state of the melt and thus the expected graphite shape. Hence, it is still possible to perform the correction step by addition of magnesium and/or inoculant, but only as long as the pig iron is at the required casting temperature. The other procedure is called cerium-misch metal-method from the Foundry Institute in Leoben, Austria. Here the appropriate amount of cerium-misch metal is added to the melt to acquire desired microstructure.

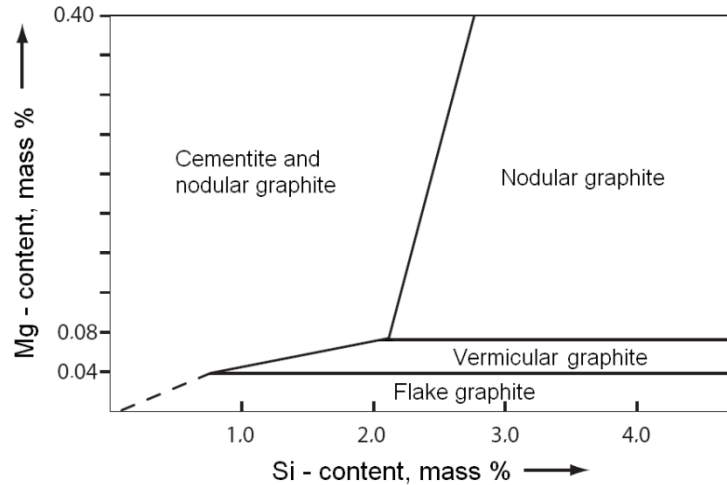


Figure 2.8 Mg- and Si-content determine the morphology of graphite. Only small process window exists for CG. The sulfur content in the sample is 0.04 % (after [24]).

#### 2.1.4 MALLEABLE CAST IRON (TG)

Malleable cast irons differ from other types of irons in that they have an initial as-cast white structure that is a structure consisting of iron carbides in a pearlitic matrix. The heat treatment (also known as tempering) of malleable iron determines the final structure of this iron. It consists of temper graphite (Figure 2.9) and pearlite, pearlite and ferrite, or ferrite matrix.

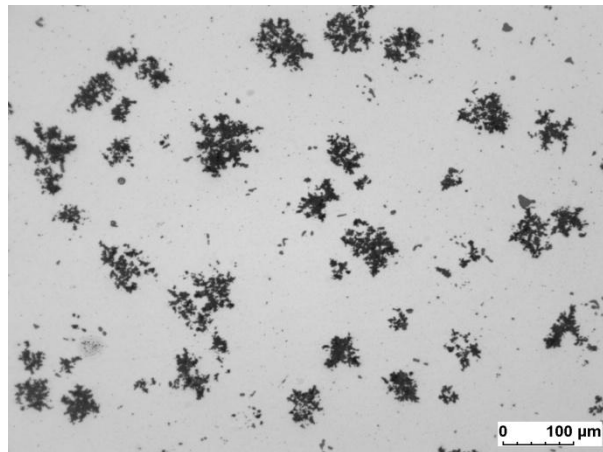


Figure 2.9 Malleable cast iron (optical micrograph, magnification 200x).

Excellent thin wall components with highly complex geometry can be founded with malleable cast iron. It possesses high toughness, good welding properties and machinability. One of the high advantages is that the component properties are equal in all stress direction. Malleable cast iron has big potential concerning mass reduction and direct production in the near final

shape. Required properties can be surely tailored by the tempering process [25]. Due to the long time heat treatment the processing is quite expensive.

## 2.2 INFLUENCE OF THE GRAPHITE MORPHOLOGY ON THE PROPERTIES OF CAST IRON

Some publications about cast iron are summarized here to show, how the properties of cast iron depend on its microstructure, which can be viewed as graphite inclusions in iron-matrix. Properties of the matrix are determined by its phase composition [7], [26]. Next to the matrix composition, graphite inclusion having different shape, size and complex arrangement have a great influence on the effective properties of cast iron [8], [27], [28]. The influence of graphite morphology on mechanical and thermal properties has long been a subject for the study of cast irons [29], [30]. In the past few years, compacted graphite iron [21], [31], [32] has received considerable attention due to its good combination of mechanical and thermal properties.

### 2.2.1 MECHANICAL PROPERTIES AND DENSITY OF CAST IRON

Graphite flakes are responsible for the lack of appreciable ductility in gray iron and for the ease, with which it can be machined. By breaking up the matrix, these flakes decrease the strength of the iron; in fact, their influence is so pronounced that it often outweighs all other factors controlling strength. Graphite flakes produce these effects in various degrees according to their size, distribution and amount [3]. The analytical and experimental research of e.g. Volchok et al. [28] confirms the presence of a reliable correlation between the shape of the graphite inclusions and the mechanical properties of the cast iron. On the other hand there is no definite relationship between tensile strength and hardness because of the marked influence of the shape, size and distribution of the flake on the strength without a corresponding effect on hardness [3].

An important property of ductile iron is that it is an elastic material like steel, and that stress is proportional to strain under loads up to the proportional limit. Though is the elasticity modulus of ductile iron lower than that of steel due to the presence of graphite. In flake graphite iron, proportionality of stress to strain exists only with extremely light loading and beyond that, permanent deformation occurs. Gray iron does not follow Hooke's law, because the flake graphite, in addition to interrupting the matrix, causes internal notches which act to concentrate stress locally at the ends of the graphite flake when a load is applied [3] (see Figure

## 2.2 Influence of the Graphite Morphology on the Properties of Cast Iron

2.10). Ductile iron combines the process advantages of cast iron with mechanical properties resembling those of steel and in addition, it retains the important advantage of excellent wear resistance, machinability and corrosion resistance of gray cast iron [3].

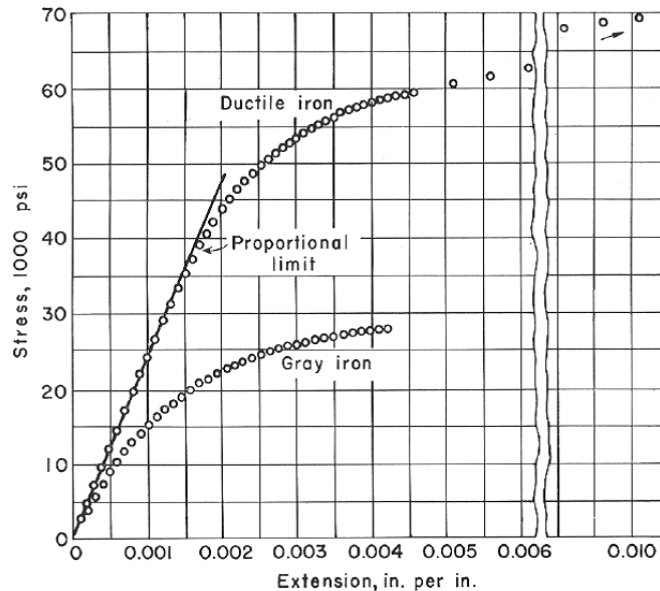


Figure 2.10 Stress strain relation in ductile iron and gray cast iron [3].

The excellent wear resistance accounts to the presence of graphite which contributes directly to the lubrication of rubbing surfaces and also provides reservoirs for accommodating and holding lubricants. Good mechanical wear resistance is an extremely important property since most properly designed machinery eventually fails by wear. Due to this, cast iron is present in a number of applications, including crankshafts, gears and many other items. There are certain items, such as piston rings in internal combustion engines, which are lubricated in a marginal manner, and which could not be made of any other material without extensive redesign and without some sacrifice in performance. The variations in graphite morphology cause the significant changes in total material loss through abrasion [9]. Cast iron with spheroidal graphite (SG) shows a proportional rise of material loss through abrasion to the cycle number. For cast iron with vermicular (CG) and flake graphite (FG) at first the slope is steeper. It flattens with increasing cycle number, stays though higher as for SG. The difference between CG and FG is low, and grows with increasing cycle number apart. Such behavior is an effect of tension concentration, which is determined by the continuity of the matrix. The matrix continuity is defined by the graphite shape. In the case of flake graphite low continuity of the matrix and high stress concentration effect in comparison with SG and CG promotes much quicker crack initiation and thus the ablation occurs earlier. CG has a higher mean distance between gra-

phite inclusions as FG, which means the higher continuity of the matrix. The stress concentration effect for CG is thus lower as for FG.

Another important physical property of iron is its damping capacity. Using various types of cast iron can solve many problems that are caused by vibrations. The damping capacity of gray iron is much higher than that of steel or other kinds of iron. This behavior is attributed to the graphite structure of gray iron. This damping capacity decreases with increasing strength, because the larger amount of graphite present in the lower-strength irons increases the energy absorbed [6]. Ductile irons also show a capacity for damping in mechanical parts and gears. The properties of ductile iron closely resemble those of medium carbon steel and can replace steel under many conditions of use [3]. Compacted gray irons have a damping capacity between that of gray and ductile irons. Malleable irons exhibit good damping and fatigue strength and are useful for long service in highly stressed parts. The production of high internal stresses by quenching malleable iron can double the damping capacity, which is then gradually reduced, as tempering relieves residual stresses [6].

Physical properties such as density, thermal conductivity, specific heat, electrical resistivity, and damping capacity define the use of cast iron. Certain properties are affected more by shape, size, and distribution of graphite particles than by any other attribute of the structure. The microstructural distribution affects the density of cast iron, whereas, the shape and distribution of the graphite particles directly affects cast iron's thermal and electrical conductivity. The three factors that largely affect density of iron are the type of microconstituents present, the composition, and temperature. Graphite has a low density. So the larger the amount of graphite in iron, the lower the density of that iron. Silicon also lowers the density of iron. Tensile strength decreases with increasing graphite content, and lower-strength irons of all types generally exhibit this lower density [6]. This relationship between tensile strength and density is shown in Table 2.1. For ductile iron, density is largely affected by carbon content and by the degree of graphitization and any amount of microporosity.

Table 2.1 Physical Properties of Gray Iron as a Function of Tensile Strength [6].

Tensile Strength, MPa	Density, g/cm <sup>3</sup>	Thermal conductivity at indicated temp., W/m·K			Electrical resistivity at 20°C, μΩ·m
		100°C	300°C	500°C	
150	7.05	65.7	53.3	40.9	0.80
180	7.10	59.5	50.3	40	0.78
220	7.15	53.6	47.3	38.9	0.76
260	7.20	50.2	45.2	38	0.73
300	7.25	47.7	43.8	37.4	0.70
350	7.30	45.3	42.3	36.7	0.67
400	7.30	43.5	41.0	36	0.64

## 2.2 Influence of the Graphite Morphology on the Properties of Cast Iron

Compacted graphite irons have densities similar to those of both gray and ductile irons. The density of malleable irons is higher than that of other unalloyed or low-alloy irons because of their lower graphite content. Completely annealed ferritic malleable iron also has a lower density than the pearlitic and martensitic matrix irons. In white irons, the increasing carbon content tends to decrease density and an increasing amount of retained austenite in the structure tends to increase density.

### 2.2.2 THERMAL AND ELECTRICAL CONDUCTIVITY

Like density, the thermal conductivity of cast irons is affected by factors attributed to the microconstituents. Graphite morphology, microstructure, alloying additions, and temperature all influence both thermal and electrical conductivity. Rukadikar et al. [33] proves that among these factors, next to the temperature, the graphite shape is the most influencing. Important at the same time are the shape, size and orientation of graphite. As the shape of graphite changes from flake to intermediate forms to fully spherical shapes there is less difference between the thermal or electrical conductivity of the cast iron and that of steel. Ductile irons have higher electrical conductivity and lower thermal conductivity than gray irons at all temperatures [6], [34] (see Figure 2.11).

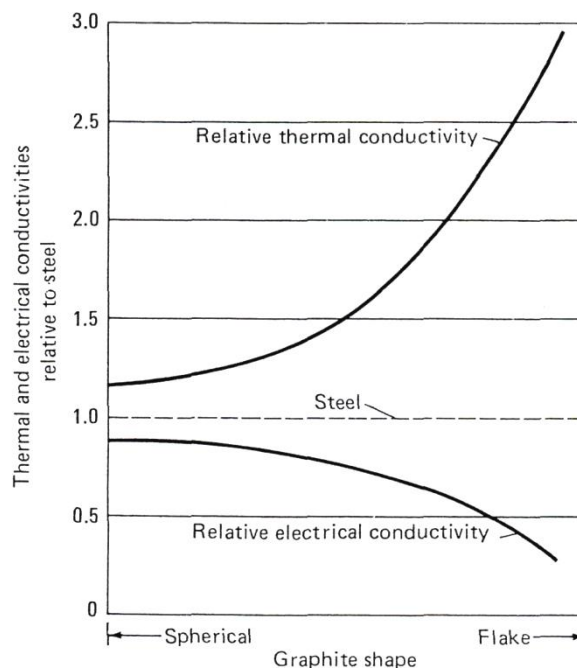


Figure 2.11 The influence of graphite morphology on the thermal and electrical conductivities of cast iron in comparison to steel [35].

The ferritic gray, malleable, ductile, and compacted graphite irons have higher thermal conductivities than iron with a pearlitic matrix (compare Table 2.4). Graphite exhibits the highest thermal conductivity of all the microconstituents in cast irons. Thus, the thermal conductivity of gray irons increases as the amount of free graphite increases and as the flakes become coarser and longer. According to Hecht et al. [27], linear correlation exists between the mean flake graphite length and conductivity. Longer graphite platelets cause greater conductivity as shorter lamellae. Flake graphite type D, as well as short A-graphite flakes, reduce the conductivity drastically. This effect is based on the structure of graphite. The thermal conductivity along the c-axis is low, along the a-axis very high. Gray iron with longer lamellas has more basis planes for the heat flux which results in higher diffusivity and thermal conductivity. The thermal conductivity of cast iron with compacted graphite is also due to the longish graphite shape considerably higher than for ductile iron and corresponds to gray iron with highest strength. This behavior is due to the fact that compacted graphite is interconnected much like flake graphite [6].

The factors that influence thermal conductivity, graphite structure, matrix constituents, alloying elements, and temperature influence as well the electrical resistivity of cast irons. The resistivity of all types of cast irons increases with temperature. Carbon and silicon have the greatest influence on the electrical conductivity of cast iron. The higher is the carbon and the silicon content the lower is the conductivity of the iron. Graphite has the lowest conductivity of all cast iron microconstituents. Thus, it acts as a barrier for the electron transport. Coarse flake graphite structures give the highest resistivity, with a lowering of the resistivity as the flakes become finer.

### 2.2.3 ELECTROMAGNETIC PROPERTIES FOR NON-DESTRUCTIVE MICROSTRUCTURE CHARACTERIZATION

The knowledge about tailoring of the cast iron microstructure and thus producing the required mechanical properties provide an enormous use of these materials in many modern technologies. Now the main goal is next to the efficient production costs to provide the quantitative, reproducible and, if possible, non destructive method of microstructure control. Quantitative characterization of the microstructure can be well performed on metallographic sections with the help of image analysis (see chapter 6). This method is objective, but destructive and can be executed only on some limited number of chosen pieces out of production series. Physical characteristics can be used for the non-destructive testing as an indicator of the microstructure and can be even integrated in the production process. Electromagnetic properties were found

to be promising for this application [36]. Now the exact correlation of microstructure and properties, and understanding of physical phenomena has to be done.

Ferromagnetic properties of bulk material are used for the application of the electromagnetic testing procedure in order to perform non-destructive material characterization. The measurements derived from the 3MA (Micromagnetic Multiparameter Microstructure and Stress Analysis) depend on the microstructure and on the internal stresses [37]. There is a correlation between electromagnetic properties of the material and its permeability and resistivity. In order to perform correct interpretation of the measured electromagnetic signal and internal microstructure the complete understanding of microstructure influence on the electric and magnetic properties is required.

As pointed out by Hashin and Shtrikman [38], the problem of the prediction of the effective magnetic permeability, dielectric constant, electrical conductivity, thermal conductivity and diffusivity of heterogeneous media are mathematically analogous. Considering the complexity of the task, in this work the problem was narrowed to the analysis of the microstructure effect on the electrical properties. The goal is to correlate the property with the quantitative microstructure characteristics and when possible suggest a model which is acceptable for other material properties e.g. permeability. Knowing that the shape of graphite particles in the same e.g. pearlitic matrix causes various cast iron properties (Table 2.2), partial influence of the graphite morphology will be primarily considered in this work.

Table 2.2 Comparison of the properties of FG-250, CG-500 and SG-700 [32], [39].

Property	Measuring unit	FG-250	CG-500	SG-700
Tensile strength, $R_m$	MPa	250-350	500	700
Fracture strain, $\varepsilon_f$	%	0.3-0.8	1	2
Elastic Modulus, E	GPa	103	170	177
Thermal conductivity, $\lambda$	W/(m·K)	45	40	30
Electrical resistivity, $\rho$	$\mu\Omega\cdot m$	0.73	0.60 <sup>2</sup>	0.54
Maximum permeability, $\mu$	$\mu H/m$	220-330		501

### 2.3 ANALYTICAL MODELS AND PREDICTION OF MATERIAL PROPERTIES

There are a number of correlations between microstructural parameters and material properties conducted by this microstructure, e.g. compare [40]. These correlations mostly have an

<sup>2</sup> Measured value for CG-400

empirical character. Generally volume fraction or specific surface area (or some other basic characteristic) and certain material property were measured for the series of samples to analyze their interdependency. Afterwards a model was adapted on the experimental values.

### 2.3.1 CALCULATION OF THE EFFECTIVE PROPERTIES OF THE COMPOSITES

The many approaches and predictive equations that have been proposed are summarized in review articles and textbooks, several of which are recent contributions to the subject [41], [42], [43], [44], etc.

#### 2.3.1.1 BOUNDING SCHEMES

On a macroscopic scale, which is large in comparison to the scales of the components, a composite behaves like a homogeneous solid with its own set of thermo-physical properties. It has long been recognized that, for the provision of the analytical expressions for such composite effective properties, full information concerning the microstructural arrangement of the two phases is necessary. Excluding the simplest arrangements (e.g. stacks of plates parallel or perpendicular to the applied field) such information is quite difficult to determine. An easier way is to bracket them by bounds or limits: upper and lower values between which the effective properties are located [45].

A composite of two constituents has an electrical and a thermal conductivity which is located between those of the individual components. The simplest of the mixing rules and bounds are the parallel and serial addition respectively, of the corresponding conductivities. Below, different models are presented for predicting electrical conductivity. Thermal conductivity can be predicted by the same models.

A composite containing parallel continuous graphite plates in the pearlite matrix, for example, would have conductivity, parallel to the plates, given by the rule of mixtures (ROM):

$$\sigma = V_{Gr} \cdot \sigma_{Gr} + V_{Pearl} \cdot \sigma_{Pearl}. \quad 2.3$$

Here  $V$  is the volume fraction and  $\sigma$  the electrical conductivity of the corresponding phase. Equation 2.3 is an upper bound: in any other direction the conductivity is lower. The transverse conductivity of a parallel plate composite lies near the lower bound:

$$\sigma = \frac{\sigma_{Gr} \cdot \sigma_{Pearl}}{V_{Pearl} \cdot \sigma_{Gr} + V_{Gr} \cdot \sigma_{Pearl}}. \quad 2.4$$

These bounds are useful for macroscopically anisotropic composites with isotropic phases. For an isotropic composite, equation 2.3 overestimates the effective conductivity, whereas equation 2.4 underestimates it. Effective composite properties are often not simple relations (mixtures rules) involving the phase volume fraction only. Complex interactions depend on details of the microstructure.

Hashin-Shtrikman (HS) variation bounds establish more rigorous upper and lower bounds on the effective electrical conductivity  $\sigma_{eff}$  of macroscopically isotropic composites with an arbitrary microstructure [46]:

$$\sigma_{lo} + \frac{V_h}{\frac{1}{\sigma_h - \sigma_{lo}} + \frac{1 - V_h}{3\sigma_{lo}}} = \sigma_{lower} \leq \sigma_{eff} \leq \sigma_{upper} = \sigma_h + \frac{1 - V_h}{\frac{1}{\sigma_{lo} - \sigma_h} + \frac{V_h}{3\sigma_h}} \quad 2.5$$

where  $\sigma_h$  and  $V_h$  are the electrical conductivity and volume fraction of the high-conductive phase, respectively, and  $\sigma_{lo}$  the electrical conductivity of the low-conductive phase. The upper bound usually accounts for the case where the less-conductive phase is embedded in the better-conducting matrix. The lower bound, on the other hand, generally corresponds to the case where the better conducting phase is embedded in a matrix of the less-conducting phase. For low to moderate phase contrast in the considered property, such a procedure can bracket the property with bounds that are relatively close. The Hashin-Shtrikman bounds are the best possible bounds on the effective conductivity of isotropic two-phase composites with a given only the volume fraction information.

With increased microstructural information, e.g. isotropic phase arrangement or two-, three-, or n-point correlation distributions, the bounds can be narrowed, further increasing the provided precision of the prediction [41], [47]. An example is the so called 3-point bounds. In the case of electrical conductivity, the effective conductivity of the composite  $\sigma_{eff}$  can be given as a function of the matrix conductivity  $\sigma_m$ , the inclusion conductivity  $\sigma_i$ , the volume fraction of inclusion phase  $V_i$  and a microstructural parameter  $\zeta_i$  that carries the three-point information. Milton [48] has given the bounds initially derived by Beran [49] in a simplified form. In case of  $\sigma_i=0$  the 3-point upper bound is given:

$$\sigma_{eff} = \frac{2\sigma_m(1 - V_i)(1 - \zeta_i)}{V_i + 2(1 - \zeta_i)} \quad 2.6$$

The case  $\zeta_i=0$  or 1 corresponds to the upper and lower Hashin-Shtrikman bound, respectively.  $\zeta_i$  values for various matrix/inclusion topologies have been calculated or determined by numerical simulation.

### 2.3.1.2 PREDICTIVE SCHEMES

For large contrast, however, as in the electrical conductivity of metal/ceramic composites, or even of graphite/iron matrix in cast iron, the bounds lie far apart and the admitted values can vary by one to several orders of magnitude. In case of high phase contrast it might therefore be preferable to use an analysis that takes the actual basic arrangement and shape of the two phases into account instead of bounding approaches. Several types of predictive schemes can be distinguished in the literature. Most are based on the solution of the intensity field within an ellipsoidal inclusion embedded in a matrix subjected to a remotely applied field [47]. The ellipsoids can describe elongated, spherical or flat inclusions and the field within an ellipsoidal inclusion is uniform. At low inclusion concentrations, the problem is often simply solved by assuming no interaction between inclusions.

Weber et al. [47] measured the effective electrical conductivity of a heterogeneous medium containing randomly oriented non-conducting angular or equiaxed inclusions. Depending on particle systems the mean-field approach (or Maxwell/Mori-Tanaka scheme), the two-phase and generalized (or three-phase) self-consistent schemes overestimates significantly, slightly or underestimates the effective electrical conductivity. Overall, the differential effective medium approach (DEM) was found to be the only predictive scheme that adequately predicts the effective conductivity of two-phase materials of a non-conducting material embedded in a conducting matrix, for both equiaxed and angular particles [47] and for Al-Si alloys [50]. I. Sevostianov et al. [51] has also shown that the electrical conductivity of the closed-cell aluminum foam is well predicted by the differential scheme for randomly oriented spheroidal pores.

The differential effective medium (DEM) scheme [41], [46], [52] is based on the solution for the dilute case of the intensity field in an ellipsoidal inclusion in a matrix subjected to a remotely applied field. The basic approach is as follows. Consider a composite with an arbitrary volume fraction of inclusion phase and replace it by a homogeneous material having the same effective properties. If we now replace an infinitesimal quantity of the equivalent homogeneous material by inclusion phase, the infinitesimal change in effective property of the new composite is given by the dilute solution.

This postulate leads to a differential equation that allows accessing the effective properties at any volume fraction by integration, starting at zero volume fraction of inclusion and the effec-

tive property equal to that of the matrix. Predictions for spherical, aligned and arbitrarily oriented spheroidal inclusions can be made [47].

It has been pointed out, that this procedure is strictly valid for hierarchical microstructures [43] where the subsequent levels of inclusions have significantly increasing size, as this justifies the replacement of the composite by a homogeneous material prior to every infinitesimal step.

The equations for prediction of the effective electrical conductivity  $\sigma_{eff}$  as a function of the volume fraction of inclusion phase  $V_i=1-V_m$ , where  $V_m$  is the volume fraction of the matrix and the electrical conductivity of the matrix  $\sigma_m$  (for the case  $\sigma_i=0$ ) for the case of spherical inclusions (Eq. 2.7) and randomly oriented spheroidal inclusions (Eq. 2.8) are as follows:

$$\sigma_{eff} = \sigma_m(1 - V_i)^{3/2} \quad 2.7$$

$$\sigma_{eff} = \sigma_m(1 - V_i)^{(1/(1-S^{eq}))} \quad 2.8$$

In the latter case, the effective polarization factor  $S^{eq}$  is given by [50]

$$\frac{1}{1 - S^{eq}} = \frac{1 + 3S_{\perp}}{6S_{\perp}(1 - S_{\perp})} \quad 2.9$$

where  $S_{\perp}$  is the polarization factor perpendicular to the shortest main axis of an oblate spheroid, itself given by

$$S_{\perp} = \frac{q}{2(1 - q^2)^{3/2}} (\cos^{-1}(q) - q(1 - q^2)^{1/2}) \quad 2.10$$

with  $q \leq 1$  being the aspect ratio of the spheroid.

As shown later, the models presented do not accurately predict the effective conductivity of interpenetrating phase composites. They do not take into account the level of connectivity of the phases involved.

### 2.3.1.3 FINITE ELEMENT METHODS

As opposed to the procedures described above, there are intentions to calculate macroscopic material properties (e.g. properties of composite or polycrystalline material) from knowing the special microstructure arrangement and local physical properties (e.g. electrical properties for each phase and on the phase boarders). Such works are motivated by the development of the

numerical methods for solution of partial differential equations, such as Finite Element Methods (FEM).

Modeling the effective properties of particle-reinforced metal-matrix composites is based on a real structure and can be done mainly in two different ways: one can directly import the experimentally obtained real structure into FE software [53], [54] or generate model structures that have similar statistical functions as the experimentally obtained ones [55]. The statistically equivalent modeling approach becomes very difficult in 3D, since, besides the position of the particles, their sizes, orientations, and shapes must be taken into account according to the corresponding marked correlation functions [56]. Due to these difficulties, direct simulation of real structures seems to be more straightforward; however, at the cost of a much larger modeling effort required to capture the variability of the microstructure. In order to obtain the average properties more volumes have to be selected from the real structure than “statistically equivalent” models to be simulated. Before simulating the real structure one has to solve also the problem of sampling, i.e., how the different simulation windows should be selected from the large reconstructed volume. This simulation window should not be smaller than a representative volume element, i.e., the smallest material volume that contains all microstructural information and can be considered for estimation of the effective properties.

It is clear that the effective properties of cast iron with different graphite morphologies cannot be predicted by only considering the graphite volume fraction and properties of the individual phases (matrix and inclusions). Shape descriptive parameters based additionally on the area of the phase interfaces and particle topography provides better microstructure-property relationships, but not self-contained for all graphite morphologies. One of the goals of this work is thus to find common dependency of the effective properties from 3D graphite shape, considering the different graphite crystal structure.

## 2.3.2 EXISTING CORRELATIONS FOR CAST IRON

### 2.3.2.1 MECHANICAL PROPERTIES

For cast iron most of the investigated microstructure-property correlations were concerning mechanical properties. Cast iron can be viewed as a composite material consisting of ferrite (bcc-iron alloy), graphite and cementite ( $\text{Fe}_3\text{C}$ ). The graphite morphology determines substantially the properties of cast iron such as tensile strength and ductility. Thus, the shape and the volume fraction of the graphite particles influence the properties of cast iron.

Cooper et al. [57] reports that the elastic properties of the composite materials can be predicted by the simple micromechanical models based on the volume fraction of the graphite

inclusions and the bulk, shear and elasticity moduli of the iron matrix and the graphite flakes. The theoretical models of Voigt [58], Halpin-Tsai [59], Hashin [43], [60], Wu [61], Rossi [62] and Reuss [63] were developed to estimate the Young's modulus (E-Modulus) of cast irons which have been modeled as two-phase composites with randomly oriented graphite particles embedded in an isotropic iron matrix. Graphite platelets are approximated by single crystals, whereas nodular graphite particles are polycrystalline. This leads to different values of E-modulus for graphite. By comparing the experimental value of the Young's modulus of cast iron with flake graphite with theoretical models, it can be seen that the experimental value lies close to the predictions of Wu and Rossi. These models are based on disk-shaped inclusions that reflect the shape of the graphite flakes. The experimentally measured value for the Young's modulus of cast iron with spheroidal iron is in close agreement with the predicted values of Hashin and Halpin-Tsai. The Hashin model is based on a random distribution of spherical-shaped particles reflecting the reinforcement geometry for the spheroidal cast iron [57].

### 2.3.2.2 PHYSICAL PROPERTIES

Considerable input to the estimation of physical properties of cast iron was done by Johan Helsing and Göran Grimvall [64]. First they have calculated the conductivities of microstructural constituents of cast iron: ferrite, cementite and graphite. Second, they made an estimation of the properties of pearlite. The following equations will be equally used for the estimation of properties of the cast iron samples analyzed in this work (see section 5.3 and appendix 9.1).

*Ferrite:* Both phonon and electron contribution to the thermal conductivity of ferrite was taken into consideration:  $\lambda = \lambda_{ph} + \lambda_{el}$ . The thermal conductivity of alloyed ferrite in cast iron was estimated according to the following formula:

$$\lambda(Fe\ al.) = \left( \frac{1}{\lambda_{ph}(Fe)} + \sum_i A'_i c_i \right)^{-1} + \left( \frac{\rho(Fe)}{L_e T} + \frac{1}{L_0 T} \sum_i \rho'_i c_i \right)^{-1} \quad 2.11$$

where  $\lambda_{ph}(Fe)=17.6$  W/mK and  $\rho(Fe)=0.1$   $\mu\Omega \cdot m$  have been estimated for pure ferrite by Williams et al. [65] from measurements on bcc Fe.  $A'_i$  are the calculated [65] constants describing the effect of the alloying elements on the  $\lambda_{ph}$ ,  $c_i$  are the concentrations (at. %) of the alloying elements,  $\rho'_i$  are the corresponding resistivities per at. % (see Table 2.3).  $L_e=2.03 \cdot 10^{-8}$  W $\Omega$ /K<sup>2</sup> is the measured Lorenz number (at 300 K) [64] for the term involving  $\rho(Fe)$  and the Lorenz number  $L_0$  is for the part based on  $\rho_{el-def}$ .

Table 2.3 Experimental values for the coefficients  $\rho'_i$  and  $A'_i$  [65], [66] used to calculate the impurity scattering of alloyed ferrite from equation 2.11.  $A'_{Mn}$  estimated by [64].

	Al	Sn	Si	Ti	Cr	Mn	Ni	Mo	Ru	W
$\rho'_i, (\mu\Omega\cdot\text{m/at.}\%)$	0.064	0.1	0.07	...	0.046	0.05	0.027	0.048	0.045	0.05
$10^3 \cdot A'_i, (\text{mK/W at.}\%)$	7	...	8	3	0.1	10	4	13	15	40

Electrical conductivity of alloyed ferrite was estimated also considering the influence of various chemical compositions:

$$\rho(\text{Fe al.}) = \rho_{el-ph} + \rho_{el-magn} + \rho_{el-def} = \rho(\text{Fe}) + \sum_i \rho'_i c_i \quad 2.12$$

*Cementite:* As the thermal and electrical conductivities of cementite ( $\text{Fe}_3\text{C}$ ) are not well known Helsing and Grimvall [64] have summarized all known estimations [67], [68], [69], [70], calculated the electrical conductivity  $\rho(\text{Fe}_3\text{C}) \approx 1.07 \mu\Omega\cdot\text{m}$  and chosen thermal conductivity for subsequent modeling  $\lambda(\text{Fe}_3\text{C}) = 8 \text{ W/m}\cdot\text{K}$ .

*Graphite:* Graphite has hexagonal lattice symmetry. The thermal conductivity is strongly anisotropic. Along the hexagonal planes, the conductivity  $\lambda_a = \lambda_{\parallel}$  is very high. Experiments at room temperature on pyrolytic graphite [71] result in  $\lambda_{\parallel} \approx 2000 \text{ W/m}\cdot\text{K}$  and  $\lambda_{\perp} \approx 10 \text{ W/m}\cdot\text{K}$ . The thermal conductivity of synthetic polycrystalline graphite, where the grains are oriented so that the effective conductivity is isotropic, is in the range of 25-200  $\text{W/m}\cdot\text{K}$  according to many reported data [71]. It is then obvious that  $\lambda_{\parallel}$  is very sensitive to lattice defects.

The anisotropic characteristics of graphite conductivity should be considered by the modeling of effective properties of cast iron, thus  $\lambda_{\parallel}(\text{graph}) = 500 \text{ W/m}\cdot\text{K}$ ,  $\lambda_{\perp}(\text{graph}) = 10 \text{ W/m}\cdot\text{K}$  and  $\rho_{\parallel}(\text{graph}) = 0.5 \mu\Omega\cdot\text{m}$ ,  $\rho_{\perp}(\text{graph}) = 10000 \mu\Omega\cdot\text{m}$  were chosen.

*Pearlite:* When dealing with the overall conductivity of cast iron, pearlite should be considered as a separate phase, with different conductivities along the cementite lamellae ( $\lambda_{\parallel}$ ) and perpendicular to the lamellae ( $\lambda_{\perp}$ ). Effective properties can be calculated from the estimated values of parallel (Eq. 2.3) and serial coupling (Eq. 2.4) or Hashin-Shtrikman (HS) bounds (Eq. 2.5), which consider pearlite as a single phase with anisotropic conductivities. For a specimen which can be considered as a polycrystalline material of pearlite grains, and with random grain orientation equation 2.13 yields the estimated isotropic conductivity.

$$\lambda_{eff} = \frac{1}{4} [\lambda_{\parallel} + (\lambda_{\parallel}^2 + 8\lambda_{\parallel}\lambda_{\perp})^{1/2}] \quad 2.13$$

Knowing the physical properties of the individual microstructure constituents (see Table 2.4 and also appendix 9.1) the effective properties of cast iron with different graphite morphologies can be estimated according to the existing predictive and bounding schemes.

Table 2.4 The thermal conductivity  $\lambda$  and the electrical resistivity  $\rho$  of phases and structural components at 300 K [64].

	$\lambda$ , (W/m·K)	$\sigma$ , ( $10^6$ S/m)	$\rho$ , ( $\mu\Omega\cdot\text{m}$ )
Pure ferrite <sup>3</sup>	78.5	10	0.1
Alloyed ferrite	30	2.78	0.36
Cementite	8	0.93	1.07
Graphite a	500 (293-419) <sup>4</sup>	2	0.5 <sup>5</sup>
Graphite c	10 ( $\approx 85$ ) <sup>4</sup>	0.0001	10000 <sup>5</sup>
Lamellar alloyed pearlite ( $\lambda_{\parallel}$ , $\sigma_{\parallel}$ , $\rho_{\parallel}$ )	27.3	2.55	0.392
Lamellar alloyed pearlite ( $\lambda_{\perp}$ , $\sigma_{\perp}$ , $\rho_{\perp}$ )	22.5	2.24	0.447

It can be seen that ferrite has higher thermal conductivity than pearlite. Cementite can lower the cast iron thermal conductivity. The thermal conductivity parallel to the graphite basal plane is very high and graphite, in this condition, is the phase with the highest thermal conductivity. So, a graphite shape that eases the thermal conductivity along the basal plane must result in maximum thermal conductivity [72]. This is the case of grey cast iron, as can be seen in the Figure 2.12 [73].

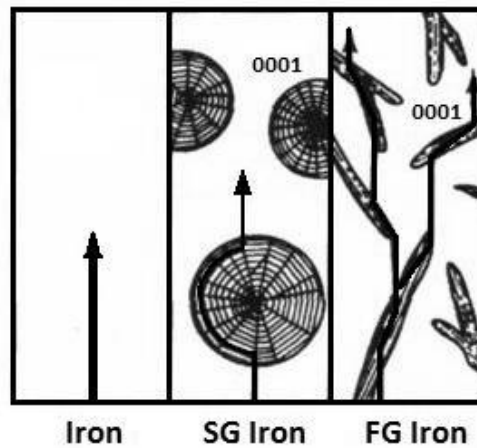


Figure 2.12 Thermal conduction scheme. The thermal conductivity of graphite parallel to basal plane is higher than perpendicular [73].

<sup>3</sup> Reference [65]

<sup>4</sup> Source [161]

<sup>5</sup> Source [160]



---

### 3 QUANTITATIVE MICROSTRUCTURE CHARACTERIZATION

---

One of a material scientist's most important tasks is to find a correlation between the material microstructure and its properties. How it was shown in the previous section not only the composition of the material but more often the arrangement of different phases influence the resulting properties. Quantitative image analysis can be successfully used for the characterization of such arrangements. With its help is the characterization for many regular microstructures now explicit and can often be automatically realized. This is, however, not the case for irregular graphite particles in cast iron.

#### 3.1 BASIC CHARACTERISTICS OF QUANTITATIVE IMAGE ANALYSIS

##### 3.1.1 PARTICLE BASED PARAMETERS

When talking about particles<sup>6</sup> one has to keep in mind that they can either be discrete and even convex, or be spatially interconnected with other particles, and in extreme case form a network [74]. One talks about simply connected particles when the objects are discrete.

The characterization theorem of Hadwiger [75] says that all features of one particle, which possess the special properties regarding its size, shape, topology, etc., can be represented as a linear combination of following four parameters:

$V$  – the volume of the particle,

$S$  – the surface of the particle,

$M$  – the integral of the mean curvature of the particle and

$K$  – the integral of the total curvature of the particle.

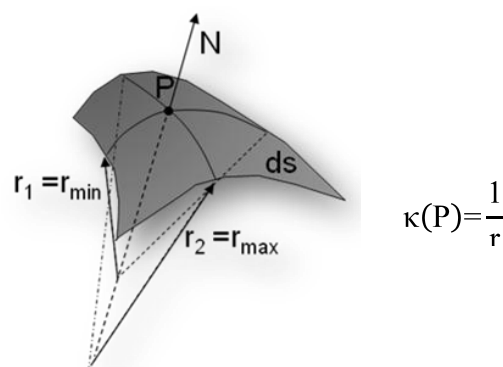


Figure 3.1 Scheme for the explanation of curvature integrals.

---

<sup>6</sup> The term particle is a synonym to inclusion, grain, pore, fiber, lamellae, etc.

The curvature  $\kappa(P)$  of the point  $P$  on the surface is defined by the curvature radius  $r$ , which can be applied to the surface element  $ds$  of the particle surface, see Figure 3.1.  $r_1$  and  $r_2$  characterize the smallest and the biggest curvature radii of the surface element  $ds$ . The mean curvature is the mean value of the both respective curvatures  $\kappa_1(P)$  and  $\kappa_2(P)$ , and the total curvature is the product  $\kappa_1(P) \cdot \kappa_2(P)$ . The values  $M$  and  $K$  are acquired through the integration of the mean and total curvature respectively over all surface elements of the particle [74], [76]:

$$M = \frac{1}{2} \int (\kappa_1(P) + \kappa_2(P)) ds = \frac{1}{2} \int \left( \frac{1}{r_1} + \frac{1}{r_2} \right) ds \quad 3.1$$

$$K = \int \kappa_1(P) \cdot \kappa_2(P) ds = \int \frac{1}{r_1} \cdot \frac{1}{r_2} ds \quad 3.2$$

The four features  $V$ ,  $S$ ,  $M$  and  $K$  are arranged according to their geometrical dimensions. The volume has a dimension  $m^3$ , the surface has a dimension  $m^2$ , and both curvature integrals have the dimension  $m^1$  and  $m^0$  respectively, i.e.  $K$  is dimensionless.

### 3.1.2 FIELD BASED PARAMETERS

The densities of the particle features are used to characterize the components of the microstructure. These densities are parameters with respect to sample volume. Hence, the volume density, i.e. volume fraction, of the microstructural component is the quotient out of the total volume of this component in the sample and the total sample volume. Volume fraction ( $V_V$ ) directly reflects the materials composition, i.e. the phase structure. The density of the surface area ( $S_V$ ) depends primarily on the kinetic aspects of the material fabrication, and influences significantly the mechanical (e.g. Hall Petch effect) and physical properties [77]. Density of the integral of mean curvature ( $M_V$ ) characterizes the geometrical arrangement (i.e. shape) of the second phase e.g. inclusions, which serve for example as the obstacles by dislocation or domain movement during deformation and magnetization respectively. Density of the integral of total curvature ( $K_V$ ) is mainly influenced by the nucleation velocity [78].

The volume density is dimensionless, the specific surface area has a dimension  $m^{-1}$ , the density of the first curvature integral  $M_V$  has the dimension  $m^{-2}$ , and  $K_V$  has the dimension  $m^{-3}$ . These four densities build the basis for the description of microstructural components. They are thus called basic characteristics in the quantitative image analysis.

### 3.1.3 STEREOLOGICAL EQUATIONS FOR CALCULATION OF THE BASIC CHARACTERISTICS

The volume fraction ( $V_V$ ), the specific surface area ( $S_V$ ) and the specific integral of the mean curvature ( $M_V$ ) can be calculated from the 2D microstructural images according to the stereological equations [78]. Delesse [79], Rosiwal [80], Thompson [81], and Glagolev [82] have consequently proved that the parameters area fraction  $A_A$ , linear fraction  $L_L$  and point fraction  $P_P$  acquired respectively with the help of the area method, lineal analysis and point count method can be used to determine the volume fraction  $V_V$  (see Table 3.1). The estimation of the density of the surface area ( $S_V$ ) can also be done from the area and lineal analysis. In 1945 Saltykov [83] has presented the derivation of the following equation:

$$S_V = \frac{4}{\pi} L_A = 2N_L \quad 3.3$$

where  $L_A$  is the length of the line per unit of surface, and  $N_L$  is the point number per line length. The integral of mean curvature can be calculated with the help of area method from  $\chi_A$  (see Table 3.1).  $\chi_A$  is a Euler number per unit area. It describes the topology of the objects and in the case of simply connected objects it is equal to particle number per unit area ( $N_A$ ).

Table 3.1 Stereological equations.

Spatial structure	Area method	Lineal analysis	Point count method
$V_V$	= $A_A$	= $L_L$	= $P_P$
$S_V$	= $\frac{4}{\pi} L_A$	= $2N_L$	
$M_V$	= $2\pi\chi_A$		
$K_V$			

The equation for the volume fraction can be applied to all homogeneous structures even if they are not isotropic. The stereological equations for  $S_V$  and  $M_V$  are only valid in the isometric case. In the case of anisotropic structure either microstructure adapted models [78], which, depending on the assumption, can be inconsistent, or the actual 3D microstructural images are required. 3D images are also necessary for the estimation of the specific integral of total curvature ( $K_V$ ), as well as other topological parameters, such as Euler number ( $\chi_V$ ), particle number ( $N_V$ ) and connectivity ( $C_V$ ), which cannot be calculated from the elementary ste-

reological method. Thus, 3D images provide remarkable information gain in comparison with 2D. The 3D analysis is especially indispensable, when not periodic, not convex and not symmetric structures have to be characterized. Such structures, depending on their measurement and shape, can appear significantly different in 2D as in 3D. And thus flawed conclusions about the material properties can be derived. It is a challenge is to find unambiguous relationships between 2D and 3D parameters for such complex microstructures. Further goal is to develop some statistical models, which can replace real 3D images and can be used for the simplified but correct simulations of the materials properties (see also section 2.3.1.3).

## 3.2 CHARACTERIZATION AND CLASSIFICATION OF GRAPHITE MORPHOLOGY IN 2D

Various graphite morphologies in cast iron are an excellent example of complex microstructures mentioned in previous section. Due to extensive application and wide range of properties of cast iron, which depend in particular on the graphite shape, is the characterization and classification of graphite inclusions very important. Up to now analysis was limited to 2D observations, which does not reflect the 3D complexity, but is preferable for the routine quality control. Hence, the characterization and classification of graphite morphologies from the 2D images was the matter of research for many material scientists.

### 3.2.1 CLASSIFICATION ACCORDING TO NORM DIN EN ISO 945

State of art is the subjective comparison of the real microstructures with standard series images of the two industrial norms ASTM 247-47 and DIN EN ISO 945 (Figure 2.2). By this the job of metallographers was facilitated. Although the empiric, idealized series images can not reflect the variety of the different graphite morphologies and allow wide range of subjective judgments depending on the expert. Especially drastic differences were demonstrated on the example of the flake graphite arrangements (Figure 3.2).

This leads over again to disagreements between cast iron consumers and foundry industries. Additionally, is the subjective comparison with ideal series images very time intense and cannot be accepted any more due to the growing requirements on the properties and thus on the correct characterization of the microstructure of cast iron.

The complexity of the empiric classification of diverse graphite types is caused by its irregular, very complex and inconsistently non convex 3D shapes. As though the quality control is based on the 2D plane sections, which are formed by the intersection of the random planes with the graphite particles, one should always count with indistinct classification.

In addition a quantitative determination of, for example, the volume fraction for every specific graphite type cannot be done. At the same time, it is known, that the graphite morphology, shape, size, and distribution have a significant impact on the properties of the cast iron (see section 2.2). Therefore, it is very important to determine the volume fraction of each graphite type and the size distribution of graphite particles. A quantitative image analysis is a reliable tool for this task. Its implementation has made the quantitative characterization of the different microstructures possible.

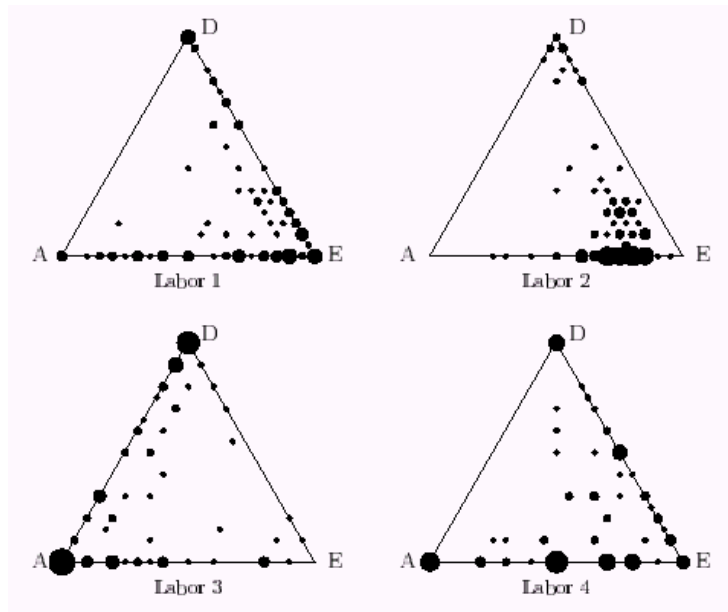


Figure 3.2 Round Robin Test for graphite classification – subjective classification of flake graphite arrangements for 120 chosen microstructure images by the experts in four different laboratories, which specialize on cast iron [84]. When for example laboratory 2 assigned the graphite morphology primarily to E-graphite, laboratory 3 had the opinion that there is mostly A- and D-graphite. These results underline the importance of the objective and reproducible classification.

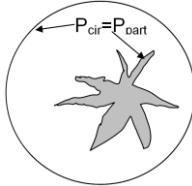
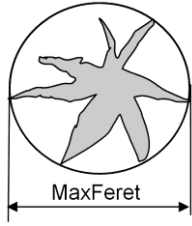
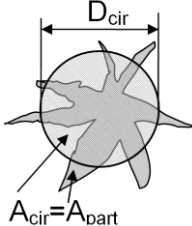
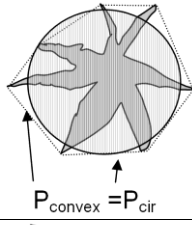
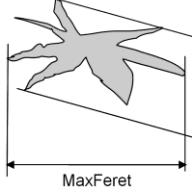
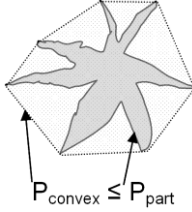
#### 3.2.2 SHAPE CHARACTERIZATION

Many materials scientists, mathematicians and computer scientists have been working on the question of classification of different graphite morphologies. A differentiation between the six graphite types (Figure 2.2) may be made according to their shapes. Shape criteria can be used to characterize and separate irregular graphite particles. It has been found that majority of the shape parameters which are described in [85], [86], [87] and [88], can be reduced to only six most important characteristics listed in Table 3.2.

All of those shape parameters can be easily calculated from the two-dimensional geometric characteristics which were determined automatically, e.g. the area ( $A$ ), perimeter ( $P$ ), convex perimeter ( $ConvexP$ ), and Feret diameter [89]. The measurement can be automated with a suitable image analysis system. The positive characteristic of all of those shape parameters is

that they are dimensionless. In addition, their values range between 0 and 1 depending on the particle shape, providing easy and clear-cut shape characterization.

Table 3.2 Shape parameters [85], [86], [87], and [90].

Shape parameter	Formula		Definition
Sphericity	$\frac{A}{A_{cir1}} = \frac{4\pi \cdot A}{P^2}$		Ratio between object area (A) and the area of the circle (A <sub>cir1</sub> ) with the same perimeter as the object's perimeter (P)
Roundness	$\frac{A}{A_{cir2}} = \frac{4 \cdot A}{\pi \cdot (MaxFeret)^2}$		Ratio between object area (A) and the area of the circumscribed circle (A <sub>cir2</sub> )
Circularity	$\frac{D_{cir}}{MaxFeret} = \sqrt{\frac{4 \cdot A}{\pi \cdot (MaxFeret)^2}}$		Ratio between the diameter of the circle (D <sub>cir</sub> ) with the same area as the object area (A) and the object's maximum Feret diameter (MaxFeret)
Compactness	$\frac{A}{A_{cir3}} = \frac{4\pi \cdot A}{(ConvexP)^2}$		Ratio between object area (A) and the area of the circle (A <sub>cir3</sub> ) with the same perimeter as the object's convex perimeter (ConvexP)
Aspect ratio	$\frac{D_{min}}{D_{max}} = \frac{MinFeret}{MaxFeret}$		Ratio between the object's minimum (MinFeret) and maximum Feret diameter (MaxFeret)
Convexity	$\left(\frac{ConvexP}{P}\right)^2$		Squared ratio between object's convex perimeter (ConvexP) and its perimeter (P)

One of the most widely used shape parameter is particle sphericity also known as shape factor. It compares the object's area (A) to the area of the circle (A<sub>cir1</sub>) having the same perimeter as the perimeter of the object (P). Other shape parameters such as roundness, compactness, and circularity similarly compare the object to an ideal circle, which has a different definition

for all of those shape parameters (see Table 3.2). As a result, the sensitivity of shape parameters proves to be very different for discrimination between shapes. The aspect ratio describes the elongation of objects, but cannot give any information about the complexity of the object shape. For instance, the value of the aspect ratio of a star always is equal to 1 (Figure 3.3).

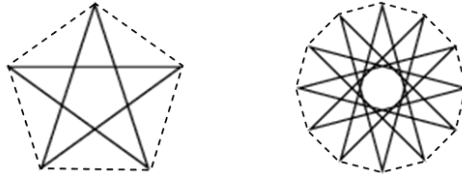


Figure 3.3 Star polygon. Dashed line is a convex perimeter.

The convexity of the object is defined as the square of the relationship of the convex perimeter to the perimeter of the object. An object of a convex shape has a convexity which is equal to 1. The rougher, the wavier, and the more complicated is the outline of the object, the smaller is the value of its convexity.

The differentiation of complex particles according to their shape parameters described in [76], [85], [86], [87] and [91] admittedly is not trivial. The use of only these parameters is not sufficient for a classification of the variety of graphite morphologies.

#### 3.2.3 OTHER APPROACHES TO GRAPHITE CLASSIFICATIONS

##### 3.2.3.1 FRACTAL DIMENSION

In some recent works of Ruxanda et al. [85], Li et al. [86] and Lu et al. [92] the parameter “fractal dimension” in a combination with other shape parameters was successfully used for the graphite classification. However, several disadvantages are associated with this method and it cannot yet be used for the efficient quality control [85]. The value of the fractal dimension calculated from the image of only one magnification with the help of morphological transformations does not always correlate with the correct value acquired from the analysis of the same particles at different magnifications.

##### 3.2.3.2 MORPHOLOGICAL OPERATIONS

J. Ohser [84] introduced a method, which makes it possible to classify different flake graphite configurations by applying morphological image transformations. Each pixel of the graphite phase is classified according to both the size of the lamellae surrounding it and the distance between adjacent lamellae [93]. The result of such measurement for each image is a matrix, the coefficients of which correspond to the numbers of appropriately classified graphite pix-

els. The  $ij$ -th coefficient is the number of pixels that was assigned to the  $i$ -th size class and the  $j$ -th distance class. These coefficients contain the implicit information about the fraction of different flake graphite arrangements. The classification according to this method requires a prior training step, where the measured data (i.e. the implicit information) are linked to the subjective classification (the expert's knowledge).

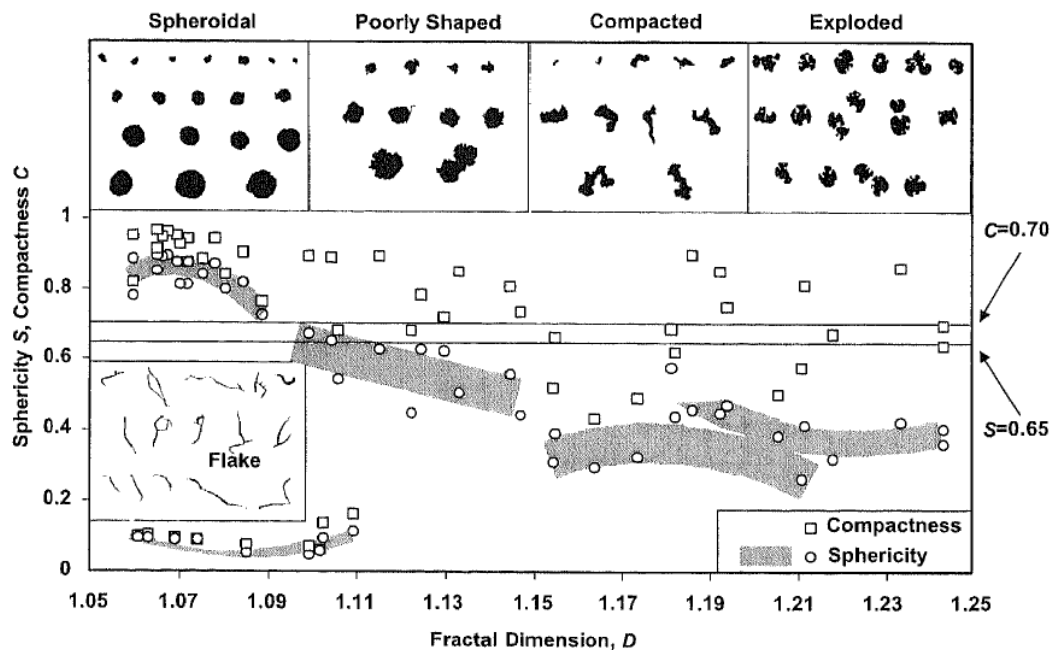


Figure 3.4 Ranges of the fractal dimension and the shape factors for different types of graphite [85].

### 3.2.3.3 SUPPORT VECTOR MACHINE

The referenced articles by K. Roberts [94], [95] report that the support vector method was employed to classify flake graphite. The author has used 14 Haralick coefficients [96] and 6 field-based image analytical parameters [78]. As a result the combination of parameters was defined, which play the most essential role for the classification. Roberts has proposed to increase classification quality by the extension of the already 20 different parameters by the texture and shape parameters.

### 3.2.3.4 “FUZZY LOGIC”

L. Wojnar [91] used the “fuzzy logic” together with the shape parameter for such classification (see Figure 3.5a). The main advantages of the application of the fuzzy logic is, that it enables quantification of particles which do not fit the assumed templates, and that it is relatively close to our human way of quantification. The example of the application of the fuzzy logic to shape analysis is shown in Figure 3.5b.

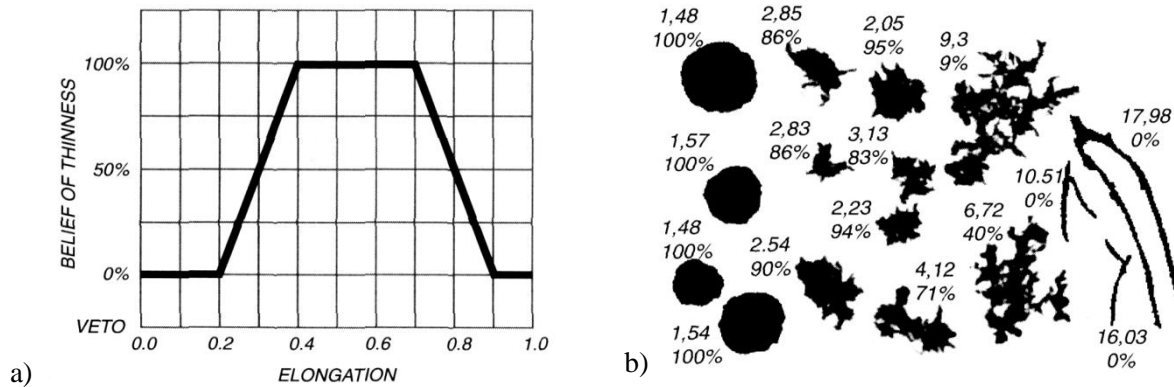


Figure 3.5 a) Schema of the fuzzy logic and b) application of the fuzzy logic for the classification of the graphite particles. Upper number denotes the value of shape factor and lower number in % informs how well the particle fits as a circular shape.

All the methods described above give the equivalent weight to 2D sections through the graphite particles of different size and, except for the fractal dimension, do not consider the effect of the resolution, i.e. magnification and the calibration factor. They are relatively sophisticated and often require a prior training step. In addition some of the methods are concentrated only on the flake graphite arrangement. Admitting that five different arrangements of flake graphite have a big chance of coexisting in the cast iron microstructure, flake graphite is only one of the six graphite types (Figure 2.2). Modern developments in the foundry technology are able to tailor microstructure and produce cast iron with advanced properties and mixed graphite morphology. Thus, the unambiguous recognition and classification of basic graphite types is indispensable.

Such classification will allow clear correlations between cast iron microstructure and its properties. Although considering only 2D images it might be not possible to understand the distinct factors determining the bulk properties of the material.

### 3.3 CHARACTERIZATION IN 3D

In order to achieve the goal of correct identification of 2D sections of a certain graphite class, the analysis of the real 3D microstructure of individual particles of different graphite morphologies can be very helpful. Besides, 3D analysis of complex graphite morphologies will give the information about material interconnectivity and thus help to understand and predict the effective properties of cast iron materials.

Some three dimensional tomographic methods were developed for the analysis of the non organic materials. The well established x-ray microtomography has a resolution down to 1  $\mu\text{m}$  [97]. This method is non destructive but has limited chemical sensitivity. The use of the synchrotron beam allows nowadays tomographic imaging with sub micrometer resolution as well

as the in-situ observation of the microstructure development during dynamic processes (e.g. [98]). The partial coherence of the beam leads to the new contrast mechanism (phase contrast) and thus allows the imaging of the materials, which were quasi invisible for the conventional x-ray tomography. By the Focused Ion Beam (FIB) serial sectioning, although the investigated region on the sample surface is almost completely removed, the rest of the sample remains preserved. The advantage of FIB-nanotomography is not only the high resolution (down to 10 nm), but also different contrast methods that can be used, which can characterize the crystallographic orientation (using Electron Backscatter Diffraction – EBSD) [99] and composition of the phases (using Energy Dispersive X-Ray – EDX) [100]. The sophisticated particularity of FIB-nanotomography is that anisotropic voxel result from the combination of the SEM and FIB. Transmission Electron Microscope (TEM) tomography allows the 3D characterization with even higher resolution [101], [102], but it is limited to the very small sample volume. Investigated samples have to meet the requirement of material transparency for the electrons (TEM) or photons (TXM). The atom probe, which uses field ion desorption from ultra-high curvature tip, coupled with time-of-flight mass spectrometry and a position sensitive detector, provides the 3D reconstruction of the structure and chemistry of the tip with atomic resolution. Disadvantage is that only some cubic micrometer small volumes can be analyzed and for their preparation rather special and sophisticated techniques are required. For heterogenic materials such an analysis on extremely small samples cannot be representative for the whole structure [103] and thus will not be used in this work for 3D characterization.

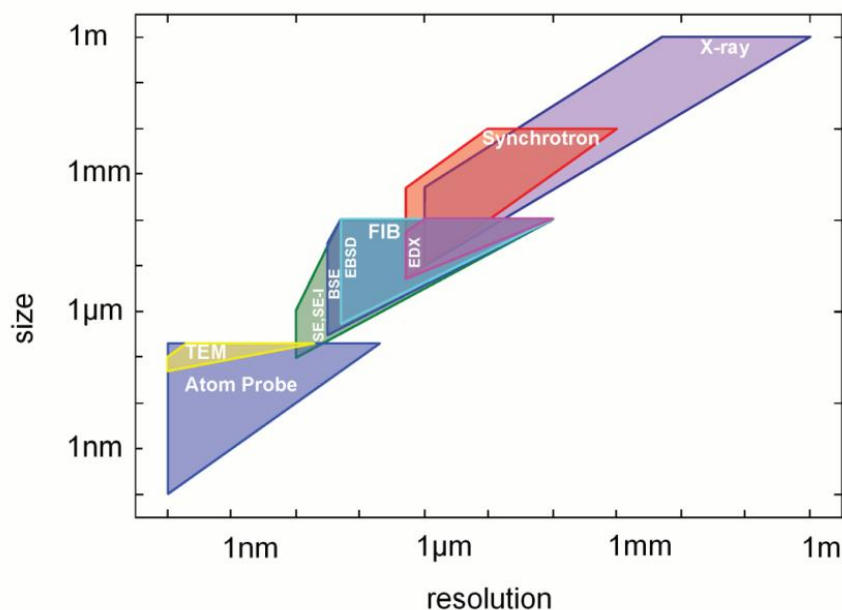


Figure 3.6 The resolution possibilities of the tomography methods for the investigated volume with certain edge size.

Figure 3.6 gives the overview of the tomographic methods mentioned above. Clearly visible is the overlap between synchrotron, x-ray and FIB-tomographies, which can serve as a basis for the comparison investigations of the physical background of the image providing signals. The combination of different tomographic methods can provide 3D characterization of the microstructure over all relevant size scales.

#### 3.3.1 X-RAY AND SYNCHROTRON MICROTOMOGRAPHY

X-ray tomography collects the attenuation of the x-ray beam as a function of the rotation angle to acquire two dimensional images [104]. The series of such images is gathered as a function of the distance along the object and connected in the 3D volume. One of the biggest difficulties during the measurement of the attenuation of x-ray is the signal noise ratio and signal localization. The Cone-Beam X-ray tomography (CBXRT) method was suggested to handle this problem and provided the improvement of the signal noise ratio [105]. In CBXRT two dimensional attenuation data is simultaneously collected with the help of assembled detectors. This method increases the signal noise ratio, and in some cases even the interpolation method is not necessary for the 3D volume reconstruction [104]. However the difficulty of the CBXRT is that the collected data needs to be processed with a complex deconvolution algorithm. Whether or not this technique finds the application in materials science is still a question.

X-ray tomography can be applied for the reconstruction of the 3D morphology and in some cases even the distribution of the chemical elements in the material. The element distribution can be acquired from the x-ray attenuation coefficients, which depend on the chemical compounds [106]. Due to dependency of the x-ray attenuation from both chemical composition and the density of the material one needs to be cautious by the interpretation of the results [97]. Additional difficulty is that the sensitivity of the technique drastically decreases when the sample is composed out of the elements with low atomic number  $Z$ . The difference between the absorption coefficients for the hard x-rays is very low for such elements [107]. The considerable advantage of the 3D x-ray tomography is though the fact, that the investigation does not depend on the sample shape and material composition [108].

Compared with many other characterization methods the final resolution is one of the most important aspects by the x-ray tomography. Significant results were reached through the further development of beam source [109], optics [110], [111], detector and reconstructing algorithms [112].

Recently synchrotron source has been used to obtain high spatial resolution. The resolution down to 0.5  $\mu\text{m}$  can be reached employing a synchrotron beam line. This non destructive high resolution method allows further manipulation with the sample for other experiments. It is even possible to investigate the microstructure development and chemical transformation in material as a function of time [113], [114], [115], [116], [117].

Unlike the conventional x-ray tubes, synchrotron beam source offers continuous energy spectra, which is combined with the high photon flux. Employing the perfect crystal monochromator it is possible to choose one monochromatic beam with sufficiently high photon flux for an efficient imaging. Additionally the monochromatic beam is used for the precise measurement of the sample density. Beam hardening is almost completely eliminated, which is indispensable for the polychromatic standard x-ray tube and which leads to the artifacts in the tomographic imaging. High photon flux allows imaging with high spatial resolution and high signal-noise ratio in relative short time [118]. The linear x-ray attenuation coefficients can be exactly determined for the materials with low atomic number  $Z$  for the energy range of x-ray beam between 10 keV – 100 keV with the help of parameterization of Jackson and Hawkes [119], [120]. Thus, the examination of the inside structure of the materials with low  $Z$  became possible [118], [120].

Aluminum-graphite composites have been successfully analyzed recently with the help of x-ray microtomography with the resolution 2-3  $\mu\text{m}$  [121] and synchrotron tomography with the resolution 0.7  $\mu\text{m}$  [122]. Although Al and C have similar densities it was possible to achieve good contrast between phases due to sufficient variation of linear attenuation coefficient for photons in the range of 40 to 60 keV. Sánchez [121] has also shown, that if the attenuation variation is too large, for example graphite infiltrated with antimony (Sb) it is difficult to differentiate between phases. In addition the high mass attenuation coefficient of Sb leads to reconstruction artifacts when using a polychromatic source.

Even higher resolution was required for the exact 3D characterization of graphite particles in cast iron. Thus, the first studies were performed with the help of FIB-nanotomography.

### 3.3.2 FIB-TOMOGRAPHY – NEW TOOL

The idea of FIB-tomography is based on the metallographical technique of serial mechanical polishing and observation of each section with optical or scanning electron microscopy. Advanced serial sectioning with much smaller interlayer spacing can be achieved by means of ion milling with the focused ion beam (FIB) technique. Inkson et al. [123] has for the first time localized in 3D space the phase borders of the (sub) micrometer large grains of FeAl

nanocomposites with the accuracy better than 100 nm. In his second work [124] 3D mapping of Cu-Al multi layers after deformation with nano-indentation is presented. However, with the single-beam FIB technique, the stage has to be tilted and repositioned between each in-plane erosion and out-of-plane imaging step. Thereby, the mechanical tilting of the stage induces imprecision that limits the resolution and reproducibility of the interlayer spacing. As a result, the data is not suitable for quantification of microstructural features at the submicrometer scale. To some extent, this limitation has been overcome with the more recent dual-beam FIB machines, which consist of an ion column for milling and an electron column for SEM imaging. Holzer et al. [103] has reached in his research of BaTiO<sub>3</sub> sample the resolution of  $5.9 \times 6.8 \times 16.6 \text{ nm}^3$ . It was shown, that through the combination of FIB and SEM a variety of different phenomena can be analyzed in 3D.

The resolution of FIB-nanotomography depends mainly on the precision of the target preparation with focused ion beam and achievable resolution of the signal (e.g. SEM). Hence, the highest resolution of FIB-nanotomography is when applying secondary electron imaging ( $\sim 1 \times 1 \times 10 \text{ nm}^3$ ). EDX FIB-nanotomography has the worst resolution (according to the accelerating voltage  $> 300 \times 300 \times 300 \text{ nm}^3$ ). The resolution of approx.  $50 \times 50 \times 50 \text{ nm}^3$  was reached with EBSD FIB-nanotomography [99]. These two mentioned contrast methods available in the Dual Beam workstation give the complete information about the chemical compositions of materials and crystallographic orientation of the individual grains.

The additional advantage of the FIB-nanotomography in comparison with all other 3D methods is that the small localized region on the relatively large sample can be chosen aiming at the particular result and analyzed with extremely high resolution. This allows much better control of the representative analysis of the heterogenic microstructures. When analyzing 3D arrangement of the microstructural elements two following aspects have to be taken in consideration. The voxel size (i.e. resolution) has to be sufficiently small to provide exact characterization of the microstructure compounds and later to conduct credible simulations [125]. And the analyzed volume has to be sufficiently large to allow the statistically relevant conclusions about the microstructure and to acquire reliable predictions about the material properties calculated from simulations. The upper limit, i.e. the biggest investigated volume, depends on the maximal sputtered volume with the ion beam in a practicable time period. Realistic volumes which can be analyzed with FIB-nanotomography vary depending on the used ion beam current from  $1 \times 1 \times 1 \text{ } \mu\text{m}^3$  to about  $100 \times 100 \times 100 \text{ } \mu\text{m}^3$ . Thus it is clear, that FIB-nanotomography is complementary to already established tomography methods: microtomography with synchrotron and x-ray from one side and TEM-nanotomography from the other.

### 3.3.3 ANALYSIS OF SPATIAL TOMOGRAPHY IMAGES

The determination of the four basic characteristics directly from the 3D images was thoroughly discussed in [78] and [126]. The procedure is based on the integral geometric formulas such as Crofton formulas and the modifications of the Hadwiger recursive definition of the Euler number. The integrals appearing in the Crofton formulas and Hadwiger recursive definition are so discretized for the implementation in microstructural image analysis, that the „measurement“ of the basic characteristics can be performed through the simple “counting” of the elements in the digitalized image. The elements are pixels (voxels) or neighboring configurations of pixels.

The volume fraction of the phase ( $V_V$ ) can be acquired through simple counting of image elements (voxels) which belong to this phase. The consideration of the length and surfaces of the individual image elements, as well as their weight, is required by the determination of the specific surface area ( $S_V$ ) and the integral of the mean curvature ( $M_V$ ). The precision of the estimation depends on the size of the elements, and thus on the resolution of the 3D images, as well as on the right choice of the weight of the individual elements. The weight coefficients are defined by the shape of the elementary cell of the 3D image, i.e. by the voxel size in  $x$ -,  $y$ - and  $z$ -direction. CT-images have equidistant voxel size, whereas anisotropic voxels have to be considered in case of FIB-Nanotomography. L. Helfen has concentrated in his work [127] in particular on the effect of the resolution on the estimation of  $S$  and  $M$  and on the anisotropy of the microstructure. Euler number ( $\chi_V$ ) characterizes particle complexity and connectivity. In [128] was shown, that its determination and thus the determination of the integral of the total curvature ( $K_V$ ) depends significantly on the chosen connectivity, i.e. the rule according to which the neighboring pixels are being found. The systematic mistake measured for the different estimations of the Euler number does not disappear with the increasing resolution [128], [129]. It was shown, at which resolution and volume fractions of the phase the evaluation of the Euler number is less faulty. Although no clear conclusions could have been drawn showing which neighbor system is best suited for the estimation of Euler number.

The necessity on the unambiguous and relatively easy algorithms for the 3D microstructure characterization has remarkably grown in the last 10 years. This is undoubtedly connected with the new developments of the 3D material characterization methods. A lot of questions though, as for example the characterization of complex, non convex morphologies, are still to be answered. The analysis of the influence of the resolution, anisotropy for such microstructures is the following sophisticated task for the mathematicians and materials scientists.

## II. EXPERIMENTAL



---

## 4 EXPERIMENTAL PROCEDURE

---

For the reliable quantification of material properties it is important to have a quick, consistent and reproducible method of analysis. New questions of microstructure characterization require the development of new experimental approaches and quantitative analysis techniques. Yet, the first task in order to assure adequate microstructure characterization is an accurate free of artifacts specimen preparation.

### 4.1 SAMPLE PREPARATION

#### 4.1.1 CHEMICAL COMPOSITION

The samples of cast iron with either spherical (SG), or flake (FG), or vermicular (CG) graphite, as well as samples of malleable cast iron (TG) were investigated in this work. Samples were provided by Halberg Guss GmbH. No information about the chemical composition of malleable cast iron was available.

Table 4.1 Chemical composition of cast iron samples with flake (FG), vermicular (CG) and nodular (SG) graphite.

Alloying elements, weight %	FG <sub>1</sub>	FG <sub>2</sub>	FG <sub>3</sub>	CG <sub>1</sub>	CG <sub>2</sub>	CG <sub>3</sub>	SG
C	3.29	3.35	3.29	3.68	3.68	3.61	3.68
Si	2.07	2.17	2.03	2.21	2.12	2.14	2.23
P	0.049	/	/	0.027	0.018	/	/
S	0.11	0.093	0.105	0.0105	0.0096	0.009	0.006
Mn	0.65	/	/	0.36	0.38	/	/
Cr	0.496	/	/	0.051	0.041	/	/
Cu	1.294	/	/	1.164	1.022	/	/
Ti	0.032	/	/	0.011	0.013	/	/
Sn	0.1	/	/	0.121	0.108	/	/
Mg	0	0.001	0.001	0.012	0.013	0.008	0.026
Ni	0.104	/	/	0.032	0.022	/	/
N	0.0168	/	/	0.011	0.008	/	/

#### 4.1.2 METALLOGRAPHIC PREPARATION

The samples were cut, embedded in resin and prepared on an automatic grinding and polishing machine “RotoPol 22” of the Struers Company in two steps: grinding and polishing (see Table 4.2).

The surface roughness was characterized after each of the four last preparation steps in order to prove, which metallographic preparation procedure provides the optimum surface quality of the polished macro section.

Table 4.2 Sample preparation procedure.

	Steps	 Grinding	 Polishing		
	Surface	SiC - Paper	MD – DAC		
	Grain size	220, 500, 800, 1200	6µm	3µm	1µm
	Lubricant	Water	Lubricant green		
	[r.p.m.]	300	150	150	150
	Force [N]	10	5	5	5
	Time [min]	each 2-5	5	5-10	10

#### 4.1.3 SURFACE QUALITY

The surface topography of the cast iron samples was analyzed with the help of the white-light interferometer “Zygo New View 200” equipped with “3D Imaging Surface Structure Analyzer”. The vertical resolution is in the order of 0.3 nm whereas the lateral resolution is between 0.73 and 11.8 µm depending on the used objective [130]. Following parameters were determined:

*PV* – the distance in µm between the highest and the deepest point of the surface;

*rms* – the square deviation of all measuring points *N* of the surface from the mean value;

$$rms = \sqrt{\frac{\sum_{i=1}^n y_i^2}{N}} \quad 4.1$$

*R<sub>a</sub>* – the linear deviation of all measuring points of the surface from the mean value.

$$R_a = \frac{\sum_{i=1}^n y_i}{N} \quad 4.2$$

The planar surface, which is satisfactory for examination under the optical microscope, was obtained already after polishing the samples with 3  $\mu\text{m}$  diamond suspension. It is true, however, that the topography is very distinctive (Figure 4.1).

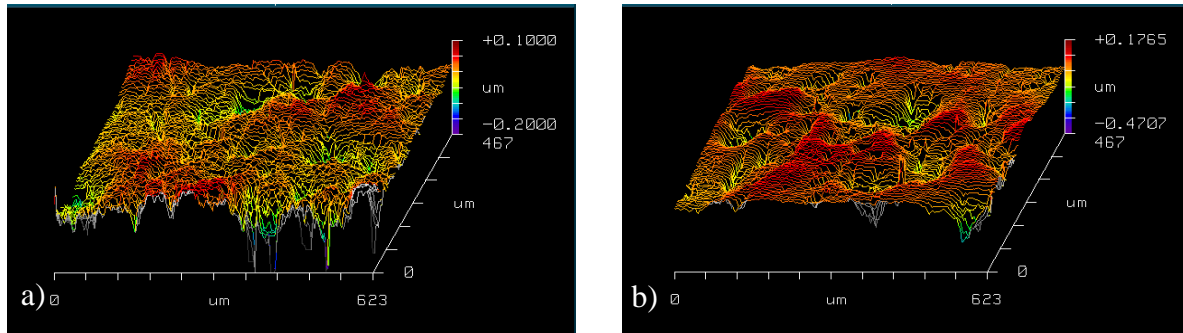


Figure 4.1 Surface topography of cast iron with a) flake and b) vermicular graphite after the preparation step with 3  $\mu\text{m}$  diamond suspension (magnification 100x).

The surface quality is improved and the topography of the graphite particles is reduced after subsequent polishing with a 1  $\mu\text{m}$  diamond suspension. The topography of the surface after polishing with 3  $\mu\text{m}$  and 1  $\mu\text{m}$  diamond suspension is compared in the Figure 4.2 (magnification 800x).

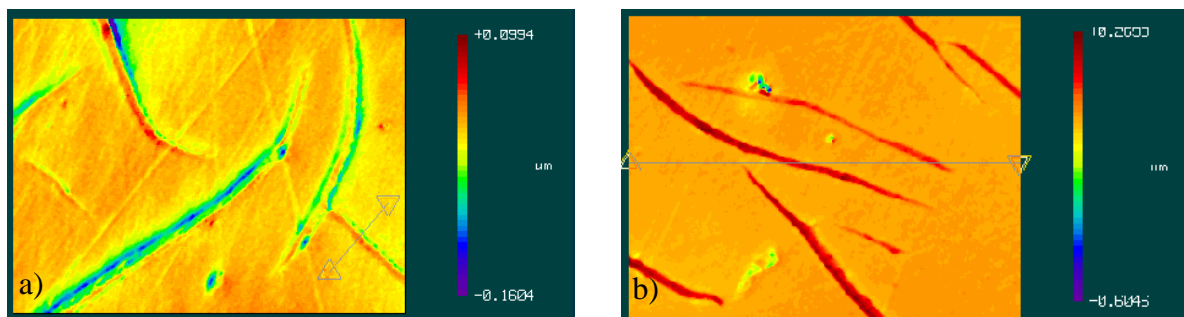


Figure 4.2 Comparison of the preparation quality of the cast iron sample with flake graphite after the polishing a) 3  $\mu\text{m}$  and b) 1  $\mu\text{m}$  diamond suspension.

The final polishing of the surface with an OPS suspension caused the unfavorable microstructure changes on the sample surface which increased the surface roughness. The results of the topography analysis are summarized in the Figure 4.3.

The investigations made have shown that the preparation with polishing down to 1  $\mu\text{m}$  diamond suspension yields best results. Surface quality is very important for the reason that an increased topography leads to inaccuracies in detecting the phase boundaries between the matrix and graphite particles. This is especially important analyzing the cast iron samples with flake graphite. The relatively large specific surface area ( $S_V$ , see section 3.1.2) of the flake graphite particles heavily influences the precision of the quantitative analysis.

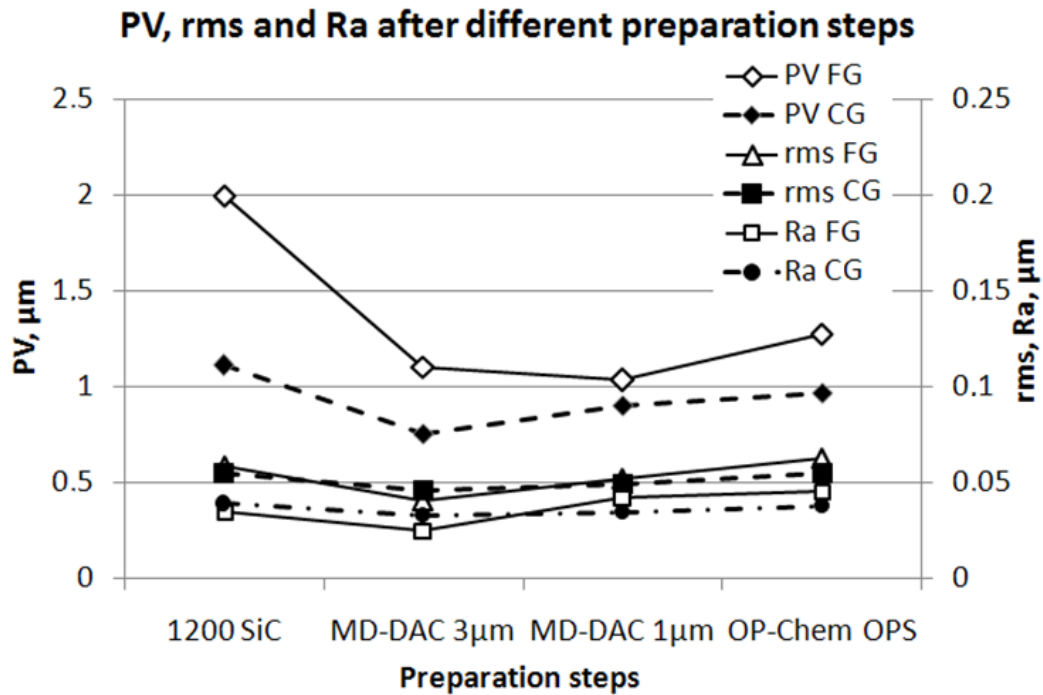


Figure 4.3 The results of surface topography measurements of cast iron with flake and vermicular graphite.

#### 4.1.4 CHEMICAL ETCHING

Next to graphite morphologies the matrix microstructure plays an important role for the properties of cast iron. An efficient way for visualizing the pearlitic structure is the chemical treatment with solution containing 90 ml of ethanol 96 % and 10 ml of nitric acid 65 % for two seconds. Already after such a short attack lamellae of pearlite are clearly visible (Figure 4.4a).

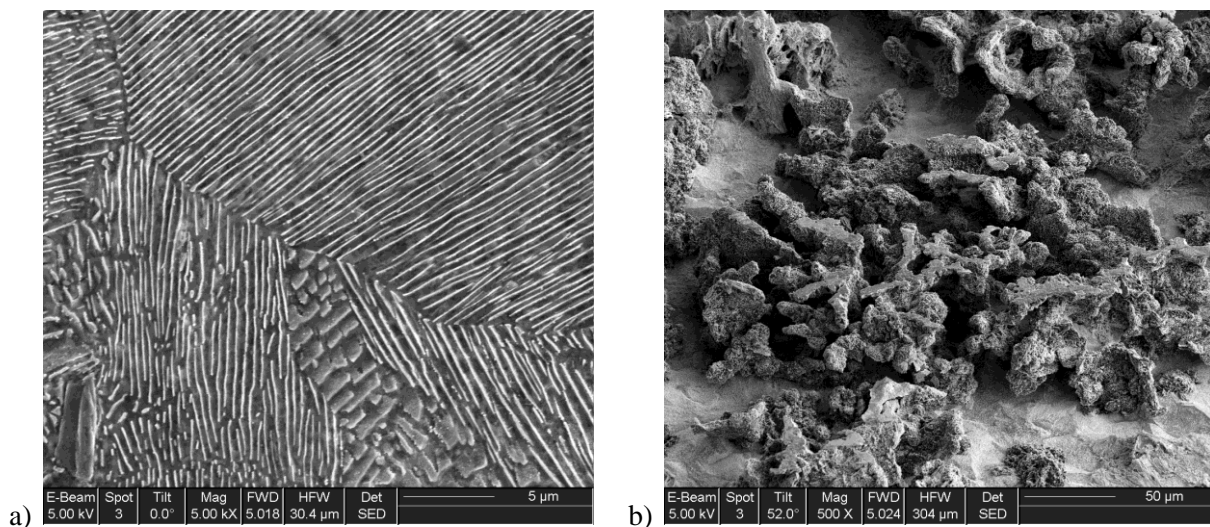


Figure 4.4 Cast iron sample with vermicular graphite etched for a) two seconds (magnification 5000x) and b) two hours (magnification 500x).

The ferrite regions appear to be considerably lighter in the image of the optical microscope. It was found, that the matrix microstructure is homogeneous and, if it is not further mentioned, the volume fraction of ferrite is less than 1 %. The pearlite lamellae distance depends on the thickness of the founded sample. The thickness of all investigated samples was 9 mm, so the distance of pearlite lamellae was constant and equal to  $0.5 \pm 0.03 \mu\text{m}$ .

Further use of the etching reagent (up to two hours) allows the complete exposition of individual graphite particles (Figure 4.4b). This procedure has shown to be very successful for the 3D characterization of graphite morphology with the help of FIB nanotomography (see also section 4.2.3).

## 4.2 MICROSCOPIC CHARACTERIZATION OF THE MICROSTRUCTURE

### 4.2.1 OPTICAL AND SCANNING ELECTRON MICROSCOPY

The microstructural analysis of the geometrical graphite shape occurred with the help of optical and scanning electron microscopy.

#### 4.2.1.1 OPTICAL MICROSCOPY

Microstructural images were captured with an optical microscope (Olympus® BX60) in the bright field mode. A CCD-camera type A101f of the Basler AG, Ahrensburg was used which produced an image at a resolution of about  $1300 \times 1030$  pixels. For the first studies the magnification of  $200\times$  was chosen, providing relatively high digital resolution (pixel size  $0.66 \mu\text{m}$ ) which allows exact determination of structural characteristics [85]. In addition, it is possible to measure a sufficiently large surface area when several images are combined together. The chosen imaging procedure made representative characterization of the structure possible while keeping any distorting border effects at the minimum.

In order to analyze the influence of the magnification effect on the graphite characterization further images of optical microscope were taken at the magnification  $100\times$ ,  $200\times$ ,  $500\times$ , and  $1000\times$ .

#### 4.2.1.2 SCANNING ELECTRON MICROSCOPY (SEM)

Additionally, graphite inclusions were investigated with Dual Beam™ Strata 235 of FEI Company, Eindhoven (NL) consisting of a high-resolution scanning electron microscope (SEM) equipped with a field emission gun and a focused ion beam (FIB). SEM images were acquired in the secondary electron modus at different (incl.  $500\times$ ,  $1000\times$ ,  $2000\times$ , and  $3000\times$  for the analysis of resolution dependency) magnification. Digital resolution of the images de-

depends on the scan velocity and can be calculated from the magnification and image size ( $1024 \times 884$  pixels). An acceleration voltage of 5 kV and a spot size 3 was used in the search modus and 20 kV for imaging and investigations of chemical composition (EDX).

#### 4.2.1.3 ENERGY DISPERSIVE X-RAY ANALYSIS (EDX)

Chemical analysis by EDX has been performed on the polished samples, cross sections and even TEM specimens. A carbon TEM sample holder was especially designed for the x-ray elemental mapping on the TEM foils [131]. In comparison with EDX analysis on a bulk sample, higher resolution can be achieved since the depth of interaction between the electrons and the material is reduced to the thickness of the specimen (approx. 100 nm, see also [132]). The measurements were performed by energy dispersive spectroscopy with an accelerating voltage of 20 kV using EDAX instruments detector and EDAX Genesis<sup>MR</sup> Software.

#### 4.2.1.4 ELECTRON BACK SCATTERED DIFFRACTION (EBSD)

A TSL EBSD system was used for analysis of the crystallographic orientation of the samples. Thus, it was possible to study the orientation of pearlite grains. No satisfactory back scattered signal was acquired from polycrystalline graphite inclusions of any type even after polishing with the low current ion beam. High absorption of electron signal and low perfection of graphite crystals served the reason for this effect. STEM or TEM observations were required to analyze the orientation of graphite inclusions.

### 4.2.2 TRANSMISSION ELECTRON MICROSCOPE (TEM) STUDY

#### 4.2.2.1 TARGET PREPARATION OF TEM-FOILS WITH FIB WORKSTATION

Dual Beam<sup>TM</sup> Strata 235 workstation was equally used to prepare TEM thin foils. In order to do this, two trenches have been milled on both sides of the region of interest generally in the middle of the particle. While gradually reducing the ion beam current, the specimen was thinned down to 1  $\mu\text{m}$ . After reaching this thickness, the sample was back-tilted to  $7^\circ$  and the foil was partially cut free with a U-shaped pattern, still connected to the substrate via two thin branches at the top (Figure 4.5a). For in-situ lift-out, a micromanipulator “Kleindiek MM3A” was inserted into the chamber. The micromanipulator tip was positioned over the TEM foil and was slowly lowered until it contacts the specimen. The specimen and the tip were welded by depositing a rectangular Pt layer using the electron beam. When the specimen and the tip were fixed together, the specimen was cut free from the substrate. The specimen, now only fixed to the tip of the micromanipulator, was lifted out (Figure 4.5b) and moved to a pre-cut Cu TEM grid, where it was fixed again by electron-deposited Pt (Figure 4.5c).

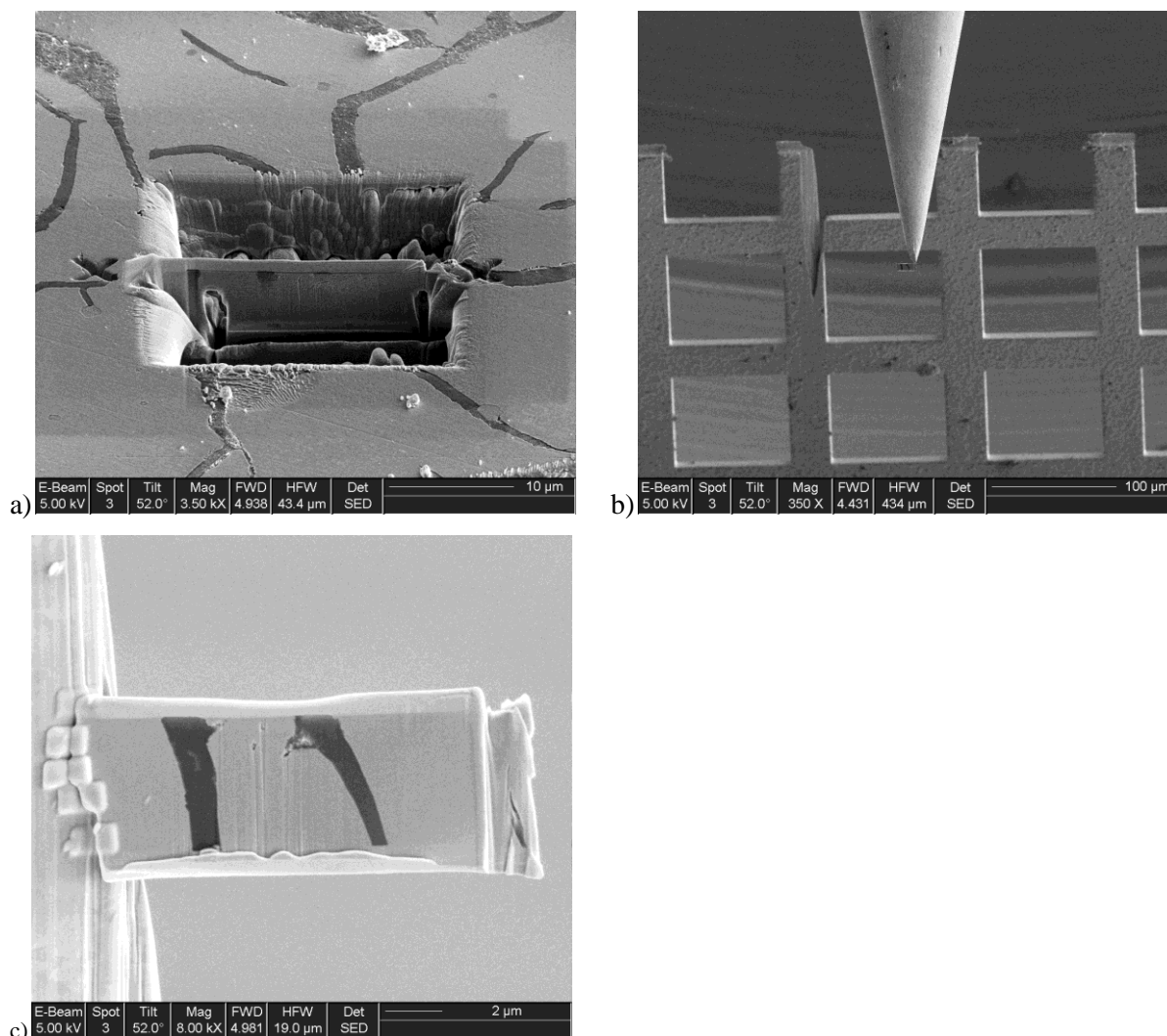


Figure 4.5 TEM specimen preparation using FIB on a graphite particle. a) The lamella is milled on both sides. The specimen is cut free from the substrate and is fixed to the micromanipulator tip to be extracted (b) in situ lift-out procedure. c) TEM foil soldered to the Cu grid.

On the Cu grid, the specimen was finally thinned down to a thickness of approximately 100 nm using small ion beam apertures of 30 and 50 pA at 30 kV at an incident angle between  $0.5^\circ$  and  $1.2^\circ$ . Difficulties by thinning occurred due to the different phases present in the TEM foil. To reduce the edge amorphisation the low tension polishing at 5 kV at a  $4^\circ$  angle was applied. For more details see [133], [134].

For the first observation of the microstructure, a scanning transmission detector (STEM) was used in the dual beam workstation using an acceleration voltage of 5 or 18 kV and the ultra-high resolution mode of the electron microscopy.

### 4.2.2.2 TEM STUDIES

TEM analysis was carried out with a Jeol JEM 200 CX at an operating voltage of 200 kV. Both direct imaging for elucidation of the microstructure and selected area diffraction for phase identification were used. In addition, EDX (Oxford Isis) analysis was performed in or-

der to identify the chemistry of the different phases. In some cases before TEM Analysis an additional Ar-ion cleaning stage at 5 kV was employed.

### 4.2.3 FIB NANOTOMOGRAPHY

#### 4.2.3.1 GENERAL PRINCIPLES OF FIB-NANOTOMOGRAPHY

Focused Ion Beam (FIB) tomography [103] is based on a serial slicing technique employing a FIB/SEM dual beam workstation. In principle, the method consists of performing serial FIB cross-sections through the volume that is chosen for the analysis. Each exposed surface is imaged with an electron microscope (Figure 4.6) either in secondary or backscattered electron contrasts or using EDX-mapping similar as described in [100]. In this configuration, the sample does not have to be removed from the microscope and the analysis is performed automatically (or partly automatically in case of 3D EDX-FIB tomography[135]) using a scripting routine. A dual beam workstation (FEI Strata DB 235) equipped with a FIB column employing a Ga liquid metal ion source, and a high resolution field emission electron microscope was used. The angle between the FIB and the SEM column is  $52^\circ$  and the sample surface is oriented perpendicular to the ion beam during cross-sectioning. In order to protect the sample surface, to improve the quality of the FIB polishing, and to create a sharp boundary at the upper edge of the polished area, a large Pt-layer was deposited over the area of interest prior serial sectioning. Before starting the automated serial sectioning procedure, a comparatively large trench using a regular cross-section was milled in front of the graphite particles. The choice of the milling and imaging parameters determines the resolution of the individual images and the spacing between the slices [103]. Hence, these parameters should be adapted to the size of the graphite particle being analyzed.

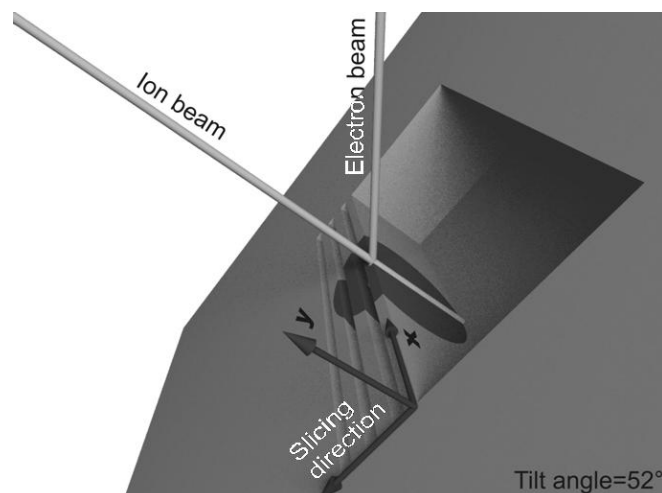


Figure 4.6 Schematic illustration of the geometrical configuration for the serial cross-sectioning procedure.

### 4.2.3.2 ANALYSIS OF THE COMPLEX GRAPHITE PARTICLES

Four samples of malleable cast iron and cast iron with flake (FG), vermicular (CG) and spherical (SG) graphite particles were investigated in this work.

*FIB parameters:* Following Holzer et al. [103] at least ten sections have to be collected through a particle for accurate 3D reconstruction. The diameter of graphite inclusions vary between 10  $\mu\text{m}$  for nodular graphite and more than 100  $\mu\text{m}$  for vermicular and flake graphite. In addition, apart from nodular graphite, graphite particles are strongly non-convex and irregular. From 2D analysis of optical micrographs it was found, that for correct characterization and classification a pixel resolution of at least 0.6  $\mu\text{m}$  has to be used [85]. Considering the minimum pixel resolution and the size of the graphite particles, an ion beam current of 20 nA was used for the tomography in order to remain within a suitable time frame (40-50 sec milling time for each slice). The beam diameter is estimated to be in the order of 300 nm (FEM simulation, FEI). Hence, a resolution of 300–500 nm should be expected for 3D tomography which is acceptable for the graphite particles analyzed in this work. The total time depends on the time for milling and the time for imaging ( $\sim 2$  min/slice). Thus, a region of 80  $\mu\text{m} \times 80 \mu\text{m}$  can be analyzed though serial sectioning of 200 slices within 6–7 h.

*The use of selective carbon milling precursor:* In general the sputter yield of phases with different chemistry is not the same. In order to modify the sputter yield, FIB milling can be performed while flushing the chamber with different gases for enhanced or depressed sputtering [97]. In the case of graphite in cast iron, this possibility is especially important due to the large difference in the sputter yield of graphite and iron, respectively. Graphite particles in cast iron represent a volume fraction of about 10 % and have a considerably lower sputter yield in comparison to the iron matrix. Without using any gas additives, the graphite particles are very inefficiently sputtered and ridges of graphite remain in the sputtered region (see Figure 4.7a). This problem can be overcome by using a selective carbon milling precursor (SCM) during the sputtering process. Water vapor, the active gas component, proved to drastically increase the material removal rate of carbonaceous materials (by a factor of 20 for PMMA, and 10 for diamond [136]).

When performing serial sectioning, redeposition and shadowing occurs and leads to a decrease of the usable sample surface for imaging (Figure 4.7). In [103] a U-shaped groove was used which significantly reduced such effects. In the case of the relatively large graphite grains investigated in this study, this procedure appeared to be too time-consuming. Therefore, a sample etching procedure was developed which removes most of the iron matrix surrounding the graphite prior the serial sectioning routine.

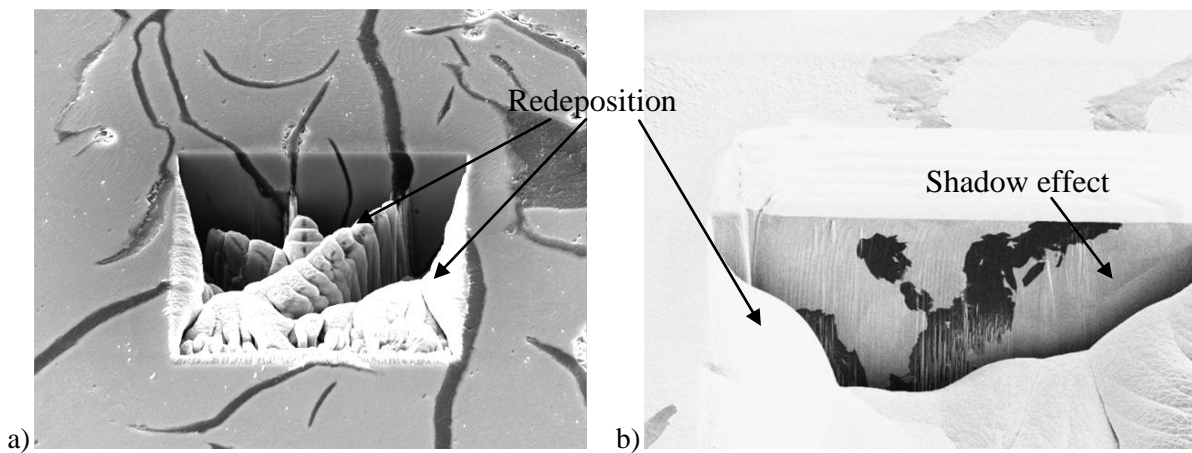


Figure 4.7 Sputtering of cast iron a) without and b) with SCM precursor. SEM images, sample at 52° tilt.

*Deep chemical etching of the iron matrix:* In addition to the aforementioned practical reason, an examination of a polished cast iron sample is difficult because of a sampling problem: it is impossible to locate a suitable graphite grain underneath the surface. If it appears at the surface, the complete shape of the grain cannot be studied. Furthermore, the three-dimensional particle morphology under the visible surface cannot be predicted. Therefore, in theory a much larger sample volume would have to be sectioned in order to randomly find a suitable graphite particle. In order to circumvent this problem, a heat treatment was first carried out to dissolve cementite in eutectoid pearlite and thus increase the volume fraction of ferrite. Subsequently a deep selective etching of the ferrite was performed prior serial sectioning (similar as already described in section 4.1.4). Using a mixture of 90 % ethanol and 10 % nitric acid for approximately 2 h, it was possible to expose almost entire single graphite particles (Figure 4.8).

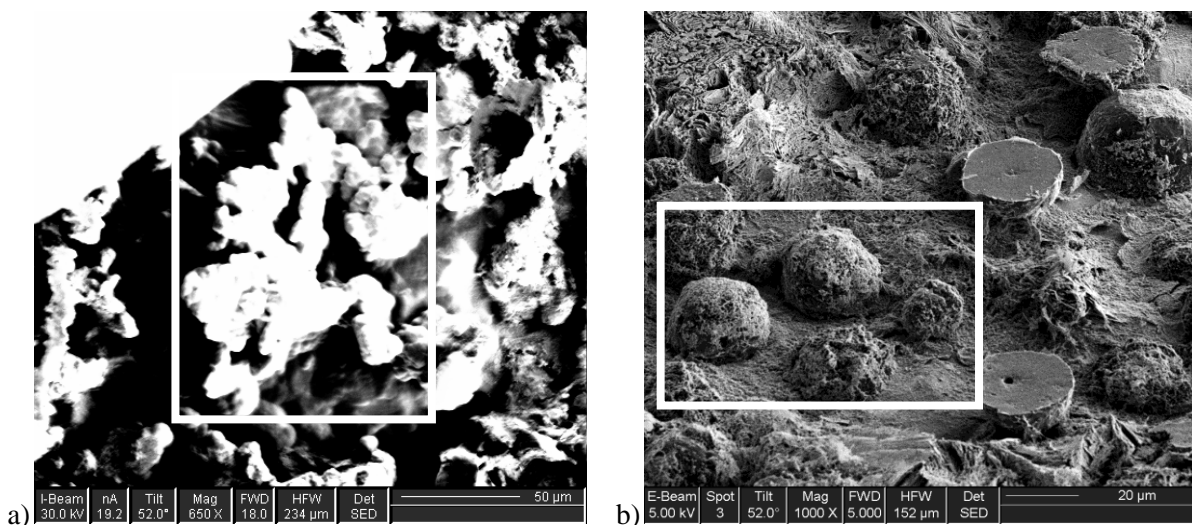


Figure 4.8 Deep etched cast iron samples a) ion image of region of interest and SCM precursor needle (upper left corner); b) nodular cast iron sample (electron image 52° tilt).

*Serial sectioning:* The graphite particles are covered with a large Pt-layer of about 0.5–1  $\mu\text{m}$  thickness using in-situ Pt deposition. As discussed above, the FIB was operated at 30 kV accelerating voltage and 20 nA beam current for serial sectioning. For secondary electron imaging, an accelerating voltage of 5 kV was used. Due to sample pre-treatment, the newly developed method considerably reduces the time of FIB usage and thus ion source consumption and hence can successfully be applied to analyze the 3D graphite morphology.

*Alignment and 3D reconstruction:* The image stack gathered during the serial sectioning procedure was analyzed using the 3D reconstruction software package Amira®. First, the voxel dimensions were determined by considering the scan rate and the magnification of the electron images. Second, a correction in the y-direction to account for an image distortion caused by a 52° sample tilt was performed. The voxel size in the z-direction is determined by the distance between individual slices. The voxel parameters for the some samples analyzed in this study are listed in Table 4.3.

Table 4.3 The voxel parameters for the 3D characterization.

Sample	Magnification	Number of slices	Voxel size, nm		
			x	y	z
FG-1	800	200	185.2	235	500
FG-2	1600	64	93	118	310
FG-3	1500	206	99	126	333
CG-1	1500	200	106.4	135	333
CG-2	750	306	198	251	500
SG in cast iron sample with vermicular graphite	2000	160	75	95	333
TG	1000	167	149.2	189.3	500
SG	1500	240	98.5	125	333

Third, the images were aligned using the Pt-sample interface, and afterwards the segmentation of the image stack was carried out. It was not possible to use automatic thresholding segmentation. Hence, the graphite particles were masked by manual inspection using different image software tools. Once the graphite phase in all individual images has been segmented, Amira is able to create a 3D polygonal surface model. For further quantitative analysis, the software package a4i was used on 2D slices through the reconstructed graphite grains. MAVI Software was employed for direct analysis of 3D images.

## 4.3 QUANTITATIVE IMAGE ANALYSIS IN 2D AND 3D

### 4.3.1 IMAGE PROCESSING AND BINARIZATION

2D images acquired from optical microscopy, SEM, TEM, and even EDX-maps, as well as 3D images from FIB-tomography can be used for quantitative characterization of the microstructure. Generally digital cameras used in the combination with above mentioned techniques provide gray scale images. Image analysis algorithms support the detection of microstructure constituents through image segmentation and object labeling. The problems of image processing are discussed in detail in [74], [84].

To assist correct segmentation various image processing algorithms (often associated with the image acquiring technique) are applied. Shading correction is indispensable for the optical light microscopic images and in some cases SEM images of cross-sections to provide uniform illumination. Smoothing filters (average, mean [90]) are often used to minimize noise of SEM images. Sharpening filters [90] provide exact determination of the phase borders. As though using different filters always lead to certain changes of image only limited amount of filters was consistently applied to either optical micrographs or SEM images of cast iron microstructure.

Subsequently, image segmentation was performed assigning the gray value below certain threshold to foreground (objects e.g. graphite inclusions) and above – to background (e.g. iron matrix). The correct threshold value was chosen where possible automatically as a local minimum of the gray values distribution in the 2D or 3D image, and thus eliminating subjective manual choice. Object labeling was performed automatically using “object search” in 2D [90] and labeling algorithm in 3D [137].

### 4.3.2 DETERMINATION OF BASIC PARAMETERS FROM 2D IMAGES

#### 4.3.2.1 2D PARTICLE BASED PARAMETERS

The 2D characterization and classification of graphite particles or, strictly speaking, its two dimensional microsection, was performed with the help of the image analysis system a4i Analysis of the Aquinto AG (now Olympus). The particle based method was chosen to characterize single irregular two-dimensional objects. With this method every single graphite particle can be individually characterized, identified and assigned to a certain class. Geometrical characteristics, shape parameters, its position in a cross-section and with regard to other particles were determined for each isolated particle. Geometrical features used for graphite characterization were also required for the calculation of the classification parameters (see

Table 3.2). These are in particular area, perimeter, convex perimeter, and Feret diameters (Figure 4.9). Area was calculated by simple counting the pixel belonging to the object considering the calibration factor derived from the image magnification. Perimeter was determined according to the following formula:

$$P = \frac{4}{\pi} (Pro0^\circ + Pro45^\circ + Pro90^\circ + Pro135^\circ), \quad 4.3$$

from the length of the projection in the directions  $0^\circ$ ,  $45^\circ$ ,  $90^\circ$  and  $135^\circ$  [90] (see Figure 4.9b). Convex perimeter is determined from the four Feret diameters.

$$ConvexP = \frac{4}{\pi} (Feret0^\circ + Feret45^\circ + Feret90^\circ + Feret135^\circ) \quad 4.4$$

The Feret diameters are determined in every direction from  $0^\circ$  to  $175^\circ$  with the step of  $5^\circ$ . The largest of these values is called *MaxFeret* and describes the elongation of the object, the smallest – *MinFeret*.

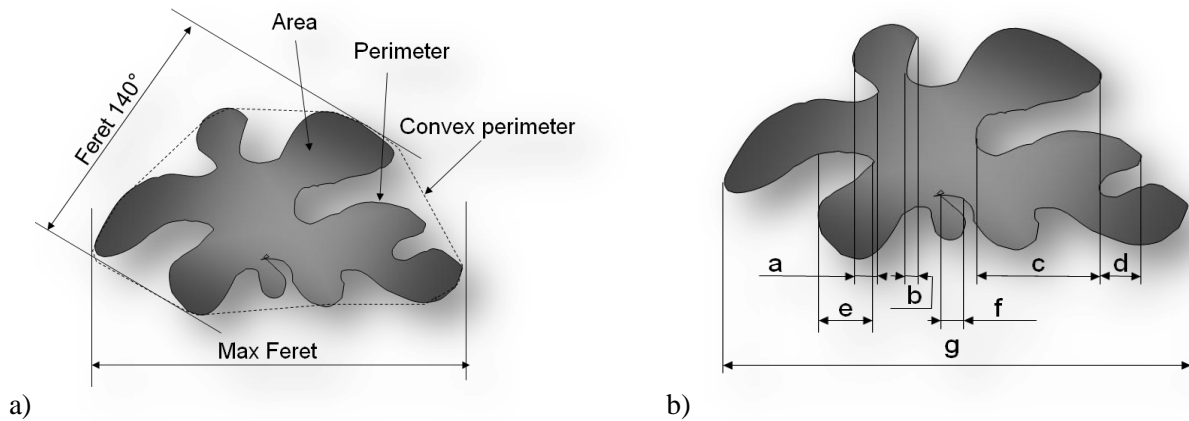


Figure 4.9 a) Geometrical features of an object. b) Example of projection in the direction  $90^\circ$ :  $Pro90^\circ = a + b + c + d + e + f + g$ .

Having this geometrical parameter all shape parameters shown in Table 3.2 were calculated. Another important object parameter is its Euler number  $\chi$ . It describes the particle connectivity and can be calculated in 2D according to the formula:

$$\chi = N - C = \frac{1}{2} (Nr. (A) - Nr. (B) - Nr. (C) + Nr. (D)). \quad 4.5$$

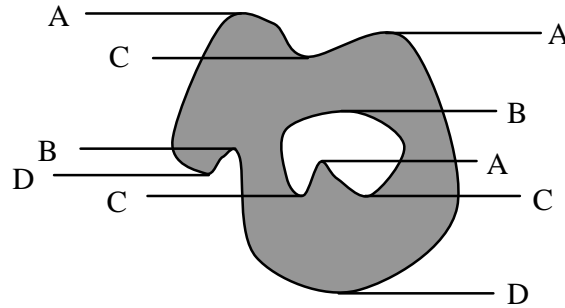


Figure 4.10 Tangents of the type A, B, C and D for the calculation of the Euler number.

By the calculation of the mean value of the particle features only particles entirely presented in the 2D image have to be taken into account. Particles which are cut by the image boarder have to be ignored as they falsify the results of the particle features. Clearly larger particles are more likely cut by the boarder than the small ones. Thus, either suitable image magnification (which often means lower resolution) has to be chosen to provide sufficiently large microstructural images or the combination of some high resolution images (higher magnification) has to be performed.

*Statistical analysis of particle based parameters:* All acquired features for each particle were exported from the image analysis software and further analyzed with Microsoft Excel or OriginLab. The shape parameters are the basis for the classification of the graphite. Thus, the analysis of the wide spectrum of particles is very important for the correct classification. The arithmetical mean value  $\bar{\mu}$  gives the information about the average of the measured values:

$$\bar{\mu} = \frac{1}{N} \sum_{i=1}^N x_i \quad 4.6$$

here  $N$  is the number of the measured particles. The standard deviation  $\bar{\sigma}$  describes the degree of deviation of the individual measured value  $x_i$  from the mean value  $\bar{\mu}$  :

$$\bar{\sigma} = \sqrt{\frac{1}{N-1} \sum_{i=1}^N (x_i - \bar{\mu})^2} \quad 4.7$$

Confidence interval  $CI$  is defined as an interval which encloses the measured value  $x_i$  with a certain probability. It is calculated from the number of measured values  $N$ , mean value  $\bar{\mu}$ , standard deviation  $\bar{\sigma}$  and the level of confidence. For example the 95 % confidence interval is calculated like:

$$CI = 1.95996 \cdot \bar{\sigma} \quad 4.8$$

The higher the confidence level, the higher the confidence interval  $CI$ . The increasing number of measured values reduces the  $CI$ .

It should be mentioned that the optical impression of the microstructure is defined in general by the large objects. The statistical analysis is though dominated by the small objects, which amount is often much higher than the amount of the larger objects. This fact can be taken into consideration either by eliminating small objects entirely or by introducing certain weights in the calculation of mean values. Area fraction is suggested as the weighting factor for the calculation of the area weighted mean value  $\bar{\mu}$ :

$$\bar{\mu} = \frac{\sum_k \bar{\mu}_k \cdot A_{Ak}}{A_A} \quad 4.9$$

here  $\bar{\mu}_k$  is the mean value for the size class  $k$  (e.g. according to the DIN EN ISO 945),  $A_{Ak}$  the area fraction of all particles of the size class  $k$ ,  $A_A$  the total area fraction of the phase. Standard deviation of value  $\bar{\mu}$  was calculated using the derivative of the formula 4.9 for each parameter:

$$\bar{\sigma} = \sqrt{\left(\frac{\partial \bar{\mu}}{\partial \mu_1}\right)^2 \cdot \sigma_{\mu_1}^2 + \left(\frac{\partial \bar{\mu}}{\partial \mu_2}\right)^2 \cdot \sigma_{\mu_2}^2 + \dots + \left(\frac{\partial \bar{\mu}}{\partial A_A}\right)^2 \cdot \sigma_{A_A}^2} \quad 4.10$$

#### 4.3.2.2 FIELD BASED PARAMETERS

Basic characteristics ( $V_V$ ,  $S_V$ ,  $M_V$ ) of the quantitative image analysis were calculated from the 2D images according to stereological equations (see Table 3.1) automatically with the help of a4i Analysis. The acquired features do not refer to individual particles but characterize the microstructure in general. Thus, no boarder correction has to be done. Additionally, particle number per unit area  $N_A$  as a widely used field feature was determined. This parameter is well suited for the characterization of the microstructures with simply connected objects in 2D. Only for the limited amount of microstructures with particles of the certain shape and distribution particle number per unit area  $N_A$  can be used for the estimation of the particle number per unit volume  $N_V$ . Actual  $N_V$ , or  $\chi_V$  and thus  $K_V$  can be determined only from the 3D images for other microstructure types.

### 4.3.3 QUANTITATIVE ANALYSIS OF 3D IMAGES

The three dimensional characterization was carried out with the help of the software system MAVI (Modular Algorithms for Volume Images) for the processing and analysis of 3D images developed at the Fraunhofer ITWM. MAVI is specialized in the characterization of the geometry of complex microstructures: volume, surface area, integrals of curvature, and Euler number can be determined for the complete structure and isolated objects. Up until now, 3D images acquired with x-ray and synchrotron tomography were successfully analyzed using MAVI algorithms. In this study the analysis of the data with anisotropic voxels (in the  $x$ -,  $y$ -, and  $z$ -directions) was done for the first time.

MAVI's core is complemented by various filters and transformations, techniques for image segmentation and object isolation. In order to perform accurate characterization at the first step, the voxel dimensions was specified (see Table 4.3) and the stack of images was segmented. The module “object labeling” assigns every connected object in the image a certain grey level, which is unique for each object. The connectivity of the pixels depends on the chosen neighborhood [128]. In this work the neighborhoods 26/6 and 14/1 were chosen for the calculation of the particle features, as the most used in the algorithms for the determination of the Euler number [138]. The field features as well as the particle features were determined. The algorithms used in MAVI to perform the measurement of characteristic structure parameters are described in detail in [78], [126], [128] and [139].

## 4.4 MEASUREMENT OF THE ELECTRICAL RESISTIVITY

### 4.4.1 FOUR-POINT METHOD FOR MEASURING ELECTRICAL RESISTIVITY

Electrical resistivity at room temperature was measured using a four-point direct current technique. The measurements were performed with the setup built at our institute. Scheme on the Figure 4.11 shows the position of the contacts. Here the constant current  $I$  (mA) flows through the current cables and screws, which also serve for the sample fixation, and the voltage drop  $U$  is measured across the Cu wire contacts. The wires are fixed 7 mm apart parallel to each other. Now the resistance of the sample can be measured according to the Ohm's law. The considerable advantage of the four-point method is, that the possible potential drop on the contacts delivering current as well as the resistance of the measuring cables are excluded from the measurement.

The sample geometry was controlled by the following use of the experimental setup for the analysis of the gradient samples from the motor blocks. The specimens are cuboids,

$10.00 \pm 0.06$  mm long, and  $2.50 \pm 0.08$  mm wide and thick. Although the fixing screws ( $\varnothing$  2 mm) do not provide contact with the entire side surface of the sample, the calculated error is negligible. This estimation was performed within the verification of the resistivity measurements with the help of FEM-simulations with FlexPDE[140].

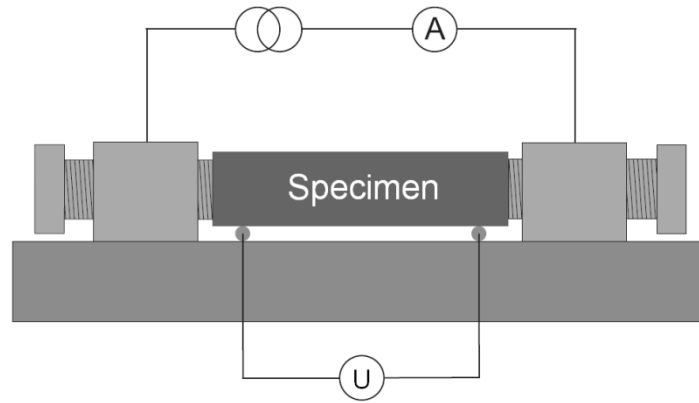


Figure 4.11 Scheme of the contact configuration (side view). The specimen is fixed by two screws, which also serve as the current contacts. Underneath the sample the voltage drop is acquired from two parallel wires. Full contact of the sample with the wires is assured by the additional sample fixation from the top (here not shown).

#### 4.4.2 DETERMINATION OF ELECTRICAL RESISTIVITY ( $\rho$ )

The equipment for measuring current and voltage used for the four-point measurement of the electrical resistance was from Keithly Instruments, Inc., Cleveland, Ohio, USA (Model 2400 Series Source Meter and Model 2000 Multimeter). The computer program (developed in our institute) operates the applied current and the measurement of the voltage drop via IEEE-488 port of the Model 2400. The program is also used to input the current parameters and output the data as a text file.

To assure representative results each sample was measured 12 times, subsequently releasing and straining the screw and turning the sample  $90^\circ$ . The data is imported in the data analysis system of OriginLab. The measured values are linearly fitted in Ohm's line (Figure 4.12), the slope of which gives the electric resistance  $R$  of the sample.

The resistance depends on the sample geometry. The specific, i.e. geometry independent, electrical resistivity  $\rho$  can be calculated according to the following formula:

$$\rho = R \cdot \frac{hw}{d} \quad 4.11$$

where  $h$  is the height and  $w$  the width of the sample, in mm;  $d$  is the distance between both Cu-wires, also in mm. Thus mean value and standard deviation of the specific resistance is acquired from 12 measurements for each cast iron sample.

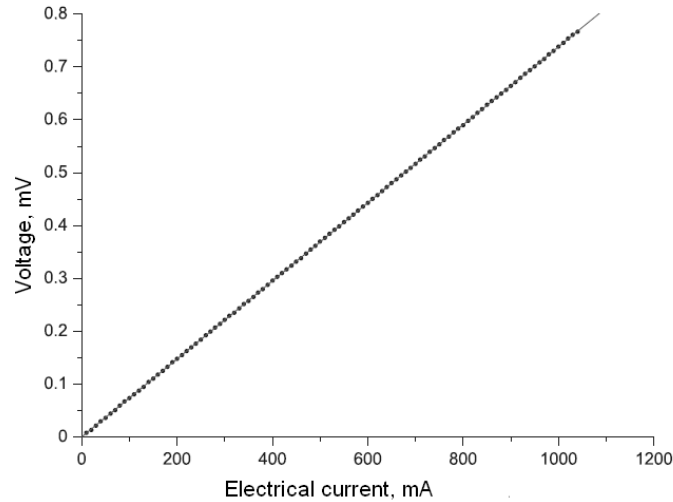


Figure 4.12 Voltage-current curve, consisting from 104 mess values of electrical resistance measurements. Ohm's line is acquired from linear fitting; its slope corresponds to electrical resistance.

## 4.5 FEM SIMULATIONS IN 2D AND 3D

The estimation of the electrical and thermal properties of the cast iron with the help of FEM simulations was performed in order to find and understand the correlations with its micro-structure. The estimations of the electrical properties of cast iron have been compared with experimental results and theoretical models.

The simulations in 2D were performed with the FlexPDE (PDE Solutions Inc.) program, in 3D using GeoDict (ITWM) system. Both finite element simulations are based on numerical solving of the partial differential equations with certain boundary conditions.

### 4.5.1 USING FLEXPDE

The stationary thermal and electrical problem was simulated in 2D-space for different ideal structures in order to understand the conductivity phenomena. For the thermal conductivity problem the FEM program solves the Laplace equation:

$$\nabla(-\lambda \cdot \nabla T) = 0 \tag{4.12}$$

where  $\lambda$  is the given thermal conductivity and  $\nabla T$  the temperature gradient. Stationary problem of electrical conductivity can be described by following equation:

$$\nabla \vec{J} = \nabla(\sigma \vec{E}) = \nabla(-\sigma \cdot \nabla V) = 0 \quad 4.13$$

where  $\vec{J}$  is the electrical current density,  $\vec{E}$  electrical field strength,  $\sigma$  given electrical conductivity and  $\nabla V$  the voltage gradient.

Further the principle of the simulation will be explained on the example of the problem for thermal conductivity only, but the problem for the electrical conductivity is similar.

The heat flux is generated by applying a temperature gradient on the sample. It is described by Fourier's law that relates the heat flux  $J$  in  $J \text{ m}^{-2} \text{ s}^{-1}$  to the temperature gradient  $dT/dl$  in  $\text{K m}^{-1}$ . Fourier's law may be expressed in the following form:

$$J = -\lambda \frac{dT}{dl} \quad 4.14$$

Here, the thermal conductivity  $\lambda$  in  $\text{W m}^{-1} \text{ K}^{-1}$  is the proportionality constant between heat flux and temperature gradient. If one knows the temperature gradient  $\Delta T$ , the size of the analyzed region  $a$  and the heat flux  $J$ , the thermal conductivity  $\lambda$  can be calculated as follows:  $\lambda = J \cdot a / \Delta T$ .

Due to the difference of the values of thermal conductivity of the matrix and graphite inclusions is the heat flux in the composite not homogeneous and its mean value cannot be measured. Thus two homogeneous regions are intentionally added (see Figure 4.13). The heat flux there is homogeneous and can be easily measured along the line  $L_1$  or  $L_2$ . The mean heat flux  $J$  along a horizontal line is always constant, only its distribution in the composite is varying. The temperature has to be measured along the lines  $L_3$  and  $L_4$  to determine the temperature gradient. Due to the composite microstructure temperature deviation of some degrees is present. The mean temperature  $T_m$  for both lines is calculated from the integral of the temperature profile divided by the length  $b$  of the analyzed region.

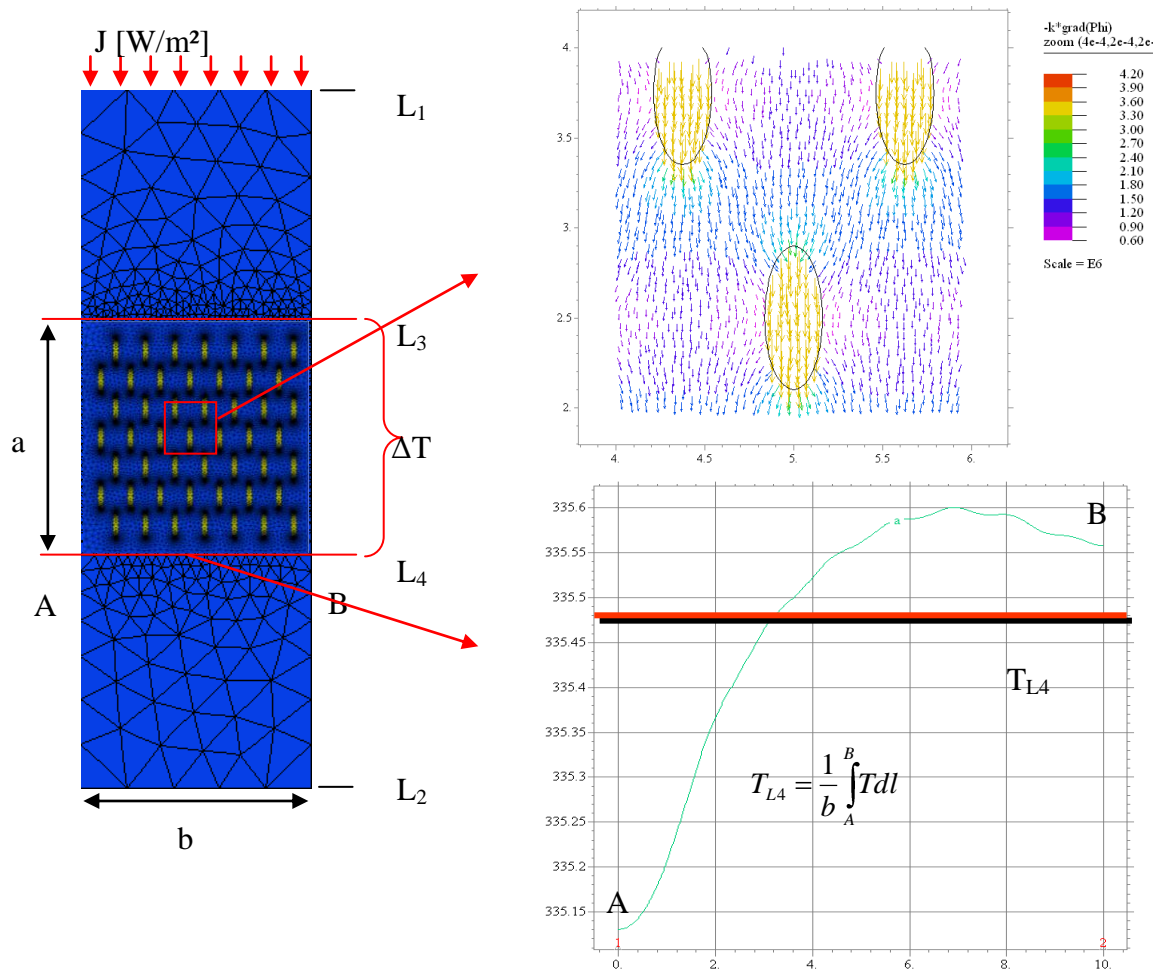


Figure 4.13 Simulation principal of thermal conductivity of composite material.

#### 4.5.2 USING GEODICT

Simulation of the thermal and electrical conductivity problem on the 3D data sets was performed with the help of GeoDict software, developed at ITWM for simulation of structures and structure-property relationships [141]. The electrical problem was solved in analogy to the thermal one.

Thermal conduction is the heat transfer mechanism relying on the energy exchange between neighboring molecules in solids, liquids and gases along a temperature gradient. Thermal conductivity  $\lambda$  in  $\text{W m}^{-1} \text{K}^{-1}$  is the proportionality constant between heat flux and temperature gradient, as shown in the equation 4.14.

Computations of the thermal conductivity were done for the sub-volumes in  $x$ -,  $y$  and  $z$ -directions. Only thermal conductivity is considered in this study, but not convective heat transfer and heat radiation.

The stationary heat equation is solved with periodic boundary conditions. Similar to many other materials, it is characteristic for the heat flow problem in cast iron that one has to deal

with high contrast in the thermal conductivities of the two individual phases, namely graphite and iron matrix. This is achieved by harmonic averaging and explicitly introducing the jumps across the material interfaces as additional variables. The continuity of the heat flux yields the needed extra equations for these variables. The mathematics involved in the simulation and the solver of the GeoDict software have been comprehensively described by Wiegmann and Zemitis [142].

The simulated thermal and electrical conductivity problem is based on the literature values and calculations of the conductivities for individual microstructure constituents according to equations described in Helsing et al. [64] summarized in the Table 9.3.



### III. RESULTS AND DISCUSSIONS



---

## 5 ELECTRICAL PROPERTIES

---

The measurements of the electrical resistivity were performed on the cast iron samples as a preparation step for the correlation of the cast iron microstructure with non-destructive electromagnetic testing. This relatively simple method was used in order to find exact correlation between cast iron microstructure and its electrical properties. Nontrivial information about the microstructure was first incorporated with electrical properties via statistical correlation functions. Further analysis was done step by step involving each time more details about the complex graphite microstructure.

This chapter presents the experimental results of the measurement of the electrical resistivity and thus conductivity of cast iron with different graphite morphologies. First correlations with basic microstructural characteristics are done. The influence of individual microstructural constituents is discussed.

### 5.1 ELECTRICAL RESISTIVITY OF CAST IRON WITH DIFFERENT GRAPHITE MORPHOLOGIES

The results of the electrical resistivity are presented in the Table 5.1. The mean values of all measured samples of cast iron with flake, vermicular and nodular graphite correspond very well with literature values summarized in the Table 2.2.

Table 5.1 Specific electrical properties of cast iron samples.

Type of cast iron	Amount of samples	$\rho$ , ( $\mu\Omega\cdot\text{m}$ )	$\sigma$ , ( $10^6\cdot\text{S/m}$ )
Cast iron with flake graphite (FG)	10	$0.74 \pm 0.03$	$1.36 \pm 0.05$
Cast iron with vermicular graphite (CG)	8	$0.60 \pm 0.03$	$1.68 \pm 0.08$
Cast iron with nodular graphite (SG)	4	$0.53 \pm 0.02$	$1.88 \pm 0.05$
Malleable cast iron (TG)	4	$0.284 \pm 0.009$	$3.52 \pm 0.11$

Malleable cast iron has the lowest resistivity value due to the high volume fraction of approx. 35 % of ferrite in the matrix. The iron matrix of all other samples consists to 99.8 % of pearlite. To exclude additional factors and to study only the influence of the graphite morphology on the electrical properties of cast iron, only samples with pearlitic matrix were further considered: cast iron with nodular (SG), vermicular (CG) and flake graphite (FG).

## 5.2 INFLUENCE OF PARTICLE VOLUME FRACTION, 2D PARTICLE DENSITY, 2D SIZE

Consequently the microstructure of all samples was analyzed and quantified. Electrical resistivity is plotted versus the basic parameters of quantitative image analysis: volume fraction ( $V_V$ ) (Figure 5.1a) and specific surface area ( $S_V$ ) (Figure 5.1b) of the graphite in cast iron microstructure. Volume fraction in all cast iron samples varies between 7.3 and 15 %. Considering the error bars, no dependency of the graphite volume fraction ( $V_V$ ) on the electrical behavior of the cast iron could have been confirmed. In comparison to cast iron with nodular graphite, surface density ( $S_V$ ) increases for vermicular graphite and reaches its maximum for some samples of cast iron with flake graphite. Although increasing cast iron resistivity weakly correlates with increasing surface area density within the cast iron samples of one graphite morphology, the electrical properties do not explicitly depend on this microstructural parameter.

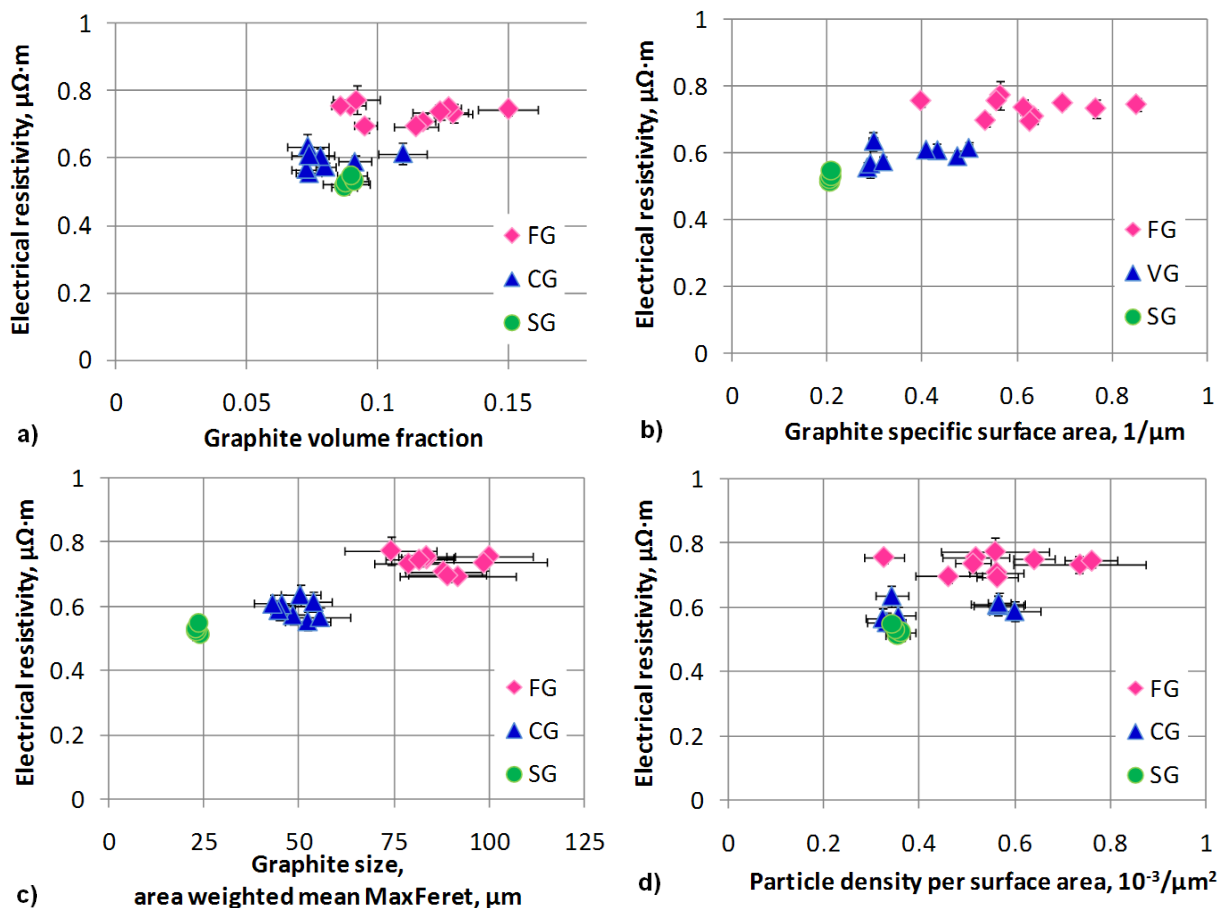


Figure 5.1 Electrical resistivity of cast iron with flake, vermicular and nodular graphite plotted as a function of a) graphite volume fraction, b) graphite specific surface area, c) graphite size and d) graphite particle density per surface area.

## 5.2 Influence of Particle Volume Fraction, 2D Particle Density, 2D Size

Similar tendency can be noticed in Figure 5.1c. Cast iron samples with nodular, vermicular and flake graphite have characteristic values for the electrical resistivity and for the size of the graphite particles. Evidently thin long graphite lamellae represent a significantly larger obstacle for the electron movement than vermicular particles and even more than graphite nodules. As this dependency is not a continuous function over all graphite morphologies, the parameter particle size cannot be considered to be a criterion corresponding to cast iron conductivity. No continuous dependency of electrical conductivity on the particle density was found either (Figure 5.1d).

None of the above mentioned parameters was sufficient enough to describe the dependence between graphite microstructure and electrical properties of cast iron. In order to achieve a reliable correlation, the parameter characterizing the graphite morphology was proposed to be considered. Volume fraction of the respective graphite morphology present in the cast iron sample promises to provide unambiguous relationship to physical properties. Thus, the graphite morphology has to be clearly classified. As in most of the cases, the convenient way to analyze microstructure restricts to the two dimensional observations, the classification of graphite 2D-sections has to be performed. The first classification approaches were done with the help of shape parameters (see section 3.2). Figure 5.2a shows that electrical resistivity decreases according to certain power law with increasing aspect ratio. Aspect ratio is one of the shape parameters chosen from the Table 3.2 also used in the prediction models discussed in section 2.3.1.2.

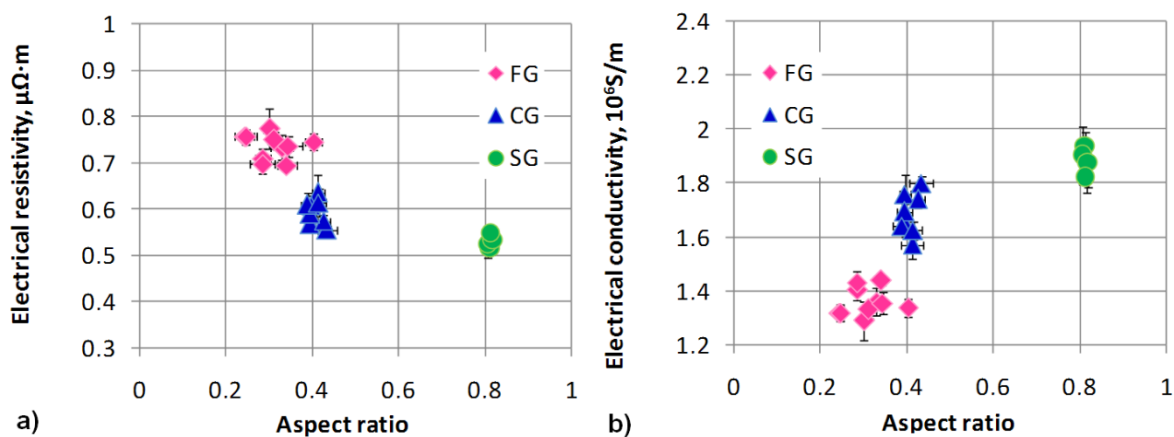


Figure 5.2 Electrical resistivity and conductivity of the cast iron plotted as a function of particle shape (area weighted aspect ratio).

The diagram above correlates well with Figure 2.11 from the literature, considering the fact that the value for aspect ratio for perfectly circular particles is equal to 1 and the aspect ratio value for complex lamellar particles approaches to 0. Similar dependencies were also acquired

with other shape parameters mentioned in the Table 3.2. For different graphite morphologies the values of different shape parameter vary considerably. Table 5.2 summarizes some of the shape parameter values for flake, vermicular and nodular graphite, as well as the other field and particle features, acquired from the 2D image analysis.

Table 5.2 Microstructural characteristics of cast iron samples with flake (FG), vermicular (CG) and nodular (SG) graphite. Values given for graphite phase.

Graphite morphology	Field features			Particle features, area weighted mean values			
	$V_V$ , %	$S_V$ , $10^{-3}/\mu\text{m}$	$N_A$ , $10^{-3}/\mu\text{m}^2$	MaxFeret, $\mu\text{m}$	Aspect ratio	Compactness	Roundness
FG	11.2±0.7	623±127	0.56±0.07	87±11	0.31±0.02	0.20±0.01	0.11±0.01
CG	8.2±0.6	374±88	0.46±0.04	49±5	0.41±0.02	0.35±0.02	0.20±0.01
SG	8.9±0.6	206±1	0.35±0.02	23±2	0.81±0.01	0.89±0.01	0.74±0.01

The physical background of these phenomena can be studied with the help of finite element simulation and compared with analytical models.

### 5.3 COMPARISON WITH THE ANALYTICAL BOUNDS

For the comparison of cast iron properties with the simplest bounds described in the section 2.3.1.1 it has to be taken into consideration, that graphite conductivity is anisotropic. Thus, the bounds were calculated with both values for the graphite conductivity in *a*- and *c*- crystallographic direction. The value for pearlite conductivity was calculated according to the equation 2.13 as shown in the appendix 9.1. As the phase contrast between thermal conductivity of graphite in *a*-direction and pearlite is relatively low this effective property can be set in brackets with bounds which are relatively close (see Figure 5.3). Especially Hashin-Shtrikman bounds calculated with the value for graphite conductivity in the *a*-crystallographic direction approach somewhat near to the literature values for cast iron with flake and vermicular graphite. This also proves that the thermal conductivity in cast iron with these types of graphite is conducted mainly by the conductivity in the graphite in the *a*-direction: even more in flake graphite than in vermicular graphite. Conductivity of the cast iron with nodular graphite is in the range of conductivity of pearlitic matrix. This means first, that graphite conductivity in nodules is between the values for conductivity in *a*- and *c*-crystallographic direction, approaching more the value of the conductivity of graphite in *c*-direction, and second that cast iron property is mainly controlled by the conductivity of pearlite.

For large phase contrast, however, as in the electrical conductivity of cast iron, the bounds are far apart (see Figure 5.4).

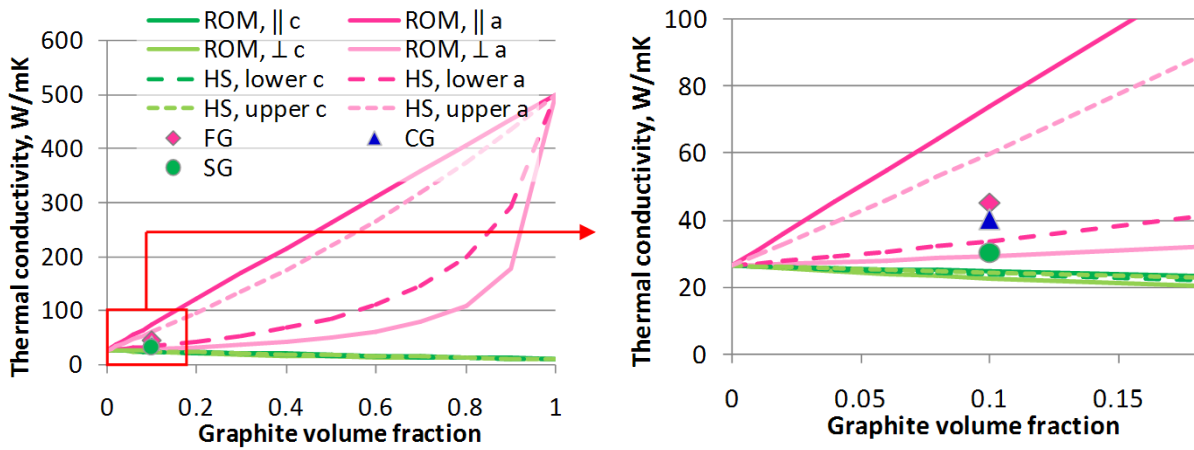


Figure 5.3 Bounds for the thermal conductivity for the cast iron calculated by the rule of mixture (ROM) (see Eq. 2.3 and 2.4) and Hashin-Shtrikman (HS) upper and lower bounds (see Eq. 2.5) compared with the values from the literature [32].

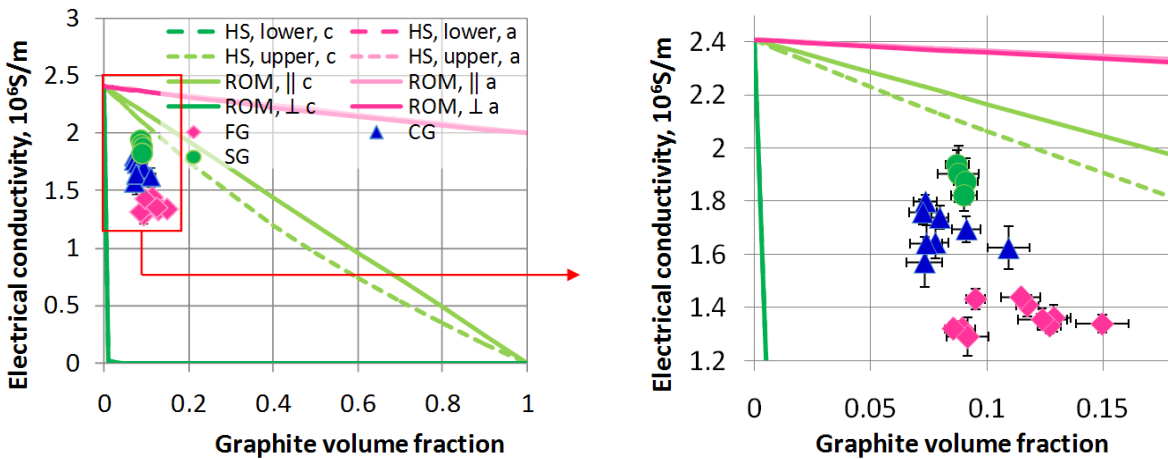


Figure 5.4 Bounds for the electrical conductivity for the cast iron calculated by the rule of mixture (see Eq. 2.3 and 2.4) and Hashin-Shtrikman upper and lower bounds (see Eq. 2.5) compared with the experimental results.

It is remarkable, that the experimental values of the electrical conductivity are situated far away from boundaries calculated with graphite conductivity equal to graphite conductivity in  $a$ -direction and concentrate entirely within the boundaries calculated using graphite conductivity in  $c$ -direction. Considering the theories about graphite growth and crystallographic structure, it can be assumed, that effective graphite conductivity is between conductivities in  $a$ - and  $c$ -direction and is much lower than the conductivity of the pearlitic matrix. Thus, graphite serves as an obstacle on the way of electrons. Conductivity in  $c$ -direction predominates for the flake graphite. From the Figure 5.4 it can be stated, that the decrease in electrical conductivity in cast iron with nodular, vermicular and flake graphite cannot be explained by only volume fraction of the graphite phase. Graphite shape can be considered as one of the most important factors. The known approaches (see section 2.3.1.2) for the estimation of the effective properties of the composite materials with high contrast in the properties of the individual

components (conductivity of the inclusions equal to 0) did not well correlate with the experimental results (Figure 5.5). Here the experimentally determined values of the aspect ratio (Table 5.2) were used to estimate the effective cast iron properties according to the differential effective medium (DEM) scheme for randomly oriented spheroidal inclusions (Eq. 2.8). With the given shape parameter values this scheme considerably overestimates the experimental results. According to the scheme the values of the aspect ratio of the vermicular and flake graphite particles should be below 0.1.

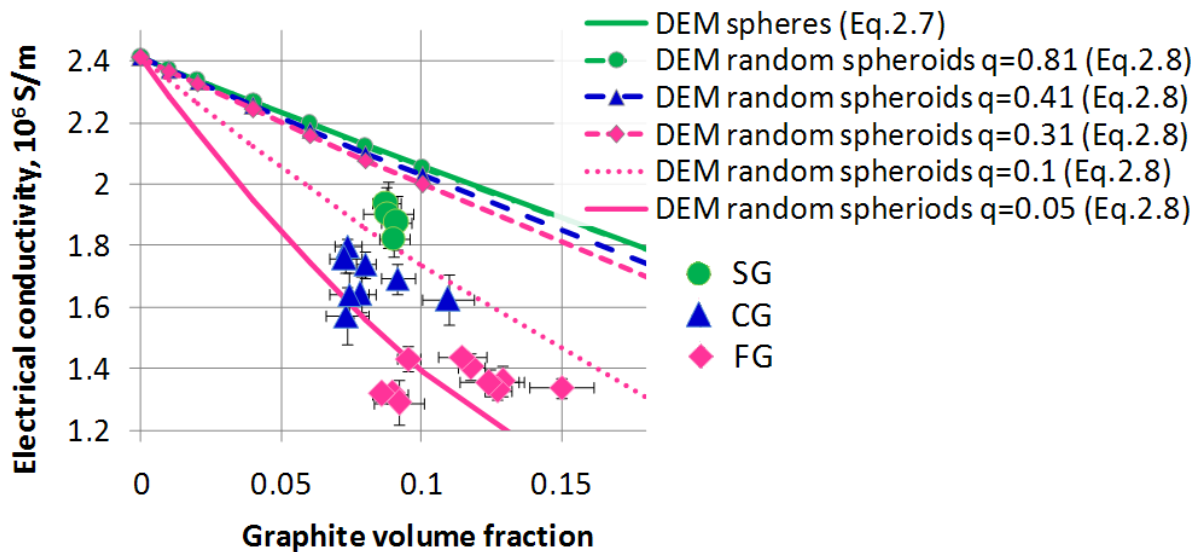


Figure 5.5: Comparison of the experimental values of the electrical conductivity of cast iron with nodular (SG), vermicular (CG) and flake graphite (FG) with effective conductivity values predicted according to the differential effective medium (DEM) scheme (see section 2.3.1.2).

Comparing the experimental results with existing models it can be concluded that following microstructural parameters need to be considered for the correct estimation of the effective properties of cast iron with different graphite morphology:

- volume fraction of the graphite phase ( $V_V$ );
- graphite shape, size and density, which calculation is generally derived from the basic parameters surface area density ( $S_V$ ) and the density of the integral of the mean curvature ( $M_V$ ), accessible from the 2D image analysis;
- graphite 3D arrangement, which can be described by the fourth basic characteristic – the density of the integral of the total curvature ( $K_V$ ), accessible only from the 3D image analysis.

Considering the fact, that the cast iron with specific graphite morphology (shape) possess the specific values of the electrical and thermal conductivity and assuming the possible existence

of the cast iron of the mixed microstructure, the fraction of the respective graphite type have to be described quantitatively. Thus, the correct classification of each individual graphite particle is strongly strived for.

Besides, in order to make sufficient estimation of the effective conductivity of the graphite of different morphology, special attention has to be given to the characterization of the graphite crystallographic structure.



---

## 6 GRAPHITE CLASSIFICATION

---

The difficulties for the empiric classification of respective graphite types are caused by their irregular, very complex and generally non convex 3D shapes. Since generally only 2D planar sections, which appear from the random cut through the graphite particle, are available for the quality control, is the classification in some special cases uncertain.

It is evident, that there are always 2D sections through non convex graphite particles of different morphology that cannot be clearly assigned to certain 3D type. Those are especially the ones, that lie on the boarder of the graphite particle and thus posses only very limited information about the real shape or even the ones that break up into several individual sections, which though belong to only one particle considering the space connectivity.

That is why this problem should be treated in three steps:

- *Definition of the initial situation:* i.e. conventional image analysis measurement of the statistically secured shape varieties of the as much as possible homogeneous graphite arrangements and its classification based on the currently available techniques.
- *3D analysis of the graphite morphology:* The determination of the possible shape variety and probability of the 2D sections based on some chosen real 3D graphite particles acquired with the help of FIB-nanotomography.
- *Optimization of 2D classification:* Analysis of the most proficient microstructural parameters for these 2D section variations in order to optimize the 2D classification.

This chapter addresses the first step. Following two steps were treated in the chapter 7. Different graphite morphologies were objectively characterized and the classification algorithm was developed using 2D image analysis. The influence of the objectively described graphite morphology on the effective conductivities of the cast iron was analyzed.

### 6.1 2D SHAPE ANALYSIS OF GRAPHITE MORPHOLOGIES

#### 6.1.1 ANALYSIS OF DIN SERIES IMAGES USING PARTICLE BASED METHOD

Since up to now a characterization of graphite morphologies was often carried out by comparing real structures with ideal standard images from EN ISO 945, those images (see Figure 2.2)

were used first for the examinations. All shape parameters of Table 3.2 were determined for the ideal graphite types.

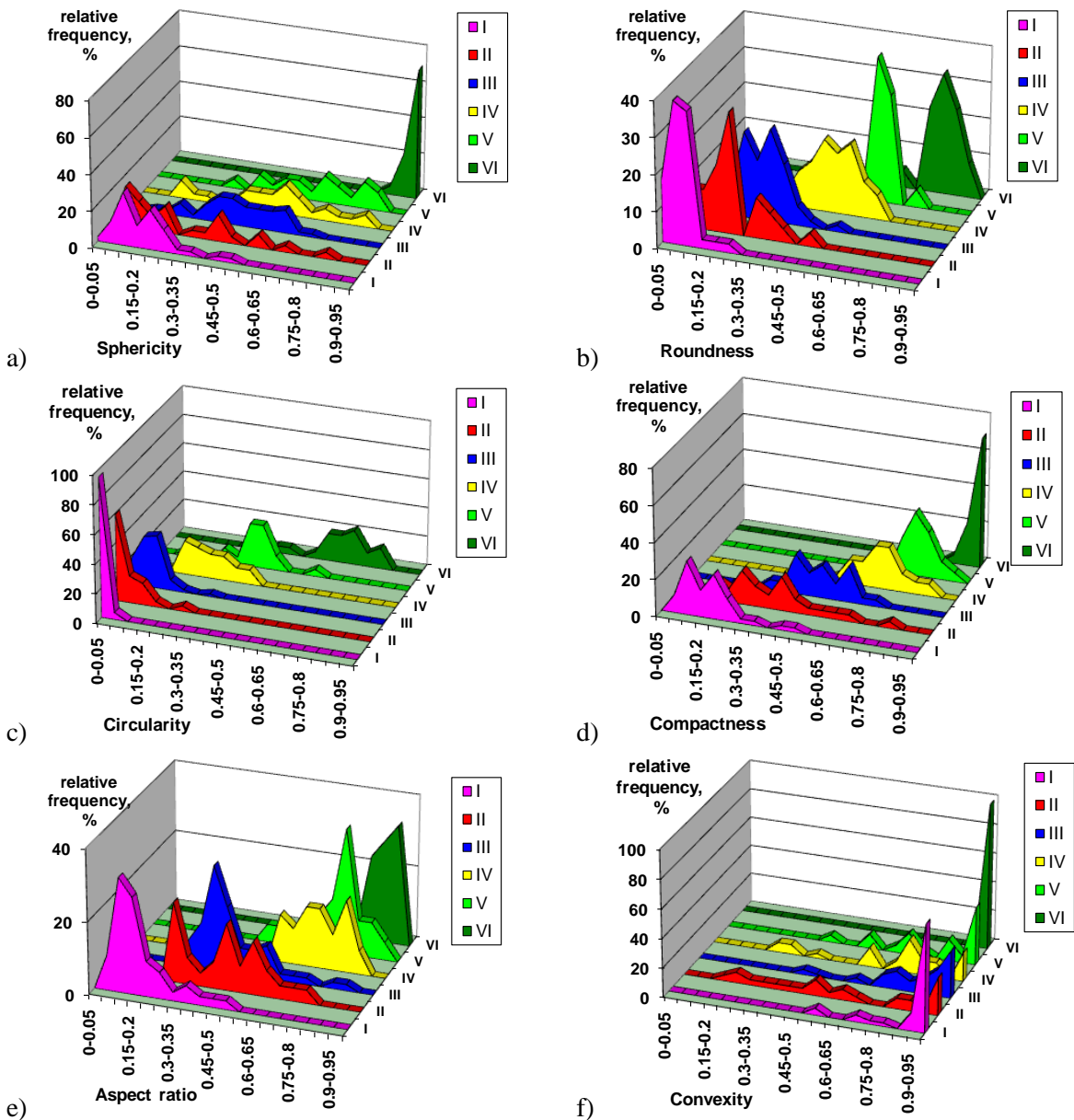


Figure 6.1 Distribution of shape parameters: a) sphericity, b) roundness, c) circularity, d) compactness, e) aspect ratio and f) convexity for the six graphite types according to DIN EN ISO 945 (Figure 2.2).

It was found, that the values of most shape parameters intensely overlap with each other for different graphite morphologies. The best results for a further classification were obtained with the aid of the parameters roundness and compactness. The distributions of those parameters for ideal graphite types can be seen in Figure 6.1b) and d). However, we admit that even those shape parameters cannot be used alone for a graphite differentiation.

These two shape parameters were applied simultaneously to reduce the overlapping. Figure 6.2 shows the mean values and the 95 % confidence interval for roundness and compactness which were measured for different ideal graphite morphologies of EN ISO 945.

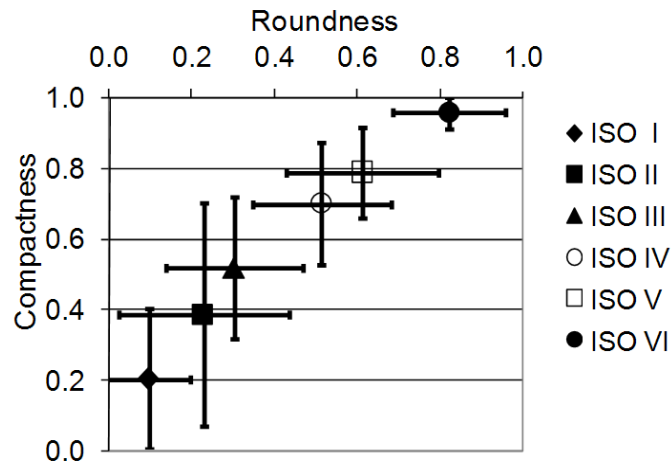


Figure 6.2 Mean values of compactness and roundness with a 95 % confidence interval for six graphite types from DIN EN ISO 945.

The precision of a classification naturally depends on the chosen confidence interval. A small confidence interval results in low accuracy whereas a large confidence interval increases accuracy, but causes certain overlap of identification domains. In the case of the selected confidence interval of 95 %, it is still possible to discriminate well between the ideal graphite types I, III, IV-V, and VI. Graphite type II occurs as a faulty graphite type in real castings and will no longer be taken into account because of the strong overlap of its identification range with neighboring domains. The DIN graphite types IV and V feature very similar values of roundness and compactness and, therefore, it is necessary to thoroughly study their real modifications. In this work those two graphite types were analyzed together and called „IV-V graphite“.

### 6.1.2 ANALYSIS OF THE REAL GRAPHITE MORPHOLOGIES

A shape analysis of the real lamellar, vermicular, and nodular graphite particles, and graphite morphology in malleable castings (typical optical micrographs can be seen in Figure 6.3) proved that the shape parameter roundness and compactness are suited for a classification. The results are summarized and compared to the results of the ideal graphite types in Figure 6.4.

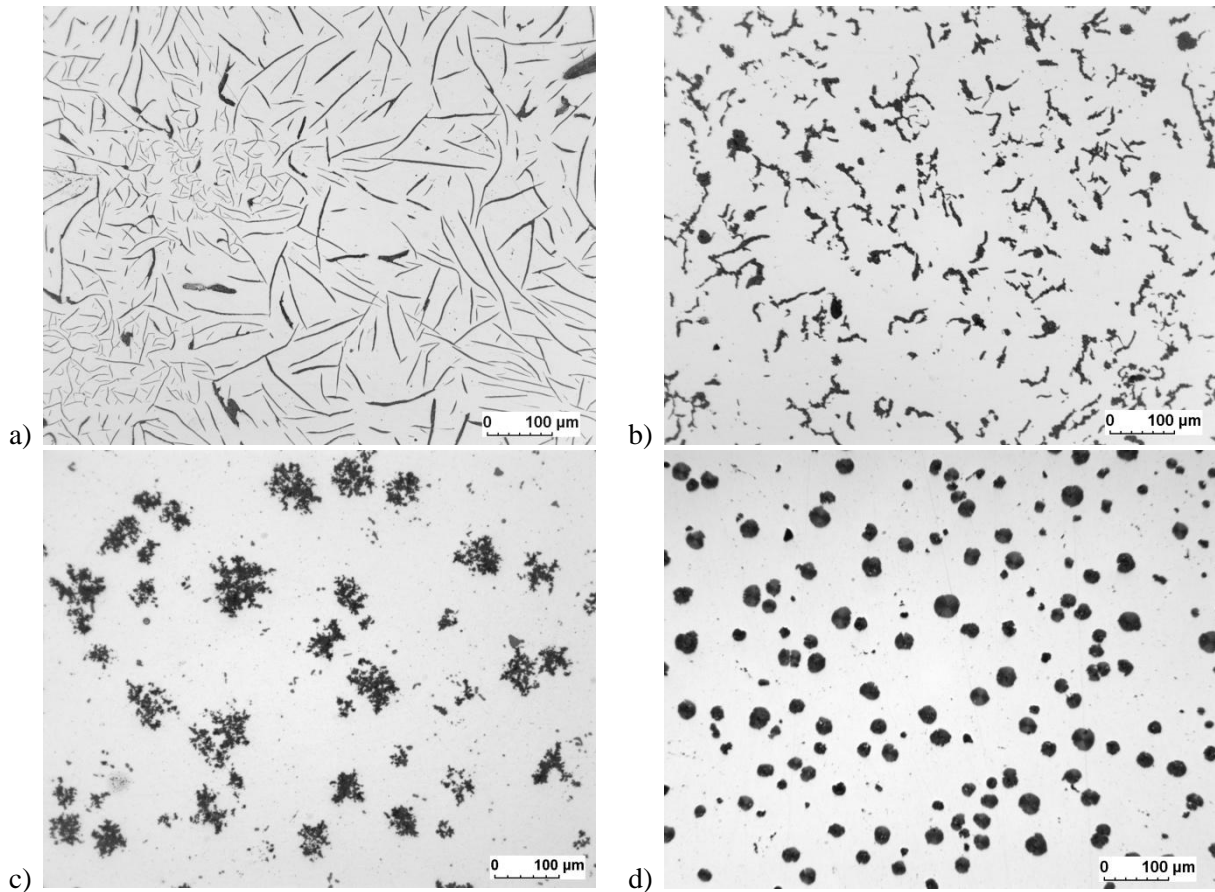


Figure 6.3 Optical micrographs of cast iron with a) lamellar graphite (I), b) vermicular graphite (III), c) temper graphite (IV-V), and d) nodular graphite (VI).

The mean values of the shape parameters for real graphite morphologies agree with respective identification ranges for ideal graphite types. However, standard deviations have increased because of an experimental scatter. This results in an expansion of the confidence interval and, ultimately, causes identification domains to overlap. More specifically, it becomes a problem to separate the graphite types I (flake) and III (vermicular) due to the overlap.

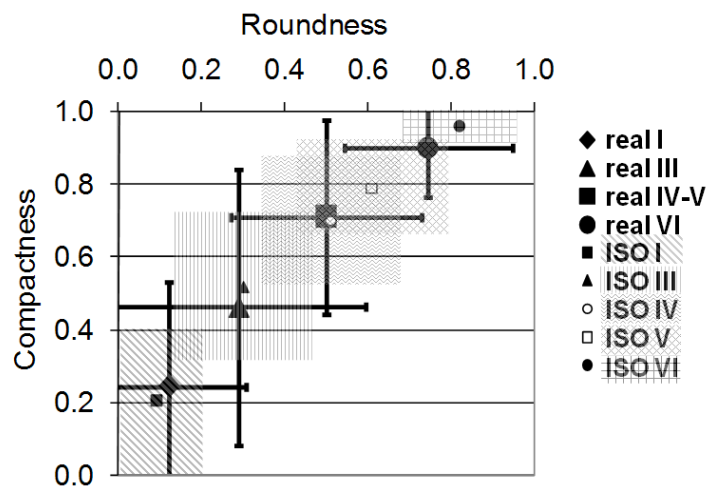


Figure 6.4 Comparison of compactness and roundness for ideal and real graphite types.

## 6.1.3 SHAPE SIZE DEPENDENCY

An analysis of particle shapes alone is not sufficient for the precise classification. The observations of graphite morphologies which were made at large magnifications in the SEM have suggested that a classification can be clearly improved by taking into account that particle shape depend on particle sizes. Castro et al. [143] have also noticed in his study that the mean value of one of the shape parameters depends on the minimal particle size considered in the analysis. The European Standard ISO 945 gives guidelines for determining graphite size. Eight size classes (guiding values) were defined (Table 6.1).

Table 6.1 Size classes according to DIN EN ISO 945.

Size class, R	1	2	3	4	5	6	7	8
Object size, MaxFeret, $\mu\text{m}$	> 1000	500 – 1000	250 – 500	120 – 250	60 – 120	30 – 60	15 – 30	< 15

In the following, the maximal Feret diameter (*MaxFeret*) is used as a size parameter. It is suited best for the purpose because it describes the actual object dimensions whereas the mean diameter is characteristic for nodular graphite particles only and is unable to reflect the size of elongated lamellar graphite particles. Figure 6.5 shows flake graphite particles of different size classes. The extreme differences in shape explain the large scatter of experimental values of shape parameters (see Figure 6.4).

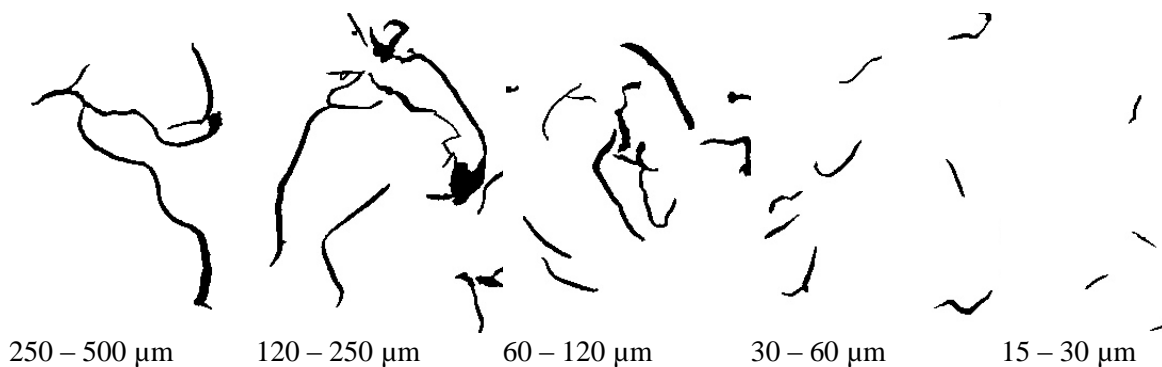


Figure 6.5 Flake graphite of size classes R3-R7 (from left to the right).

The shape of graphite particles of different types and different sizes was analyzed. The results are summarized in Figure 6.6.

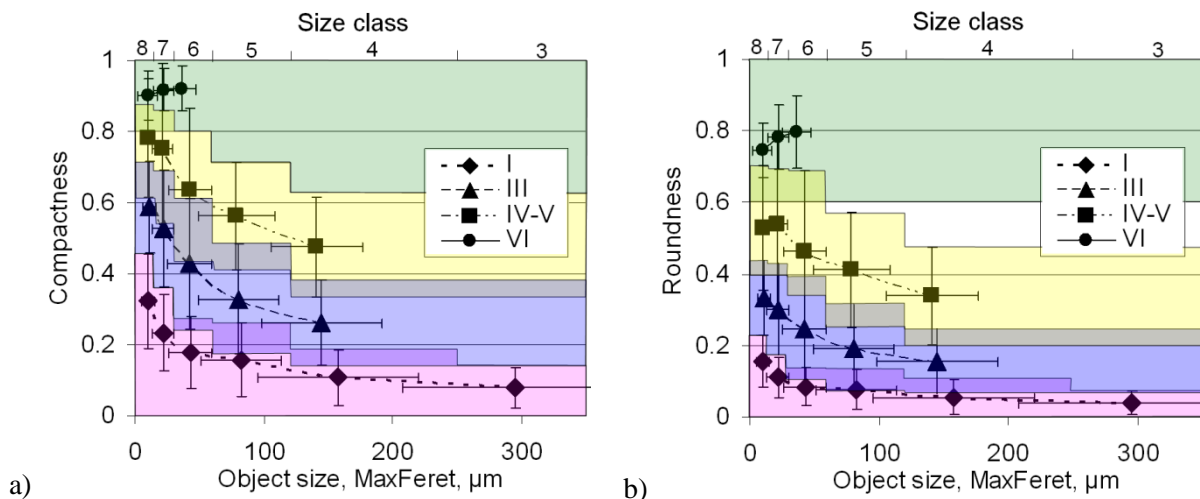


Figure 6.6 Shape of irregular graphite particles as a function of object size. The latter is given as maximum Feret diameter.

Generally, for all graphite sizes different graphite types nodular (SG), temper (TG), vermicular (CG), and flake (FG) possess different values for the shape parameters roundness and compactness. The variations related to the particle size exist also within each graphite type. According to the shown tendency lines one can see, that in case of TG, CG and FG the shape parameters compactness and roundness decrease more or less with increasing particle size. Vermicular particles show steeper drop as flake particles. The shape parameters reach almost their constant values for the flake graphite with the particle size higher than 60 – 100  $\mu\text{m}$ . The smaller sections of the size class R8 of all graphite types can be less well differentiated. This is especially pronounced by their large standard deviation.

Nodular graphite shows on the contrary another tendency: with increasing *MaxFeret* the values of the shape parameters increase. Closer analysis of the nodular particles confirms that the nodules of the size class R6 approach at most the circle shape, which causes the highest values of the shape parameters.

Each data point in the graphs in the Figure 6.6 is the mean value of the shape parameters for the specific graphite type of a certain size. The 95 % confidence interval determines the classification limits for the respective flake, vermicular, nodular graphite and graphite in malleable castings. The shape-and-size interdependence requires using different classification limits for different size classes. Neglecting this fact leads to a faulty classification. For instance, small-sized lamellar graphite particles of the size classes R6, R7 and R8 can be classified as vermicular graphite and large vermicular particles of size classes R1 to R3 as lamellar graphite.

## 6.2 CLASSIFICATION USING IMAGE ANALYSIS TECHNIQUES

### 6.2.1 CLASSIFICATION ALGORITHM

The categorization in more than two classes was carried out with the help of parallelepiped classifier. Its structure can be explained on the example with two object parameters for the classification in two classes (I and III) (see Figure 6.7). Rectangles  $P_I$  and  $P_{III}$  correspond to the objects classes I and III. They can be described through the projection on the coordinate axis. Thus, the rectangle  $P_i$  can be defined for the object class  $i$  ( $i = I, III$ ) knowing the limits  $g_{ix}, G_{ix}, g_{iy}, G_{iy}$  for each object parameter  $x$  and  $y$ . The limits are calculated from the mean values for respective graphite type and size class plus ( $G_{ij}$ ) resp. minus ( $g_{ij}$ ) the 95 % confidential interval, as e.g. shown in the Figure 6.6.

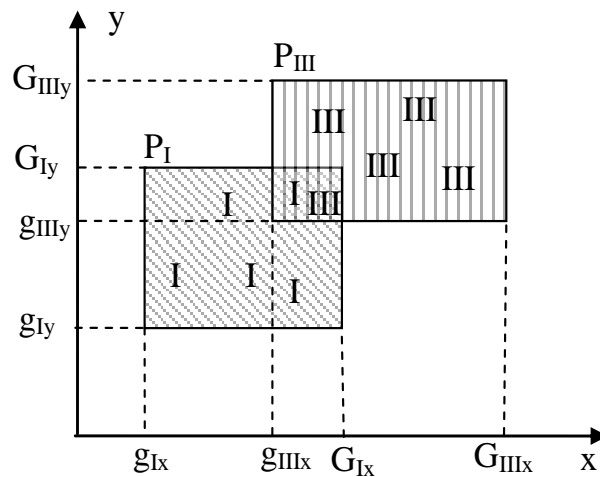


Figure 6.7 Principle of the classification.

The results of the analysis of the graphite shape were used to develop a new classification method on the basis of parallelepiped classifier which allows the good discrimination between the real graphite types I, III, IV-V, and VI. Three object parameters (*MaxFerret*, roundness, and compactness) were employed to determine the classification limits of four graphite types. This defined the identification domains. An analysis was made for each individual object and its parameters were determined. If the three object parameters mentioned above

- are clearly within one identification domain the object will be assigned to the respective class of flake (I), vermicular (III), IV-V or nodular (VI) graphite;
- are within the overlapping range of the two identification domains the object will belong to either of the two classes;

- are outside of all identification domains the object will not belong to any of the four graphite type classes.

## 6.2.2 RESULTS OF THE AUTOMATIC CLASSIFICATION OF GRAPHITE

The complex graphite particles were identified and classified using the newly developed classification method. The results are depicted in Figure 6.8.

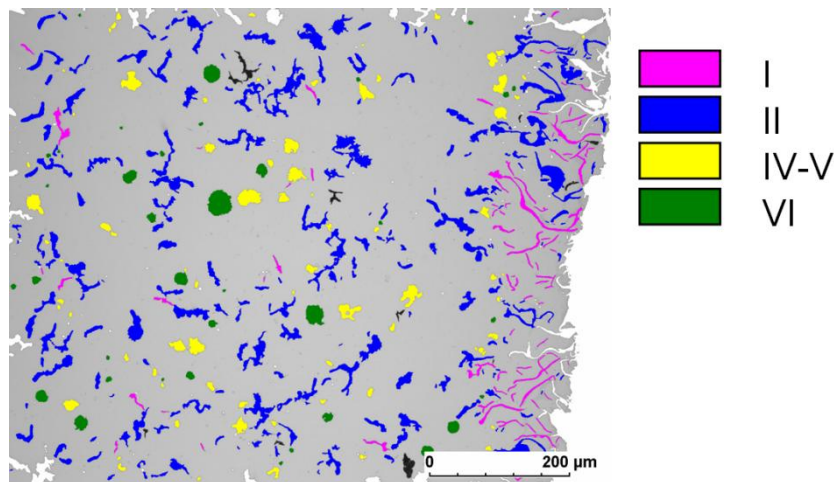


Figure 6.8 Results of classification for a cast iron structure containing different graphite morphologies.

The limits for the classifier are summarized in the appendix 9.2. Since object parameters are largely contingent upon a digital image resolution [85], [92] and this method relies on the results from the images of only one magnification, the use of this classificatory presupposes the 200× magnification with a pixel size of about 0.7 μm. We do not recommend the use of minor magnifications with correspondingly larger pixel sizes for a graphite classification because the identification domains come to strong overlap and any further precision achievable in classification will only be low.

When the above preconditions are fulfilled, the use of shape parameters roundness and compactness as well as considering the object size results in a clear-cut classification of irregular complex graphite particles. Graphite types I (flake), III (vermicular), IV-V and VI (nodular) can be classified employing the particle-based method. The newly developed classification algorithm further allows the determination of the structural characteristics (volume fraction, size distribution, position, etc.) for each graphite type individually.

### 6.2.2.1 COMPARISON WITH MANUAL ANALYSIS ACCORDING TO DIN EN ISO 945

To evaluate the results of the graphite classification the samples were prepared for the comparing experiment. The marks on the analyzed regions increased the accuracy of the estima-

tion. The optical micrographs with the 200× magnification were acquired for the automatic classification. Cast iron microstructure and graphite inclusions were analyzed. One example of such classification is shown in the Figure 6.9. The microstructure of the same five samples was analyzed in the Institute for Material Examination of the Central Labor GmbH Leipzig according to DIN EN 945. The characterization refers not to the disposed microstructural images but merely to the complete polished surface. The introduced evaluation is to be considered as a mean value for the whole surface. The results of the automatic classification as well as the manual characterization are summarized in the Table 6.2.

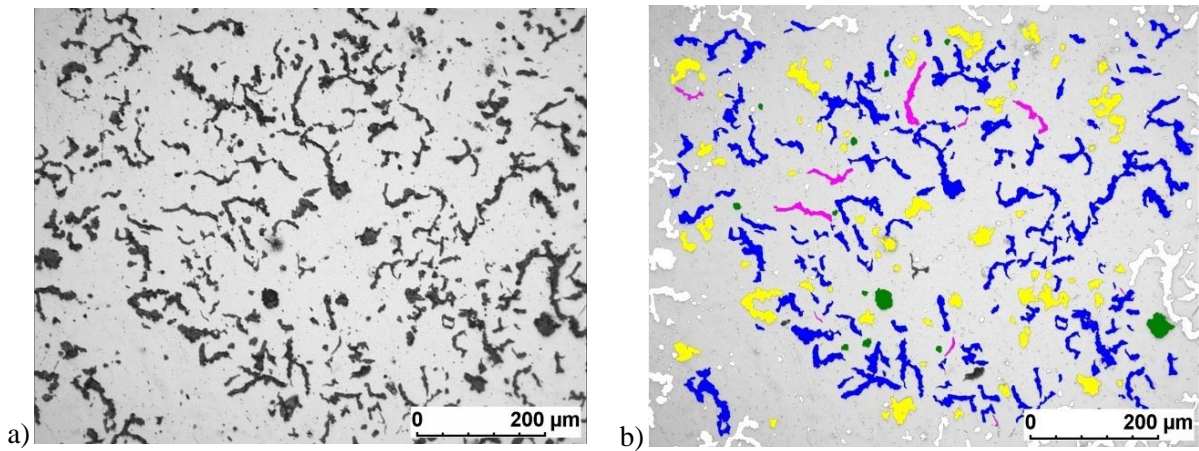


Figure 6.9 a) Cast iron microstructure of the Sample 1, and b) results of the classification.

Table 6.2 Summary of the results of the quantitative microstructure analysis and classification and subjective evaluation according to DIN EN 945.

	Sample 1	Sample 2	Sample 3	Sample 4	Sample 5
<b>Objective automatic characterization and graphite classification</b>					
Particle density /10 <sup>4</sup> , 1/μm <sup>2</sup>	2.93 ± 0.28	3.03 ± 0.29	3.36 ± 0.23	4.12 ± 0.33	4.62 ± 0.39
Area weighted mean values of					
MaxFerret, μm	65.91 ± 7.89	58.61 ± 6.38	67.16 ± 7.58	57.08 ± 6.88	44.23 ± 5.65
Compactness	0.40 ± 0.06	0.36 ± 0.05	0.41 ± 0.06	0.40 ± 0.06	0.47 ± 0.08
Roundness	0.25 ± 0.05	0.22 ± 0.05	0.25 ± 0.05	0.25 ± 0.05	0.31 ± 0.08
Graphite volume fraction, %	13.04 ± 1.18	11.90 ± 1.34	11.72 ± 0.96	10.68 ± 0.75	10.88 ± 1.36
Volume fraction of each graphite type					
I	0.23 ± 0.13	0.36 ± 0.17	0.35 ± 0.18	0.55 ± 0.28	0,31 ± 0,18
III	9.68 ± 1.00	9.69 ± 2.03	8.83 ± 0.91	8.09 ± 1.07	6,92 ± 1,51
IV-V	2.72 ± 0.84	1.66 ± 0.39	2.00 ± 0.34	1.48 ± 0.51	2,52 ± 0,33
VI	0.42 ± 0.23	0.19 ± 0.17	0.54 ± 0.36	0.55 ± 0.28	1,14 ± 0,52
Fraction of each graphite type, when total graphite fraction is 100 %					
I	1.79 ± 1.11	2.97 ± 1.37	3.00 ± 1.50	5.15 ± 2.63	2.82 ± 1.72
III	74.99 ± 4.94	80.94 ± 4.27	75.34 ± 4.73	75.56 ± 5.67	62.81 ± 8.03
IV-V + VI	23.22 ± 4.61	16.09 ± 3.92	21.67 ± 2.78	17.11 ± 5.11	34.37 ± 6.28
<b>Subjective manual evaluation according to DIN EN 945</b>					
Graphite type I, %	0	0	0	0	10
Graphite type III, %	80-90	80-90	90	85-90	60
Graphite type VI, %	10-20	10-20	10	10-15	30

Vermicular graphite is mainly present in the five analyzed cast iron samples: approx. 2 vol. % of all graphite particles were automatically classified as flake graphite, approx. 3 vol. % as nodular graphite, and about 15 % as graphite type IV-V. The results correspond very well with each other. Although, the nodular graphite particles (type VI) according to DIN EN ISO 945 were classified as graphite type IV-V by the automatic classifier (see Table 6.2). Opposite to subjective analysis automatic classification provides always objective and reproducible results and allows the complete and quick microstructure description.

### 6.2.3 EXTENSION OF GRAPHITE CLASSIFICATION ON DIFFERENT MAGNIFICATIONS

The attained classification method provides good results for the classification of the different graphite morphologies from the optical micrographs of heterogenic cast iron samples. Although it was developed using our laboratory specific equipment it has the potential of being prescind from the specifications of microscope or image acquisition equipment (e.g. digital camera). Studying the influence of chosen magnification and thus on digital resolution of the micrographs on the microstructural parameters, especially those used for differentiation of graphite particles, the general dependencies can be integrated in the classification algorithm. For such research several particles (i.e. the 2D sections) of four graphite types: FG, CG, TG, and SG, and different size classes (see Table 6.1) were selected. In case of flake graphite 2D sections from the size class R8 (0 - 15  $\mu\text{m}$ ) to R4 (120 - 250  $\mu\text{m}$ ) were observed, whereas nodular graphite sections were only from R8 (0 - 15  $\mu\text{m}$ ) to R6 (30 - 60  $\mu\text{m}$ ). A sufficiently large number of particles of each graphite type and each size class were chosen in order to make a statistically correct statement. Images of the selected particles were acquired with optical and scanning electron microscopy with mentioned above (see section 4.2.1) magnifications. The acquired images were analyzed with software a4i Analysis (see also section 4.3.2).

#### 6.2.3.1 SIZE-SHAPE DEPENDENCY OF THE GRAPHITE MORPHOLOGIES FOR DIFFERENT MAGNIFICATIONS

The results in the following section extent already performed analysis (section 6.1) to different magnifications. In Figure 6.10 the shape parameter compactness is plotted vs. size parameter *MaxFerret* for four graphite morphologies.

The tendency observed in the section 6.1.3 for all graphite morphologies changes only insignificantly with increasing magnification. The values for the shape parameters lie in the case of SG, FG and CG for all magnifications close to each other. Only the values for the magnification 100 $\times$  generally sheer somewhat out of the line. Magnification 100 $\times$  is less well suited, as

the particles are represented by only few pixels which restrict the accuracy by the determination of their geometrical features and thus shape parameters (see also [85]). The values of the temper graphite particles show for all magnification the wide scatter range.

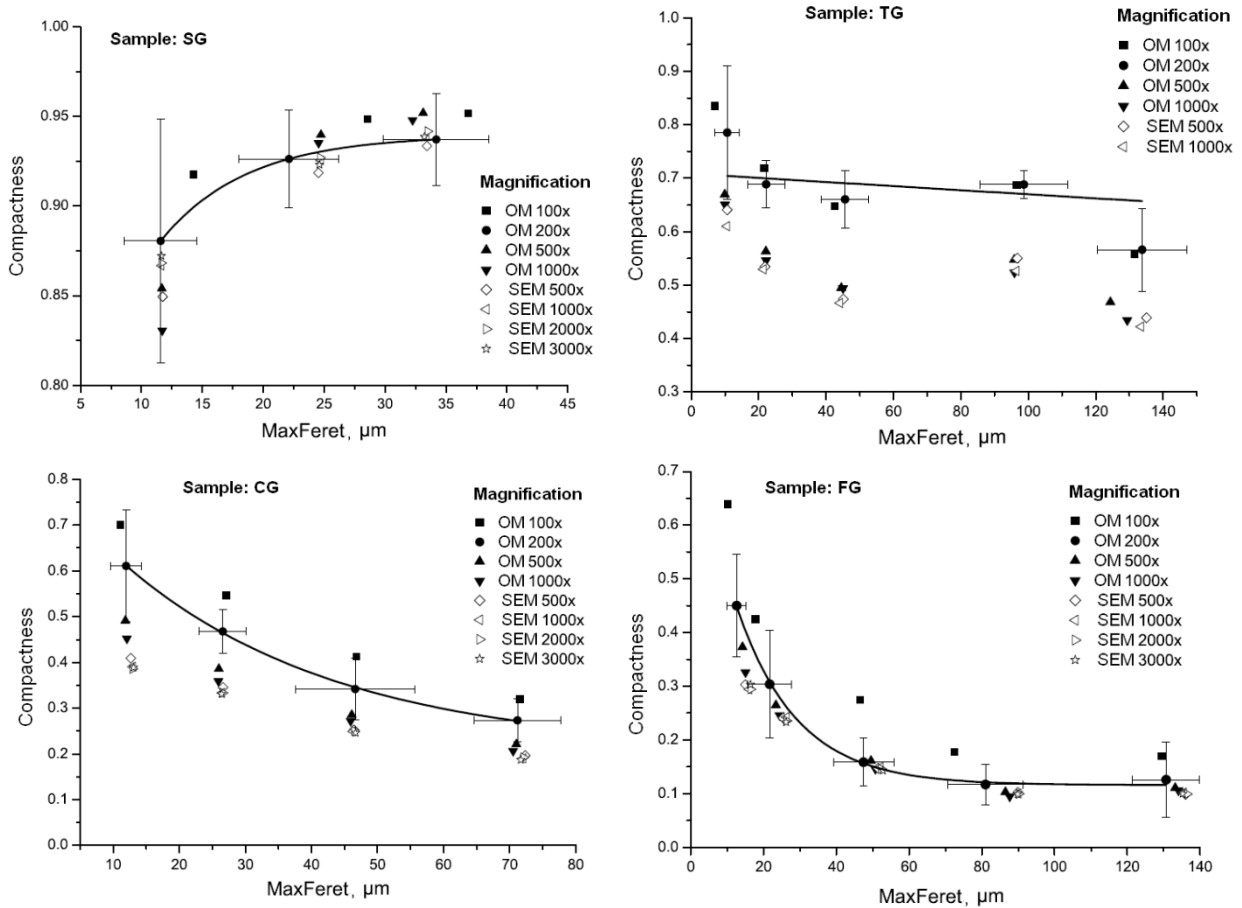


Figure 6.10 Dependency of the parameter compactness on the particle size for different magnifications.

The values of shape parameters acquired from scanning electron microscope images, which are of 1000 $\times$ , 2000 $\times$ , and 3000 $\times$  magnification, are extremely close to each other and are almost identical. Due to high resolution of the scanning electron microscope even the small particles of the size class R8 ( $\leq 15 \mu\text{m}$ ) appear as sufficiently large objects. And additionally, due to the high resolution, the exact separation between particle and matrix can be performed straightforward and precise. Thus, the shape parameters are nearly equal for all following magnifications. Although, when the size of the analyzed particles approaches the resolution limit of the scanning electron microscope, the interface is spread over several gray values. Thus, the contour of the particle will again vary depending on the chosen gray value.

Basically, starting with the magnification of 200 $\times$  the shape parameter values for different graphite morphologies fairly change. This is also valid for the shape parameter roundness (see Figure 9.1). The values become somewhat more accurate with increasing magnification, al-

though for SEM images there was not any difference, if the magnification 1000× or 3000× was used. Additionally it was noticed that with increasing magnification the standard deviations diminishes. Thus, the magnification 200× of optical microscopy is very well suited for the determination of the characteristic microstructural parameters of the graphite particles. In this case the particle parameters are acquired from the relatively large measuring field and with sufficiently high precision. Overlapping regions are acceptable. Different graphite morphologies can be accurately classified.

### 6.2.3.2 DEPENDENCY OF THE CLASSIFICATION PARAMETERS ON THE DIGITAL RESOLUTION

Figure 6.11 and Figure 6.12 present the mean values of shape parameter compactness and Figure 6.13 and Figure 6.14 of shape parameter roundness determined for particles of four different graphite morphologies and different size classes at different magnifications, i.e. different calibration factors<sup>7</sup>. One should notice that the scales of the ordinate are adjusted to different graphite types and thus cannot be directly compared with each other.

Table 6.3 shows the magnifications and corresponding values for the calibration factors. It can be seen, that optical and scanning electron micrographs have different calibration factors for the same magnification, specific for the image acquisition technique.

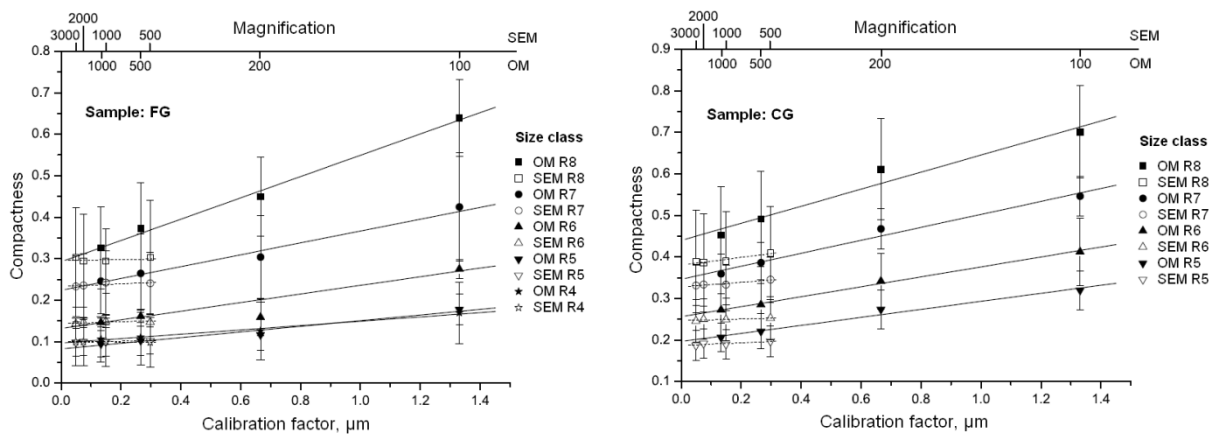


Figure 6.11 Dependency of the shape parameter compactness on the magnification for flake graphite FG (left) and vermicular graphite CG (right).

Table 6.3 Magnification considered and their calibration factors for OM and SEM.

Magnification	100	200	500	1000	2000	3000
Calibration factor OM, $\mu\text{m}$	1.306	0.6663	0.2659	0.1328		
Calibration factor SEM, $\mu\text{m}$			0.2976	0.1493	0.0746	0.0495

<sup>7</sup> With the help of the calibration factor occurs the assignment of the number of pixel to real dimensions. The units of measure are given in  $\mu\text{m}$ , referring to one pixel.

The tendencies from the previous section repeat also here. The values of the compactness and roundness decrease for the constant magnification with decreasing size class (corresponding to an increasing *MaxFeret*). In the case of nodular graphite the relations are reversed, both values raise. An exception to this is temper graphite. Shape parameter values for the size class R5 are higher than those for the size class R6.

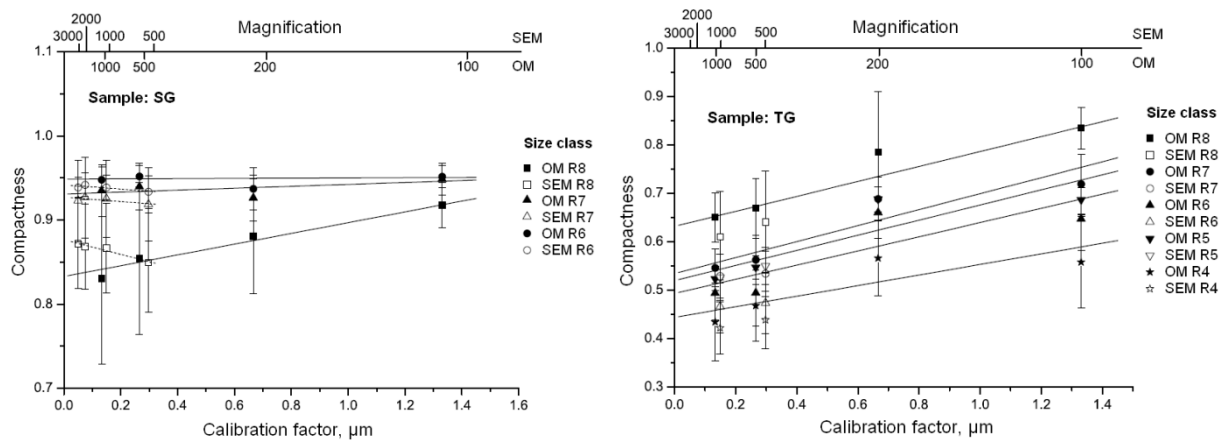


Figure 6.12 Dependency of the shape parameter compactness on the magnification for nodular graphite SG (left) and temper graphite TG (right).

The regression lines (Figure 6.11, Figure 6.12, Figure 6.13 and Figure 6.14) correspond to the values of the shape parameter for particles of the same size class. In addition the regression lines differ for the shape parameters determined on OM and SEM images.

With the help of these regression lines the following can be stated concerning the dependence of the shape parameters compactness and roundness on the magnification:

At the same given size class, the values of these both parameters decrease with increasing magnification. This however applies only for the values acquired from optical micrographs of flake, vermicular and temper graphite. Additionally for flake and vermicular graphite it can be seen that the regression lines for the particle with small *MaxFeret* (large size class) have greater slopes than those with larger *MaxFeret*. The reason for such behavior of the shape parameters may be found in the low resolution of the optical microscope. In addition to low resolution the fractal dimension, which characterizes the contour roughness, plays a certain role, as it has been already pointed out by Ruxanda et al [85], Li et al. [86] and Lu et al. [92]. The higher the magnification, the more accurately can the edge of the particle be determined. The particle perimeter somewhat increases and particle area strongly decreases (e.g. see Table 6.4) with increasing magnification. This behavior depends on the graphite morphology and also on the roughness of the graphite contour. Hence according to the Table 3.2 the values for shape parameters also reduce.

Table 6.4 Example of the variation of particle parameters depending on the magnification. Values are given for the largest flake graphite particle. The variations of perimeter are minimal due to the relatively flat contour of flake graphite, which corresponds to the fractal dimension value close to 1. This is not the case for vermicular ( $D=1.17$ )<sup>8</sup> and temper ( $D=1.28$ ) graphite (see [85]). Never the less the variations of shape parameters are considerable.

Calibration factor, $\mu\text{m}$	2.7	1.3	0.67	0.27
Perimeter, $\mu\text{m}$	943	937	945	972
Area, $\mu\text{m}^2$	2424	1447	1089	908
Compactness	0.066	0.041	0.031	0.027

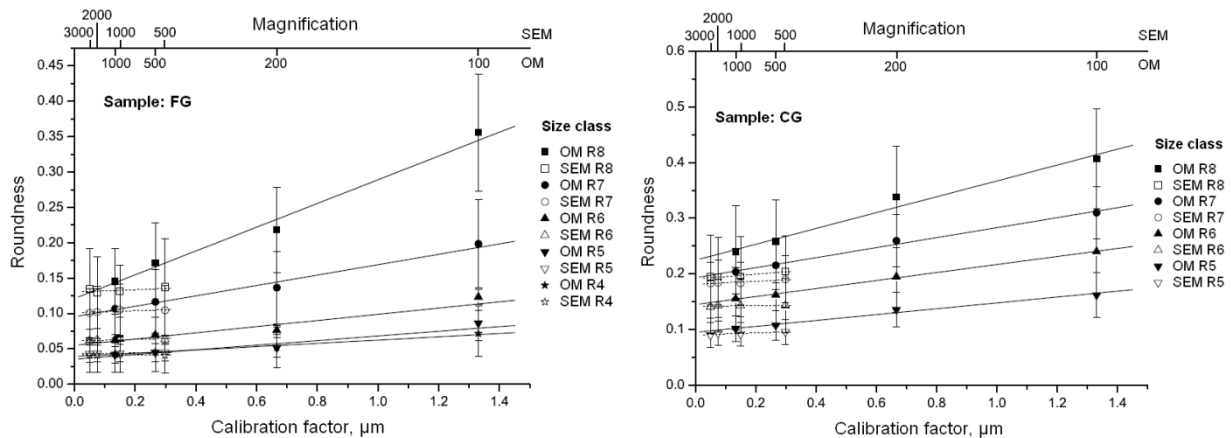


Figure 6.13 Dependency of the shape parameter roundness on the magnification for flake graphite FG (left) and vermicular graphite CG (right).

No specific tendency was found for the nodular graphite. Values for compactness and roundness for the size class R7 and R6 do not depend on the resolution. The reason for this is the nearly perfect spherical shape of the nodular graphite inclusions, which in two-dimensional section is ideally represented by a circle. Both shape parameters compare the particle area with area of the circle. The area and perimeter of the circle is practically independent from the magnification; and thus the fractal dimension strives for the value 1. Small particles of the size class R8 (0 – 15  $\mu\text{m}$ ) show some dependency from the magnification due to their very irregular shape. Jagged contour of these particles provokes the higher value of fractal dimension and thus similar to the particles of vermicular and temper graphite behavior of the shape

<sup>8</sup> D is a fractal dimension.

parameters. However the shape variation of nodular graphite particles with increasing magnification is insignificant.

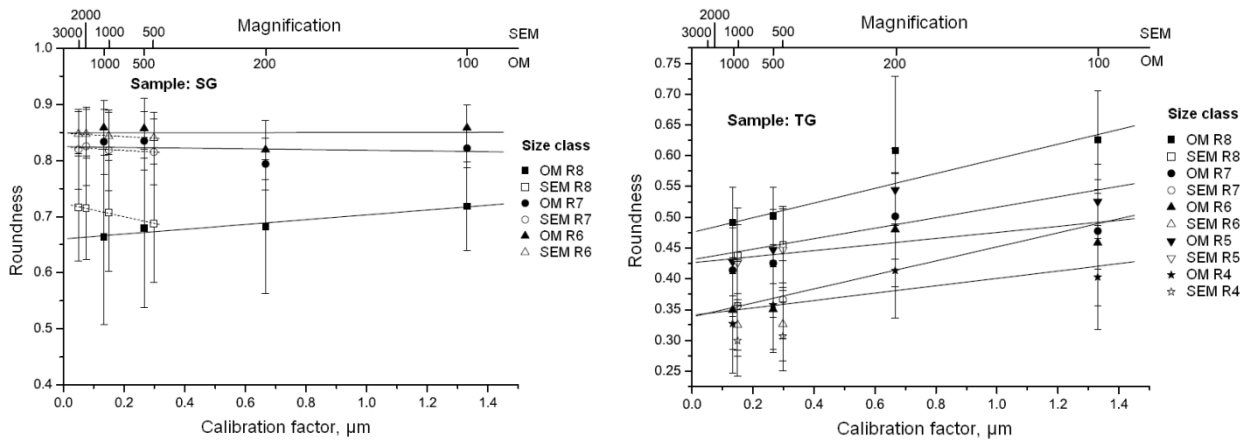


Figure 6.14 Dependency of the shape parameter roundness on the magnification for nodular graphite SG (left) and temper graphite TG (right).

The results acquired from the scanning electron microscope images are somewhat different. Here the values of both parameters are almost the same for FG and CG for all considered magnifications. Thus, there is no any dependency on the magnification. The reason is in the high resolution of the scanning electron microscopic images, which possibly compensate the influence of the fractal dimension. An exception is again nodular graphite of the size class R8, for which the regression line has a negative slope. However the standard deviations are relatively large, and thus it can be concluded that considering the error of the measurement not any dependency exists for the shape parameters of small nodular graphite sections on the magnification of SEM-images.

### 6.2.3.3 CLASSIFICATION ALGORITHMS BASED ON THE REGRESSION LINES

The task of the regression analysis is to determine the curve  $y = f(x)$  which brings the measured values in most simple functional relationship. First it should be decided which function type can be considered. The position of the measured values (see section 6.2.3.2) can be approximated with linear function:  $y = a + bx$ , where  $y$  is the shape parameter and  $x$  is the calibration factor. Least-squares analysis is applied in order to determine the suitable estimates for  $a$  and  $b$ . These values can be found in appendix 9.4 for particles of each graphite type and each size class.

Now the classifier can be created for each possible magnification resp. each possible calibration factor  $x$ . Mean values of the shape parameters roundness and compactness are calculated with the help of regression lines. The upper and lower limits for the identification do-

mains are determined by adding and subtracting the value of 95 % confidential interval. Additionally it was possible to define separately the overlapping region, which made it possible to quantify the error caused by particles having similar shape values (see [144]).

### 6.3 SUMMARY AND APPLICATION OF 2D GRAPHITE CLASSIFICATION

#### 6.3.1 OUTLINE FOR 2D GRAPHITE CLASSIFICATION

In this study, particle-based methods of microstructural image analysis were used to classify different graphite morphologies. The significant benefit of this method is that all shape parameters can be easily determined employing a commercially available image analysis system. It was found that the shape parameters roundness and compactness are suited best for a classification of the graphite morphologies I (flake), III (vermicular), IV-V, and VI (nodular). A novel method developed using particle size as an additional criterion leads to a significant improvement in classification of complex graphite particles.

As the results of the examination reveal, the shape of irregular graphite particles changes simultaneously with particle size. The complexity of the shape is statistically restricted for the small planar sections of an object. Small planar sections are more likely to be convex and to have a regular contour. Due to the limited image resolution a measurement of shape of the particles, which are only a few pixels in size, becomes very inaccurate. At small object sizes there is always a bias towards a circular or rectangular shape.

The analysis of the influence of the magnification on the shape parameters have shown that values acquired from optical micrographs and scanning electron microscope images depend differently on the calibration factor (i.e. magnification). The values of the shape parameters determined from the optical micrographs decrease with increasing magnification caused by the relatively low resolution and the effect of fractal dimension. No influence of the magnification on the values of shape parameters was found for nodular graphite and for values determined from SEM-images. From the regression lines i.e. their parameters, which were determined from the dependencies of the shape parameters on the magnification, it is now possible to generate the classifier for any magnification. Magnification 200× (calibration factor approx. 0.7 μm) is well suited for the characterization of graphite morphology, as it provides relatively large field of analysis and high accuracy by the determination of characteristic particle parameters.

The newly developed classification method which employs shape and size parameters improves currently available image analysis procedures and provides a reproducible and distinct

identification of different graphite morphologies. The accuracy of the classification is limited by the size of overlapping identification domains for different graphite morphologies, which in worst case represent 10 – 15 % of the area of all graphite inclusions. The employment of additional particle parameters can improve the classification accuracy.

### 6.3.2 INFLUENCE OF THE FRACTION OF GRAPHITE OF DIFFERENT MORPHOLOGIES ON THE PHYSICAL PROPERTIES

The developed classification algorithm was used to characterize the microstructure of the specimens mentioned in chapter 5. Graphite particles in each cast iron sample were classified and their area fraction was calculated for the fraction of all graphite inclusions equal to 100%. As though the fraction of the graphite is different in different cast iron samples (see Table 5.2), the electrical conductivity was normalized to exclude its influence. Thus, the results for all ten FG, eight CG and four SG-cast iron samples can be compared in the Figure 6.15.

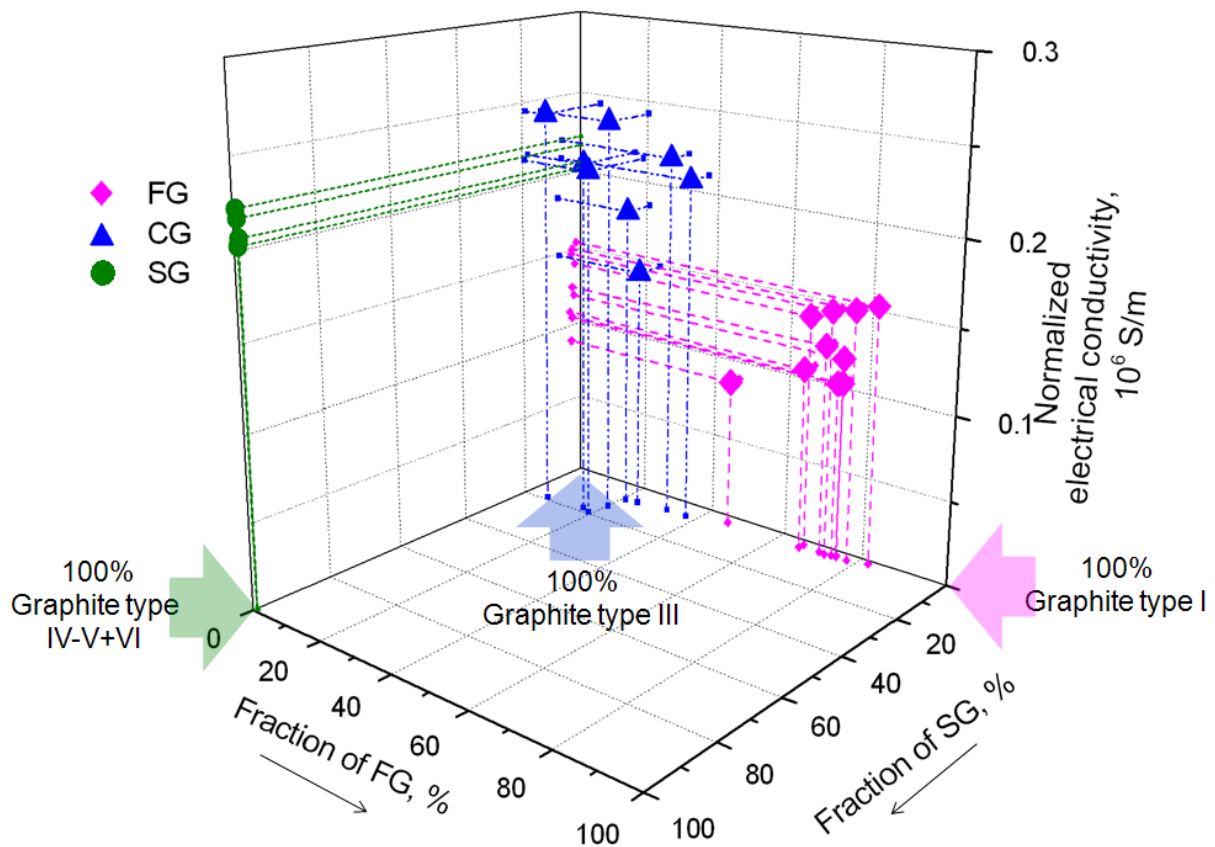


Figure 6.15 Electrical conductivity of cast iron with flake (FG), vermicular (CG) and nodular (SG) graphite presented vs. area fraction of graphite classified as flake (I), vermicular (III) or the graphite types IV-V + VI. Total graphite fraction in cast iron sample is taken for 100 %.

If all graphite particles were classified as vermicular graphite the data would concentrate in the origin of the coordinate system. In the analyzed cast iron samples with vermicular graphite

some particles were assigned to type I and some to type IV-VI. The amount of the respective type can be seen on the projection on the  $x - y$  plane. In samples with flake graphite over 70 % of area of the graphite particles were classified as type I, the rest is mostly type III. Almost all particles were classified as types IV-V or VI in the cast iron sample with nodular graphite.

The diagram shows well that electrical conductivity of cast iron correlates with the amount of the respective graphite type. When cast iron sample with vermicular graphite contains particles which were classified as flake graphite (type I) the conductivity reduces. If it contains nodular graphite particles (type VI) the conductivity does not change significantly. The lower volume fraction of graphite in vermicular cast iron samples CG (see Table 5.2) is compensated by the complex shape of the vermicular graphite particles, which eventually leads to lower conductivity in comparison to cast iron with nodular graphite SG (see Figure 5.2b).

Proving that the graphite shape plays the most important role on the properties of the cast iron, an attempt can be done to find a simple model and to conduct the finite element simulations. If the results of the simulation correlate well with the experimental results the suggested model could be used to estimate the variety of different properties of cast iron. In order to perform reasonable approximation of the effective conductivity the properties of the individual phases have to be known. Whereas for the pearlite matrix it was possible to calculate the thermal and electrical conductivity (see appendix 9.1) the analysis of the graphite crystal structure had to be performed in order to estimate the conductivity of the anisotropic complex graphite particles of different shape.

---

## 7 3D GRAPHITE CHARACTERIZATION

---

In this chapter particles of different graphite morphologies were characterized in 3D. The aim was first to describe the particle 3D shape and spatial arrangement in order to complete and optimize the classification of the graphite and to analyze the influence of these factors on the cast iron properties. At the same time the analysis of the nucleation, growth and crystallographic structure of different graphite types was performed, which was used to support some nucleation and growth mechanisms, made it possible to describe them quantitatively and suggested the way to estimate the effective properties of the graphite of different types.

### 7.1 GRAPHITE MORPHOLOGY AND CRYSTAL STRUCTURE

The characterization of three-dimensional graphite morphology was performed using FIB/SEM-tomography. Different contrasting methods were employed to depict the particularities of graphite formation. Focused ion beam (FIB) enabled TEM foil preparation at the specifically chosen regions, which allowed the examination of graphite crystal structure.

#### 7.1.1 DESCRIPTION OF THE 3D GRAPHITE MORPHOLOGY

After alignment of the initial high resolution SEM serial sections of the FIB-tomography, it was possible to observe the morphology of graphite particles and their internal structure at the virtual cuts from all different directions (Figure 7.1). Such examinations made it possible to understand, especially in the case of complex graphite particles, their real three dimensional shape and to introduce first assumptions about the particle nucleation and growth directions.

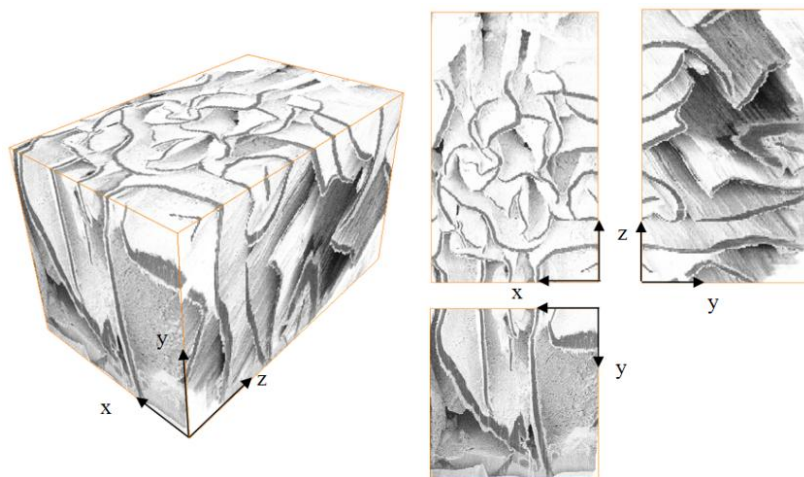


Figure 7.1 Slices of 3D image of cast iron with flake graphite. The x-y planes are the collected SEM images while the x-y and y-z are reconstructed via interpolation.

7.1.1.1 SPHEROIDAL (NODULAR) GRAPHITE (SG)

The reconstructed 3D-model of four nodular graphite particles is shown in Figure 7.2a. Two different nodule structures can be observed: a regular, smooth, and almost perfectly spherical type (Figure 7.2b), and a coarser type with a relatively large amount of pores and/or inclusions (Figure 7.2c). The coarser surface of the second type seems to result from secondary growth of graphite on an originally smooth surface. In addition, the microstructure of the first nodule type is indicative of the homogeneous growth of crystallites whereas the second nodule type seems to represent an agglomerate of several smaller nodule particles. In Figure 7.2, the nodules 2 and 3 belong to the first type whereas the nodule No. 1 unequivocally belongs to the second type. The shape of particle No. 4 is clearly more irregular and seems to represent a compound type. It is interesting to notice that both types of nodular graphite appear directly next to each other.

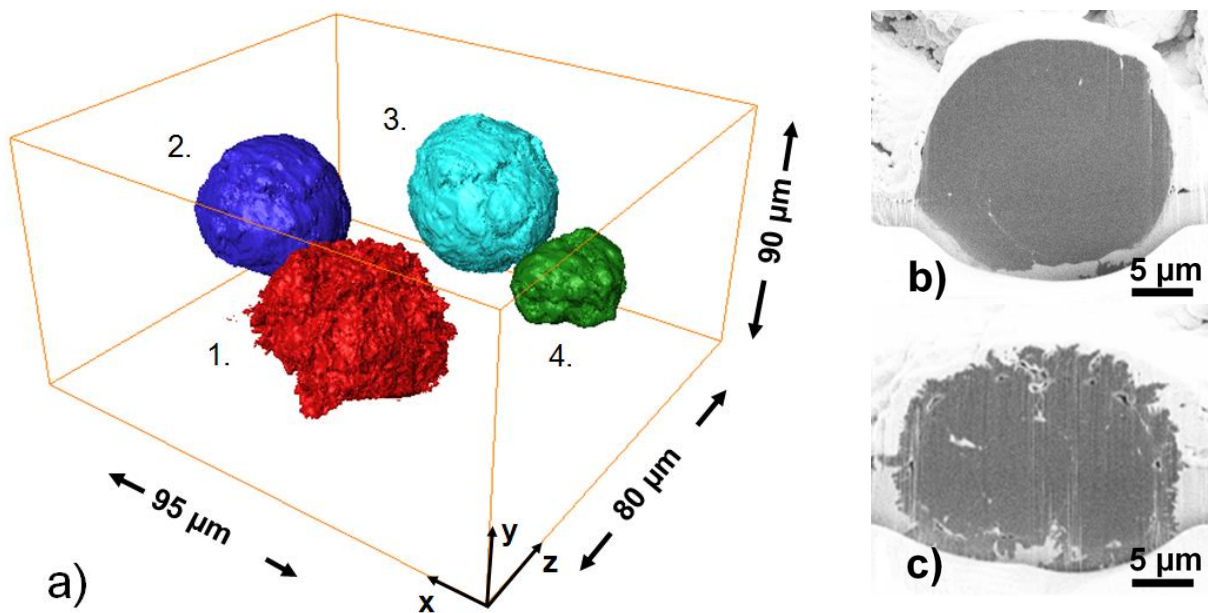


Figure 7.2 a) 3D reconstructed nodular graphite particles (SG); inside microstructure of nodular graphite particles b) No. 2 (blue) and c) No. 1 (red).

Nodular graphite of both these types can be equally observed in the cast iron with vermicular graphite (Figure 7.3). Here the relatively large particle contains one nucleus in the middle and radially distributed pores and/or iron inclusions.

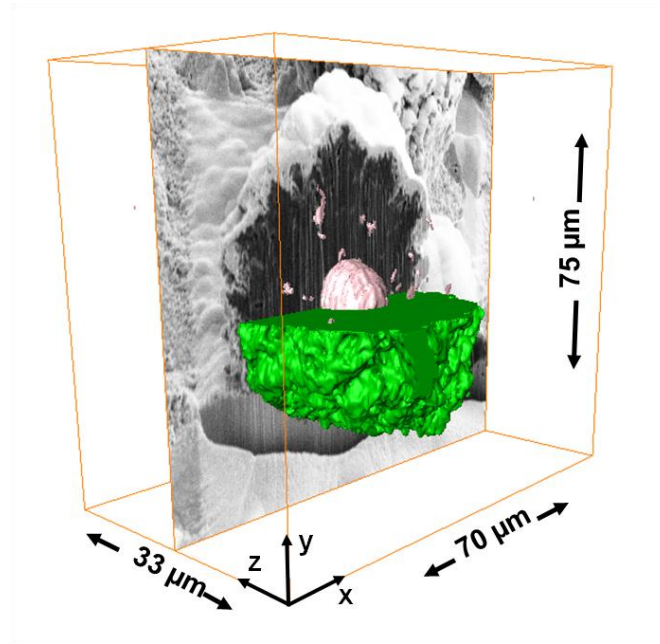


Figure 7.3 Irregular nodular graphite particle in cast iron sample with vermicular graphite. Heterogeneous nucleus detected by the FIB-Nanotomography with SE contrast.

The observation of nodular graphite particles with scanning electron microscope and during FIB-tomography has shown that almost all particles contain some heterogeneous nuclei: small (100 – 200 nm) or large (up to couple of  $\mu\text{m}$ ) (see Figure 7.3). As the probability that large nucleus can be cut by the 2D section is relatively high, it was possible to analyze their chemical composition already on the 2D sections. Large amount of sulfur was always detected in the nuclei. Additionally, some inclusions contained Mg and Ca, other Al and O, and some additionally the rare earth element Ce and La, when they were present in the melt. No dependency between the nucleus size and particle size was found. Particles with the nucleus containing both MgS core and shell composed of the rare earth materials were more regular (Figure 7.4) than the nodules without rare earth shell (Figure 7.5).

The graphite particles with irregular surface often had considerable amount of heterogeneous inclusions. These white inclusions are mainly distributed radially from the center of the nodule. In order to constrain the chemistry of inclusions, EDX analysis was performed on cross-sections of the second nodule type. The EDX signal shows a clear peak of Fe, implying the presence of Fe inclusions, enclosed in the graphite particle.

In order to assure the results of the chemical analysis on the polished specimens the EDX-maps were also acquired during the serial cross-sectioning. Figure 7.6 shows the FIB cross-section in secondary electron contrast and corresponding EDX-map. Analysis reveals the chemical composition of the inclusions inside of the nodular graphite particle, which were clearly visible already with secondary electron contrast. Nucleus is mainly composed of MgS.

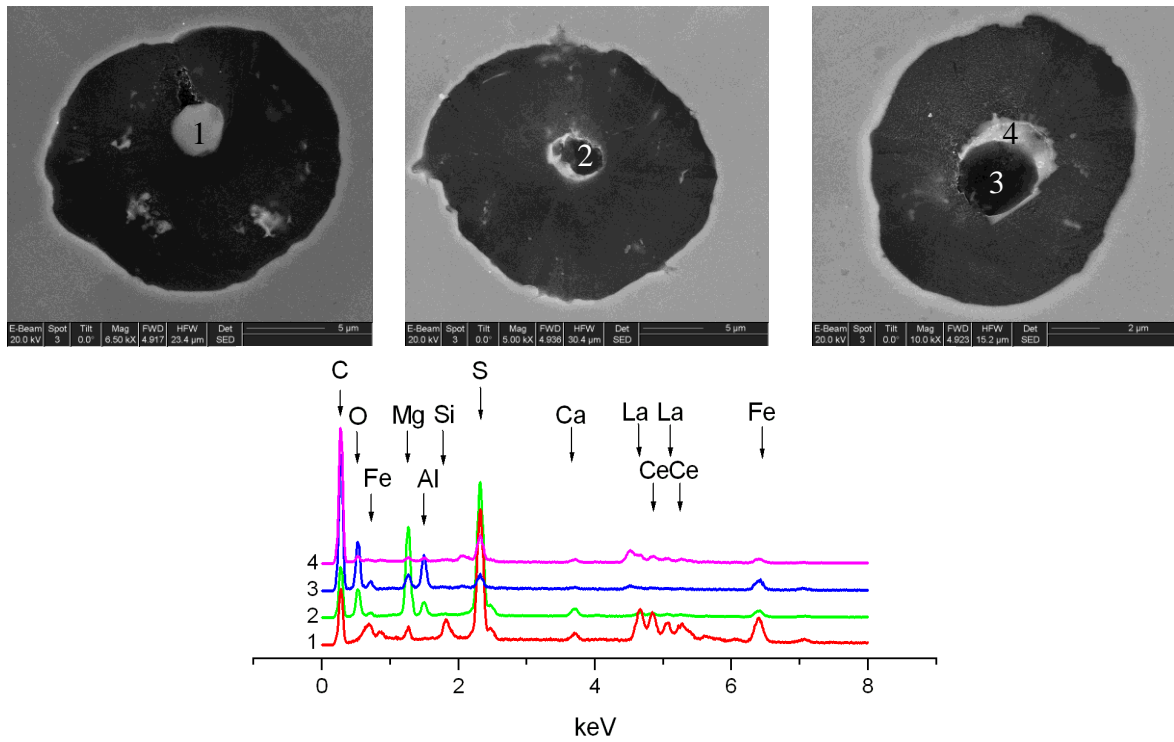


Figure 7.4 Chemical composition of nucleus in smooth nodular graphite.

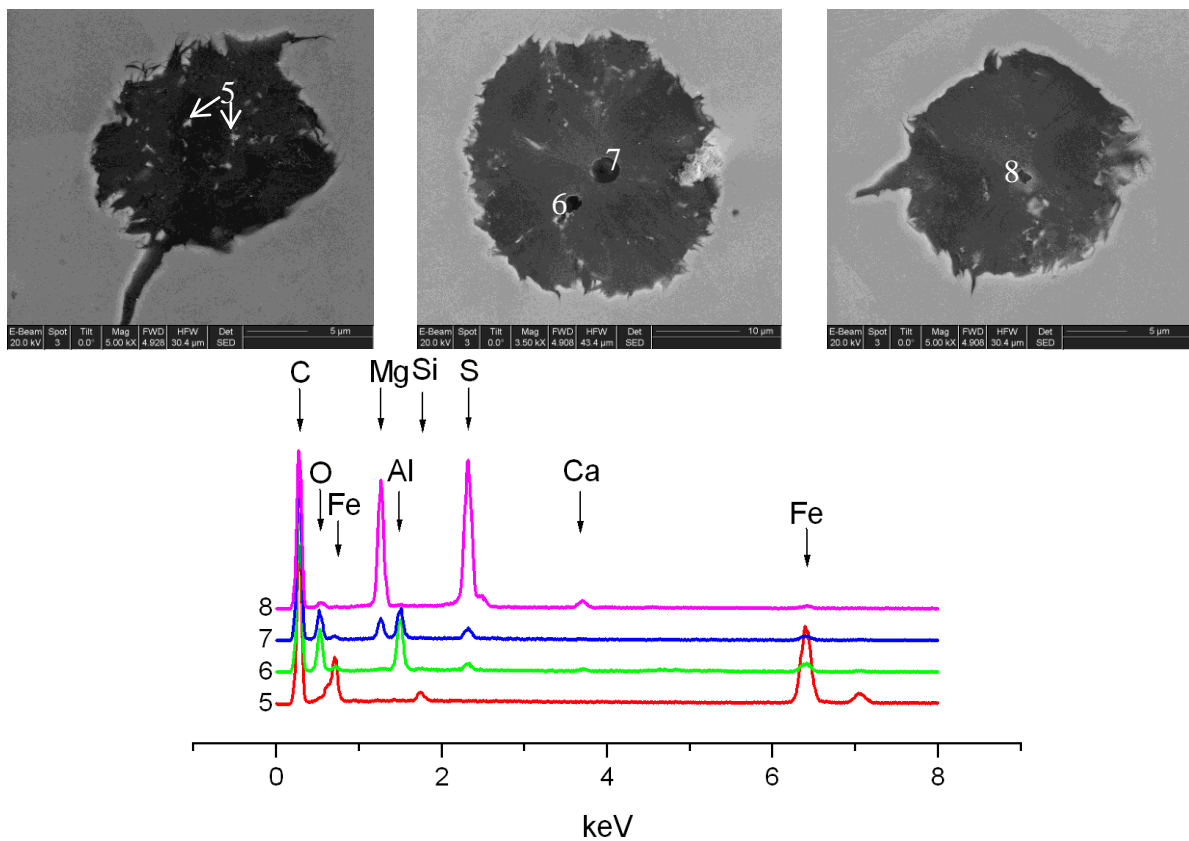


Figure 7.5 Chemical composition of nucleus in ragged nodular graphite.

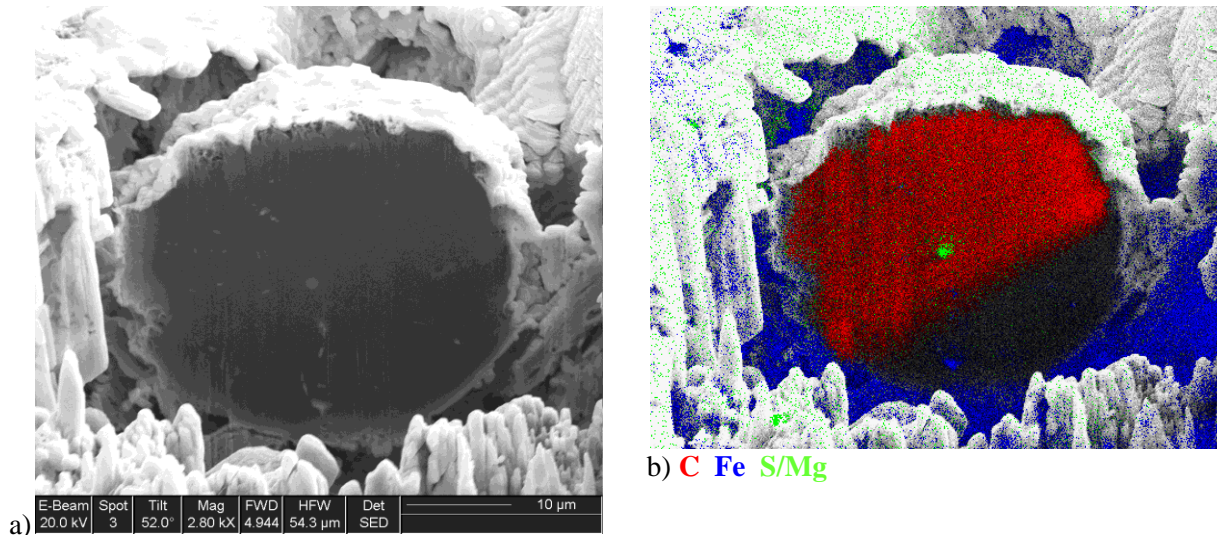


Figure 7.6 FIB cross-section through the nodular graphite particle and EDX-map. Mg and S compose the graphite nucleus, other inclusions consist of Fe.

### 7.1.1.2 TEMPER GRAPHITE (TG)

Three-dimensional analysis of graphite in malleable cast iron (Figure 7.7a) has revealed a very different graphite structure compared to ductile cast iron. The graphite particles are relatively large (~ 70 μm in diameter) and seem to represent composite particles consisting of an agglomerate of numerous irregular smaller particles.

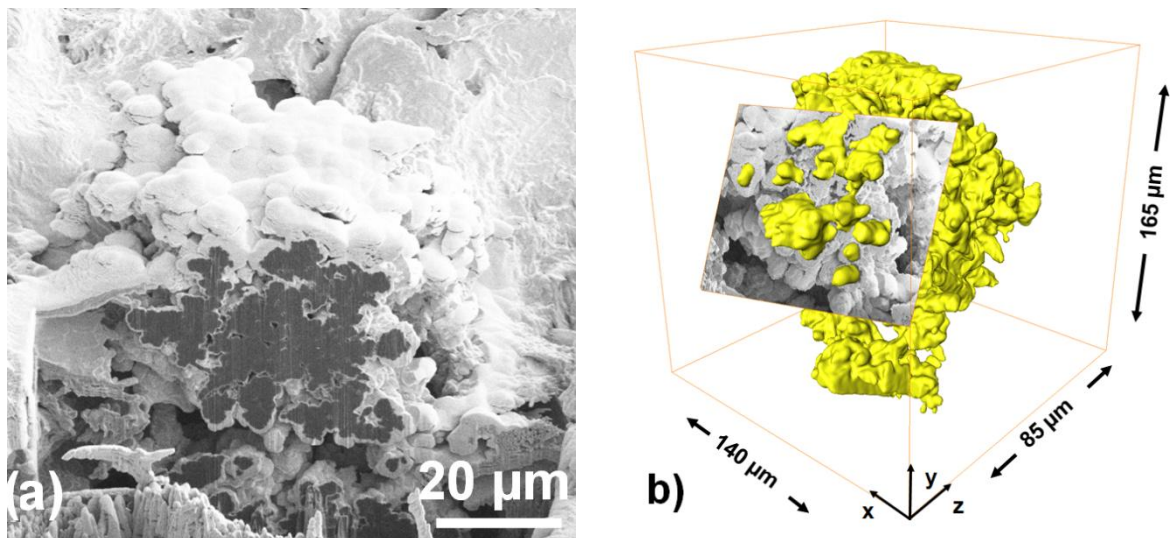


Figure 7.7 a) Temper graphite (TG) microstructure in malleable cast iron revealed in the FIB cross-section; b) 3D shape reconstruction with Amira.

In 2D cross-sectional analysis, due to the strongly irregular shape of the particles, the occurrence of more than one intersection with the sample surface (see Figure 7.7b) might lead to the false conclusion that more than one particle is present. If automatic 2D classification

schemes are used, the analysis will be incorrect concerning both the particle density and the particle shape. In addition to agglomeration, a relatively large amount of micropores seem to be present inside the graphite precipitates (Figure 7.7a).

#### 7.1.1.3 COMPACTED (VERMICULAR) GRAPHITE (CG)

Figure 7.8 shows the investigated vermicular particles. Due to the deep chemical etching of the iron matrix, the particles are largely exposed (Figure 7.8a and b). For a better understanding of the 3D-shape Figure 7.8c and d also depict reconstructed oblique slices through the particles. The shape might be described as coral-like with long and relatively flat rounded branches (see Figure 7.8e and f). As shown in Figure 7.8c, an inclusion of a second phase is observed in the middle of the investigated particle. In some cases there are several nuclei in one particle (Figure 7.8d). Due to the high complexity of the vermicular graphite particles it is though very rare to cut the vermicular particle exactly through its nucleation centre.

EDX analysis on cross-sections of the same sample show that these inclusions consist of MgS (see Figure 7.9). Thus, the chemical composition of the nuclei of the vermicular graphite particles is similar to the composition obtained for nuclei in spheroidal graphite already shown by Tartera et al. [145]. Careful examination of the individual images of all serial slices reveals that the graphite initially grows with a near-spherical shape. Due to the variation of the chemical composition of the liquid iron further branching occurs in different directions. As a result, a strongly irregular 3D-shape, as described above, containing relatively large pores is observed.

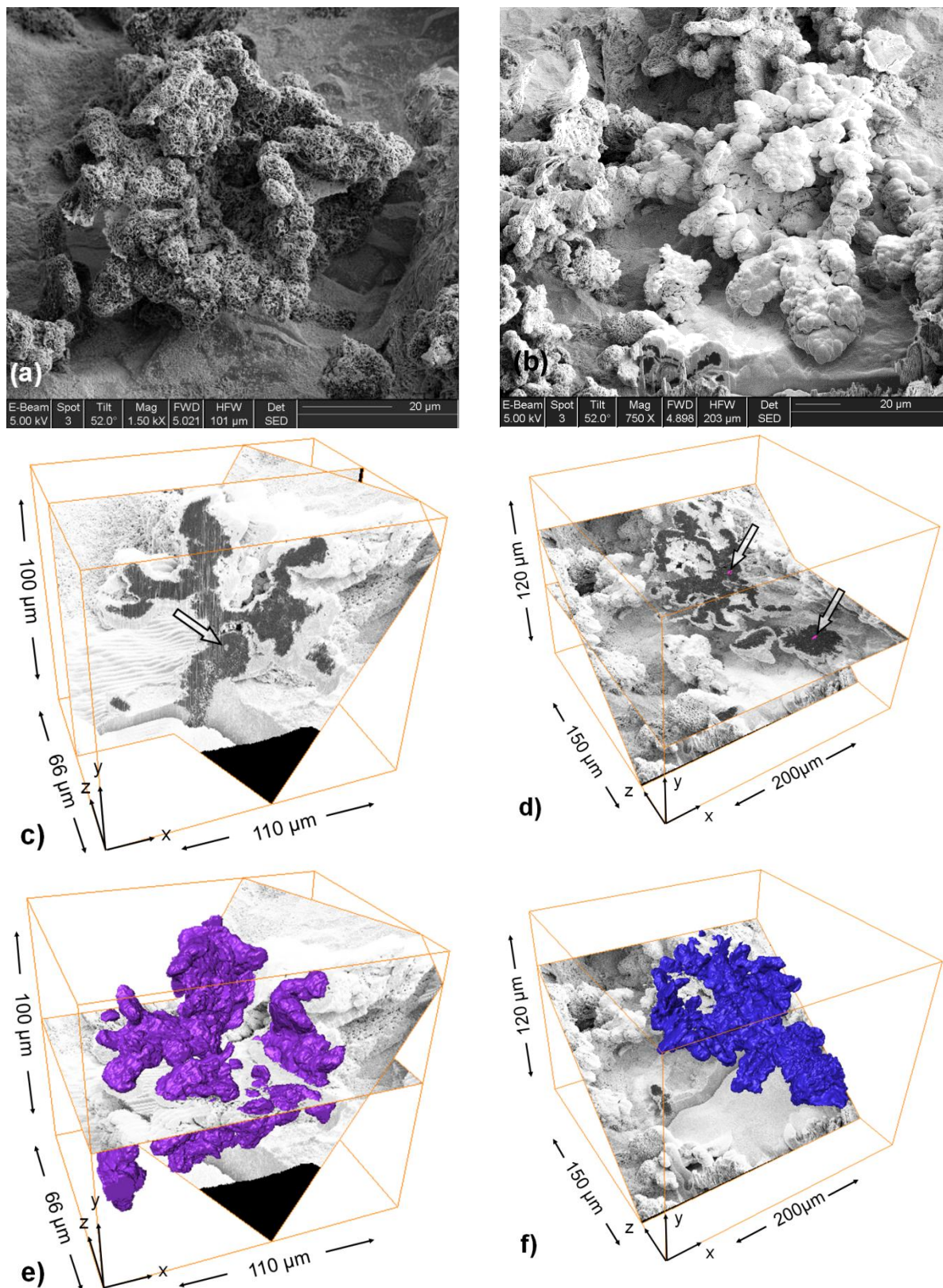


Figure 7.8 a) and b) SEM images of vermicular graphite particles (CG1 and CG2), deep etched; c) and d) axial (x-y) initial and reconstructed oblique slices. Heterogenic nuclei are shown with arrows; e) and f) reconstructed 3D shape of vermicular graphite particles.

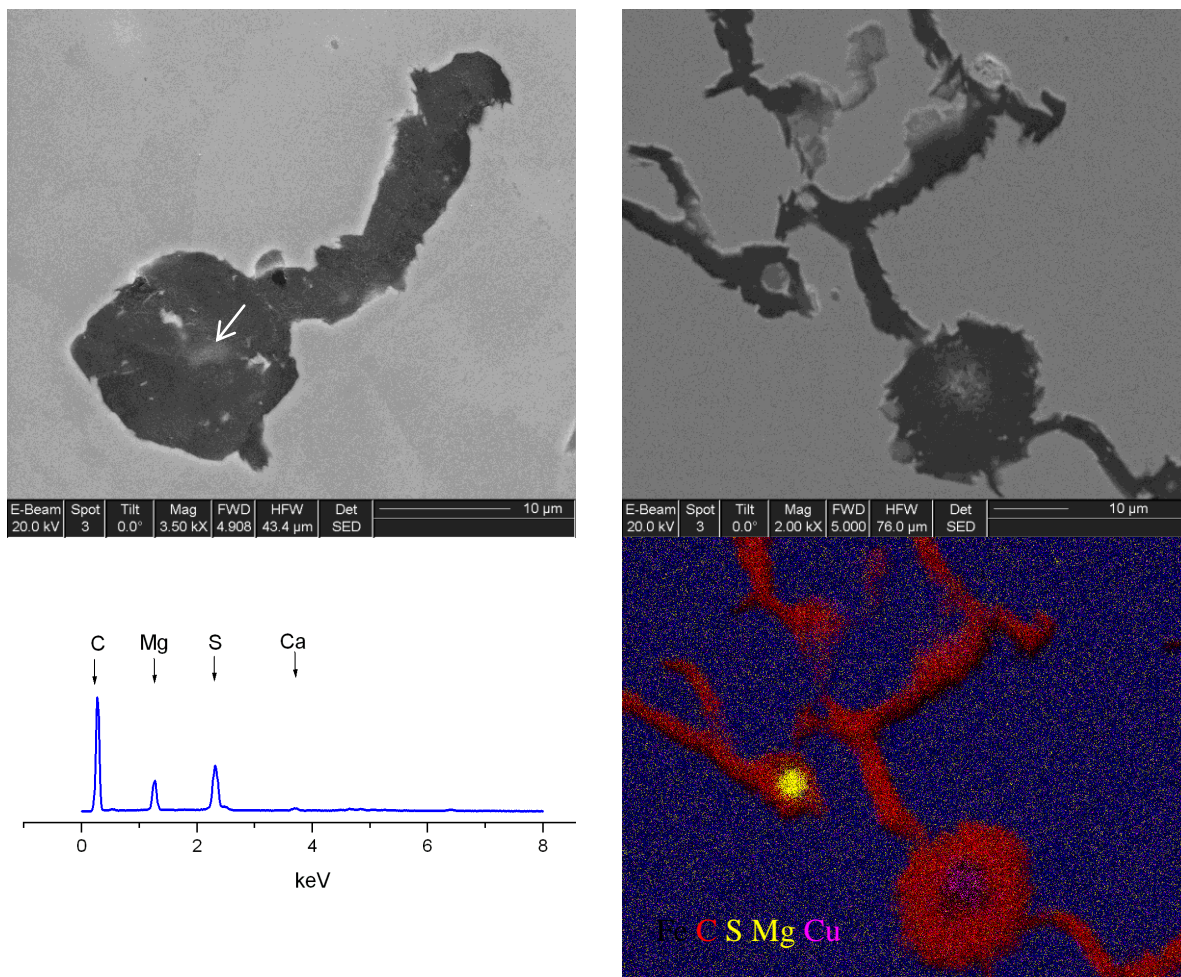


Figure 7.9 Chemical composition of the nuclei in vermicular graphite.

#### 7.1.1.4 LAMELLAR (FLAKE) GRAPHITE (FG)

As a last example, cast iron with flake graphite was analyzed. The flake graphite was arranged in large eutectic cells. It should be noted that due to the extremely large size (up to 200-400 μm) of the eutectic cells, only the particles in the middle of the eutectic cells could be studied. The SEM images of the deep etched cast iron sample are seen in the Figure 7.10a and Figure 7.11a. The sample includes the flake graphite of the arrangements B, as well as the D-graphite according to the DIN EN ISO 945 (Figure 2.5). The 3D reconstructions of the graphite particles (Figure 7.10b, Figure 7.11b and Figure 7.13), generated with the help of Amira™, show the significant difference of the graphite morphology. Particles of D-graphite (FG2) (Figure 7.11) are considerably smaller and have much higher density. It was found that almost all particles are connected in the investigated volume. Hence, due to their large size, only a sub volume of one compound flake graphite could be analyzed.

## 7.1 Graphite Morphology and Crystal Structure

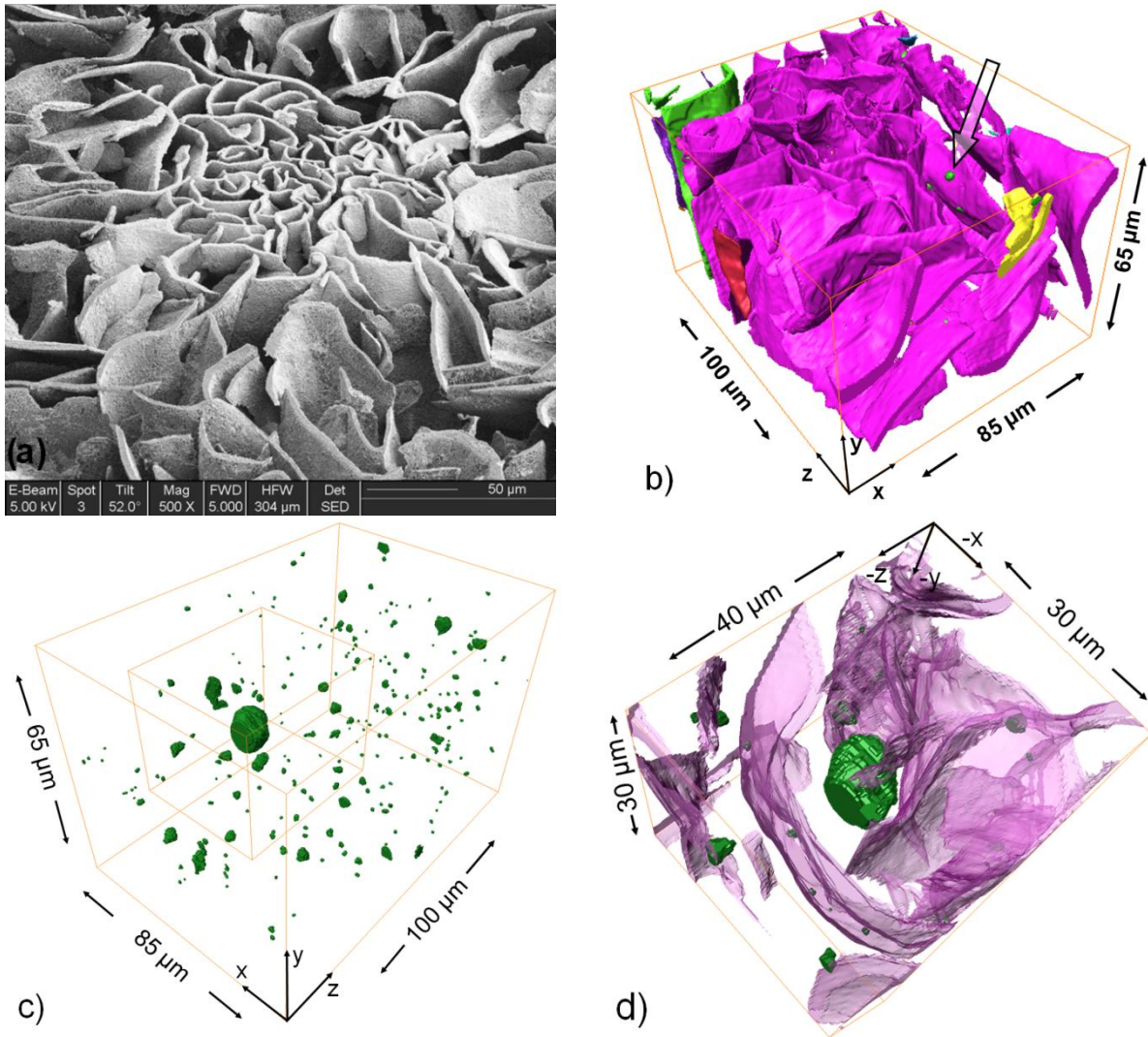


Figure 7.10 a) SEM image of flake graphite, deep etched; b) Reconstructed 3D structure (FG1); c) Inclusions in the investigated region; d) Cropped out magnified region with inclusions and flake graphite.

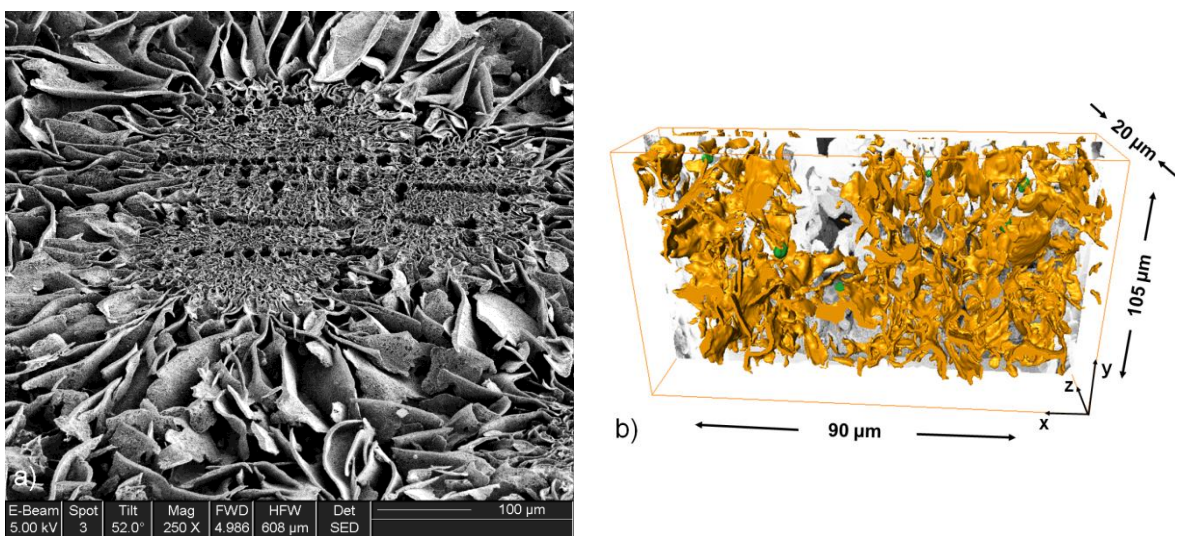


Figure 7.11 a) SEM images of the deep etched cast iron with D flake graphite; b) 3D reconstruction of the graphite structure in the centre of the eutectic cell (FG2).

The type B flake graphite (FG1) particles in the eutectic cell form a complicated network of thin 1-2  $\mu\text{m}$  thick graphite planes as shown in Figure 7.10b (marked in magenta). Numerous small inclusions were found on the surfaces of these planes and even in their interiors (Figure 7.10c, d).

From EDX analysis on other parts of the samples it was determined that the inclusions are precipitates of MnS. According to J. Tartera [146], the MnS acts as a substrate in the absence of inoculants. Its formation temperature and crystalline structure make it suitable for graphite nucleation. MnS-nucleus was observed in the middle of the eutectic cell. The nucleus contains very small amount of Mg, which have possibly served as a heterogenic nucleus for MnS. Graphite envelopes the MnS (Figure 7.12), which is especially well seen on the 3D reconstruction (Figure 7.13).

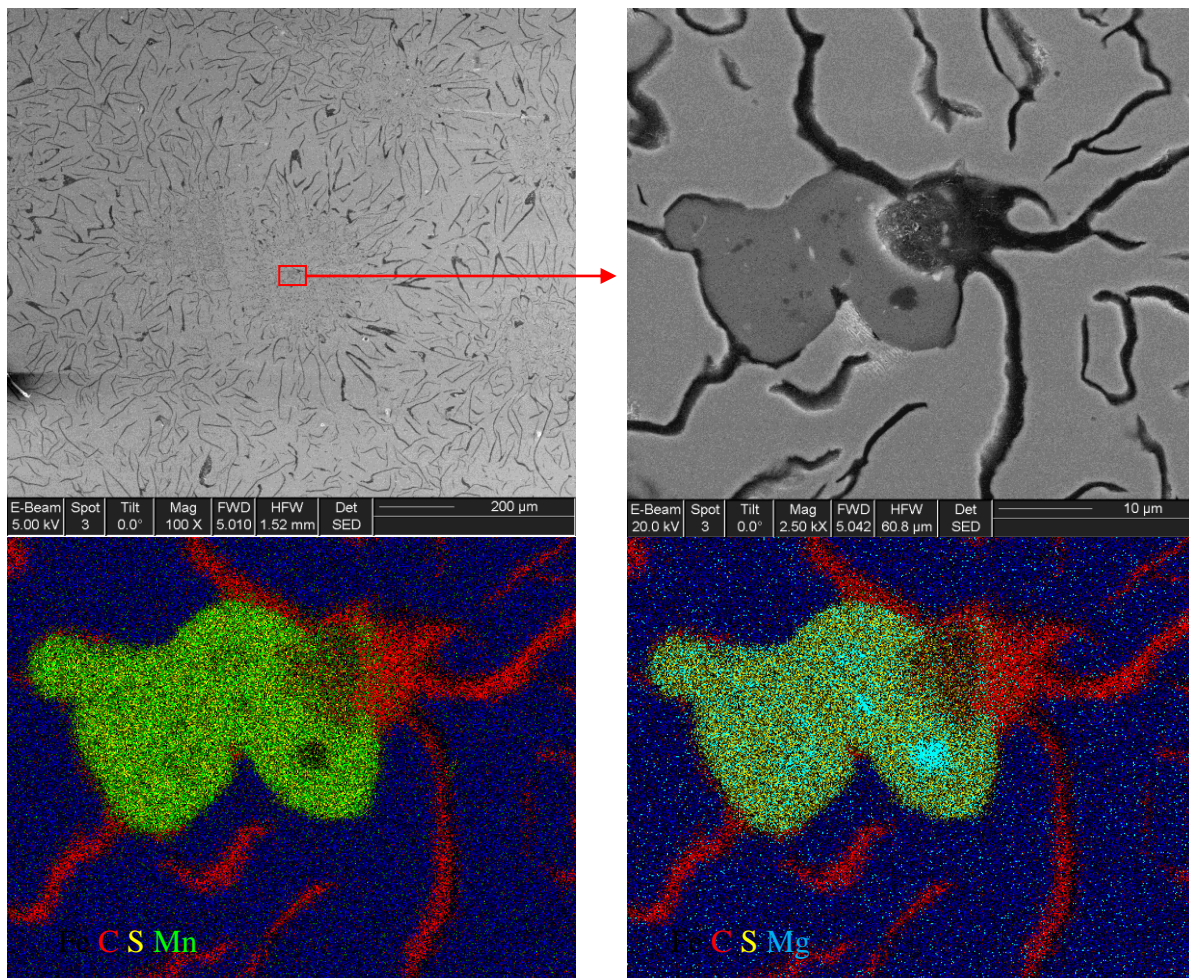


Figure 7.12 Eutectic cell with large MnS-nucleus of the eutectic cell in the cast iron with flake graphite.

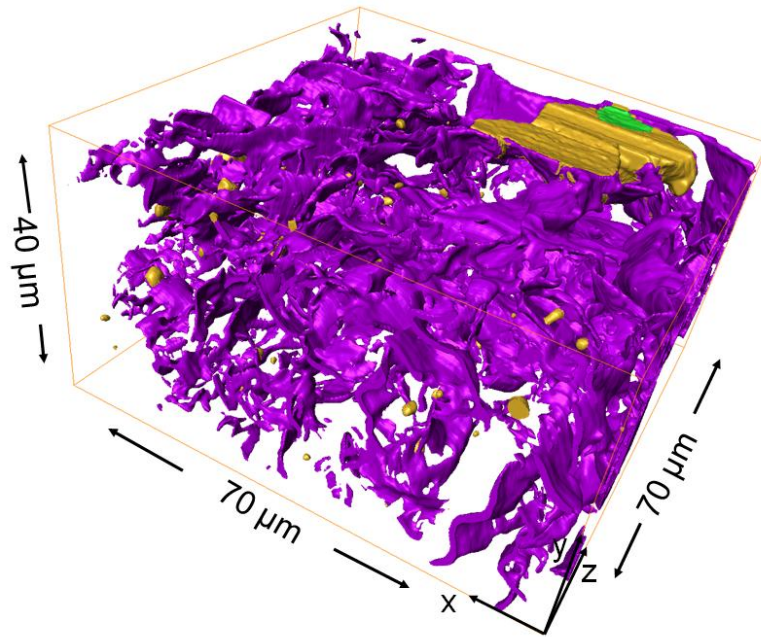


Figure 7.13 3D reconstruction of the flake graphite structure (FG3) and nuclei in the center of the eutectic cell presented in the Figure 7.12. Flake graphite envelopes the large MnS nuclei.

Unfortunately, the low heat of formation of MnS slows up its formation, making possible an increase of supercooling before nucleation, with the danger of the formation of type D graphite (Figure 7.11).

### 7.1.2 GRAPHITE NUCLEATION, CRYSTAL STRUCTURE AND GROWTH MECHANISMS

The crystallographic structure of the graphite inclusions was successfully analyzed on the TEM-foils acquired using target preparation with FIB workstation, as described in section 4.2.2.1. Structure of the graphite directly connected to the nucleus was of particular interest. It was possible to position the TEM-foil so that various aspects of the graphite growth could be studied. The nodular graphite chosen for analysis contains both the regular grown region (Figure 7.14a to the right of the particle) and graphite arm (Figure 7.14a to the left). The influence of the chemistry, structure and the orientation of the nuclei on the graphite growth was studied.

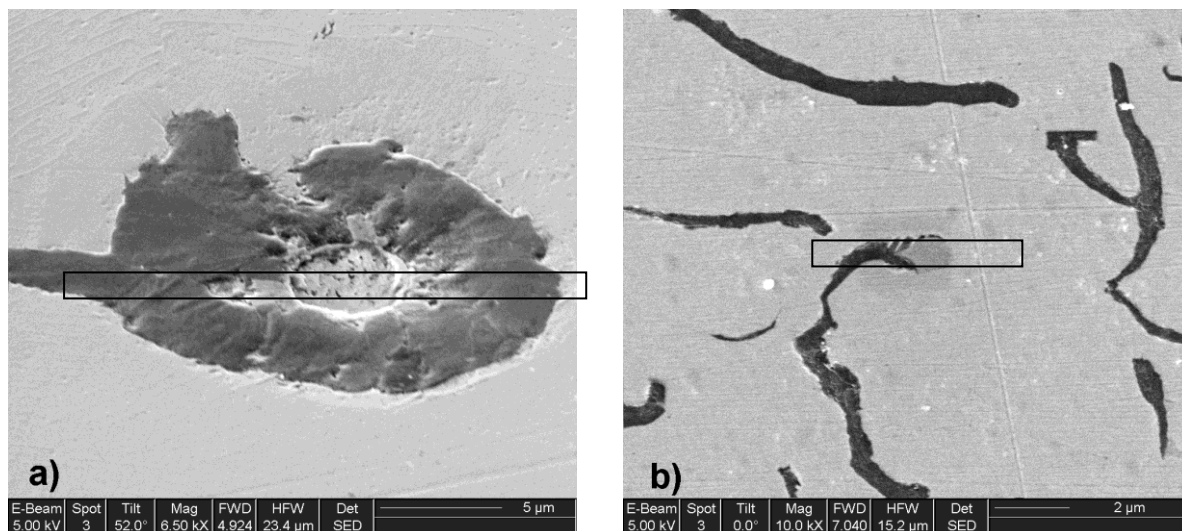


Figure 7.14 The TEM-foil was positioned through the nuclei and adjacent graphite: e.g. a) nodular and b) flake. The influence of the nuclei structure on the graphite structure was of the particular interest. Here nodular graphite (a) is developed correctly on the right side of the nuclei and on the left side the irregularities of the nuclei seem to lead to the growth of the arm disturbing the ideal spherical shape.

The radial growth of the graphite conical crystals well seen in the Figure 7.15 has been already observed using different microscopic techniques by [13], [147], [148] and [149]. Here for the first time it was possible to acquire high resolution images containing nucleus in the center of the nodule. This image is in accordance with the growth scheme suggested by [11].

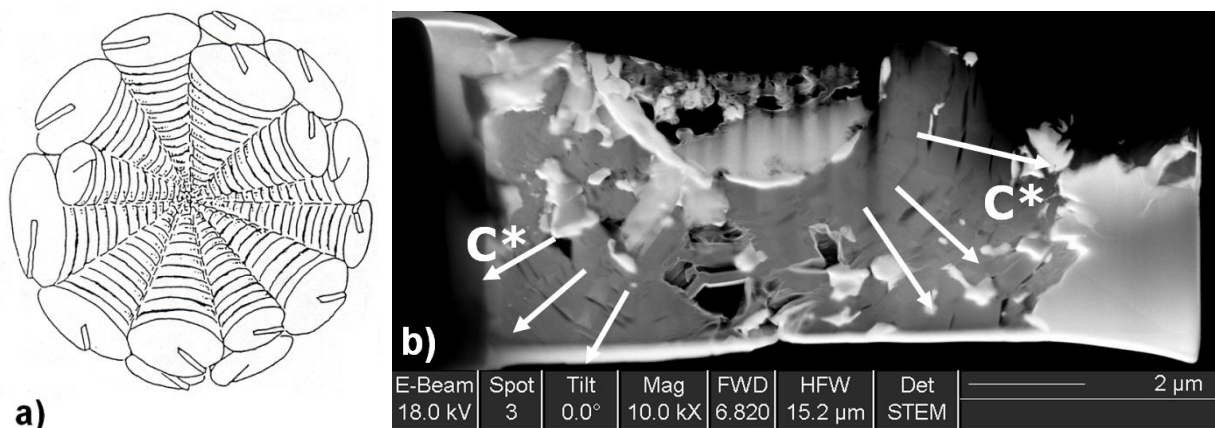


Figure 7.15 a) Improved structure model of nodular graphite [13] to the Double and Hellawell's cone-helix model[11]. b) Crystallographic structure of the nodular graphite. STEM image. Multi phase nuclei and numerous inclusions and pores in the nodule are well seen.

The nucleus is composed of a core and an envelope from which the graphite grows. The core is formed by magnesium sulfide (and CaS) (see Figure 7.16, region 5) and the outer shell contains mainly cerium-lanthanum sulfides (regions 1 and 6). Llorca-Isern et al. [149] has suggested that the shell is composed of CeS, MgS and La as lanthanum oxide. According to the EDX-maps and point spectra acquired in this work oxygen is present only in combination with magnesium and aluminum, and thus it was proved that shell consists mainly of cerium-

lanthanum sulfides. As it was stated by Tartera et al. [147], in order to promote the formation of crystals on a nucleating agent, the interface between the nucleus and the liquid should be of higher energy than that between the nucleus and the crystal solid. A means of maximizing this condition is to provide a nucleant crystal relationship that is associated with a good crystallographic fit between the respective crystal lattice. The efficiency is believed to be increased for decreasing values of relative lattice discrepancy (see Table 7.1). Growth of faceted phases occurs in well defined atomic planes thus creating angular surfaces. Graphite is a faceted crystal bounded by low index planes.

Such correlations were observed with TEM. The orientation of the graphite crystal *c*-axis is perpendicular to the  $\langle 100 \rangle$  directions of MgS. The lattice parameters of the graphite in [100] and [010] direction correspond to the distance between Mg and S atoms, the half of the lattice parameter of MgS (Table 7.1).

Table 7.1 Characteristics of several compounds which can act as a nucleus for graphite [146], [150].  $\Delta H(\text{CeS}_2)$  was not available in the literature.

	C	MgS	MgO	CeS	LaS	CeS <sub>2</sub>	La <sub>2</sub> O <sub>3</sub>
$\Delta H$ kJ/mol		-346	-143.8	-459.4	-456		-1793.7
Melting point, °C	3652	> 2000	2800	2450	2300		2315
Crystal system	Hexagonal	Cubic	Cubic	Cubic	Cubic	Orthorhombic	Hexagonal
Lattice parameters in Å	a=2.47 c=6.79	a=5.19	a=4.21	a=5.78	a=5.85	a=8.1 b=4.1 c=16.2	a=3.94 c=6.13

Large rectangular inclusions (see Figure 7.16, region 3) containing Mg, Si and Al to the left side of the particle seem to hamper the regular nodular graphite growth. Large pores are induced as can be seen in the Figure 7.15b. They might as well serve as the reason for graphite branching, as seen on the Figure 7.14a.

On the right side of the particle the structure is relatively homogeneous. Several Fe-containing inclusions closer to the border of the nodule seem to interrupt regular graphite growth. The interaction of the graphite structure with such Fe-containing inclusions is well seen in Figure 7.17a. The possible scheme of the graphite growth with the presence of heterogeneous inclusions is shown on the Figure 7.17b. Considering the big amount of inclusions inside the particle 1 on the Figure 7.2a and particle on the Figure 7.3 it can be stated that their coarse surface is due to this effect.

Thus, the suitable nucleants initiate the spherical graphite growth, which is hindered by incoherent inclusions.

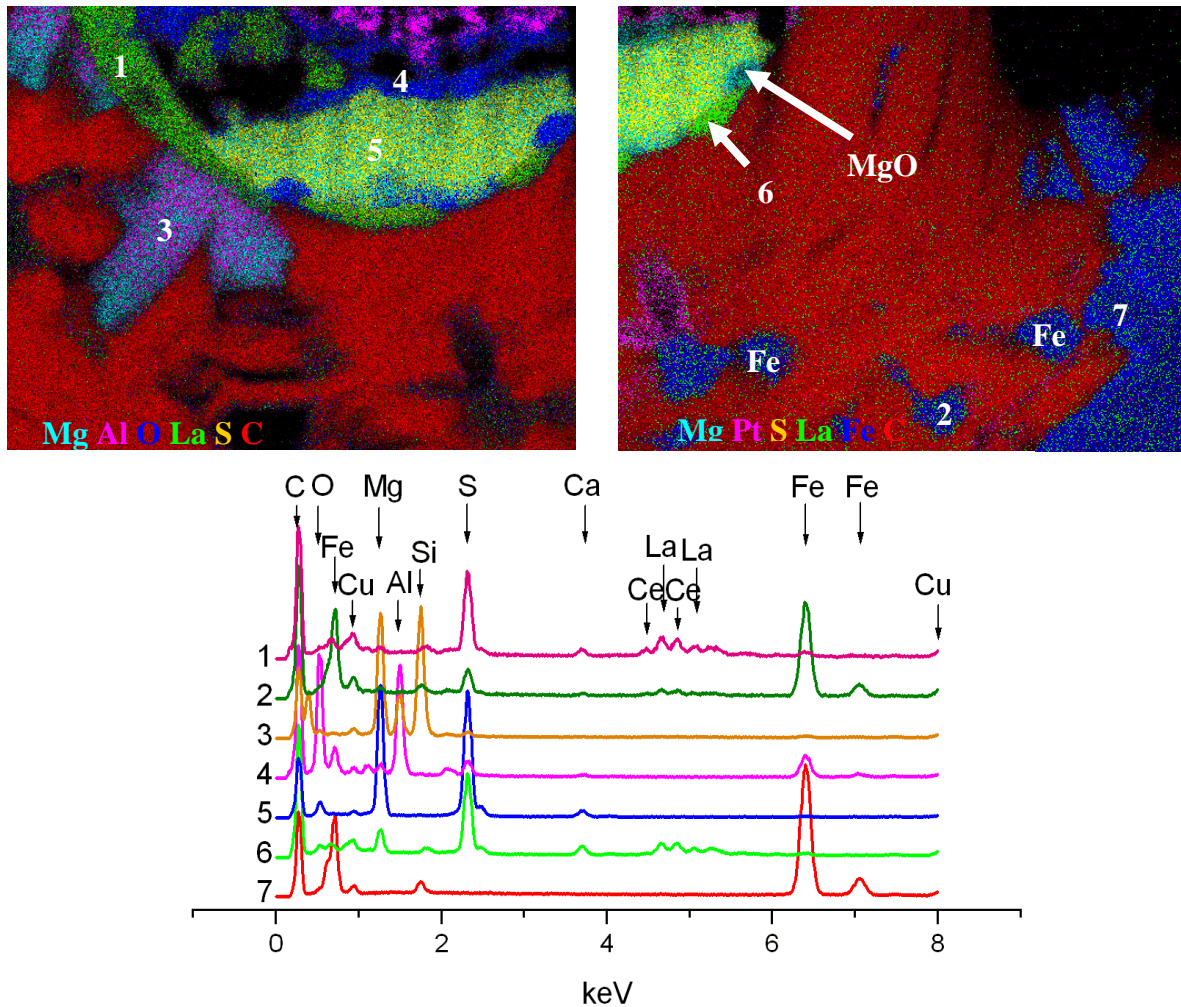


Figure 7.16 EDX-mapping and spectra for different phases in nodular graphite with nucleus. EDX-analysis was performed on the approx. 100 nm thin TEM-foils providing the chemical composition of object with size down to 150-200 nm (e.g. inclusions 2 and 6). Due to the still relatively large interaction volume, only qualitative analysis of individual inclusions can be done.

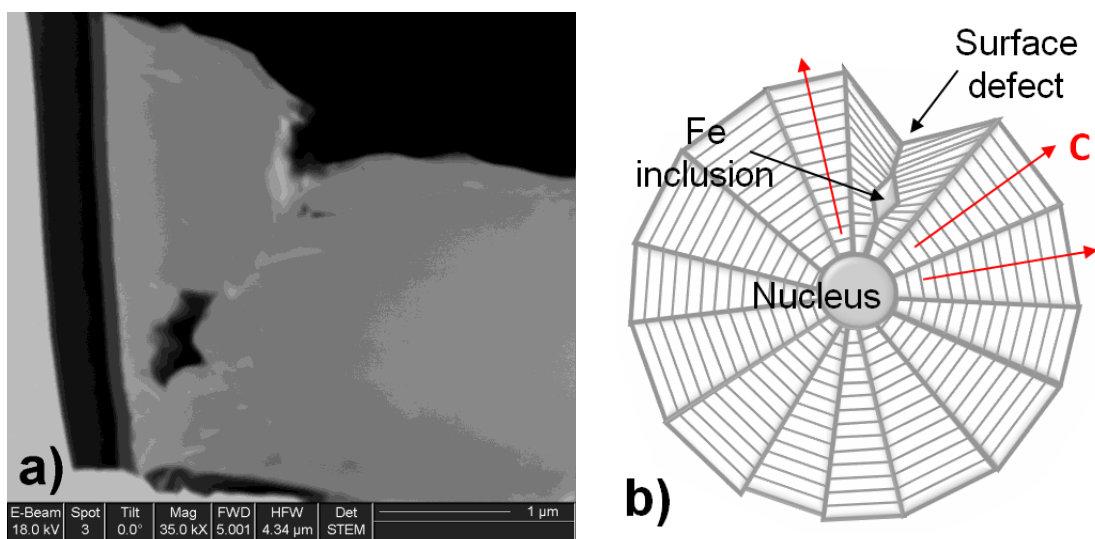


Figure 7.17 a) STEM image of Fe-inclusion interrupting the regular growth of the graphite nodule and b) the scheme of the graphite structure with defect.

STEM image on the Figure 7.18 visualizes flake graphite adjusted to the nucleus, and several other flake graphite particles. MnS was unambiguously identified as nucleus of flake graphite. It has cubic structure with lattice parameters  $a=5.224 \text{ \AA}$ .

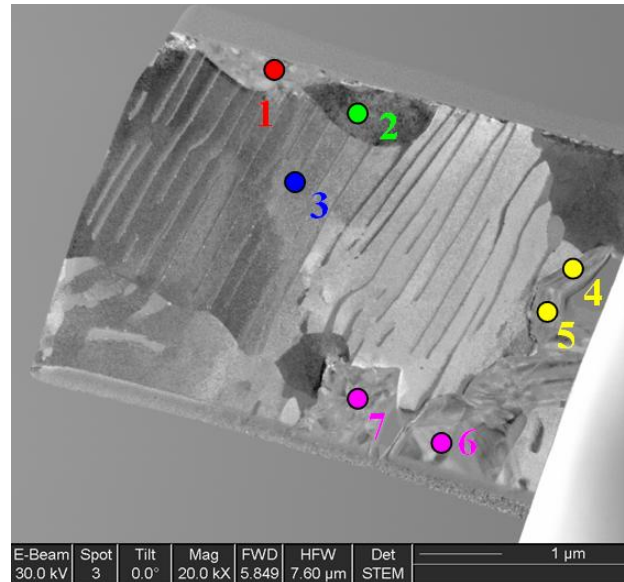


Figure 7.18 STEM image of cast iron with flake graphite and their nucleus. TEM Diffraction patterns in the marked regions.

As an evidence for the coupled growth between metal and flake graphite serves the correlation between orientations of the crystallographic lattices of MnS-nucleus, flake graphite particle and matrix (Figure 7.19).

Flake graphite of different orientations was observed on the sole TEM-specimen. The  $\langle 001 \rangle$  crystallographic direction of the graphite lattice is either perpendicular to the graphite-matrix interface (see Figure 7.18, regions 1, 4 and 5 and Figure 7.20), or in some rare cases  $\{001\}$  lattice planes lie in the observation plane (regions 6 and 7). The intermediate rotation around the  $c$ -axis also mentioned in the work of Double and Hellawell [151] is clearly seen in the diffraction pattern 7 (Figure 7.20).

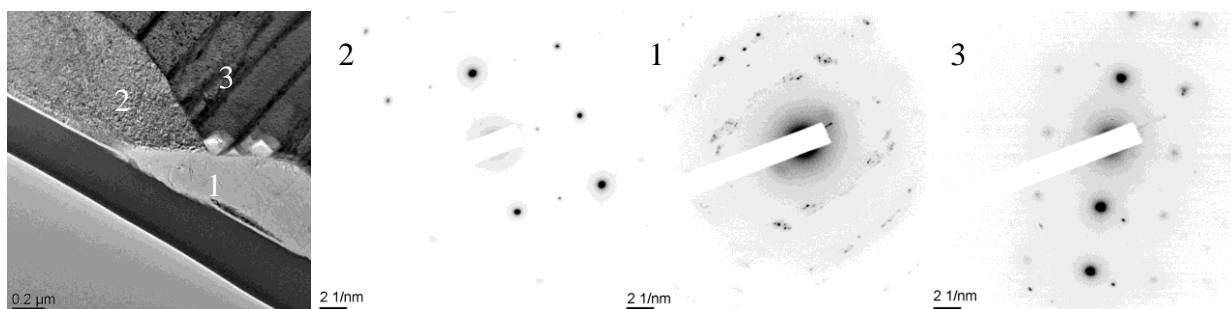


Figure 7.19 TEM-image and diffraction patterns of MnS-nucleus, adjustment graphite and surrounding matrix.

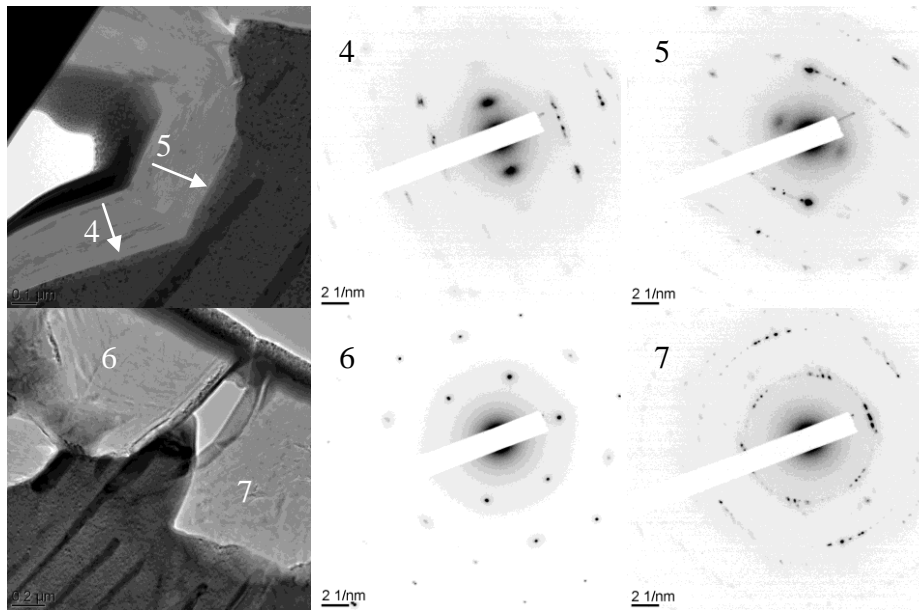


Figure 7.20 Diffraction patterns of the flake graphite crystallographic structure.

Roviglione et al. [152] has shown with the help of X-ray diffraction characterization that flake graphite has a strong crystallographic growth direction (GD) relationship with austenite:  $\langle 110 \rangle_{\text{Gr}}$ ,  $\langle 100 \rangle_{\text{Gr}} \parallel \langle 100 \rangle_{\gamma} \parallel \text{GD}$ . She assumed the existence of the preferential plane coupling at their interface. In the center of the eutectic cell (where the TEM-specimen was taken) each nucleus initiates own growth direction consistent with its own crystallographic orientation and local temperature gradient. By the coalescence of such regions flake graphite seems easily to adapt to the varying flow direction of matter and heat by branching, twinning, twisting and bending. Roviglione [153] has stated that such accommodation of the flakes to the rapidly changing condition can only be explained if its growth is diffusion controlled.

Two different regions equivalent to two different growth mechanisms are seen on the TEM-specimen through the vermicular graphite particle (Figure 7.21a): one of the nodular graphite on the bottom and one of the flake graphite at the top. The observed crystallographic structure is consistent with the assumption made by Llorca-Isern et al. [149] and Tartera et al. [145]. Compacted graphite grows initially as a spheroid and later developing branches which grow similar to the flake graphite. As though the following growth of the  $(10\bar{1}0)$  interface is unstable the initiation of a twin/tilt of boundaries occurs. The twin/tilt growth mechanism of compacted graphite was proposed by Zhu et al. [154]. It is consistent with the observation done by Roviglione et al. [152]. No favorite crystallographic direction was found for the vermicular graphite even by its directional growth. Figure 7.21b shows that compacted graphite is composed of small and compacted randomly oriented flakes.

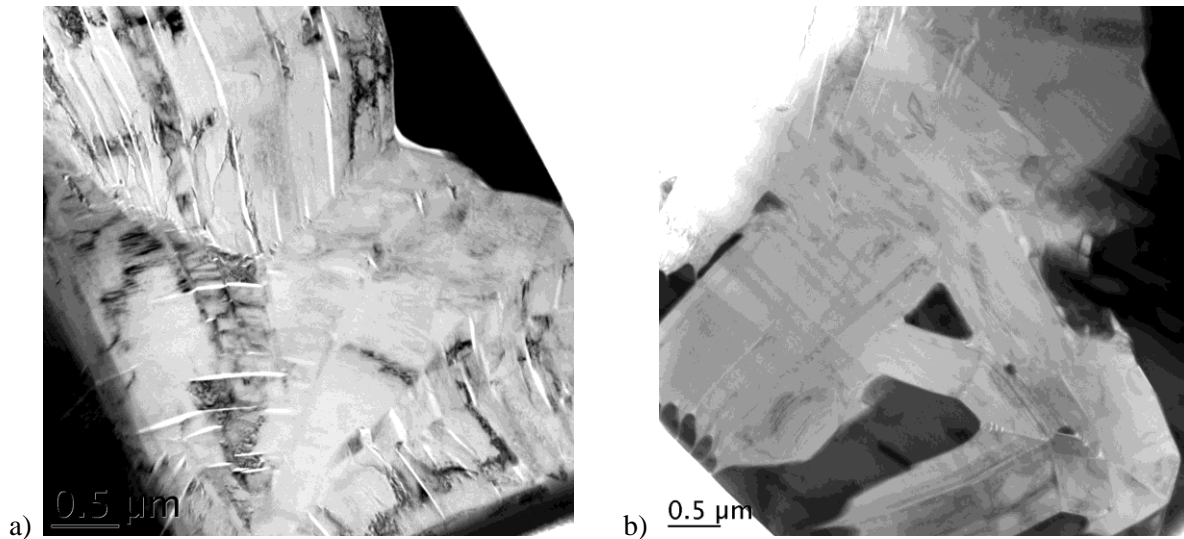


Figure 7.21 Structure of the vermicular graphite a) presumably near the nucleus and b) closer to the boarder. The vermicular particle grows initially nodular like, branches grow in a-direction. Small compacted randomly oriented flakes compose the resulting particle inducing the high irregularity of the vermicular graphite surface.

The intermediate chemical composition of the cast iron with vermicular graphite results thus in the intermediate growth mechanisms of the graphite inclusions. Moderate magnesium and rare-earth elements additions binds up the oxygen and sulfur in the nucleus and initiates spheroidal growth. Heterogeneous defects in the nodule as well as the sufficient amount of oxygen and sulfur in the residual melt result in branching. This demonstrates the strong influence of trace components during casting.

The resulting complex shape of different graphite particles is quantitatively characterized with the help of 3D image analysis. Although temper graphite does not follow the same solidification process its shape was analyzed in this work in order to give the complete overview of different graphite types.

## 7.2 3D ANALYSIS OF RECONSTRUCTED 3D MODELS

With the help of 3D analysis, the special structure characteristic parameters can be directly determined from the spatial images without any shape assumptions. The interpretation of the 3D structural parameters is not often obvious and thus discussed in this work.

### 7.2.1 COMPARISON OF THE PARAMETERS FOR THE INDIVIDUAL GRAPHITE PARTICLES OF DIFFERENT MORPHOLOGY

Individual graphite particles were described quantitatively regarding their basic characteristics and shape. With the help of the advanced image analysis techniques the influence of the nucleus and inclusions on the growth mechanism of the graphite was analyzed.

#### 7.2.1.1 BASIC CHARACTERISTICS

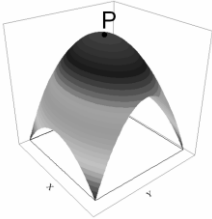
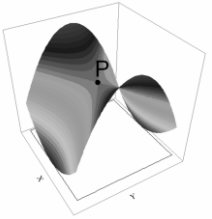
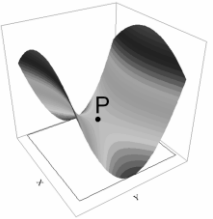
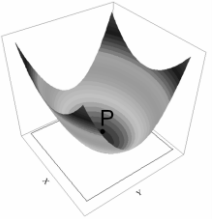
The 3D analysis has shown that the particles of different morphology possess characteristic values of 3D structure parameters, which are presented in the Table 7.2. For the description of the individual 3D particles the basic structural parameters were used: volume ( $V$ ), surface area ( $S$ ), integral of mean curvature ( $M$ ), and integral of total curvature ( $K$ ). The volume densities of these parameters: volume fraction ( $V_V$ ), specific surface area ( $S_V$ ), density of the integral of mean ( $M_V$ ) and total ( $K_V$ ) curvature serve as a basis for microstructure characterization. To determine these values with good accuracy the relatively large volume, which contains a large amount of discrete or connected particles, is required. Thus, these 3D field features were determined exclusively for the cast iron samples with flake graphite.

Table 7.2 3D particle parameters of nodular (SG), vermicular (CG) and temper (TG) graphite calculated with MAVI software.

Particle	V, $\mu\text{m}^3$	S, $\mu\text{m}^2$	M, $\mu\text{m}$	K	$\chi$	$\chi_{\text{fill holes}}$
SG1-1	8805	6558	-2898	-1445	-115	-284
SG1-2	10006	2987	-491	251	20	-35
SG1-3	11242	3595	-1046	666	53	-72
SG1-4	1926	1346	-540	427	34	-27
SG2	13412	7938	-4165	7691	612	-531
TG	78130	34885	102	-980	-78	-99
CG1	43420	28814	453	-603	-48	-92
CG2	81302	44652	2245	-364	-29	-57

$V$  characterizes the particle volume;  $S$  indicates the value of the particle surface. The integral of mean curvature  $M$  depicts the geometrical configuration (viz. the shape) of the inclusions. It is calculated according to the equation 3.1. The surface curvature at the point  $P$  can be described by its minimum  $r_1$  and maximum  $r_2$  radius. There are four different surface elements which can occur (Table 7.3). The fraction of certain surface elements and the ratio between two curvature radiuses determine the value of the integral of mean curvature  $M$ .

Table 7.3 Shape of the surface elements  $P$  and their local curvature  $M_p$ .

Convex	Saddle1	Saddle2	Concave
			
$ r_1  <  r_2 ,$ $r_1 > 0, r_2 > 0$ $M_p > 0$	$ r_1  <  r_2 ,$ $r_1 > 0, r_2 < 0$ $M_p > 0$	$ r_1  <  r_2 ,$ $r_1 < 0, r_2 > 0$ $M_p < 0$	$ r_1  <  r_2 ,$ $r_1 < 0, r_2 < 0$ $M_p < 0$

The first curvature integral  $M$  of the spheroidal graphite particles SG1-1 and SG2 is  $\ll 0$ . The reason for this is the very rough contour, the large amount of saddle2 surface elements and the large amount of pores, which corresponds to the existence of the concave surface elements. The contour of the spheroidal particles SG1-2, SG1-3 and SG1-4 is considerably smoother and more convex. A small amount of pores causes the negative value of  $M$ . Temper and vermicular graphite particles have a positive value of the integral of mean curvature as a consequence of the high fraction of convex and saddle1 surface elements.

The integral of total curvature  $K$  depends directly on the Euler number of the particles ( $K = 4\pi\chi$ ). The Euler number is a topological characteristic, which describes the spatial connectivity and is calculated in the three-dimensional space according to the following equation:

$$\chi = N - C = N + N_{Holes} - N_{Tunnels}, \quad 7.1$$

where  $N$  is the particle number,  $C$  is the connectivity;  $N_{Holes}$  is the amount of holes, which are connected components of the matrix and correspond to concave surface elements, and  $N_{Tunnels}$  is the number of tunnels associated with saddle surface elements. For the convex particle without pores and tunnels the connectivity is equal to 0. In general, the connectivity is always equal to zero when particles, even if they are not convex, are simply connected with each oth-

er. Hence the Euler number is equal to the particle number. On the other hand, for the complete connected network (only one particle)  $N_V$  is much smaller than  $C_V$ , and the number of tunnels (which is equivalent to the presence of saddle surface elements) corresponds to the connectivity [76].

The Euler numbers of the smooth SG1-2, SG1-3 and SG1-4 particles are positive and not equal to 1 due to the small amount of enclosed pores (correlated with concave surface elements) which number exceeds the amount of tunnels. The Euler numbers for SG1-1, TG, CG1 and CG2 (see Table 7.2) particles are negative, which means that the amount of saddle surface elements exceeds the amount of convex and concave surface elements.

### 7.2.1.2 3D SHAPE DESCRIPTION

In addition to the basic characteristics, different shape factors have been determined (see Table 7.4) for all graphite inclusions mentioned above. 3D shape factors  $f_1$ ,  $f_2$  and  $f_3$

$$f_1 = 6\sqrt{\pi} \frac{V}{\sqrt{S^3}} \qquad f_2 = 48\pi^2 \frac{V}{M^3} \qquad f_3 = 4\pi \frac{S}{M^2}$$

can be computed from the parameters  $V$ ,  $S$  and  $M$ . They vary between 0 and 1 comparing the object with a spherical object. While shape factor  $f_1$  can be calculated for any types of complex objects, reasonable estimation of factors  $f_2$  and  $f_3$  can be done only for the simply connected objects (without holes and tunnels). Thus, this shape factors cannot be applied to describe complex particles as analyzed here. Shape parameter  $f_1$  was determined for the particles after filling all impurities (holes). The difference between resulting volume and particle volume represents the volume of impurities  $V_{Fe}$ . (see Table 7.4).

The shape factor 1 compares the particle volume to the volume of the sphere of the same surface ( $S$ ) and thus is similar to the 2D shape parameter sphericity (see Table 3.2). The complex and rugged contour increases the surface of the particle, and thus reduces the value of the shape factor 1. Hence the rugged nodular graphite particles SG1-1 and SG2 have the value of  $f_1$  closer to the values for vermicular (CG) and temper graphite (TG) particles rather than to the smooth nodular particles SG1-2 and SG1-3.

3D shape parameters for “compactness” and “roundness” can be equally deviated from the measured particle 3D characteristics:

$$f_4 = 6\sqrt{\pi} \frac{V}{\sqrt{S_{Convex}^3}} \qquad 7.2$$

$$f_5 = \frac{6V}{\pi d_{max}^3} \quad 7.3$$

They compare only the outer particle contour with the ideal sphere without taking particle spatial connectivity into consideration. Shape factor 6 describes the external convexity of the inclusions. The CG particles are least convex and the smooth SG1-2 and SG1-3 particles are most convex.

Any of the suggested 3D shape parameters differentiates unambiguously the analyzed graphite morphologies providing various information about their roundness, compactness and convexity. 3D analysis permits the full description of the structure in three dimensional space via different particle characteristics.

Table 7.4 Graphite particle shape parameters.

Particle	$f_1 = 6\sqrt{\pi} \frac{V}{\sqrt{S^3}}$	$f_4 = 6\sqrt{\pi} \frac{V}{\sqrt{S_{Convex}^3}}$	$f_5 = \frac{6V}{\pi d_{max}^3}$	$f_6 = \frac{V}{V_{conv}}$	$V_{Fe}, \mu m^3$	$V_{VFe}, \%$	$V_{nucl.}, \mu m^3$
SG1-1	0.21	0.43	0.40	0.46	107	1.22	0.5
SG1-2	0.72	0.65	0.75	0.69	26	0.26	0.2
SG1-3	0.65	0.66	0.70	0.69	45	0.40	0.1
SG1-4	0.50	0.57	0.60	0.60	20	1.04	-
SG2	0.23	0.51	0.39	0.57	153	1.14	339
TG	0.13	0.27	0.25	0.30	37.8	0.05	-
CG1	0.095	0.16	0.14	0.12	35	0.08	12
CG2	0.092	0.10	0.04	0.12	30	0.04	22

### 7.2.1.3 INFLUENCE OF NUCLEUS AND FE-INCLUSIONS ON THE GROWTH MECHANISMS

As it was already shown in the section 7.1.2, nuclei, pores and inclusions have an important influence on the growth mechanisms of the graphite. Nuclei were found almost in every particle. They are composed mainly of MgS, and in the case of the smooth nodules partly enclosed in the sulfides of La and Ce. The radially distributed inclusions in the nodular graphite contain iron. Table 7.4 summarizes the measured volume of the nuclei and inclusions in different graphite particles.

The distribution of the amount of the graphite voxels in 3D with regard to the distance from their nucleus was characterized with the help of the Euclidean distance transformation (EDT). The transformation assigns each voxel the gray value, which is proportional to its distance from the nucleus (or several nuclei) as it is shown on the Figure 7.22.



Figure 7.22 Demonstration of the Euclidean distance transformation (EDT) on one 2D section (CG1). Each voxel obtains a gray value, which is proportional to its distance from the nucleus. The lighter is the gray value; the further away is the voxel from the nucleus.

Assuming that the nucleus is the origin of the particle, the growing process can be characterized with the help of the EDT. Figure 7.23 depicts the distribution curves for three nodular graphite (SG) and two vermicular graphite (CG) particles. With the exception of SG1-1 are the curves for the nodular graphite particles SG1-2 and SG1-3 almost identical. Due to the rough surface of the SG1-1 particle its distribution is somewhat lower to the right of the maximum than the curves for other nodular graphite particles.

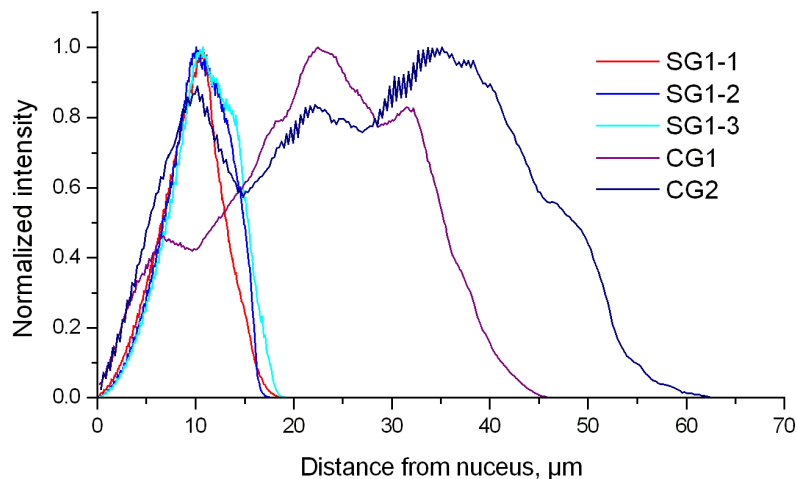


Figure 7.23 Normalized distribution of the intensity of the voxel grey values for different graphite particles. Each grey value corresponds to the distance from the particle nucleus.

The distribution curves for both vermicular graphite particles in the Figure 7.23 follow at the beginning the distribution for the nodular shape, which indicates its initial formation as graphite nodules. Branching occurs due to the local variations of the chemical composition of the melt as well as due to the inclusions, which inhibit the regular graphite growth. The eventually resulting shape is typical for vermicular graphite particles, coral-like. The vermicular graphite particle 1 (CG1) has considerably higher fraction of the voxels belonging to branches

and thus is considerably more complex than the particle CG2. The integration of this distribution curves provides the quantitative characterization of the 3D particle arrangement in regard to their growth mechanisms. The fraction of the vermicular graphite particle 1 (CG1) grown according to the mechanism for spherical particles was determined to be 13 %. 87 % of the particle volume belongs to branches. For the vermicular graphite particle 2 (CG2) this proportion is equal to 22 to 78 %. Thus, level of branching can be characterized by the quotient of the fraction of branches to the fraction of initial nodule: 6.7 for CG1 and 3.5 for CG2.

3D quantitative characterization of the growth mechanisms supports the observation of crystal structure of different graphite morphologies.

#### 7.2.1.4 QUANTIFICATION OF THE SURFACE ROUGHNESS

It has been also shown with the help of distance transformation that the amount of the impurities influences the surface roughness of the nodular particles of about the same size. The volume fraction of impurities is clearly higher in the particle SG1-1 with a rough surface and they are concentrated closer to the boarder of the nodule.

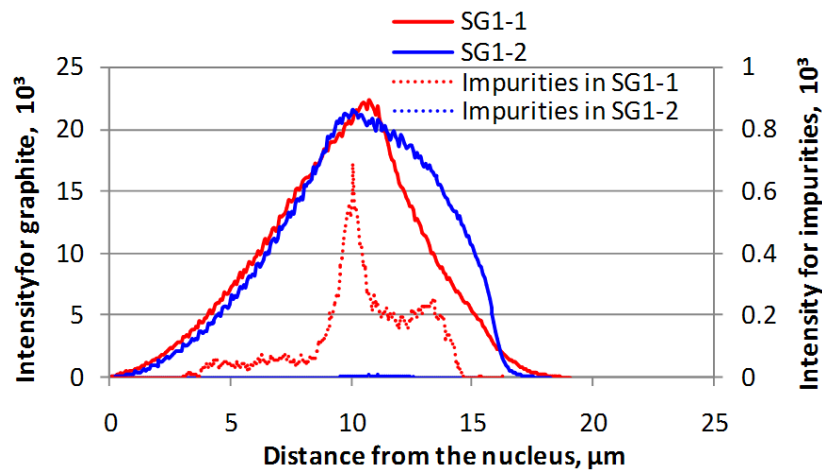


Figure 7.24 The amount of to the particle and impurities (Fe-inclusions and pores) belonging voxels as a function of the distance from the nucleus.

Table 7.5 Particle exterior surface ( $S_{\text{FillHoles}}$ ) and the quotient of the surface after morphological operations to  $S_{\text{FillHoles}}$  used as quantitative characteristics of the surface roughness of the complex objects.

Particle	$S_{\text{FillHoles}}, \mu\text{m}^2$	$S_{\text{Close}}/S_{\text{FH}}$	$S_{\text{Open}}/S_{\text{FH}}$
SG1-1	5819	0.566	0.662
SG1-2	2790	0.967	1.036
SG1-3	3251	0.754	0.787
SG1-4	1191	0.759	0.873
SG2	7393	0.598	0.667
TG	34747	0.801	0.854
CG1	28635	0.862	0.884
CG2	44550	0.911	0.868

The effect of the impurities on the resulting surface roughness of the complex particles was analyzed with the help of the morphological operations. The surface of the particle measured after conducting the operations “close” ( $S_{close}$ ) or “open” ( $S_{open}$ ) is compared to the external particle surface (Table 7.5). The lower the quotient the higher the roughness of the surface. It was found that the surface roughness increases (see Figure 7.25) with increasing fraction of the impurities (see Table 7.4)

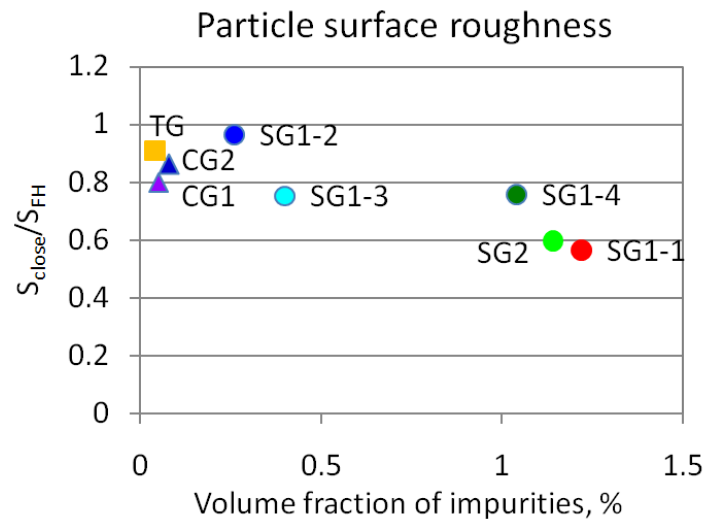


Figure 7.25 The influence of the impurities on the surface roughness of complex graphite particles characterized using morphological operations.

## 7.2.2 ANALYSIS OF THE CONNECTED FLAKE GRAPHITE STRUCTURE WITH THE HELP OF 2D AND 3D FIELD BASED PARAMETERS

Further aim of the study is to characterize the cast iron with flake graphite. The subjective differentiation based on the comparison with standard series images from DIN EN ISO 945 was found to be especially problematic for the following graphite arrangements: A- and C-graphite, A- and E-graphite, D- and E-graphite, B- and D-graphite [155]. The distinction is important as different graphite arrangements can coexist in the sample, e.g. regions of D-graphite can form in the center of the eutectic cell of B-graphite, and thus influence the material properties. In the work of K. Roberts [95] it was shown that the stereological parameters play the main role for distinction between the flake graphite arrangements mentioned above. Parameters found to be especially important were volume fraction ( $V_V$ ) and quotient of the integral of mean curvature ( $M_V$ ) and the specific surface area ( $S_V$ ). These values can be determined not only in 2D with the help of stereological equations [78], but also in 3D using integral geometric methods integrated in MAVI software. Thus, in the following section the

values obtained from 2D and 3D were compared and the discrepancies discussed. Additionally, 3D analysis provides topological characteristics such as connectivity and integral of total curvature ( $K_V$ ), which can explicitly quantify different flake graphite arrangements. These characteristics determined for the materials on the larger scale were found to influence the mechanical properties of, for example, Fontainebleau sandstone [156].

The 3D analysis of the flake graphite (see section 7.1.1.4) has shown that all particles are spatially interconnected with each other, although in a 2D section they may be located completely apart (see Figure 7.26). Hence particle based parameters cannot be used for their characterization. The flake graphite network morphology was characterized with the help of field based parameters (Table 7.6). The analysis was done on two complete flake graphite networks FG1 – IB (Figure 7.10), and FG2 – ID (Figure 7.11). The substantial differences between these two flake graphite arrangements (IB and ID) were determined. The results from 2D and 3D analysis were compared and the estimation of the statistical and systematic error was performed.

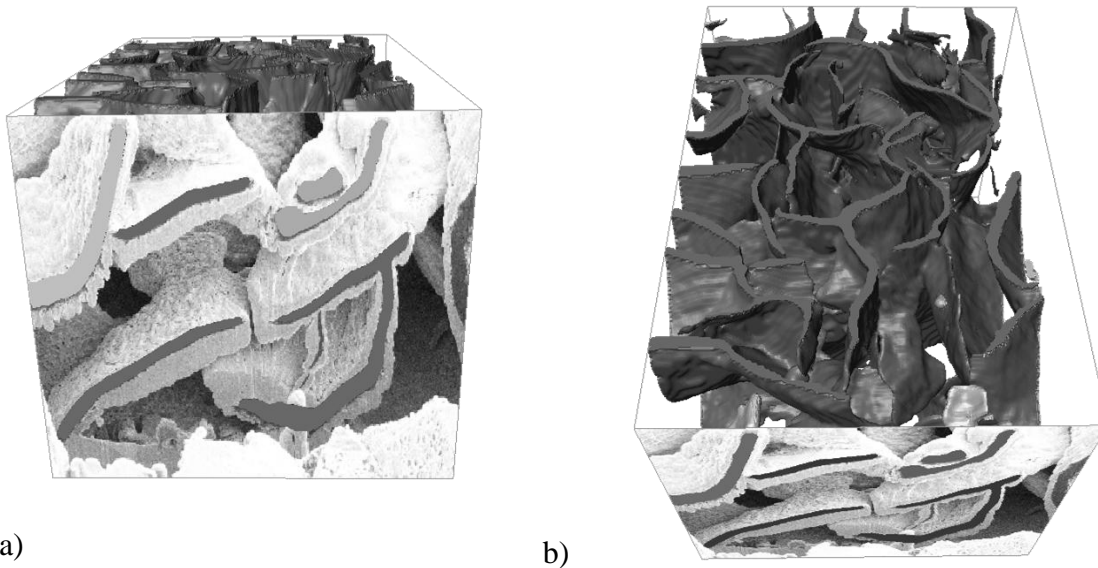


Figure 7.26 a) B-flake graphite particles FG1 in 2D section (xy-plane), b) reconstructed complex network in 3D.

The results acquired from 2D and 3D analysis are summarized in the Table 7.6.

Table 7.6 Field based parameters for the flake graphite arrangements B (FG1) and D (FG2).

Parameter	Analysis	Formula	Flake graphite	
			FG1 – I B	FG2 - I D
$V_V, \%$	2D	$A_A$	$12.78 \pm 2.56$	$8.93 \pm 0.79$
	3D	$V_V$	$12.6 \pm 0.9$	$8.73 \pm 0.39$
$S_V, \mu\text{m}^{-1}$	2D	$\frac{4}{\pi} L_A$	$0.177 \pm 0.033$	$0.39 \pm 0.03$
	3D		$0.188 \pm 0.016$	$0.39 \pm 0.09$
$d_S$			2.12	2.29
$M_V, \mu\text{m}^{-2}$	2D	$2\pi\chi_A$	$0.0157 \pm 0.0045$	$0.142 \pm 0.016$
	3D		$0.0161 \pm 0.0046$	$0.251 \pm 0.033$
$d_M$			1.00	1.02
$K_V, \mu\text{m}^{-3}$	3D		-0.014	-0.319
$\chi_V, \mu\text{m}^{-3}$	3D		$-1.14 \cdot 10^{-3}$	$-2.5 \cdot 10^{-2}$

### 7.2.2.1 VOLUME FRACTION

The volume fraction of flake graphite ID is somewhat lower than that of graphite IB due to the dendrite arrangement of the regions with and without graphite inclusions. Although the determination of the volume fraction with the help of 2D and 3D analysis provides identical results, is the precision of the determination of volume fraction ( $V_V$ ) with the help of 3D analysis significantly higher. Here only one representative spatial image has to be analyzed whereas for 2D analysis large amounts of images have to be taken into consideration in order to achieve accurate results and reduce the standard deviation. The statistical error for the volume fraction in 3D depends on the size and shape of the analyzed structure and is approximated according to the formula [74]:

$$\bar{\sigma}_{statist} \approx \sqrt{\frac{512\pi \cdot V_V^4 (1 - V_V)^4}{S_V^3 V}} \quad 7.4$$

The systematic error depends primarily on the lateral resolution of the characterization method and the image contrast. Due to the high resolution of FIB tomography and excellent contrast between the graphite inclusions and the matrix, the systematic error for the chosen resolution  $0.1 \times 0.1 \times 0.3 \mu\text{m}^3$  for the analyzed system can be neglected. Depending on the size of the analyzed microstructures the effect of the chosen resolution on the measured microstructural characteristics can be considerable (see Figure 7.27).

In the next sections it will be shown how the chosen resolution can influence the results of quantitative analysis and simulations of effective properties of composite materials.

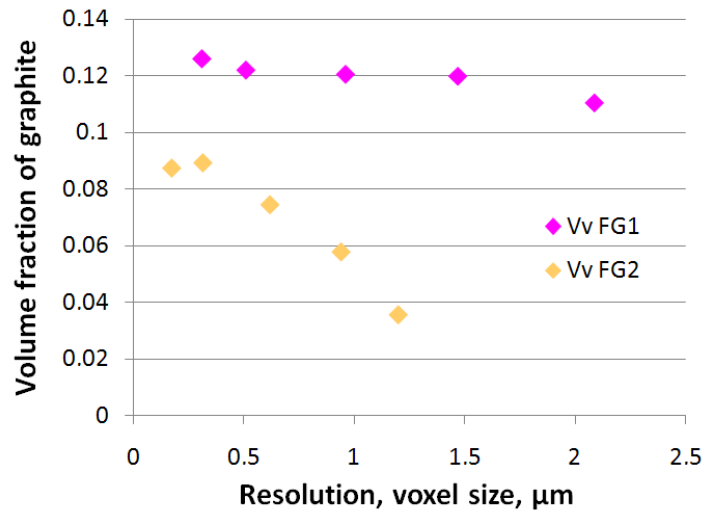


Figure 7.27 Effect of the resolution on the measurement of the volume fraction for FG1 and FG2. Size of the graphite flakes in the sample FG2 is considerably smaller than in the sample FG1. Hence, the effect of resolution is observed earlier.

#### 7.2.2.2 SURFACE AREA DENSITY AND INTEGRAL OF MEAN CURVATURE DENSITY

The inclusions of the flake graphite in cast iron possess the highest specific surface area ( $S_V > 0.1 \mu\text{m}^2/\mu\text{m}^3$ ) compared to other graphite types [84]. The surface area density of the flake graphite arrangement ID is about twice as high as that of the graphite IB. Whereas, is the difference between the values of the integral of the mean curvature of these two graphite arrangements about 10 times. The statistical error of spatial values of  $S_V$  and  $M_V$  can be determined by analyzing parts of the volume of the characterized region, assuming that each of these partial volumes is representative for the analyzed microstructure. Considering the high complexity and interconnection of the flake graphite particles in the relatively small analyzed volume the statistical error cannot be correctly estimated, as the parts of this volume are no longer representative. In order to do so, considerably larger volume, consisting of several representative sub volumes, have to be measured.

The 3D systematic errors were estimated on the images with artificially reduced resolution and thus increased voxel size. The error values for the flake graphite arrangement FG2 – ID are relatively high in comparison with the error values for graphite FG1 – IB and even with the ones determined from 2D analysis. Considering that 2D analysis was performed on the images with the highest resolution, it can be stated that for flake graphite ID the measured microstructural values depend considerably on the chosen resolution. Figure 7.28 represents the measured values of specific surface area ( $S_V$ ) and the density of the integral of the mean curvature ( $M_V$ ) on the 3D images with artificially reduced resolution. The slope characterizes the influence of the resolution, which is significantly higher for the graphite FG2 – ID as for the graphite FG1 – IB.

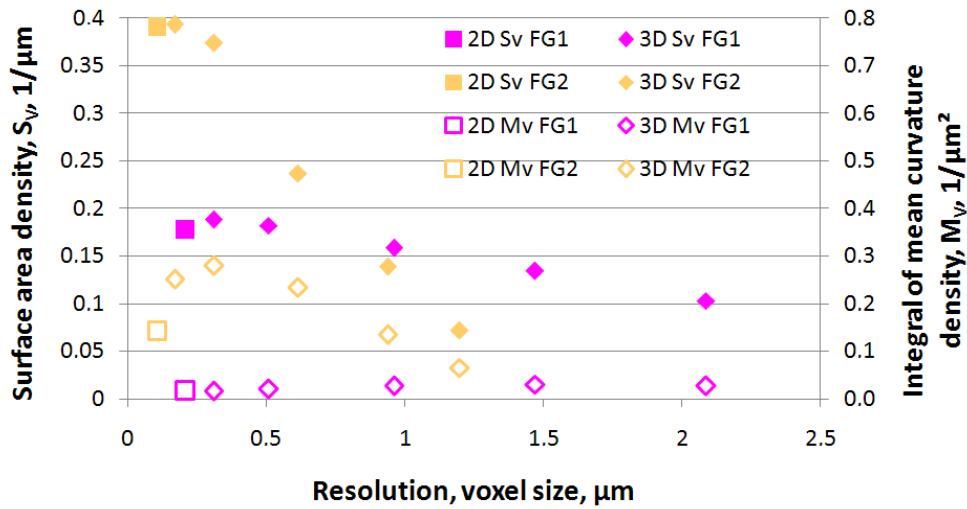


Figure 7.28 Dependence of the specific surface area ( $S_V$ ) and density of the integral of the mean curvature ( $M_V$ ) on the resolution for the flake graphite microstructures FG1 and FG2 (see Figure 7.10 and Figure 7.11).

According to stereological equations  $M_V$  as well as  $S_V$  can be calculated from the 2D images only for the isometric microstructure. From the Table 7.6 and Figure 7.28 it can be seen that for the graphite arrangement FG1 – IB the 2D and 3D values of  $S_V$  and  $M_V$  correspond perfectly with each other. The 2D  $M_V$  value for graphite FG2 – ID is somewhat different from the 3D value. The 2D measurements can be falsified by the local variation of the anisotropy, thus to assure correct results always sufficiently large data sets have to be analyzed. The 3D measurements give directly the correct results. The anisotropy of the microstructure as well as the influence of the resolution was examined here.

### 7.2.2.3 ANISOTROPY AND RESOLUTION EFFECTS

The quantities  $A_i$  and  $L_i$ , measured directly from the image, were used as the most stable quantities to describe the anisotropy.  $A_i$  is the area of projection and  $L_i$  is the length of projection in  $i$ -direction (Figure 7.29). A slight anisotropy was observed, as seen in Figure 7.1. The length of projection was found to be somewhat higher in directions  $[0y0]$ ,  $[xy0]$ , and  $[-xy0]$  which correlates with the slices in different directions from Figure 7.1. For both graphite arrangements, the area of orthogonal projection is homogeneously distributed except for the minor deviation in the  $[0y0]$  direction.

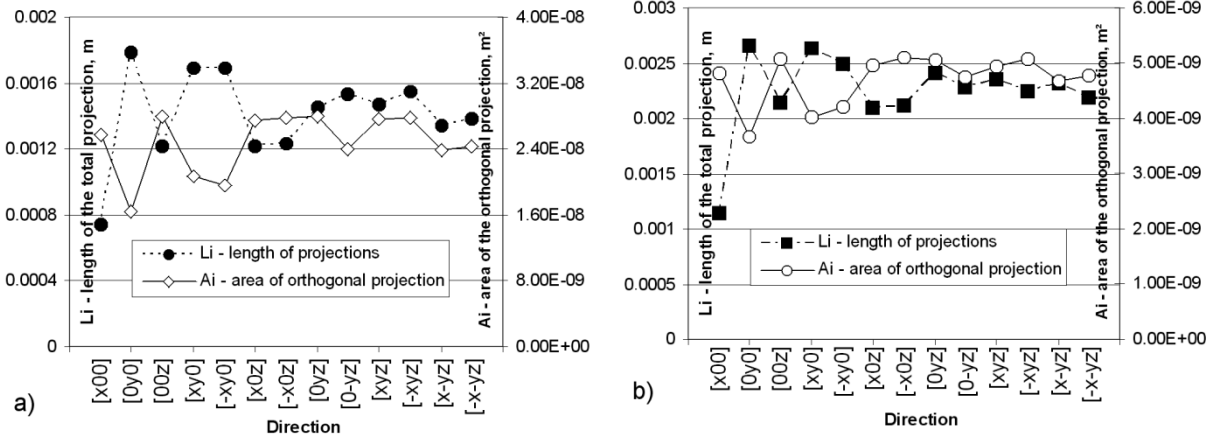


Figure 7.29 Description of the anisotropy of the 3D image. The area of orthogonal projections  $A_i$ , and the length of projection  $L_i$ ,  $i=1, \dots, 13$ , for the graphite lamellas a) IB and b) ID.

As for the graphite IB (Figure 7.10) a very good correlation of  $S_V$  and  $M_V$  values acquired from 2D and 3D was determined, and the measured anisotropy of graphite ID (Figure 7.11) is comparable to that of the graphite IB, we can deduce that the slight anisotropy detected with the help of directional analysis can be neglected. Hence the stereological equations can still be applied for the calculation of  $M_V$  from 2D images. The source of the discrepancy in the values of  $M_V$  measured in 2D and 3D for graphite ID is in the discretization error as already shown in Figure 7.28.

When the features of the structure elements are large with respect to the resolution, then the field features are independent of the lattice distance. Otherwise, they depend on the current resolution. The quantities  $d_S$  and  $d_M$  characterize the influence of the lateral resolution on the measured values  $S$  and  $M$ , respectively,  $2 \leq d_S < 3$ ,  $1 \leq d_M < 2$ . If  $d_S$  and  $d_M$  reach their minimum values, the surface is smooth enough and measured values of  $S$  and  $M$  respectively can be assumed to be robust with respect to small changes of the lattice spacing.

The relatively small values for  $d_S = 2.12$  and  $d_M = 1$  for the graphite IB indicate a low influence of the resolution on the measured values of  $S$  and  $M$ , respectively (see Table 7.6). The higher values of these parameters  $d_S = 2.29$  and  $d_M = 1.02$  for the graphite ID are an evidence of the possible deviation from the true microstructural characteristics.

Figure 7.30 shows the measured values of the fractal dimension for the parameters  $S_V$  and  $M_V$  on the 3D images with reduced resolution. Only the  $d_M$  value for the FG1 is equal to 1 and just for the resolution lower than  $1 \mu\text{m}$ . Thus, the measurement of the  $M_V$  value for FG1 for these resolutions can be considered robust. By the determination of all other  $S_V$  and  $M_V$  values the influence of the resolution has to be taken into account.

Thus it was shown, that the deviation of the 3D field features from the values determined by 2D analysis could be due to the lack of resolution.

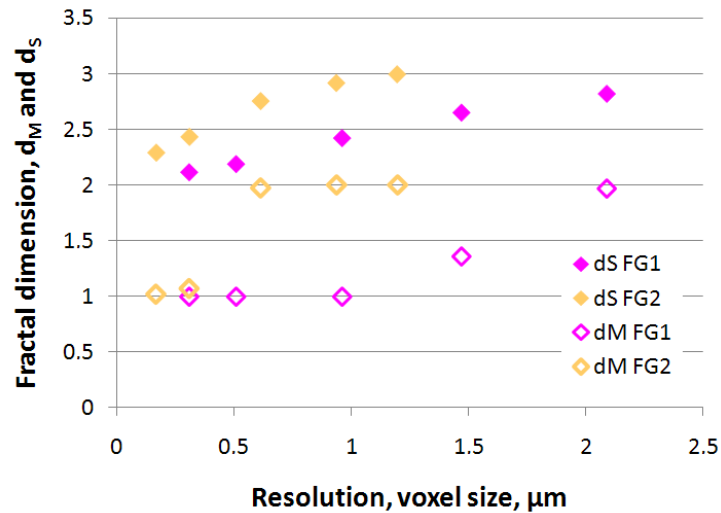


Figure 7.30 Dependence of the fractal dimension  $d_S$  and  $d_M$  on the resolution for flake graphite microstructures FG1 and FG2.

#### 7.2.2.4 DENSITY OF THE EULER NUMBER

The density of the Euler number in ID graphite is about ten times higher than that of the IB graphite. Since in 2D, the sections of almost all graphite lamellas are separated from each other (i.e. 2D connectivity equal to 0), the values of the object density ( $N_A$ ) and the density of the 2D Euler number ( $\chi_A$ ) are in a good agreement for both graphite arrangements. For the graphite IB  $N_A = 0.0026 \text{ 1}/\mu\text{m}^2$  and  $\chi_A = 0.00281/\mu\text{m}^2$  and for the graphite ID  $N_A = 0.0319 \text{ 1}/\mu\text{m}^2$  and  $\chi_A = 0.0323 \text{ 1}/\mu\text{m}^2$ . These parameters do not give any information about 3D particle distribution. All particles which are located separately in 2D sections appear to form a complicated network in 3D as it is shown in Figure 7.26. As a result the object density in the volume ( $N_V$ ) is very low. Volume density of the 3D Euler number ( $\chi_V$ ) is best suited for the description of such structures.

Table 7.7 Measured Euler number for different neighborhoods.

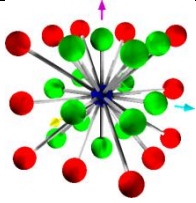
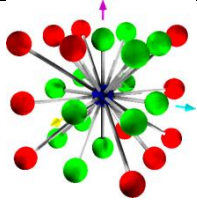
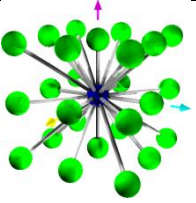
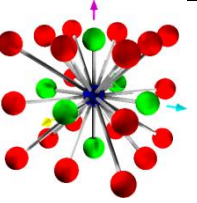
Euler number for:					
		14/1-neighborhood	14/2-neighborhood	26-neighborhood	6-neighborhood
Graphite IB	$\chi$	-612	-1224	-469	-922
	$\chi_V, \text{ 1}/\text{m}^3$	$-1.26 \cdot 10^{-3}$	$-2.53 \cdot 10^{-3}$	$-9.69 \cdot 10^{-4}$	$-1.90 \cdot 10^{-3}$
Graphite ID	$\chi$	-827	-1635	-441	-1280
	$\chi_V, \text{ 1}/\text{m}^3$	$-2.02 \cdot 10^{-2}$	$-3.99 \cdot 10^{-2}$	$-1.08 \cdot 10^{-2}$	$-3.13 \cdot 10^{-2}$

Table 7.7 shows that experimental values for  $\chi_V$  can depend highly on the chosen neighborhood. More details about this effect can be found in [128], [157], [158]. In this study the 14/1 neighborhood was used to calculate the Euler number and the integral of total curvature density ( $K_V$ ) (Table 7.6). Ohser et al. [128] has shown that it is not possible to choose an optimal adjacency. For practical applications the Euler number should be measured with respect to several neighborhoods. The bias of the measurements can then be judged by the difference between those results.

All these 3D structural parameters build the basis for the characterization of different graphite morphologies. They establish the first foundation for the quantitative understanding of materials properties.

### 7.3 ANALYSIS OF 2D SECTIONS THROUGH RECONSTRUCTED 3D MODELS

The graphite particles analyzed in 3D have very different 3D parameters which are specific for the respective type:  $V$ ,  $S$ ,  $M$ ,  $K$ , as well as the shape parameters; thus different graphite morphologies can be clearly distinguished from each other. However, as for the classical polished sample, only the 2D sections are available, identifying the respective graphite type prospectively has to be possible by means of its 2D sections.

Statistically orientated and positioned numerous 2D planes (i.e. „virtual sample surface“) have cut the reconstructed 3D particles. The frequency and shape of the thus obtained, virtual 2D sections have been analyzed for the improvement of the graphite 2D classification.

It was found that the mean amount of intersections of one plane with the coarse nodular particle ( $4.0 \pm 2.1$ ) exceeds the mean amount of intersections of the plane with the smooth nodular particle ( $1.3 \pm 0.6$ ). For the convex object this value is always equal to 1. Temper graphite (TG) which looks like a compact agglomerate of the numerous smaller irregular particles and has a large amount of relatively large pores from the intersection with a plane gives, in average,  $5.3 \pm 4.1$  individual 2D intersections. Each of them is considered to be a separate particle in the 2D analysis, thus creating a significant bias which influences the interpretation of structure-property correlations. Vermicular graphite particles (CG) appear to be coral-like with large, flat, rounded branches. Though less compact and convex than temper graphite they still have the same value of mean interceptions with the plane ( $5.2 \pm 2.6$ ).

Through the simulation of the virtual cuts through the 3D reconstructed particles of the D-flake graphite (FG2) more than 4,000 2D objects were generated and analyzed in 2D. Most of these 2D sections form two large and complex networks in 3D (Euler number equal to -315 and -390) (see Figure 7.11). The amount of the small separate 3D particles which, for exam-

ple, have been cut by the border, is approximately 250. For B-graphite (FG1) 2,700 2D sections have been characterized, which in 3D form just one big object with high connectivity (Euler number = -574) and about 50 much smaller inclusions (see Figure 7.10 and Figure 7.26). Due to the high interconnection of the flake graphite planes no correlation between amount of the 2D sections per unit area and the particle volume density can be stated.

In the case of the not connected nodular, vermicular and temper graphite such correlation is conceivable but requires the measurements of statistically large number of different graphite particles. In this study the main goal was to describe the variety of shapes of 2D sections through the 3D particle and thus to improve the graphite classification of the conventional 2D polished sample.

### 7.3.1 SIZE-SHAPE DEPENDENCY AND COMPARISON WITH 2D ANALYSIS

These obtained 2D cross-sections have been analyzed with the help of the software package a4i. Using particle based methods all relevant 2D particle parameters have been acquired including the shape parameters (roundness and compactness) which are used for automatic 2D classification of graphite morphology (see section 6.1). The relative frequency distribution of the roundness and compactness of 2D cross-sections derived from the 3D model is consistent with the results from 2D images (Figure 7.31). The area weighted mean value of roundness and compactness for flake graphite are  $0.10 \pm 0.03$  and  $0.19 \pm 0.05$  respectively, for vermicular graphite –  $0.32 \pm 0.07$  and  $0.47 \pm 0.09$ , and  $0.47 \pm 0.09$  and  $0.64 \pm 0.09$  for the graphite in malleable cast iron. For nodular graphite the shape parameters are larger and, depending on the morphology, approach the value for the ideal circle (= 1). Obviously the values for the rugged particle number 1 (SG1-1) and smooth particles 2 (SG1-2) and 3 (SG1-3) (see Figure 7.2a) are significantly different: roundness  $0.55 \pm 0.15$  vs.  $0.79 \pm 0.11$  and compactness  $0.71 \pm 0.14$  vs.  $0.91 \pm 0.07$ , respectively.

The relationship between the size of 2D particle cross-sections and the value of different shape parameters (e.g. compactness) was investigated for each graphite morphology and compared to the values from 2D cross-sections prepared by conventional metallographic methods (Figure 6.6). In the analyzed particle size range from 0 to 80  $\mu\text{m}$ , results obtained from 3D reconstruction and from 2D image analysis are entirely consistent with each other (Figure 7.31a and b).

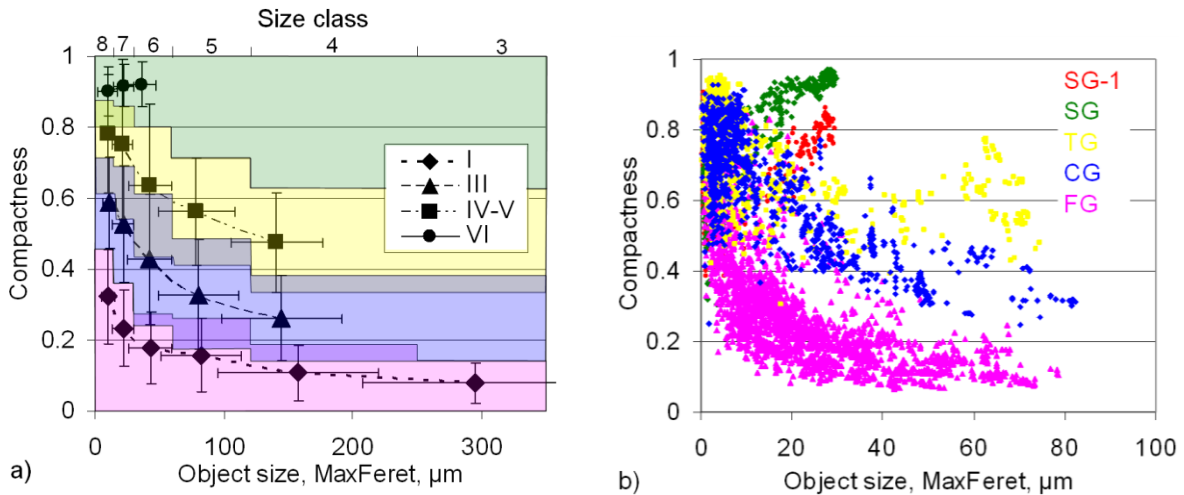


Figure 7.31 a) Shape-size dependence for graphite cross-sections from 2D images; b) Compactness of the 2D cross sections through the reconstructed 3D particles.

The existing classification scheme (see chapter 6) allows an easy distinction between flake and vermicular graphite in 2D cross-sections. Sections through the graphite in malleable cast iron, smaller than  $30\ \mu\text{m}$ , exhibit a great scatter of the shape parameter values. This leads to a relatively large overlap for different graphite morphologies as shown in Figure 7.31. As long as nodular graphite particles have a smooth surface, the previously mentioned shape parameters can be successfully used for graphite classification. The shape parameters of the 2D cross-section through the nodular particles with a rugged surface are located between those for nodular graphite and the temper graphite in malleable cast iron. From the diagram it is clear that small cross-sections ( $< 15\ \mu\text{m}$ ) for all graphite types cannot be unambiguously classified. For all graphite morphologies analyzed in this work, particles with cross-sections smaller than  $15\ \mu\text{m}$  had volume fractions between 5 and 10 %. As demonstrated above, this fact restricts the accuracy of the classification method suggested before.

### 7.3.2 IDENTIFICATION OF THE LIMITS OF 2D CLASSIFICATION

All 2D cross-sections through the investigated particles have been classified with the method developed in chapter 6 in order to be able to estimate the precision. The results are summarized in the Figure 7.32.

About 80 % of the 2D cross-sections through the flake (FG) and vermicular (CG) graphite particles were classified correctly. Less than 20 % were assigned to other graphite morphologies due to their shape parameters. Area of the 2D sections through the temper graphite particle (TG) which were classified as graphite type IV-V composed 71 % of the total graphite area. Smaller sections near the border of the particle were often assigned to vermicular graph-

ite type III (8 %) whereas sections through the middle of the particle were classified as nodular graphite type VI (21 %, Figure 7.33).

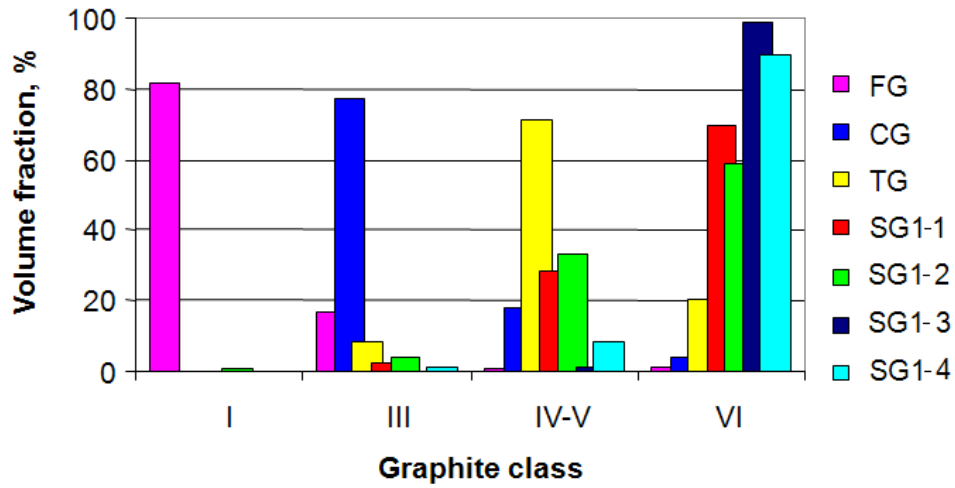


Figure 7.32 Area fraction of the 2D cross-sections through the 3D graphite particles, classified as respective graphite type.

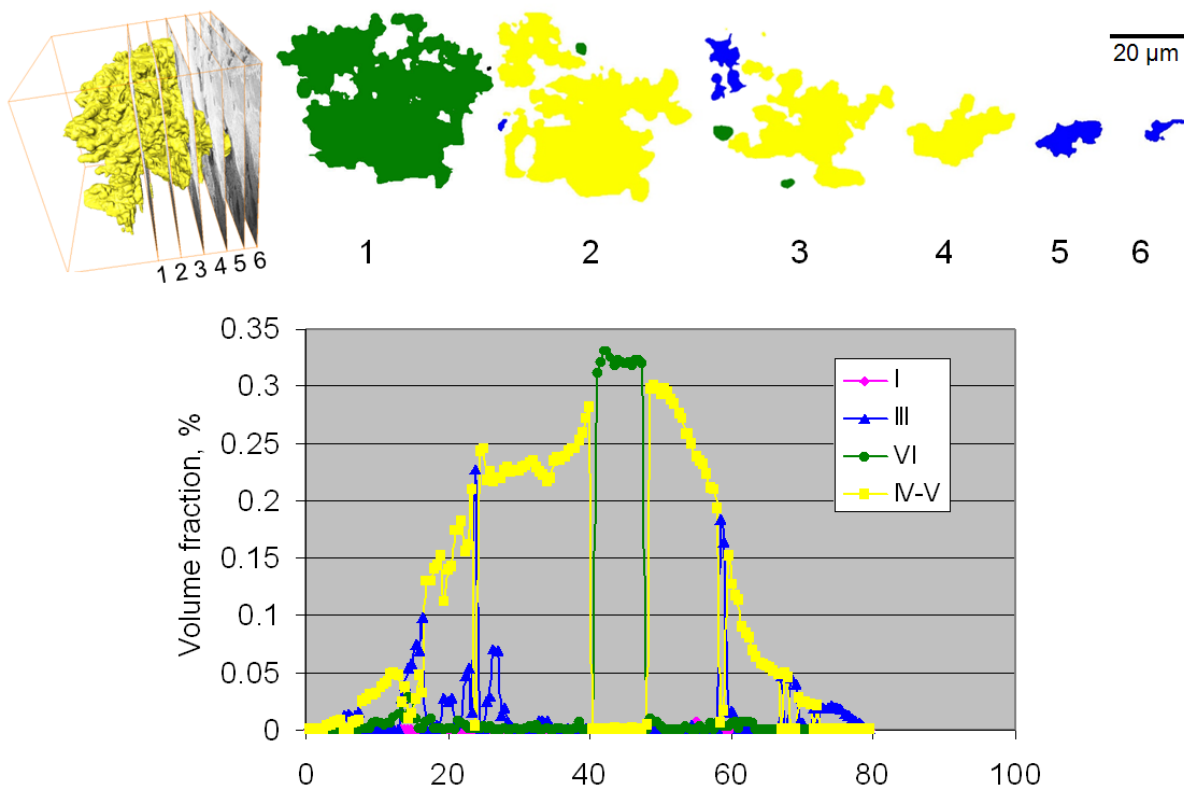


Figure 7.33 Results of the classification of 2D sections through the 3D reconstructed temper graphite particle. The outer small sections do not carry comprehensible shape information (comments in text).

The latter effect results from the compact shape of the middle part of the temper graphite. However, this particle shows relatively large pores, and thus possesses a distinctive difference from real nodular particles. Hence, the introduction of new parameters, e.g. the Euler number

(which characterizes the amount of pores in 2D-sections), can significantly improve the classification. In addition, as shown above, an incorrect classification arises in the case of small cross-sections ( $< 15 \mu\text{m}$ , Figure 7.31b) near the rim of large particles.

Ninety-nine percent of the area of all cross-sections through the nodular particles No. 2 and No. 3 (see Figure 7.2a) were classified as nodular graphite type VI. In the case of the more irregular particles No. 1 and No. 4 the area fraction of nodular graphite is only 70-75 %. This relatively large variation in the area fraction shows that the existing classification method is very sensitive to even slight shape variations.

It can be clearly seen, that for the smaller 2D sections, which appear by the sectioning of the 3D graphite particle near their border, the values for the shape parameters strongly overlap for different graphite types. It means that perceptively for the large amount of the 2D sections (the ones that are smaller than about 20 % of the particle size) no clear assignment to the certain graphite morphology should be made. The area fraction of such sections is depending on the graphite type 5-10 %. For the volume fraction of the graphite inclusions of 10 % it means only 0.5-1 %. This error cannot be avoided during the classification of the 2D sections.

The 3D characterization of the complex graphite particles has also shown that the additional parameters can considerably improve the existing 2D classification. They should take into account not only the outer shape and the surface roughness, but also the internal particle structure as for example Euler number, which in 2D describes the connectivity of the particle and the amount of “pores”.

#### 7.4 SUMMARY AND APPLICATIONS OF THE 3D RESULTS

FIB nanotomography was successfully used for the analysis of different graphite morphologies in cast iron with high resolution (down to  $0.1 \mu\text{m}$ ). With the help of 3D reconstruction and analysis software it was possible to visualize and study complex graphite particle morphologies and quantitatively characterize their geometry, shape, and connectivity. In addition to the common parameters of volume and surface area, the integrals of mean and total curvature and the 3D shape factors describe and unambiguously differentiate various graphite morphologies as well as their subtypes:

- smooth spheroidal graphite particles possess a characteristic value of Euler number  $\chi \geq 1$ , the integral of mean curvature is generally  $M < 0$ , only due to the small amount of pores;
- ragged spheroidal particles have  $\chi \ll 0$  and  $M \ll 0$ ;
- complex temper graphite particles have  $\chi < 0$  and  $M > 0$ , and

- complex vermicular particles possess  $\chi < 0$  and  $M \gg 0$ .

Clear quantitative characterization of two flake graphite arrangements was done using the 3D field features. The comparison of the 2D and 3D parameters has shown that the employed algorithms (MAVI) for the calculation of the 3D field features can be successfully applied for the spatial images with anisotropic voxels, which are characteristic for FIB tomography. The interpretation of the image anisotropy in consideration of the existence of the resolution effect is not obvious and continues to be the subject of further studies. Due to the high spatial connectivity of flake lamellas, each 2D plane cutting the network generates a large number of sections, which are considered individually in 2D and thus cause the high particle number per area ( $N_A$ ). The Euler number ( $\chi_V$ ) considers the object connectivity and thus is best suited for the description of highly connected microstructures such as flake graphite networks.

Particles integral of total curvature  $K$  (or  $\chi$ ) is the independent characteristic of spatial connectivity and has been acquired for the first time for graphite inclusions with the help of 3D research. Being the fourth degree of freedom it provides together with  $V$ ,  $S$ , and  $M$ , which can be already acquired from the 2D analysis, unambiguous identification of different graphite types. And thus contributes to the essential improvement of the classification of the complex graphite particles.

The new knowledge acquired with the help of the three dimensional analysis is of particular importance for materials science and can serve as the basis for modelling and simulation of the materials properties such as e.g. thermal conductivity ( $\lambda$ ). Here, the strong increase of the  $\lambda$  for cast iron with flake graphite morphology in comparison to cast iron with nodular and vermicular graphite cannot be explained only by the 2D shape of graphite inclusions. The perfection of the crystal structure reasonably correlated with curvature values and the three-dimensional interconnection of the highly conductive graphite phase is in all probability responsible for the considerable change in macro-properties. And as nowadays the foundries are able to control quite precisely the graphite morphology and even produce the functional gradient microstructures by the adjustment of local chemical composition of melt and processing, the exact tailoring of cast iron properties can be achieved.

#### 7.4.1 DEVELOPMENT OF ON-LINE POCA APPLICATION

The new knowledge about different graphite morphologies has served as the basis for the on-line available characterization and classification system named Particle-Oriented Classification and Analysis (POCA). Through the cooperation with Max-Planck-Institute für Informa-

tik, Saarbrücken the freeware was developed for the classification of complex graphite types with the help of the support vector machine [159].

#### 7.4.1.1 SUPPORT VECTOR MACHINE (SVM) AND CLASSIFICATION PARAMETERS

The support vector machine employs simultaneously the big amount ( $m$ ) of the image analytical parameters for the automatic categorization of the graphite particles. In principle these  $m$  parameters are used to position each particle in the  $m$ -dimensional space. The local accumulation of the particles in this  $m$ -dimensional space due to their similarity is then the basis for the categorization, even if the accumulations are not completely isolated and (partly) overlap. The support vector machine calculates the optimal  $m-1$ -dimensional hyper plane, which separates the individual local particle accumulation, so that

- on one side as much as possible particles *belonging* to the accumulation are included (in Figure 7.34 the (+) particles – so-called “recall” in data mining) and
- on the other side as much as possible particles *not belonging* to the accumulation are excluded (in Figure 7.34 the (–) particles – so-called “precision” in data mining).
- Additionally, using so known soft separation ( $\delta$ ) and thus measuring the distance from each particle to the hyper plane the *probability* can be calculated to which each particle belongs to the certain class (see also Figure 7.36).

The basis for this pure empirical classification strategy is next to the knowledge about the presumably relevant image analysis parameters also the sufficiently large training data set, which in our case was at disposal from the previously analyzed 2D sections through the real 3D particles acquired with the help of FIB-tomography.

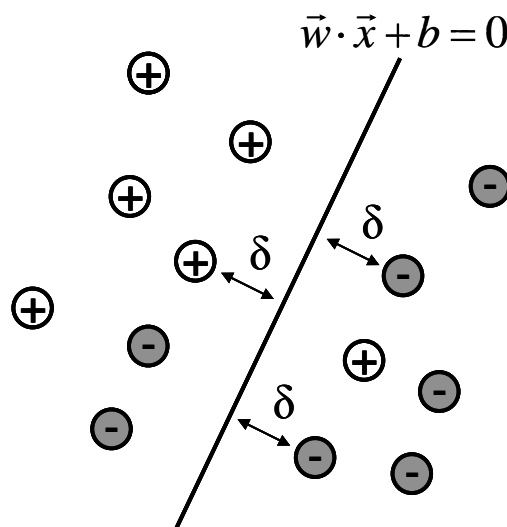


Figure 7.34 Positioning of the particles according to their  $m$  parameters in the  $m$ -dimensional space. Classification occurs through the calculation of the separating hyper plane in the  $m$ -dimensional space from the training data (comments in text).

Altogether 15 characteristic microstructure parameters (see Figure 7.35b under „Features“) were used for the automatic classification of the graphite types. The individual shape parameters were calculated from the basic characteristics and together with size class (particle size according to DIN EN ISO 945) and magnification (pixel size, see section 6.2.3) were employed as the classification parameters.

#### 7.4.1.2 SENSITIVITY ANALYSIS AND CLASSIFICATION ACCURACY

The prototype of the web-application, POCA (see [www.materialography.net](http://www.materialography.net)), was developed during the work (Figure 7.35a). The microstructural images can be uploaded, analyzed and classified with the web-interface. The classification occurs according to the models, i.e. already calculated hyper planes in our case in 15-dimensional space of the employed parameters with the help of the training images [159].

Homogeneous training images were also used for the evaluation of the classification accuracy. More than 1000 particles per graphite type were classified with different models and classification parameters. Thus, it was possible to acquire quantitative evaluation of the classification accuracy (Precision and Recall) for different already existing models. This work has shown that the classification with the help of the support vector machine provides very good results. High classification accuracy of 95 % was attained for the present test data.

The essential role of this work was next to precise classification also the estimation, which of the 15 used particle parameters carries especially great weight for the graphite categorization. The features, which with the help of sensitivity and factor analysis proved to be especially important in respective models, are emphasized in bold (Figure 7.35b).

#### 7.4.1.3 RESULTS OF THE ON-LINE CLASSIFICATION

The POCA web-interface offers next to the classification and training also the possibility for the global analysis of all parameters and particles of the certain type. The properties of the classification models and the employed features are described to the user on the overview pages. More detailed information can be found in the user manual accessible over the website [www.materialography.net](http://www.materialography.net).

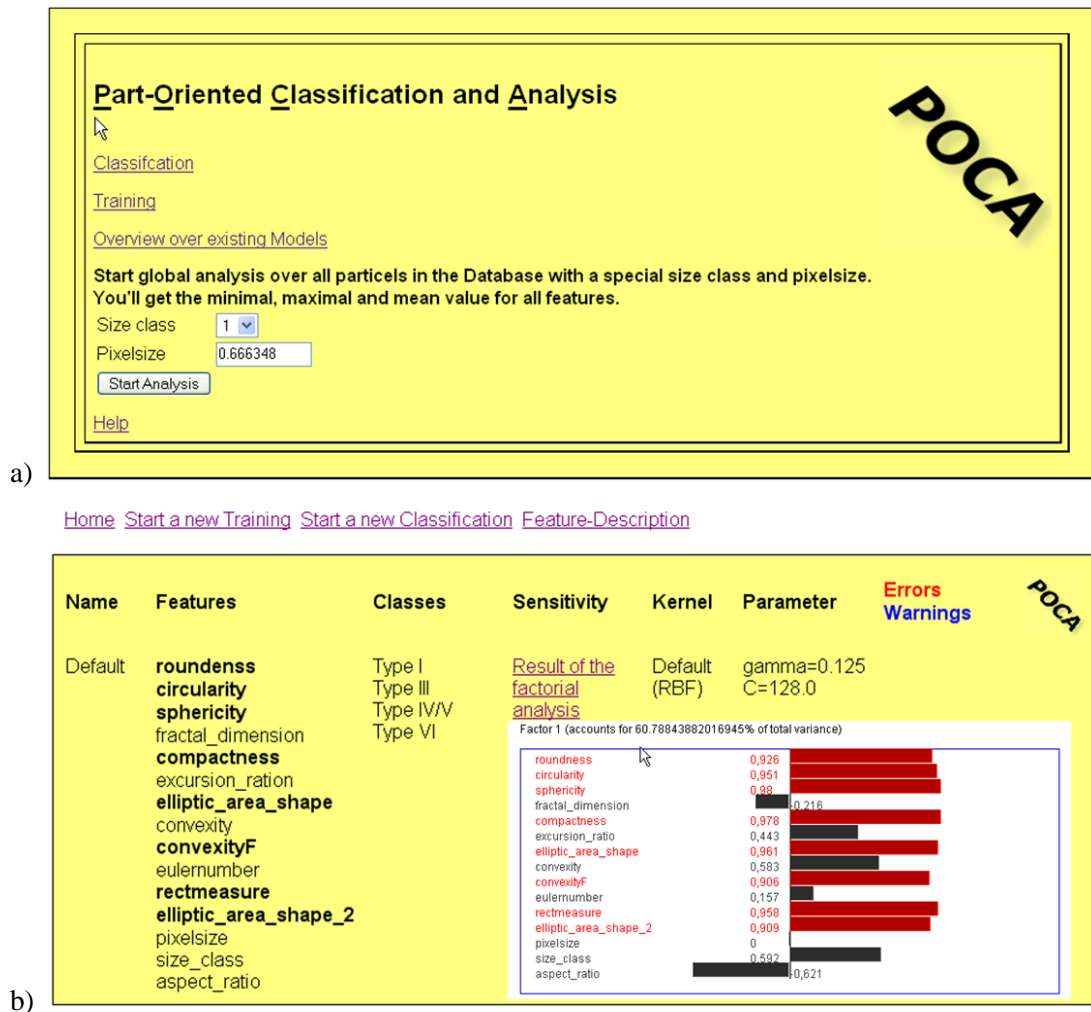


Figure 7.35 a) POCA web-interface and an access to classification, training and overview of the existing models, b) a model for the classification of the graphite morphology (Default model offered by web-interface).

The home page of POCA (Figure 7.35a) provides next to the links to classification and training in the bottom part the global feature analysis. Here one can perform the evaluation of the individual parameters (minimum, maximum, mean value and standard deviation) for the particles of certain size class and the images of the certain magnification (certain pixel size). The images uploaded by user will be classified according to the created models. The representation of the results can be chosen to be graphic or in detail for all particles (see Figure 7.36). Otherwise the user obtains only the written information of how many percent of each graphite type is present in the microstructure. Additionally, in both cases the overview over all particles and their parameters can be downloaded in the Excel-compatible format. In this summary it can be also seen, with which probability and according to which characteristic microstructural parameters are the particles assigned to respective graphite type (Figure 7.36).

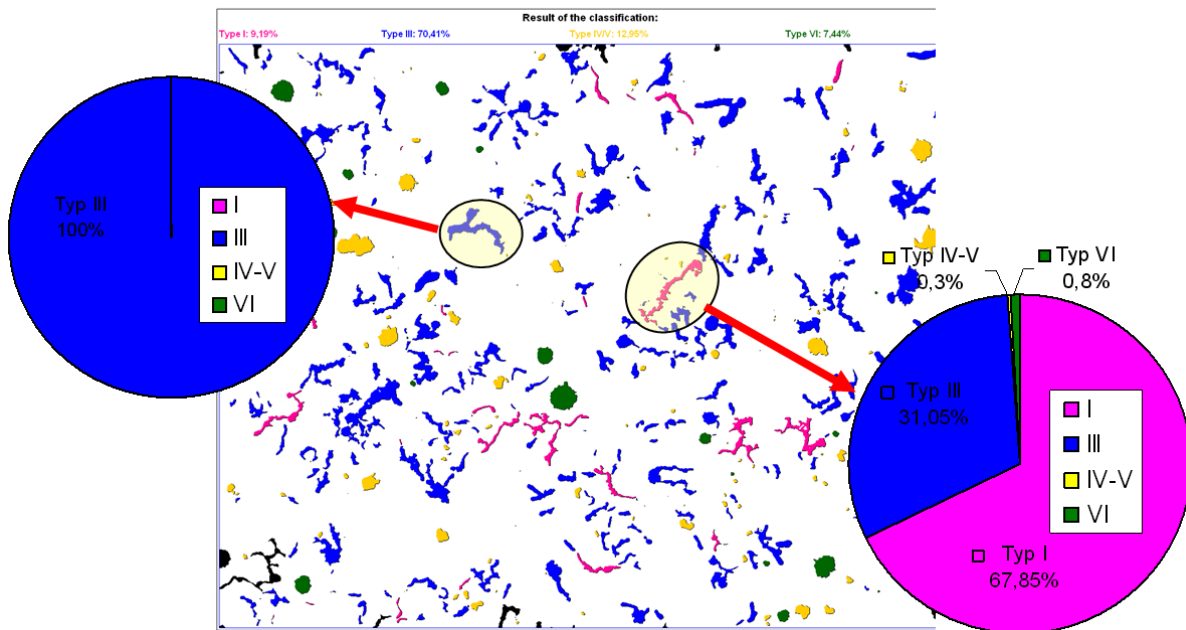


Figure 7.36 Results of the online classification with the help of support vector machine.

The developed prototype of the application, POCA, is designed so, that one can experiment with it in an easy way. The classification parameters can be excluded by training and/or by classification or the SVM adjustments can be modified.

#### 7.4.2 SIMULATIONS OF PHYSICAL PROPERTIES AND COMPARISON WITH EXPERIMENTAL RESULTS

Knowing the considerable influence of the graphite morphology on the resulting cast iron properties, and estimating the properties of the individual microstructure constituents (Table 9.3) from their chemical composition (see section 2.3.2.2 and appendix 9.1) and crystallographic structure (see section 7.1.2 and appendix 9.5) the attempt was done to find the simple microstructural model and to conduct finite element simulations. If the results of the simulation correlate well with the experimental results, the suggested microstructural model could be used to estimate the variety of different properties of cast iron. The results of the simulations were compared with experimental values of the electrical conductivity as well as with the literature values for the thermal conductivity.

##### 7.4.2.1 DEPENDENCY ON PARTICLE SHAPE AND SIZE

For the estimation of thermal and electrical properties of cast iron, it was presented as a composite material with pearlite matrix and 100 graphite inclusion (representing 10 % of the total surface fraction,  $V_V = A_A = 10\%$ ). Different graphite morphologies were represented by ellipsoids with different shape described by shape parameters: compactness between 0 (for flake

graphite) and 1 (for nodular graphite). Graphite particles were generated parallel and orthogonal to the flux direction. Considering the isotropic distribution of the particles the resulting effective properties can be approximated by the mean values. The results for thermal conductivity were compared with literature values [32] (see Table 2.2) as shown in the Figure 7.37a. Figure 7.37b presents the results of the 2D simulation of electrical resistivity and comparison with experimental results (see chapter 5).

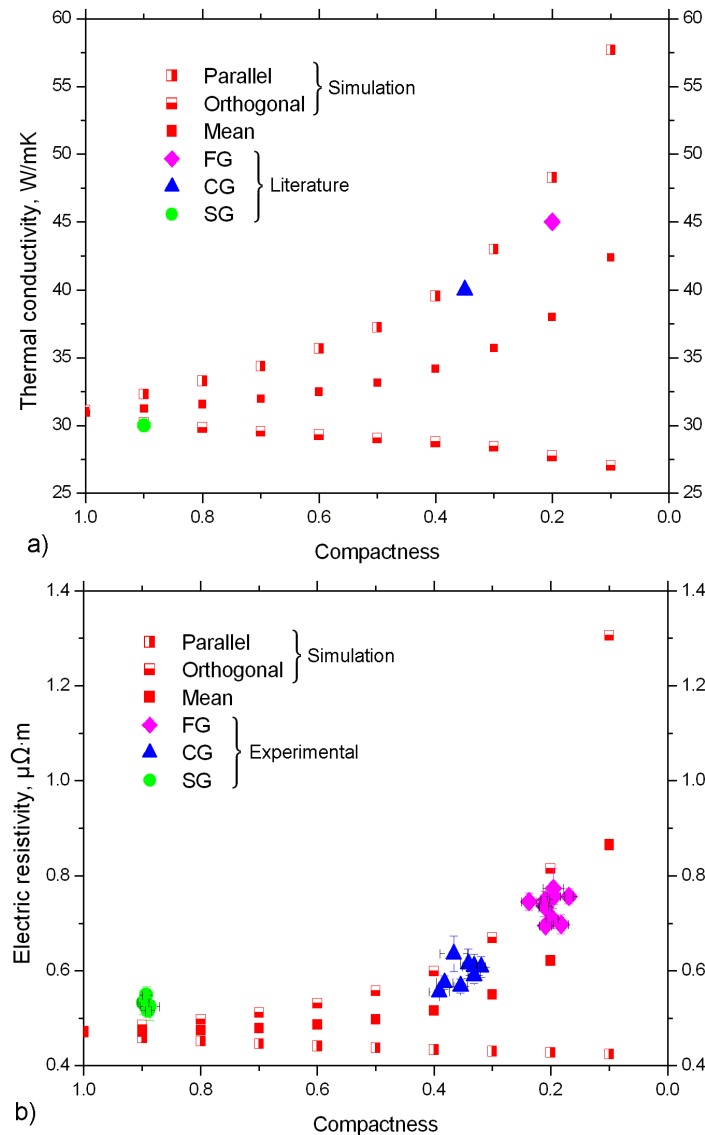


Figure 7.37 Comparison of a) thermal conductivities and b) electric resistivity obtained from 2D simulations with literature values [32] and experimental results (see chapter 5).

The simulation considers not only volume fraction ( $V_V$ ) of graphite but also its shape, which correlates with the microstructure basic characteristic  $S_V$ , and variable properties of the graphite inclusions in accordance with their crystallographic structure. Thus, the tendency of the

mean curve for both properties corresponds very well with the predictions in the literature (see Figure 2.11, [35]) and the experimental results.

When graphite particles having considerably higher thermal conductivity are oriented parallel to the flux, the heat transport occurs predominantly through the graphite along the  $a$ -crystallographic direction. In the orthogonal case graphite particles have lower conductivity (in  $c$ -crystallographic direction) in comparison to pearlite and thus reduce the effective thermal conductivity of the composite.

The results of the simulation correspond good well with the thermal conductivity of cast iron with randomly distributed graphite nodules. On the contrary, the literature values for cast iron with vermicular and flake graphite are considerably higher than the mean simulation results, approaching the parallel case.

In case of the electrical conductivity flake graphite inclusions oriented perpendicular to the flux serve as a considerable obstacle on the way of the electrons and thus increase drastically the electrical resistivity of the cast iron. The mean value of two simulated extreme cases again underestimates the effect of the complex vermicular and flake graphite inclusions.

No decisive variations have been observed when performing simulations with varying number of graphite particles and thus, for the constant volume fraction, varying graphite size for constant particle shape. For this 2D model effective properties seem to be independent from particle density which correlates with the integral of the mean curvature ( $M_V$ ). Although somewhat similar results have been observed for the experimental values of electrical conductivities (see Figure 5.1c and d) the statistically low amount of analyzed samples does not allow drawing such conclusion and further analysis is required.

Thus, it was shown that the 2D model provides efficient approximation for the microstructure composed of simple not interconnected particles (e.g. nodular graphite) and underestimates the effective values of thermal conductivity and electrical resistivity for the microstructures with complex interconnected phases (vermicular and flake graphite). The reason for this discrepancy with the experimental values for cast iron is the consideration of only two-dimensional information in the simulated model. As it was already shown in this section with the help of three-dimensional analysis, each of the graphite morphologies is characterized not only by particle shape and size but also by connectivity, which is specific for each type. Thus, this fourth basic characteristic ( $K_V$ ) which provides the information about the spatial arrangement and interconnection of complex graphite particles has to be included in the estimation of the effective properties of cast iron.

## 7.4.2.2 DEPENDENCY ON THE CONNECTIVITY OF THE STRUCTURE

The performed tomographic analysis on the cast iron made it possible to realize the 3D simulations on the real data sets with the help of the GeoDict software (Fraunhofer ITWM). Two 3D images of cast iron with flake graphite (FG1 and FG2) acquired with the help of FIB-tomography were used to estimate the effective properties.

The 3D simulation software does not allow the integration of the anisotropic properties of phases. Thus, the approximation of the graphite conductivity was done. As it was shown before, flake graphite grows in the *a*-crystallographic direction and approaches the ideal hexagonal graphite structure more than any other graphite type. Knowing, that for the cast iron with flake graphite morphology heat transport occurs mainly through the graphite flakes, the highest graphite conductivity (Eq. 9.7) was chosen for simulation of thermal properties. On the other hand, flake graphite having the lowest electrical conductivity of all microstructure constituents serves basically as an obstacle for the electrical flux. Thus, the highest electrical resistivity of the graphite (Eq. 9.8) was chosen for the simulation of electrical properties. To estimate the effective graphite properties the simulations were performed for three different values calculated using  $C = 0.2$ ;  $0.1$ ; and  $0$ .

The other parameter, which considerably influences not only the correct microstructure characterization, but also the simulation of the material properties, is the resolution of the spatial images. If not a sufficiently large amount of voxels is used to describe a pore or object, the object characterization can be wrong. There will be not enough voxels to generate the reliable field of currents and thus to perform the correct simulation. Thus, the examinations are required, in order to determine the sufficient resolution for the simulation.

The influence of the resolution on the simulation of the effective properties was studied on images with artificially reduced resolution, and thus the size of the analyzed volume. The reduction of the size of the simulated volume is often longed for, as the time required for simulation reduces and thus the efficiency rises. The resampling was realized with the help of the Amira software. Figure 7.38 shows that the reduction of the resolution influences though considerably the quality of the image; discretization effect is clearly seen on the reconstructed surfaces (Figure 7.38a and b). Starting from a certain point, where the fractal dimension of the integral of the mean curvature exceeds its minimum value 1 (compare Figure 7.30), the resolution is so low, that the thin flakes cannot be correctly represented any more (Figure 7.38c and d), which leads to the loss of the microstructural information. The influence of the resolution on the measured microstructural characteristics was already shown in the section 7.2.2.

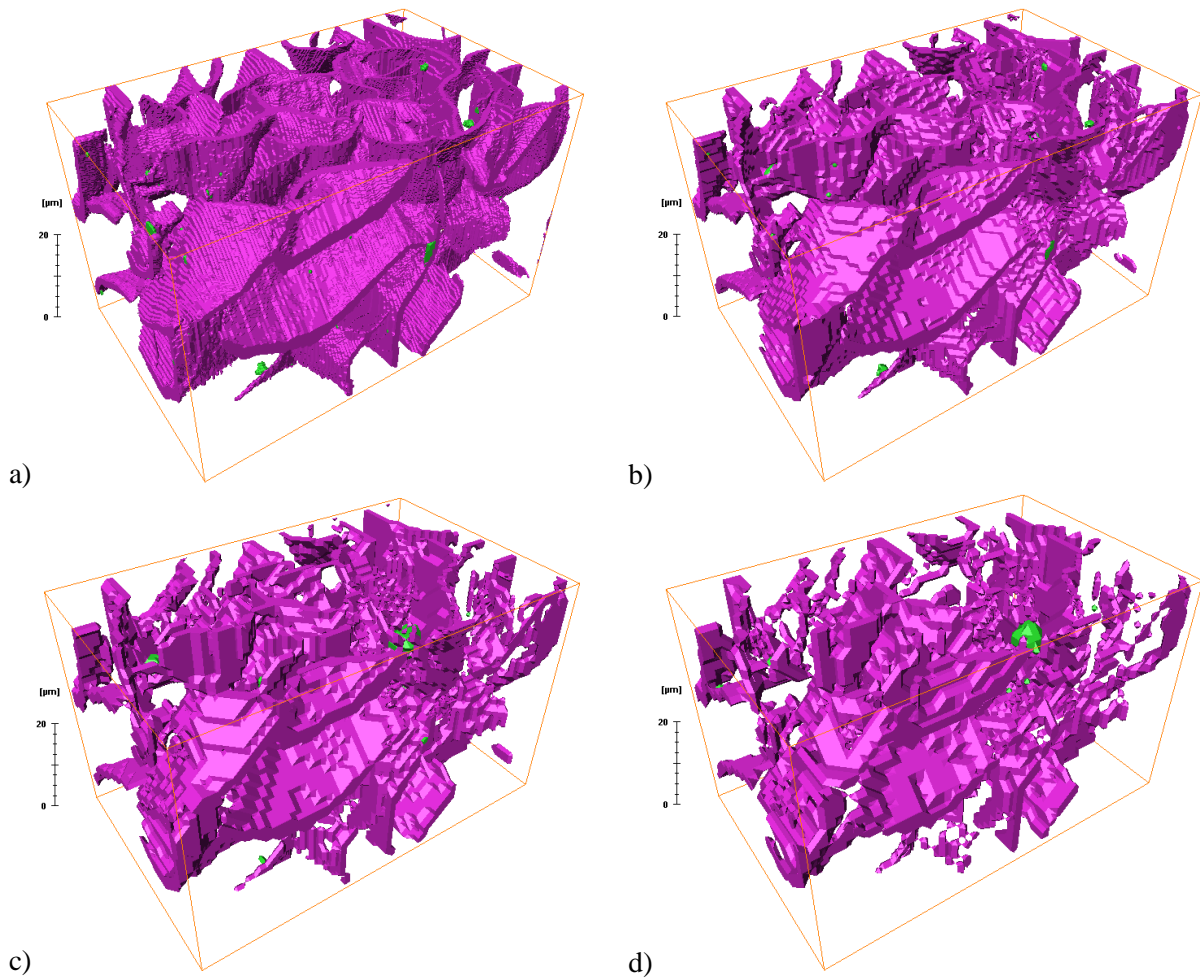


Figure 7.38 Flake graphite particles FG1 a) original image, voxel size  $0.18 \times 0.24 \times 0.5 \mu\text{m}^3$ , b) 5/4/2 resample, voxel size  $0.96 \mu\text{m}^3$ , c) 8/6/3 resample, voxel size  $1.47 \mu\text{m}^3$  and d) 11/9/4 resample, voxel size  $2.06 \mu\text{m}^3$ .

The results of the simulations of the effective conductivities are summarized in the Figure 7.39 and Table 7.8.

With the help of resampling it was possible to reduce the simulation time already between original image and after one resampling step in more than ten times (from approx. 10 min to approx. 1 min). After just one resampling step the simulation provides comparable results with the results from the original image. Although every further reduce of the resolution (increase of the voxel size) influences the results of the simulation considerably. This effect is higher for the thermal properties as for the electrical, due to different role of the graphite in the conducting system.

Hence in order to optimize the simulation time and accuracy the estimation of the effective properties can be performed on the resampled images as long as all microstructural characteristics do not change (compare with Figure 7.27 and Figure 7.28).

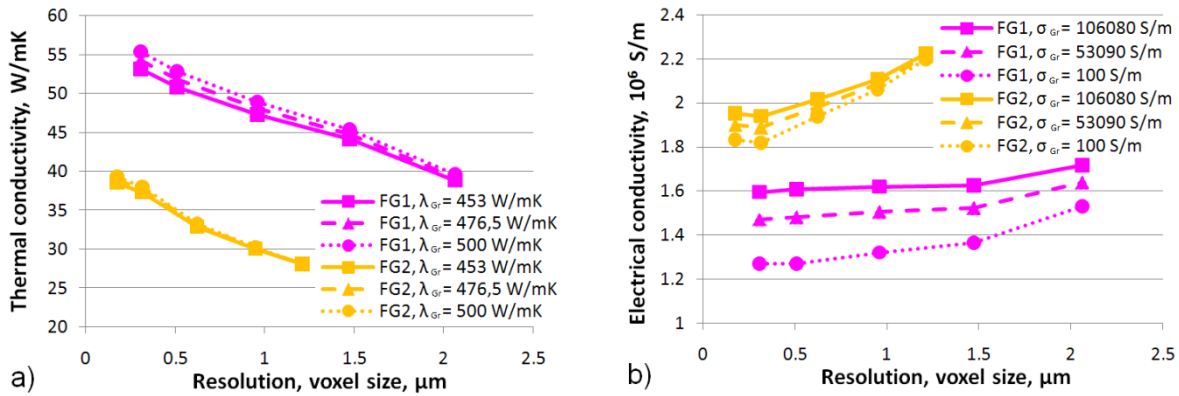


Figure 7.39 3D simulation of a) thermal and b) electrical conductivity on original FIB-tomographic images FG1 and FG2 and images with artificially reduced resolution (e.g. see Figure 7.38). Simulations were performed for different graphite conductivities calculated from the equation a) 9.7 and b) 9.8 for compactness  $C=0.2; 0.1; 0$ .

Figure 7.39 also shows that the effect of the resolution is higher, if the difference between properties of the matrix and inclusions is higher. Comparing the results of the simulation with the literature and experimental values the suggestion for the thermal and electrical conductivity of the flake graphite can be done. Although one has to keep in mind that the simulation was performed on only one limited zone in the middle of the eutectic cell, and is not representative for the bulk volume of cast iron with flake graphite (Table 7.8). As the concentration and the complexity of the graphite in the middle of the eutectic cell is the highest, the estimated properties of this local volume should be higher for the thermal and lower for the electrical conductivities. For FG1 this would mean, that properties of the graphite approach 500 W/m·K and 100 S/m (i.e.  $C = 0$ ). For FG2 the estimated values for thermal conductivity are significantly lower than the literature values and electrical conductivity exceeds the experimental values. This is due to the low volume fraction of the graphite and dendrite arrangement of the regions with and without graphite inclusions.

The certain anisotropy observed on the 3D images of flake graphite and quantified using area and length of projections in all spatial directions (see Figure 7.29) has also influenced the physical properties. Graphite flakes are oriented to the certain extent parallel to the  $y$ -axis. Hence, in this direction they provide the best heat transfer and delay least of all the electron transport in the matrix.

Using the simulation program GeoDict it was possible with the help of FIB-tomographical images to estimate the local properties of the cast iron with flake graphite. As the real 3D images were used for the simulation it was possible to implement all microstructural characteristics: volume fraction, specific surface area, integrals of mean and total curvature. It was shown that phase connectivity plays an important role for the estimation of the effective properties.

Table 7.8: Results of 3D simulation of effective properties of cast iron with flake graphite with GeoDict.

	C	Thermal conductivity, W/m·K					Electrical conductivity, $10^6$ S/m				
		x	y	z	mean	Literature <sup>9</sup>	x	y	z	mean	Experiment
FG1	0.2	50.9	61.4	47.1	53.1		1.55	1.83	1.41	1.60	
	0.1	51.9	63.0	47.9	54.3		1.42	1.76	1.24	1.47	
	0	52.9	64.6	48.6	55.4	45-65	1.23	1.65	0.94	1.27	1.36 ± 0.05
FG2	0.2	37.3	40.7	37.7	38.6		1.91	2.01	1.94	1.95	
	0.1	37.7	41.2	38.1	39.0		1.85	1.97	1.89	1.90	
	0	38.0	41.7	38.4	39.4	1.76	1.91	1.83	1.83		

Considering the hierarchical character of the microstructure for the estimation of the bulk properties, it is important to know the spatial arrangement of phases and effective properties at each characteristic scale. Cumulative implementation of the different tomographic techniques with varying analyzed volume and resolution can provide complete information about such microstructures and hence the material properties. For example FIB-tomography with high resolution can provide the information about the microstructure at different positions in the eutectic cell and computed tomography the arrangement of the eutectic cells in the bulk volume. To simulate the bulk effective properties of the material one could use the properties of the sub volumes which were precisely acquired from smaller regions with higher resolution. This procedure opens the way to study the influence of the microstructural changes (which can be simply simulated in the computer models) on the effective physical and mechanical properties of such hierarchical structures.

<sup>9</sup> Source [6], [32].

---

## 8 CONCLUSIONS

---

In this study different graphite morphologies were thoroughly analyzed in order to understand the correlation between properties and microstructure. Graphite morphology is one of the main factors controlling the mechanical and physical properties of cast iron. Thus, the first aim was to objectively classify different graphite types using an automatic image analysis system. The developed method should present the reliable alternative to the currently used subjective comparison of the real microstructure with the series of images from DIN EN ISO 945.

The first realization of the classification procedure was performed on 2D micrographs using particle based methods. After having characterized a statistically large amount of the 2D sections of different graphite morphologies, two shape factors (roundness and compactness), the most sensitive to the microstructural changes, as well as the size parameter (*MaxFeret*) were chosen for the classification. Their dependency on the magnification of the analyzed image was determined for all different graphite types. Thus, it was possible to define classification parameters independent from the individual imaging parameters (magnification, camera resolution, etc.) and to perform an automatic reproducible and unambiguous graphite classification with the help of conventional image analysis on the classical 2D sections. It was found that a magnification of 200× (calibration factor approx. 0.7 μm) provides the best compromise between the precision of the determination of the graphite particle parameters and a sufficiently large amount of analyzed inclusions for accurate statistical estimations. Thus, the newly developed algorithm is a substantial improvement to the currently used subjective classification based on the standards.

Nevertheless, the classification of the graphite morphology with the help of 2D image analysis procedures is uncertain. This is caused by an unclear categorization of the two dimensional sections of the non convex graphite types. It was shown that with these methods the classification accuracy (averaged for all graphite types) cannot reach more than 90 %.

The first ever conducted research on the 3D shape of individual graphite variants with the help of FIB microstructure tomography allowed analyzing the significant differences by means of basic characteristics and also 3D particle based parameters.

Moreover, with the help of the simulation of random sections of the reconstructed 3D shapes the limits of the 2D analysis were able to be demonstrated. In particular, it was found that the sections of the diameter less than about 20 % of their 3D particle size almost cannot be unambiguously classified.

By the analysis of the relevant parameters, it was found that, next to the image characteristic parameters roundness and compactness, the Euler number has an important effect for the non convex graphite types, but in general, the combination of the number of parameters has to be taken into consideration, in order to achieve optimum classification results for all graphite morphologies.

Due to this fact, 15 relevant parameters were simultaneously integrated in the classification strategy with the help of support vector machine. It was confirmed through analysis of the sensitivity and classification accuracy that for different graphite morphologies different parameters play the decisive role. Thus, the support vector machine was chosen as the basis for the new online application, which allows, through the application of the existing training data or through the generation of individual training data, for a very reliable classification accuracy of more than 95 % for most of the graphite types.

Tomographic characterization of the individual graphite inclusions combined with high resolution analysis of chemical and structural composition of nodular, vermicular and flake graphite provided valuable information about their nucleation, growth and spatial arrangement. Quantitative characterization was done using advanced methods of 3D image analysis.

It was found that magnesium sulfides (if existent surrounded by sulfides of La and Ce) serve as nuclei for the formation of nodular and vermicular graphite. Their growth occurs according to the model proposed by [11] and refined by [13]. The further branching of the vermicular graphite is caused by the heterogeneous defects in the nodule as well as the sufficient amount of oxygen and sulfur in the residual melt. Level of branching can be characterized by a quotient of the fraction of branches to the fraction of initial nodule in the vermicular graphite particle.

MnS is the nucleus for the flake graphite. They growth in the  $\langle 110 \rangle$  or  $\langle 100 \rangle$  crystallographic direction and the correlation between orientation of MnS and surrounding matrix structure is observed.

Considering the anisotropic properties of the hexagonal graphite structure and knowing the growth mechanisms of graphite of different morphologies, the properties of the graphite inclusions were estimated. Cast iron microstructure was approximated with a simple 2D model consisting of a pearlite matrix with graphite ellipsoids of different compactness and thus different conductivity. The simulations on this model underestimate the effective thermal conductivity and electrical resistivity of the cast iron with vermicular and flake graphite. This is

due to the fact that the 2D model does not consider important characteristic of these two graphite morphologies – their connectivity. The use of the real tomographic data for the 3D simulations of effective physical properties of the cast iron with flake graphite made it possible to implement all important microstructural parameters including connectivity. It was shown that phase connectivity is one of the determining factors for the material properties. Additionally, the influence of the resolution of the tomographic images on the estimation of the material properties was shown. The compromise between reasonable time and accuracy of the simulation can be achieved by the choice of a suitable resolution. The images can be resampled (the resolution decreased) as long as all of the microstructural characteristics do not change.

The successful implementation of 3D data from FIB tomography in simulation procedures offers a way to study the influence of microstructural changes, which can be readily simulated with computer models, on the effective physical properties of such complex microstructures. The ability to reproduce experimentally-determined values by computer simulation allows a further interesting step. By modifying the microstructures via computer modelling one should be able to define ideal searched structures through its optimization. These optimization procedures could create tailored composite structures which would in turn maximize a specific physical or mechanical property.



## IV. APPENDIX



---

## 9 APPENDIX

---

### 9.1 CALCULATION OF EFFECTIVE PROPERTIES OF MICROSTRUCTURAL CONSTITUENTS

The calculation of thermal and electrical conductivities of alloyed ferrite from the chemical composition for the samples analyzed in this work was performed according to Eq. 2.11 and 2.12. For explanations see section 2.3.2.2.

The chemical composition in at. % of cast iron samples (Table 9.1) was calculated from chemical composition in weight % ( $m_i$ ) (see Table 4.1) and atomic weights ( $A_i$ ) of the alloying elements.

$$N_i = \frac{m_i \cdot N_A}{A_i} \quad 9.1$$

$$c_i = \text{at. \%}_i = \frac{N_i}{\sum_i N_i} \cdot 100\% \quad 9.2$$

where  $N_A = 6.02 \cdot 10^{23}$  at/mole is the Avogadro constant.

Table 9.1 Chemical composition ( $c_i$ ) of cast iron samples with flake (FG), vermicular (CG) and nodular (SG) graphite.

Alloying elements, at. %	$A_i$ , g/mole	FG <sub>1</sub>	FG <sub>2</sub>	FG <sub>3</sub>	CG <sub>1</sub>	CG <sub>2</sub>	CG <sub>3</sub>	SG
C	12	13.41	13.61	13.41	14.81	14.82	14.56	14.79
Si	28	3.62	3.78	3.55	3.81	3.66	3.70	3.84
P	31	0.08	/	/	0.04	0.03	/	/
S	32	0.17	0.14	0.16	0.02	0.01	0.01	0.01
Mn	55	0.58	/	/	0.32	0.33	/	/
Cr	52	0.47	/	/	0.05	0.04	/	/
Cu	63.5	1.00	/	/	0.89	0.78	/	/
Ti	47.9	0.03	/	/	0.01	0.01	/	/
Sn	118.7	0.04	/	/	0.05	0.04	/	/
Mg	24.3	0	/	/	0.02	0.03	0.02	0.05
Ni	58.7	0.09	/	/	0.03	0.02	/	/
N	14	0.06	/	/	0.04	0.03	/	/
Fe	55.8	80.47	82.47	82.88	79.92	80.19	81.72	81.31

Knowing all parameters (see section 2.3.2.2) the thermal and electrical conductivity of alloyed ferrite can be calculated for each cast iron sample (Table 9.2). Mean values of ferrite conductivities were further used for the estimation of the pearlite conductivities with Hashin-Shtrikman bounds (Eq. 2.5) and according to the Eq. 2.13. The volume fraction of cementite

was calculated to be  $V_V(Fe_3C) = 0.114$ , the conductivities of cementite can be seen in the Table 2.4. Table 9.3 summarizes the values of conductivities used for analytical models and FEM simulations.

Table 9.2 Calculated thermal and electrical conductivities for alloyed ferrite from the equations 2.11 and 2.12.

Properties of alloyed ferrite	FG <sub>1</sub>	FG <sub>2</sub>	FG <sub>3</sub>	CG <sub>1</sub>	CG <sub>2</sub>	CG <sub>3</sub>	SG	Mean value
$\lambda$ , W/mK	27.83	30.52	31.61	28.85	29.47	30.88	30.23	29.91
$\rho$ , $\mu\Omega\text{m}$	0.41	0.36	0.35	0.39	0.38	0.36	0.37	0.37

Table 9.3 The thermal and electrical conductivities of phases used for simulations of the cast iron properties.

	$\lambda$ , (W/mK)	$\sigma$ , ( $10^6$ S/m)	$\rho$ , ( $\mu\Omega\cdot\text{m}$ )
Graphite $\lambda_a$	500	2	$0.5^{10}$
Graphite $\lambda_c$	10	0.0001	$10000^{10}$
Lamellar alloyed pearlite ( $\lambda_{\parallel}$ , $\sigma_{\parallel}$ , $\rho_{\parallel}$ )	26.7	2.43	0.412
Lamellar alloyed pearlite ( $\lambda_{\perp}$ , $\sigma_{\perp}$ , $\rho_{\perp}$ )	25.6	2.37	0.422
Alloyed pearlite Eq. 2.13	26.34	2.41	0.415

<sup>10</sup> Source [160]

## 9.2 CLASSIFICATION LIMITS

Table 9.4 Classification limits (see section 6.2.1).

Compactness	Roundness	MaxFeret, $\mu\text{m}$	Size class	Class	Graphite type
0 - 0.458	0 - 0.229	0 - 15	8	0	I
0.458 - 0.717	0.205 - 0.44	0 - 15	8	1	III
0.8 - 1	0.6 - 1	0 - 15	8	2	VI
0.4597 - 0.869	0.4 - 0.696	0 - 15	8	3	IV - V
0 - 0.364	0 - 0.168	15 - 30	7	4	I
0.364 - 0.692	0.138 - 0.432	15 - 30	7	5	III
0.8 - 1	0.6 - 1	15 - 30	7	6	VI
0.411 - 0.847	0.4 - 0.636	15 - 30	7	7	IV - V
0 - 0.282	0 - 0.138	30 - 60	6	8	I
0.244 - 0.611	0.065 - 0.391	30 - 60	6	9	III
0.8 - 1	0.6 - 1	30 - 60	6	10	VI
0.401 - 0.8	0.35 - 0.643	30 - 60	6	11	IV - V
0 - 0.262	0 - 0.133	60 - 120	5	12	I
0.173 - 0.484	0.035 - 0.314	60 - 120	5	13	III
0.708 - 1	0.572 - 1	60 - 120	5	14	VI
0.413 - 0.707	0.3 - 0.572	60 - 120	5	15	IV - V
0 - 0.185	0 - 0.104	120 - 250	4	16	I
0.142 - 0.38	0.037 - 0.248	120 - 250	4	17	III
0.623 - 1	0.486 - 1	120 - 250	4	18	VI
0.342 - 0.623	0.24 - 0.486	120 - 250	4	19	IV - V
0 - 0.141	0 - 0.073	250 - 500	3	20	I
0.141 - 0.38	0.036 - 0.248	250 - 500	3	21	III
0.623 - 1	0.486 - 1	250 - 500	3	22	VI
0.342 - 0.623	0.24 - 0.486	250 - 500	3	23	IV - V
0 - 0.142	0 - 0.073	500 - 1000	2	24	I
0.142 - 0.38	0.036 - 0.248	500 - 1000	2	25	III
0.623 - 1	0.486 - 1	500 - 1000	2	26	VI
0.342 - 0.623	0.24 - 0.486	500 - 1000	2	27	IV - V

### 9.3 ROUNDNESS: DEPENDENCY ON THE MAXIMUM FERET DIAMETER

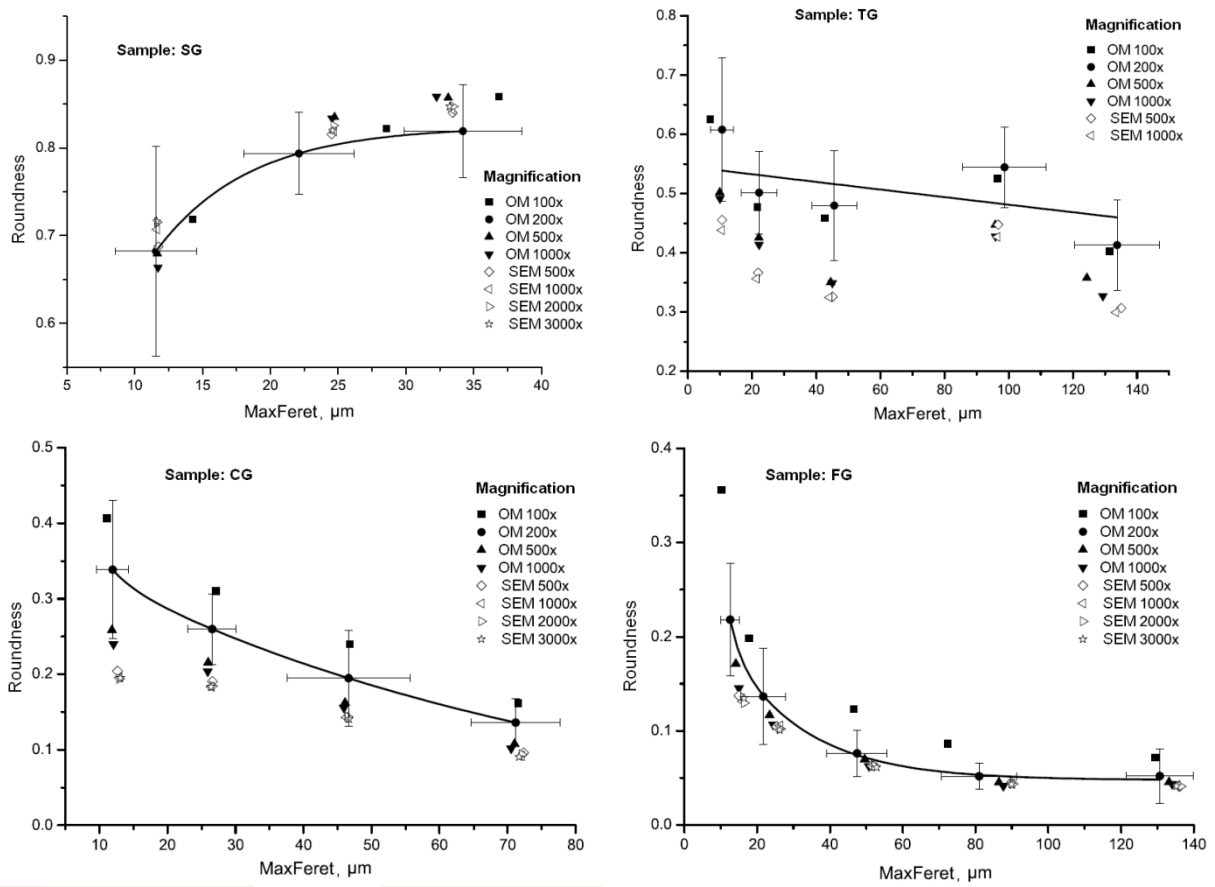


Figure 9.1 Dependency of the parameter roundness on the particle size for different magnifications.

9.4 PARAMETERS OF THE REGRESSION ANALYSIS [144]

Table 9.5 Parameters of the regression analysis  $y = a + bx$ , flake graphite (FG), compactness.

Type	Size class	OM / SEM	Parameter	
			a	b
FG Compactness	R8	OM	0.2939	0.2555
		SEM	0.2966	0.0137
	R7	OM	0.2211	0.1479
		SEM	0.2337	0.0286
	R6	OM	0.1317	0.1040
		SEM	0.1444	0.0123
	R5	OM	0.0818	0.0684
		SEM	0.0980	0.0139
	R4	OM	0.0959	0.0533
		SEM	0.1000	-0.0028

Table 9.6 Parameters of the regression analysis  $y = a + bx$ , flake graphite (FG), roundness.

Type	Size class	OM / SEM	Parameter	
			a	b
FG Roundness	R8	OM	0.1189	0.1732
		SEM	0.1306	0.0191
	R7	OM	0.0941	0.0758
		SEM	0.1012	0.0137
	R6	OM	0.0531	0.0495
		SEM	0.0616	0.0071
	R5	OM	0.0338	0.0374
		SEM	0.0428	0.0068
	R4	OM	0.0389	0.0236
		SEM	0.0414	-0.0017

Table 9.7 Parameters of the regression analysis  $y = a + bx$ , vermicular graphite (CG), compactness.

Type	Size class	OM / SEM	Parameter	
			a	b
CG Compactness	R8	OM	0.4399	0.2066
		SEM	0.3805	0.0910
	R7	OM	0.3464	0.1559
		SEM	0.3279	0.0551
	R6	OM	0.2568	0.1185
		SEM	0.2462	0.0220
	R5	OM	0.1980	0.0952
		SEM	0.1867	0.0328

Table 9.8 Parameters of the regression analysis  $y = a + bx$ , vermicular graphite (CG), roundness.

Type	Size class	OM / SEM	Parameter	
			a	b
CG Roundness	R8	OM	0.2263	0.1412
		SEM	0.1916	0.0401
	R7	OM	0.1938	0.0894
		SEM	0.1813	0.0279
	R6	OM	0.1452	0.0717
		SEM	0.1417	0.0058
	R5	OM	0.0962	0.0510
		SEM	0.0905	0.0178

## 9.4 Parameters of the Regression Analysis <[144]>

Table 9.9 Parameters of the regression analysis  $y = a + bx$ , nodular graphite (SG), compactness.

Type	Size class	OM / SEM	Parameter	
			a	b
SG Compactness	R8	OM	0.8297	0.0683
		SEM	0.8766	-0.0880
	R7	OM	0.9310	0.0114
		SEM	0.9271	-0.0252
	R6	OM	0.9487	0.0013
		SEM	0.9421	-0.0272

Table 9.10 Parameters of the regression analysis  $y = a + bx$ , nodular graphite (SG), roundness.

Type	Size class	OM / SEM	Parameter	
			a	b
SG Roundness	R8	OM	0.6611	0.0415
		SEM	0.7235	-0.1185
	R7	OM	0.8247	-0.00064
		SEM	0.8240	-0.0292
	R6	OM	0.8495	0.0006
		SEM	0.8488	-0.0302

Table 9.11 Parameters of the regression analysis  $y = a + bx$ , temper graphite (TG), compactness.

Type	Size class	OM / SEM	Parameter	
			a	b
TG Compactness	R8	OM	0.6322	0.1544
	R7	OM	0.5346	0.1650
	R6	OM	0.4936	0.1463
	R5	OM	0.5200	0.1562
	R4	OM	0.4440	0.1093

Table 9.12 Parameters of the regression analysis  $y = a + bx$ , temper graphite (TG), roundness.

Type	Size class	OM / SEM	Parameter	
			a	b
TG Roundness	R8	OM	0.4754	0.1193
	R7	OM	0.4261	0.0493
	R6	OM	0.3380	0.1138
	R5	OM	0.4312	0.0850
	R4	OM	0.3407	0.0599

### 9.5 ESTIMATION OF THE EFFECTIVE CONDUCTIVITY OF GRAPHITE

The effective conductivity of nodular graphite has been estimated using Double and Hellawell model [11], [13] from the radial and tangential conductivities of graphite. To do so a 2D model of a single graphite nodule embedded in a pearlitic matrix with the already calculated properties (see Table 9.3) was used for the simulation. The anisotropic properties of the single nodule are calculated from the properties of graphite crystal in  $a$ - and  $c$ -direction.

Assigning the origin of the coordinate system to the centre of the spherulitic graphite particle the first estimation of the conductivity of graphite nodule in each point  $(x, y)$  can be defined with trigonometric functions as follow:

$$\theta = \text{abs} \left[ \arctan \left( \frac{y}{x} \right) \right] \quad 9.3$$

$$\alpha = \text{abs} \left[ \arctan \left( \frac{kc}{ka} \right) \right] \quad 9.4$$

$$k_x = \sqrt{ka^2 + kc^2} \cdot \sin(\theta - \alpha) \quad 9.5$$

$$k_y = \sqrt{ka^2 + kc^2} \cdot \cos(\theta - \alpha) \quad 9.6$$

where  $x$  and  $y$  are the coordinates of the point for which the properties are calculated,  $ka$  and  $kc$  the conductivities of the graphite in  $a$ - and  $c$ -direction respectively (see Figure 9.2).

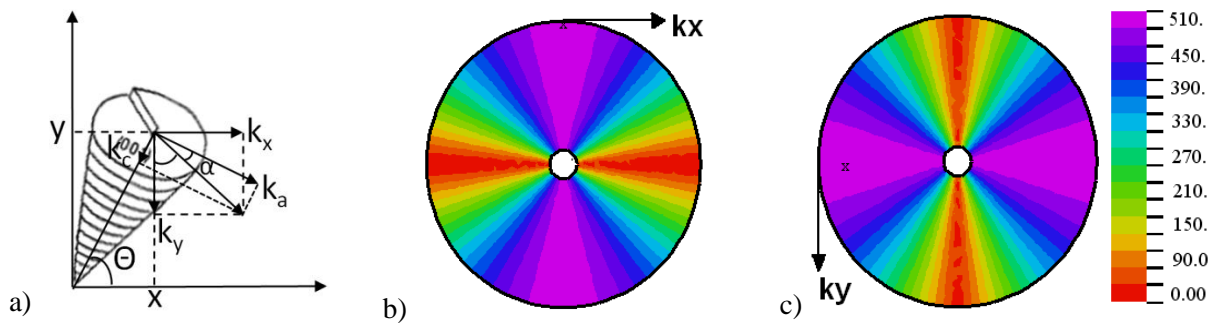


Figure 9.2 a) Scheme of the definition of the conductivities in the point  $(x,y)$  according to the Double and Hellawell model [13]. Distribution of the value of the b)  $k_x$  and c)  $k_y$  thermal conductivities in the anisotropic graphite nodule.

The following figure (Figure 9.3) shows the propagation of heat in a single graphite nodule whose properties are defined as explained before.

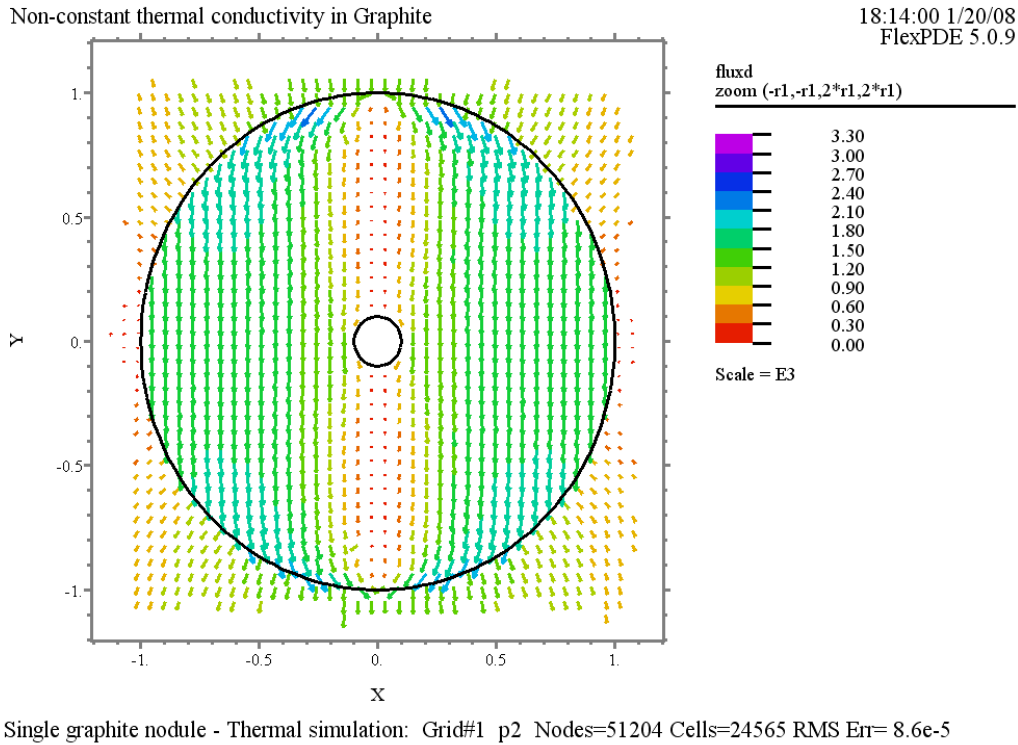


Figure 9.3 Propagation of heat in nodular graphite with real-like conductivities.

The propagation is alike the propagation proposed by Hasse [73] for the spheroidal graphite (see Figure 2.12). However, as it is very time consuming to run the simulations, if the conductivity in the graphite is defined with two different conductivities in each point, the goal was to acquire an effective conductivity for a graphite nodule.

To define both the thermal and electrical effective conductivities of nodular graphite, the heat and tension flux for real nodular graphite conductivities has been compared with the flux for nodular graphite with a unique homogeneous conductivity.

Knowing the measured flux integral and the type of the resulting temperature and tension curve, it is possible to approximate the effective conductivity of the graphite nodule by a single homogeneous conductivity. The effective conductivity of a single graphite nodule is for thermal conductivity between 260 and 265 W/(m·K) and for electrical conductivity between  $0.52$  and  $0.53 \cdot 10^6$  S/m. For the following simulations an effective thermal and electrical conductivity of 265 W/(m·K) and  $0.53 \cdot 10^6$  S/m respectively has been used for the ideal graphite nodule.

Considering the crystallographic structure of the vermicular and flake graphite (see section 7.1.2) following estimation of the thermal and electrical properties of the graphite of different morphology was proposed:

$$\lambda_{Gr} = \lambda_{sphere} \cdot V_{sphere} + \lambda_a \cdot V_a \quad 9.7$$

$$\lambda_{gr.} = \lambda_{sphere} \cdot V_{sphere} + \lambda_c \cdot V_c \quad 9.8$$

where  $\lambda_{Gr}$  is the resulting thermal conductivity of the graphite particle,  $\lambda_{sphere}$  the estimated thermal conductivity of the ideal graphite nodule ( $\lambda_{sphere}=265 \text{ W/(m}\cdot\text{K)}$ ),  $\lambda_a$  and  $\lambda_c$  are the graphite conductivities in *a*- and *c*-crystallographic directions, respectively. Approximating the shape of the graphite inclusions with 2D ellipsoids it should be considered that their conductivity will be different for the case parallel (Eq. 9.7) and orthogonal (Eq. 9.8) to the flux. The portion of corresponding conductivities was estimated from the shape of the ellipsoids according to their compactness *C* (for definition see Table 3.2):

$$V_{sphere} = C, V_a = V_c = 1 - C \quad 9.9$$

It was assumed that the compactness of the ellipsoids corresponds to the compactness of the real graphite particles, and thus describes the portion of the graphite grown as nodular graphite and flake graphite respectively.

Table 9.13 Approximation of the effective thermal and electrical conductivity of graphite particles.

Compactness	Thermal conductivity, W/m·K		Electrical conductivity, 10 <sup>6</sup> S/m	
	a-direction	c-direction	a-direction	c-direction
1.0	265	265	0.530	0.530
0.9	288.5	239.5	0.677	0.477
0.8	312	214	0.824	0.424
0.7	335.5	188.5	0.971	0.371
0.6	359	163	1.118	0.318
0.5	382.5	137.5	1.265	0.265
0.4	406	112	1.412	0.212
0.3	429.5	86.5	1.559	0.159
0.2	453	61	1.706	0.106
0.1	476.5	35.5	1.853	0.053
0	500	10	2	0.0001

---

## 10 REFERENCES

---

- [1] DIN. *Gußeisen - Bestimmung der Mikrostruktur von Graphit (ISO 945:1975); Deutsche Fassung EN ISO 945:1994*. s.l. : DIN - Deutsches Institut für Normung, 1994.
- [2] *ASM Handbook*. s.l. : ASM International, 1990. Vols. Volume 01: Properties and Selection: Iron, Steels, and High-Performance Alloys.
- [3] Gagnebin, A.P. *The Fundamentals of Iron and Steel Castings*. s.l. : N. P. : The International Nickel Company, Inc., 1957.
- [4] Bergmann, W. *Werkstofftechnik Teil 1: Grundlagen*. s.l. : Hanser Verlag, 4. Auflage, 2002.
- [5] Merkel, M. and Thomas, K.-H. *Taschenbuch der Werkstoffe*. s.l. : Fachbuchverlag Leipzig, 5. Auflage, 2000.
- [6] Davis, J. R., et al., eds. *ASM Speciality Handbook: Cast Irons*. s.l. : ASM International Handbook Committee: Materials Park, 1996.
- [7] Chou, J.-M., Hon, M.-H. and Lee, J.-L. *J. of Mat. Science*. 1990, Vol. 25, pp. 1965–1972.
- [8] Yakovlev, F. I. *Metal Science and Heat Treatment*. 1986, Vol. 28, 5, pp. 378–380.
- [9] Hatate, M., et al. *Wear*. 2001, Vol. 251, pp. 885-889.
- [10] Hasse, S. and Brunhuber, E. *Gießerei-Lexikon 2001*. s.l. : Schiele & Schön, 2000.
- [11] Double, D.D. and Hellawell, A. Growth structure of various forms of graphite. [book auth.] B. Lux, I. Minkoff and F. Mollard. *The Metallurgy of Cast Iron*. Switzerland : Georgi Publ. St Saphorin, 1975, pp. 509-525.
- [12] Itofuji, H. *Transactions of the American Foundrymen's Society*. 1996, Vol. 104, pp. 79–87.
- [13] Miao, B., et al. *J. of Materials Science*. 1994, Vol. 29, pp. 255-261.
- [14] Gorshkov, A. A. *Lit. Proizv.* 1955, Vol. 3.
- [15] Yamamoto, S., et al. *Metal Science*. 1978, Vol. 12, 5, pp. 239–246.
- [16] Röhrig, K. *Konstruieren+Gießen*. 1987, Vol. 12, 1, pp. 34-39.
- [17] Bäckerud, S.L., Nilson, N. and Stehen, H. *The Metallurgy of Cast Iron, 2nd int. Symp. on the Metallurgy of Cast Iron*. 1974, pp. 625-637.
- [18] Itofuji, H., et al. *Transactions of the American Foundrymen's Society*. 1983, Vol. 91, 4, pp. 831–840.
- [19] Itofuji, H. *Study on graphite spheroidization in cast irons*. s.l. : Kyoto University, 1994. Doctor thesis.

- [20] Liu, P.C., et al. *Transactions of the American Foundrymen's Society*. 1981, Vol. 89, pp. 65-78.
- [21] Stefanescu, D.M. and Loper, C.R. *Gießerei-Praxis*. 1981, 5, p. 76.
- [22] Kleine, A. *Innovative Konzepte im Motorenbau mit Gusseisenwerkstoffen*. s.l. : RWTH Aachen, 2002. Doctor thesis.
- [23] Dawson, S. Process control for the production of compacted graphite iron. [Online] 2005. [Cited: 11 9, 2005.] <http://www.sintercast.com/>.
- [24] Seidel, W. *Werkstofftechnik*. 5. s.l. : Hanser Verlag, 2001.
- [25] Schütt, K.H. *Temperguss - Spezialist für dünnwandige, komplexe Bauteile*. s.l. : Zentrale für Gussverwendung, 2005. 7.
- [26] Janowak, J. F. and Gundlach, R. B. *J. Heat Treating*. 1985, Vol. 4, p. 25.
- [27] Hecht, R.L., Dinwiddie, R.B. and Wang, H. *Journal of Materials Science*. 1999, Vol. 34, pp. 4775-4781.
- [28] Volchok, I.P., et al. *Fiziko-Khimicheskaya Mekhanika Materialov*. 1984, Vol. 20, 3, pp. 89-92.
- [29] Evans, E.R., Dawson, J.V. and Lalich, M.J. *AFS Int Cast Met J*. 1976, Vol. 1, 2, pp. 13-18.
- [30] Monroe, R.W. and Bates, C. E. *Transactions of the American Foundrymen's Society*. 1982, Vol. 90, pp. 615-624.
- [31] Powell, J. *Foundryman*. 1984, Vol. 77, 9, pp. 472-483.
- [32] Lampic, M. *Giesserei-Praxis*. 2001, 1, pp. 17-22.
- [33] Rukadikar, M.C. and Reddy, G.P. *Journal of Materials Science*. 1986, Vol. 21, pp. 4403-4410.
- [34] Bardes, B. ed. *Metals Handbook*. 9. Metals Park, Ohio : American Society for Metals, 1989. Vol. 1.
- [35] Walton, C.F. ed. *Gray and Ductile Iron Casting Handbook*. Cleveland : Gray and Ductile Founder's Society, 1971.
- [36] Abuhamad, M. *Gussgefüge- und Gussgradientencharakterisierung mittels 3MA*. Saarbrücken : Saarland University, 2006. Diploma thesis.
- [37] Pitsch, H. *Die Entwicklung und Erprobung der Oberwellenanalyse im Zeitsignal der magnetischen Tangentialfeldstärke als neues Modul des 3MA-Ansatzes*. IZFP- Bericht Nr. 900107-TW. Saarbrücken : Saarland University, 1989. Doctor thesis.
- [38] Hashin, Z. and Shtrikman, S. *J. Appl. Phys.* 1962, Vol. 33, 10, pp. 3125-3131.

- [39] Ferrocast (R). *Qualität aus einem Guss, Werkstoff-Normblatt Nr. 1600/4*. AGQ Normblatt 11/03. 2003.
- [40] Rhines, F.N. *Microstructology: Behaviour and Microstructure of Materials*. Stuttgart : Riederer-Verlag, 1986.
- [41] Torquato, S. *Random Heterogeneous Materials: Microstructure and Macroscopic Properties*. New York : Springer-Verlag, 2002.
- [42] Hashin, Z. *J. Appl. Mech., Transactions ASME*. 1983, Vol. 50, 3, pp. 481-505.
- [43] Milton, G.W. *The Theory of Composites* . Cambridge : Cambridge University Press, 2002.
- [44] Markov, K.Z. and Preziosi, L. *Heterogeneous Media: Micromechanics Modeling Methods and Simulations*. Boston : Birkhäuser, 2000.
- [45] Ashby, M.F. *Acta Metall. Mater.* 1993, Vol. 41, 5, pp. 1313-1335.
- [46] McLachlan, D.S., Blaszkiewicz, M. and Newnham, R.E. *J. Am. Ceram. Soc.* 1990, Vol. 73, 8, pp. 2187-2203.
- [47] Weber, L, Dorn, J. and Mortensen, A. *Acta Mater.* 2003, Vol. 51, pp. 3199-3211.
- [48] Milton, G.W. *Phys. Rev.Lett.* 1981, Vol. 46, 8, pp. 542-545.
- [49] Beran, M. *Nuovo Cimento*. 1965, Vol. 38, p. 771.
- [50] Weber, L., Fischer, C. and Mortensen, A. *Acta Mater.* 2003, Vol. 51, pp. 495-505.
- [51] Sevostianov, I., Kováčik, J. and Simančík, F. *Materials Science & Engineering A*. 2006, Vol. 420, pp. 87-99.
- [52] Ondracek, G. *Metall.* 1983, Vol. 37, 10, pp. 1016-1019.
- [53] Li, M., Ghosh, S. and Richmond, O. *Acta Mater.* 1999, Vol. 47, 12, pp. 3515-3532.
- [54] Chawla, N., Ganesh, V.V. and Wunsch, B. *Scripta Mater.* 2004, Vol. 51, 2, pp. 161-165.
- [55] Borbély, A., Biermann, H. and Hartmann, O. *Material Science & Engineering A*. 2001, Vol. 313, 1-2, pp. 34-45.
- [56] Pyrz, R. *Composites Science and Technology*. 1994, Vol. 50, 2, pp. 197-208.
- [57] Cooper, C.A., Elliott, R. and Young, R.J. *Acta Mater.* 2002, Vol. 50, pp. 4037-4046.
- [58] Clyne, T.W. and Withers, P.J. *An introduction to metal matrix composites*. Cambridge : Cambridge University Press, 1993.
- [59] Halpin, J.C. and Tsai, S.W. *Enviromental factors in composite design*. s.l. : Air Force Mat Lab, 1967. p. 423. AFML-TR 67.
- [60] Hashin, Z. *International Journal of Solids and Structures*. 1970, Vol. 6, 5, pp. 539-552.
- [61] Wu, T.T. *J. Powder Metall.* 1965, Vol. 1, p. 8.
- [62] Rossi, R.C. *J. Am Ceram Soc.* 1968, Vol. 51, 8, pp. 433-439.

- [63] Lee, Y.H., et al. *Materials Chemistry and Physics*. 2001, Vol. 72, 2, pp. 232-235.
- [64] Helsing, J. and Grimvall, G. *J. Appl. Phys.* 1991, Vol. 70, 3, pp. 1198-1206.
- [65] Williams, R. K., et al. *J. Appl. Phys.* 1981, Vol. 52, 8, pp. 5167-5175.
- [66] Bass, J. [book auth.] K.-H. Hellwege and J.L. Olsen. *Landolt-Börnstein New Series*. Berlin : Springer, 1982, Vol. III/15a.
- [67] Häglund, J., Grimvall, G. and Jarlborg, T. *Phys. Rev. B*. 1991, Vol. 44, 7, pp. 2914-2919.
- [68] Lee, M.-C. and Simkovich, G. *Met. Trans. A*. 1987, Vol. 18A, 3, pp. 485-486.
- [69] Masumoto, H. *Sci. Rep. Tohoku Imperial Univ. Ser. 1*. 1927, Vol. 16, p. 417.
- [70] Radcliffe, S.V. and Rollason, E.C. *J. Iron Steel Inst.* 1958, Vol. 189, p. 45.
- [71] Touloukian, Y. S., et al. *Thermal Conductivity. Thermophysical Properties of Matter*. New York : Plenum, 1970. Vols. 1-2.
- [72] Guesser, W. L., et al. *Revista Materia*. 2005, Vol. 10, 2, pp. 265-272.
- [73] Hasse, S. *Duktiles Gusseisen*. Berlin : Schiele & Schön, 1996.
- [74] Schumann, H. and Oettel, H. *Metallographie, 14th Ed*. Weinheim : Wiley-VCH, 2005.
- [75] Hadwiger, H. *Vorlesungen über Inhalt, Oberfläche, und Isoperimetrie*. Berlin : Springer Verlag, 1957.
- [76] Russ, J.C. and Dehoff, R.T. *Practical Stereology*. New York : Kluwer Academic/Plenum Publishers, 2000.
- [77] Herzer, G. Grain size dependence of coercivity and permeability in Nanocrystalline ferromagnets. *IEEE Trans. Magn.* 1990, Vol. 26, pp. 1397-1402.
- [78] Ohser, J. and Mücklich, F. *Statistical Analysis of Microstructures in Materials Science*. s.l. : John Willey & Sons, 2000.
- [79] Delesse, A. Procédé mécanique pour déterminer la composition des roches. *Annales des Mines*. 1848, Vol. 13, p. 379.
- [80] Rosiwal, G. *Über geometrische Gesteinsanalysen. Verhandlungen K.K. . Wien* : Geologische Reichsanstalt, 1898. p. 143. Vol. 5/6.
- [81] Thompson, E. Quantitative microscopic analysis. *J. Geol.* 1930, Vol. 38, pp. 193-222.
- [82] Glagolev, A.A. *Trans. Inst. Econ. Min.* 1933, Vol. 59, pp. 1-47.
- [83] Saltykov, A. *Stereometrische Metallographie*. Leipzig : VEB Verlag für Grundstoffindustrie, 1974.
- [84] Ohser, J., et al. *Pract. Metallography*. 2003, pp. 454-473.
- [85] Ruxanda, R. and Stefanescu, D.M. *Int. J. Cast Metals Res.* 2002, Vol. 14, pp. 207-216.
- [86] Li, J., Lu, L. and Lai, M. *Materials Characterization*. 2000, Vol. 45, pp. 83-88.

- [87] Imasogie, B.I. and Wendt, U. *J. of Minerals & Materials characterization & Engineering*. 2004, Vol. 3, 1, pp. 1-12.
- [88] Guilemany, J.M. and Llorca-Isern, N. *Pract. Metallography*. 1990, Vol. 27, pp. 189-194.
- [89] Russ, J.C. *The Image Processing Handbook 2nd. Ed.* s.l. : CRC Press Inc., 1995. p. 490.
- [90] a4i. Benutzerhandbuch, a4i Analysis. 2002.
- [91] Wojnar, L. *Image Analysis Applications in Materials Engineering*. New York : CRC Press, 1999. pp. 193-201.
- [92] Lu, Shu-Zu and Hellawell, A. *Acta metal. Mater.* 1994, Vol. 42, 12, pp. 4035-4047.
- [93] Schladitz, K., Gerber, W. and Sandau, K. *Sonderband Prakt. Metallogr.* 2000, Vol. 33, pp. 167-170.
- [94] Roberts, K., Mücklich, F. and Weikum, G. *Sonderband Prakt. Metallogr.* 2003, Vol. 35, pp. 117-122.
- [95] Roberts, K., Weikum, G. and Mücklich, F. *Pract. Metallography*. 2005, Vol. 42, 8, pp. 395-410.
- [96] Haralick, R.M., Shanmugam, K. and Dinstein, I. *Textural features for image classification*. s.l. : IEEE Transactions on Systems, Man, and Cybernetics, 1973. pp. 610-621.
- [97] Giannuzzi, L.A. and Stevie, F.A. *Introduction to Focused Ion Beams – Instrumentation, Theory, Techniques and Practice*. s.l. : Springer, 2004. pp. 281-300.
- [98] Pyzalla, A., et al. Simultaneous Tomography and Diffraction Analysis of Creep Damage. *Science*. 2005, Vol. 308, pp. 92-95.
- [99] Konrad, J., Zaefferer, S. and Raabe, D. *Acta Mater.* 2006, Vol. 54, 5, pp. 1369-1380.
- [100] Lasagni, F., et al. *Advanced Engineering Materials*. 2006, Vol. 8, 8, pp. 719-723.
- [101] Weiss, D., et al. *Ultramicroscopy*. 2000, Vol. 84, pp. 185-197 .
- [102] Koguchi, M., et al. *J. Electron Microsc.* 2001, Vol. 50, pp. 235-241.
- [103] Holzer, L., et al. *J. Microsoc.* 2004, Vol. 216, pp. 84-95.
- [104] Copley, D.C., Eberhard, J.W. and Mohr, G.A. *J. of Metals*. 1994, Vol. 46, pp. 14-26.
- [105] Defrise, M. *Comput. Med. Imag. Graph.* 2001, Vol. 25, pp. 113-116.
- [106] Owens, J.W., et al. *Mater. Res. Bull.* 2001, Vol. 36, pp. 1595-1602.
- [107] Henke, B., Gullikson, E. and Davis, J. *At. Data Nucl. Data Tab.* 54. 1993. pp. 181-342.
- [108] Fraunhofer IZfP. *Leistungen und Ergebnisse Jahresbericht 2003, Saatgutanalyse mit 3D Computertomographie*. 2003. pp. 64-67 .
- [109] Brownlow, L., et al. *Microscopy and Analysis*. 2006, Vol. 20, 2, pp. 13-15 (EU).
- [110] Bravin, A. *J. Phys. D: Appl. Phys.* 2003, Vol. 36, pp. A24-A29.
- [111] Protopopov, V., et al. *SPIE 4682*. 2002, pp. 277-285.

- [112] Zhang, J., et al. *Review of Progress in Quantitative NDE, American Institute of Physics*. 2005, Vol. 24, pp. 686-693.
- [113] Babout, L., et al. *Acta Mater.* 2001, Vol. 49, pp. 2055-2063.
- [114] Lin, C.L. and Miller, J.D. *Chem. Eng. J.* 2000, Vol. 77, pp. 79-86.
- [115] Lu, D., et al. *Mag. Res. Imaging.* 2001, Vol. 19, pp. 443-448 .
- [116] Ludwig, W. and Bellet, D. *Mater. Sci. Eng.* 2000, Vol. A281, pp. 198-203 .
- [117] Guvenilir, A., et al. *Acta Mater.* 1997, Vol. 45, 5, pp. 1977-1987.
- [118] Elmoutaouakkil, A., et al. *J.Phys.D: Appl. Phys.* 2003, Vol. 36, pp. A37-43.
- [119] Hawkes, D.J. and Jackson, D.F. *Phys. Med. Biol.* 1980, Vol. 25, pp. 1167-71.
- [120] Kirby, B.J., et al. *Phys. Med. Biol.* 2003, Vol. 48, pp. 3389-3409.
- [121] Sánchez, S.A., et al. *Advanced Engineering Materials.* 2006, Vol. 8, pp. 491-495.
- [122] Heggli, M., et al. *Adv. Eng. Mater.* 2005, Vol. 7, 4, pp. 225-229.
- [123] Inkson, B.J., Mulvihill, M. and Möbus, G. *Scripta Mater.* 2001, Vol. 45, pp. 753-758.
- [124] Inkson, B.J., et al. *J. Microsc.* 2001, Vol. 201, pp. 256-269.
- [125] Arns, C.H., et al. *J. of Petroleum Science and Engineering.* 2004, Vol. 45, pp. 41-46.
- [126] Lang, C., Ohser, J. and Hilfer, R. *J. Microsc.* 2001, Vol. 202, pp. 1-12.
- [127] Helfen, L., et al. *Proceedings SPIE - The International Society for Optical Engineering 5045.* 2003, pp. 254-265.
- [128] Ohser, J., Nagel, W. and Schladitz, K. *Image Anal. Stereol.* 2003, Vol. 22, pp. 11-19.
- [129] Serra, J. *Image analysis and mathematical morphology.* London : Academic Press, 1982. Vol. 1.
- [130] Zygo. *Zygo Corporation Technical Report.* 2007. [www.zygo.com](http://www.zygo.com).
- [131] Seiler, G. Saarbrücken : Saarland University, 2006. Studienarbeit.
- [132] Bückins, M., et al. *Sonderband Prakt. Metallogr.* 2004, Vol. 36, pp. 417-422.
- [133] Graff, A., et al. Abs 092. *Microscopy Conference Proceedings.* 2005.
- [134] Engelmann, H.-J., Volkman, B. and Zschech, E. *Pract. Metallography.* 2003, Vol. 40, 2, pp. 78-84.
- [135] Engstler, Michael. *3D-EDX Tomografie im Focused Ion Beam Mikroskop: Entwicklung, Automatisierung und Verifizierung.* Saarbrücken : Saarland University, 2007. Diploma thesis.
- [136] FEI Company. *Selective Carbon Milling, Technical Note, PN21496-B Copyright (C).* 2000.
- [137] MAVI. *Modular Algorithms for Volume Images.* s.l. : ITWM, 2005.
- [138] Lee, C., Poston, T. and Rosenfeld, A. *CVGIP: Graph. Models Image Process.* 1991, Vol. 53, pp. 522-537.

- [139] Nagel, W., Ohser, J. and Pischang, K. *J. Microsc.* 2000, Vol. 198, pp. 54-62.
- [140] Magenreuter, Th. *Zusammenhang zwischen elektrischem Widerstand und quantitativen Gefügekenngößen von Gusseisenwerkstoffen*. Saarbrücken : Saarland University, 2007. Diploma thesis.
- [141] Schulz, V., et al. *NAFEMS Simulation of Complex Flows (CFD)*. 2005.
- [142] Wiegmann, A. und Zemitis, A. EJ-HEAT: A Fast Explicit Jump Harmonic Averaging Solver for the Effective Heat Conductivity of Composite Materials. *Fraunhofer ITWM*. 2006, 94.
- [143] Castro, M., et al. *Int. J. Cast Metals Res.* 2003, Vol. 16, pp. 83-86.
- [144] Magenreuter, Th. *Abhängigkeit der formcharakteristischen Parameter Rundheit und Kompaktheit verschiedener Graphitmorphologien von der Vergrößerung*. Saarbrücken : Saarland University, 2006. Studienarbeit.
- [145] Tartera, J., et al. *Int. J. of Cast Metals Research*. 2003, Vol. 16, 1-3, pp. 131-135.
- [146] Tartera, J. *AFS International Cast Metals Journal*. 1980, Vol. 5, pp. 7-14.
- [147] Tartera, J., et al. *Int. J. Cast Metals Res.* 1999, Vol. 11, pp. 459-464.
- [148] Monchoux, J.P., et al. *Acta Mater.* 2001, Vol. 49, pp. 4355-4362.
- [149] Llorca-Isern, N., et al. *Micron*. 2002, Vol. 33, pp. 357-364.
- [150] Wyckoff, R.W.G. *Crystal Structures*. New York : Interscience, 1963. Vol. 1.
- [151] Double, D.D. and Hellowell, A. *Acta Metall.* 1969, Vol. 17, pp. 1071-1082.
- [152] Roviglione, A. and Hermida, J.D. *Mat. Characterization*. 1994, Vol. 32, pp. 127-137.
- [153] Roviglione, A. N. and Hermida, J. D. *Metallurgical and Materials Transactions B*. 2004, Vol. 35B, pp. 313-330.
- [154] Zhu, P., Sha, R. and Li, Y. *Proceedings of the Materials Research Society*. 1985, p. 3.
- [155] Stets, W., et al. *Gießerei*. 2004, 9, pp. 20-30 .
- [156] Arns, C.H., et al. *Geophysics*. 2002, Vol. 67, p. 1396.
- [157] Nagel, W., Ohser, J. and Schladitz, K. *The Euler number of discretized sets - on the choice of adjacency in homogeneous lattices in Morphology of Condensed Matter*. [ed.] K. R. Mecke and D. Stoyan. Berlin : Springer-Verlag, 2002. pp. 275-298.
- [158] Schladitz, K., Ohser, J. and Nagel, W. [ed.] A. Kuba, L. G Nyul and K. Palagyi. *13th International Conference on Discrete Geometry for Computer Imagery*. 2006, pp. 247-258.
- [159] Richter, C. *Classification of Microstructural Images based on Particle Parameters*. Saarbrücken : Saarland University, 2005. Master thesis.
- [160] Hollemann, A.F. and Wieberg, N. *Lehrbuch der Anorganischen Chemie*. 91-100. Berlin – New York : Walter de Gruyter, 1985.

*Chapter 10: References*

[161] Angus, H.T. *Cast iron: Physical and Engineering Properties*. London : Butterworths, 1976.

---

## CURRICULUM VITAE

---

### PERSONAL DATA

Name	Alexandra Velichko
Date of birth	Juli 22, 1979
Place of birth	Glazov, Russia
Nationality	Russian

### EDUCATION

March 2003 – present	PhD Student, Chair of Functional Materials, Department of Materials Science, University of Saarland. Advisor: Prof. Dr.-Ing. Frank Mücklich
January 2003	Dipl.-Ing. Materials Science and Technology, German-Russian double Diploma. Title: “ <i>Microstructure and high temperature deformation behavior of Mo-alloys</i> ”, Institute of Materials Science, TUBAF, in cooperation with Plansee AG, Reute, Austria
2001-2003	Studies in Materials Science and Technology in Freiberg University of Mining and Technology (TUBAF), Germany
1997-2001	Studies in Materials Science and Technology in Moscow State Institute of Steel and Alloys (Technological University) (MISA), Russia
1995-1996	San Gorgonio High School, San Bernardino, CA, USA Graduate diploma, GPA 3.7
1996-1997 1986-1995	School Nr. 14 with advanced study of foreign language (English), Glazov, Russia

### PROFESSIONAL EXPERIENCE

March 2003 – present	Research and teaching assistant in <i>Introduction of Materials Science</i> and <i>3D Analysis of Mirco- and Nanostructures</i> at the chair of Functional Materials, University of Saarland
March 2003 – present	Member of staff of the internet platform <a href="http://www.materialography.net">www.materialography.net</a> , since 2005: deputy of the scientific supervisor

## *Curriculum Vitae*

- August 2002– Nov. 2002      Assistant in the Institute of Materials Science, TUBAF
- August 2000 – August 2001    Internship at the State Research Institute for Rare-Earth Industry (GIREDMET), Moscow, Russia. Subject: *Powder metallurgical production of the Molybdenum oxide*
- Juli 1999                         Internship at Steel production plant “TulaCherMet”, Tula, Russia

## AWARDS

- 2007                                 DGM-Nachwuchspreis
- 2003                                 Diploma with honors from Moscow State Institute of Steel and Alloys (Technological University)
- 2001-2002                         DAAD (German Academic Exchange Service) scholarship within the double diploma program between TUBAF and MISA
- 2000-2001                         Scholarship of the scientific council of the faculty of Physics and Chemistry of MISA
- 1995-1996                         Scholarship within the exchange program FSA FLEX of US government